ARS JOURNAL

A PUBLICATION OF THE AMERICAN ROCKET SOCIETY

VOLUME 31 NUMBER 4

APRIL 1961

LOS AMOELES PUBLIS LIBRARY

MAY 16 1961

45.00



CONTRIBUTED ARTICLES

Rotating Pendulum Accelerometer . Samuel Schalkowsky and Henry P. Blazes	
Thermostructural Design—Entry Vehicles for Mars and Venus Henry T. Ponsford, Robert M. Wood, Robert E. Lowe and James F. Madewell	474
Importance of Combustion Chamber Geometry in High Frequency Oscillations in Rocket Motors J. R. Osborn and J. M. Bonnell	482
Outer Inviscid Hypersonic Flow With Attached Shock Waves Richard A. Scheuing	
Error Analysis Considerations for a Satellite Rendezvous	505
Ignition of Solid Propellant Rocket Motors by Injection of Hypergolic Fluids . Carl C. Ciepluch, Harrison Allen Jr. and Edward A. Fletcher	514
Optimum Steering Program for the Entry of a Multistage Vehicle Into a Circular Orbit.	518
Accuracy of Measuring Ballistic Missile Trajectories Frank Cooper	523
Escape From Planetery Gravitational Fields by Use of Solar Sails . Norman Sands	527
Ablation Mechanisms in Plastics With Inorganic Reinforcement	532
Size Distribution and Velocity of Ethanol Dropa in a Rocket Combustor Burning	

TECHNICAL NOTES

Some Comparisons of Stashing Behavior in Cylindrical Tanks With Flat and Conical Detections. H. Norman Abramson and Guide E. Ransleben Jr.	542
Wall Pressure Distributions During Sloshing in Rigid Tanks H. Norman Abramson and Guide E. Ransloben Jr.	545
Fluidized Solids as a Nuclear Fuel for Rocket Propulsion L. P. Hatch, W. H. Regan and J. R. Powell	547
Optical Refraction With Emphasis on Corrections for Points Outside the Atmosphere Duane C. Brown	543
Simple Method for Estimating First-Stage Boost Thrust and Specific Impulse . Robert L. Doebler	550
An Approach to Problem of Optimum Rechet Trajectories Samuel E. Monkowitz and Lin Ting	551
Application of the Mangier Transformation in Boundary Layer Flow . S. deSoto and H. Wolf	553
Small MHD Power Generator Using Combustion Gases as an Energy Source G. J. Mullaney and N. R. Dibelius	266
Similar Solutions of the Free Convection Boundary Laver Equations for an Electrically Conducting Fluid . Barry L. Resvee	557
Stability Problem of the Flow With Combustion in Variable Area Duct . Andrzej Kowalewicz	556
Rapid Method for Plug Novale Design	560
Growth of Magnetohydrodynamic Boundary Layers	562
Experimental Study of Combustion Instability in Solid Rocket Propellants	564
Operand Powered Area in an Inverse Square Law Fleid D. F. Lewden	566

DEPARTMENTS

Technical Comments			d												568
Book Notes															
New Patents.															
Technical Literature B															

SPACE POWER SYSTEMS
VOLUME 4, ARS PROGRESS SERIES... 465

PROGRESS IN ASTRONAUTICS AND ROCKETRY

Series Editor

MARTIN SUMMERFIELD

Princeton University

SPONSORED BY THE AMERICAN ROCKET SOCIETY

Volume 5 Electrostatic Propulsion

Edited by
David B. Langmuir
Space Technology Laboratories,
Inc., Canoga Park, California
Ernst Stuhlinger
NASA George C. Marshall Space
Flight Center,
Huntsville, Alabama
J. M. Sellen, Jr.
Space Technology Laboratories,
Inc., Canoga Park, California

A Selection of Technical Papers based mainly on a Symposium of the American Rocket Society held at Monterey, California, November 3, 4, 1960

May 1961, 579 pp., illus., \$5,75

Volume 4 Space Power Systems

Edited by
NATHAN W. SNYDER
Institute for Defense Analyses,
Washington, D.C.

A Selection of Technical Papers based mainly on a Symposium of the American Rocket Society held at Santa Monica, California, September 27-30, 1960

May 1961, 632 pp., illus., \$6.50

Volume 3 Energy Conversion for Space Power

Edited by NATHAN W. SNYDER

A Selection of Technical Papers based mainly on a Symposium of the American Rocket Society held at Santa Monica, California, September 27-30, 1960

March 1961, 779 pp., illus., \$7.25

Volume 2 Liquid Rockets and Propellants

Edited by
LOREN E. BOLLINGER
MARTIN GOLDSMITH
ALEXIS W. LEMMON, JR.

A Selection of Technical Papers based mainly on a Symposium of the American Rocket Society held at The Ohio State University, Columbus, Ohio, July 18, 19, 1960

December 1960, 682 pp., illus., \$6.50

Volume 1 Solid Propellant Rocket Research

Edited by
Martin Summerfield

A Selection of Technical Papers based mainly on a Symposium of the American Rocket Society held at Princeton University, Princeton, New Jersey, January 28, 29, 1960

November 1960, 692 pp., illus., \$6.50



ACADEMIC PRESS

New York and London

111 Fifth Avenue, New York 3, New York

17 Old Queen Street, London, S.W.1

German Agency: Minerva, G.m.b.H., Holbeinstrasse 25–27, Frankfurt am Main Indian Agency: Asia Publishing House, Nicol Road, Ballard Estate, Bombay 1

Space Power Systems

Ediled by NATHAN W. SNYDER Institute for Defense Analyses, Washington, D.C.

This volume completes the publication of papers given at the ARS Space Power Systems Conference held at Santa Monica, California, September 27–30, 1960. Like its companion, Volume 3, Energy Conversion for Space Power, Volume 4 also contains papers invited by the editor in order to extend the coverage of various subjects. The contents of Volume 3 were given in the March 1961 ARS JOURNAL.

Solar Systems

- NATHAN W. SNYDER and RICHARD W. KARCHER, Solar Cell Power Systems for Space Vehicles
- RICHARD W. KARCHER, Solar Cell Power System for Advent
- ROBERT C. HAMILTON, Ranger Spacecraft Power System
- SEYMOUR H. WINKLER, IRVING STEIN, and PAUL WIENER, Power Supply for the Tiros I Meteorological Satellite
- Walter C. Scott, Development of the Power Supply for the Transit Satellite
- W. H. Evans, A. E. Mann, I. Weiman, and W. V. Wright, Solar Panel Design Considerations
- DAVID H. SILVERN, An Analysis of Mirror Accuracy Requirements for Solar Power Plants
- DONALD H. McClelland, Solar Concentrators for High Temperature Space Power Systems
- DAVID L. PURDY, Solar Thermionic Electric Power System
- R. J. Campana and John B. Roes, Preliminary Design and Performance Evaluation Study of a Solar-Thermoelectric Flat Plate Generator
- R. E. HENDERSON and D. L. DRESSER, Solar Concentration Associated with the Stirling Engine
- JAMES A. RUDY, Sunflower Power Conversion System

Nuclear Systems

- H. M. DIECKAMP, The Snap II Concept
- R. D. Keen and R. R. Eggleston, Status of the Snap II Reactor
- D. L. SOUTHAM, Snap II Power Conversion Status
- M. G. Coombs and R. A. Stone, Snap II Radiative-Condenser Design
- D. J. COCKERAM and R. L. WALLERSTEDT, Snap II System and Vehicle Integration
- A. W. THIELE and M. G. COOMBS, Snap Thermoelectric Systems

- V. Keshishian, Shield Design for Snap Reactors
- F. D. Anderson and J. G. Lundholm, Jr., Evaluation of Snap Safety for Space Reactor Application
- P. D. Cohn, The Experimental and Analytical Programs for Re-entry Burnup of Snap Reactors
- J. R. Wetch and J. G. Lundholm, Jr., The Application of Snap Units in Current Space Vehicles
- R. L. Hirsch and J. W. Holland, Problems Associated with the Development of a Thermionic Conversion Reactor
- L. W. Perry and R. W. Pidd, Nuclear Reactor-Thermionic Space Power Systems
- KENNETH P. JOHNSON, Dynamic Versus Direct Conversion
- DAVID L. COCHRAN and KEITH E. BUCK, Boiling vs. Non-Boiling Liquid Metal Cooled Reactors in Rankine Cycle Space Power Plants
- JUSTIN L. BLOOM and JAMES B. WEDDELL, Thirteen-Watt Isotope-Powered Thermoelectric Generators for Space and Lunar Impact Missions
- H. H. GREENFIELD, Optimized Snap III Power Generator Design for Spacecraft
- PAUL J. DICK, Safety Analyses and Tests of a Radioisotope Powered Thermoelectric Generator

Chemical Systems

- Eugene B. Zwick, Chemical-Mechanical Space Power Systems
- James E. Bell and William H. Reid, Cryogenic Tankage for Chemical Space Power Systems

Power Requirements

- HAROLD B. FINGER and FRED SCHULMAN, Power Requirements of the NASA Space Program .
- CURTIS KELLY, Flight Vehicle Power Forecasts



WEATHER EYE"IN SPACE

RCA-NASA Development of TIROS Advances Progress in Worldwide Weather Forecasting

From its vantage point in space, TIROS is sending down to earth new, more definite pictures and data of the world's everchanging weather patterns to aid man in his ageless efforts to control the elements.

Incorporating revolutionary and advanced electronic equipment, TIROS was designed, developed and built by RCA's Astro-Electronics Division for National Aeronautics and Space Administration. Within its small circumference are miniature TV cam-

eras, tape recorders, TV transmitters, command to MEWSceivers, timing mechanisms, beacons and telemetry contribute equipment. In addition, it carries new scanning and non-scanning Infra-red Sensing Devices, developed by NASA, to measure and record the heat radiation of the earth and its cloud cover, and a revolutionary nev RCA deve Magnetic Orientation Device to capitalize on the conic activ effects of the earth's magnetic field and maintain (4,) Defen favorable orientation of the satellite for long per ods





BME'WS—RCA Electronics Equipment and Systems contribute to the alert status of the Nation's vost outer perimeter early warning system.



DAMP—at the Caribbean down-range missile testing "slot," the highly complex DAMP vessel is equipped with RCA electronic tracking devices.



ATLAS—an RCA-developed checkout and launch system reduces substantially the "countdown" period required for launching this missile.

ICA developments in miniaturization, reliability, computing and overall electonic activities are contributing to many of the nation's leading space and missile roje its. For information describing new RCA scientific developments, write Dept.



The Most Trusted Name in Electronics

RADIO CORPORATION OF AMERICA

JOURNA

PUBLICATION OF THE AMERICAN ROCKET SOCIETY

EDITOR

Martin Summerfield

ASSOCIATE TECHNICAL EDITOR

Irvin Glassman Margaret Sherman

MANAGING EDITOR STAFF EDITOR

Barbara Nowak

ART EDITOR

John Culin

ASSOCIATE EDITORS

Igor Jurkevich, G. E. Space Sciences Laboratory, Russian Supplement; George F. McLaughlin, Patents; Charles J. Mundo Jr., Raytheon Co., Guidance; Bernard H. Paiewonsky, Aeronautical Research Associates of Princeton, Flight Mechanics; M. H. Smith, Princeton University, Technical Literature Digest

ASSISTANT EDITORS

Eleanor Rosman, Carol Rubenstein, Estelle Viertel

DIRECTOR OF MARKETING

Owen A. Kenn

ADVERTISING PRODUCTION MANAGER

Walter Brunke

ADVERTISING REPRESENTATIVES

New York

D. C. Emery and Associates 400 Madison Ave., New York, N. Y. Telephone: Plaza 9-7460

James C. Galloway and Co. 6535 Wilshire Blyd., Los Angeles, Calif. Telephone: Olive 3-3223

Chicago

Jim Summers and Associates 35 E. Wacker Dr., Chicago, Ill. Telephone: Andover 3-1154

Detroit

Los Angeles

R. F. Pickrell and Associates 318 Stephenson Bldg., Detroit, Mich. Telephone: Trinity 1-0790

Atlanta

London

Joe H. Howell 1776 Peachtree Bldg., Atlanta 9, Ga. Telephone: 873-2136

B. C. Nichols 151 Fleet St. London E. C. 4, England

American Rocket Society

500 Fifth Avenue, New York 36, N. Y.

Founded 1930

OFFICERS

President Vice-President Executive Secretary Tressurer General Counsel Director of Publications

Harold W. Ritchey William H. Pickering James J. Harford Robert M. Lawrence Andrew G. Haley Irwin Hersey

BOARD OF DIRECTORS

Terms expiring on dates indicated

Ali B. Campbel Richard B. Canright William J. Cecka Jr. J. R. Dempsey Herbert Friedman rge Gerard ert A. Gross

1961 1962 1961

Samuel Herrick Arthur Kantrowitz A. K. Oppenheim Simon Ramo David G. Simons John L. Sloop Martin Summerfield

A. M. Zarem 1963

TECHNICAL COMMITTEE CHAIRMEN

William H. Avery, Ramjets R. M. L. Baker Jr., Astrodynamics G. Daniel Brewer, Solid Propellant Rockets Robert W. Bussard, Nuclear Propulsion

Bernhardt L. Dorman, Test, Operations and Support William M. Duke, Missiles and Space Vehicles

William H. Dorrance, Hypersonics

James S. Farrior, Guidance and Control Herbert Friedman, Physics of the Atmosphere and Space George Gerard, Structures and Materials Martin Goldsmith, Liquid Rockets Andrew G. Haley, Space Law and Sociology John H. Huth, Power Systems

Eugene B. Konecci, Human Factors and Bioastronautics

Frank W. Lehan, Communications and Instrumentation Peter L. Nichols Jr., Propellants and Combustion

Milton M. Slawsky, Magnetohydrodynamics

Herman E. Sheets, Underwater Propulsion Ernst Stuhlinger, Electric Propulsion Scope of ARS JOURNAL

Scope of ARS JOURNAL

This Journal is devoted to the advancement of astronautics through the dissemination of original papers disclosing new scientific knowledge and basic applications of such knowledge. The sciences of astronautics are understood here to embrace selected aspects of jet and rocket propulsion spaceflight mechanics, high speed aerodynamics, flight guidance, space communications, atmospheric and outer space ophysics, materials and structures, human engineering, overall system analysis and possibly certain other scientific areas. The selection of papers to be printed will be governed by the pertinence of the topic to the field of astronautics, by the current or probable future significance of the research, and by the importance of distributing the information to the members of the Society and to the profession at large. at large

Information for Authors

Manuscripts must be as brief as the proper presentation of the ideas will allow. Exclusion of dispensable material and conciseness of expression will influence the Editors' acceptance of a manuscript. In terms of standard-size double-spaced typed pages, a typical maximum length is 22 pages of text (including equations), 1 page of references, 1 page of abstract and 12 illustrations. Fewer illustrations permit more text, and vice versa. Greater length will be acceptable only in exceptional cases.

Short manuscripts, not more than one quarter of the maximum length stated for full

Greater length will be acceptable only in exceptional cases.

Short manuscripts, not more than one quarter of the maximum length stated for full articles, may qualify for publication as Technical Notes or Technical Comments. They may be devoted to new developments requiring prompt disclosure or to comments on previously published papers. Such manuscripts are published within a few months of the date of receipt.

Sponsored manuscripts are published occasionally as an ARS service to the industry. A manuscript that does not qualify for publication, according to the above-stated requirements as to subject, scope or length, but which nevertheless deserves widespread distribution among jet propulsion engineers, may be printed as an extra part of the Journal or as a special supplement, if the author or his sponsor will reimburse the Society for actual publication costs. Estimates are available on request. Acknowledgment of such financial sponsorship appears are so tontote on the first page of the article. Publication is prompt since such papers are not in the ordinary backlog.

sponsorship appears as a footnote on the first page of the article. Publication is prompt since such papers are not in the ordinary backlog.

Manuscripts must be double spaced on one side of paper only with wide margins to allow for instructions to printer. Include a 100 to 200 word abstract. State the authors' positions and affiliations in a footnote on the first page. Equations and symbols may be handwritten or typewritten; clarity for the printer is essential. Greek letters and unusual symbols should be identified in the margin. If handwritten, distinguish between capital and lower case letters, and indicate subscripts and superscripts. References are to be grouped at the end of the manuscript and are to be given as follows. For journal articles: Authors first, then title, journal, volume, year, page numbers; for books: Authors first, then title, journal, volume, year, page numbers; for books: Authors first, then title, publisher, city, edition and page or chapter numbers. Line drawings must be clear and sharp to make clear engravings. Use black ink on white paper or tracing cloth. Lettering should be large enough to be legible after reduction. Photographs should be glossy prints, not matte or semi-matte. Each illustration must have a legend; legends should be listed in order on a separate sheet.

Manuscripts must be accompanied by written assurance as to security clearance in the event the subject matter lies in a classified area or if the paper originates under government sponsorship. Full responsibility rests with the author.

Preprints of papers presented at ARS meetings are automatically considered for publication.

Submit manuscripts in duplicate (orig-inal plus first carbon, with two sets of illustrations) to the Managing Editor, ARS JOURNAL, 500 Fifth Avenue, New York 36, N.Y.

ARS JOURNAL is published monthly by the American Rocket Society, Inc. and the American Interplanetary Society at 20th & Northampton Sts., Easton, Pa., U. S. A. Editorial offices: 500 Fifth Ave., New York 36, N. Y. Price: \$18.00 per year, \$3.00 per single copy. Second-class postage paid at Easton, Pa., with additional entry at New York, N. Y. This publication is authorized to be mailed at the special rates of postage prescribed by Section 132.122. Notice of change of address should be sent to the Secretary, ARS, at least 30 days prior to publication. Opinions expressed herein are the authors' and do not necessarily reflect the views of the Editors or of the Society. @ Copyright 1961 by the American Rocket Society, Inc.

468

ARS JOURNAL

80-0 the of t bilit mer dete tive exte imn acce puls hea inte cou the abo cele phy met to s

T

men

niqu

app

locit

P

Nov

Eng

kow

APE

ran

ure sult

leas

req bili

of t

the

min par nun

S eter

Rotating Pendulum Accelerometer

SAMUEL SCHALKOWSKY1

General Electric Co. Philadelphia, Pa.

HENRY F. BLAZEK²

Ford Instrument Co. Long Island City, N. Y.

This paper describes the basic features of a new class of precision accelerometers particularly adapted to the measurement of slowly varying low level accelerations. The approach involves computation of acceleration from measurements of changes of angular position and time. Emphasis is to be placed upon a comparison of this new approach with the conventional torque-balance technique used extensively in existing accelerometers.

NE DISTINGUISHING feature of inertial accelerometers contemplated for use in space vehicles is the low range of acceleration which they would be required to meas-This, combined with high accuracy specifications, results in the need for a device capable of operation down to at least 10-10 g's with a resolution of something like 10-12 g'srequirements which may well cause one to reassess the suitability of instrumentation techniques used in current state of the art accelerometers.

Specific space vehicle applications for low level accelerometers are many and varied, ranging from attitude control and the monitoring of small thrusts to orbital parameter determination and sophisticated navigation systems (1-4).3 Of particular interest in the past few years (as evidenced by the number of papers presented on this subject) have been the so-called gravity-gradient techniques (1-3). Regardless of the particular system approach, the common characteristics of the latter are that they require inertial sensors with capabilities in the lower end of the acceleration range previously mentioned; in fact, it is the gravity-gradient approach which determines this lower limit and 10-10 g's is more representative of current accelerometer development goals than of the extent of applicability of gravity-gradient sensing. More immediately, however, the lower limit may be influenced by acceleration measurements associated with low thrust propulsion (in the order of fractions of a pound) of relatively heavy vehicles (on the order of 1000 lb or more) for long interplanetary missions.

The rotating pendulum accelerometer4 was evolved in the course of evaluating instrumentation techniques suitable for the measurement of the low level accelerations described above. It is to be noted that the rotating pendulum accelerometer as described herein does not reflect a particular physical device but is, more generally, descriptive of a new method for the instrumentation of an inertial sensor subjected to small acceleration forces. This method involves a fundamental departure from conventional instrumentation techniques utilizing a force or torque balance. In the proposed approach the signal acceleration is derived from angular velocity modulations of the unconstrained rotation of a pendulous mass by means of measurements of time and angular position. This approach is believed to be particularly suitable for the measurement of slowly varying, low level accelera-

The discussion which follows is intended to highlight the contrast between the rotating pendulum and conventional approaches to accelerometer instrumentation. Thus, conventional force and torque-balance methods are described first, followed immediately by the contrasting approach of the rotating pendulum accelerometer. A more detailed analysis of the pendulum motion and a discussion of computation of acceleration from the equations of motions follow. To provide criteria for the evaluation of potential performance capabilities, a generalized performance analysis is described. This is followed by a discussion of pertinent instrument design considerations in terms of application requirements. In conclusion, advantages and limitations of the rotating pendulum approach are given.

Null Method of Measurement

Considering the general category of inertial accelerometers (5), the conventional approach to the instrumentation of this device is that of introducing a constraining force or torque to balance the inertial force or torque generated by the acceleration. An output from the device is then obtained by measuring the constraint.

The above can be illustrated by considering a few specific designs. In the case of the spring-mass accelerometer, for example, the constraining force is provided by a spring and an output is obtained by measuring the distance traveled by the mass against the force of the spring (6). (Alternately, the mass may be driven by a counter force to maintain its null position, in which case the counter force is measured to provide an output proportional to the applied acceleration.) Inasmuch as a linear relationship is desired between acceleration and accelerometer output, the spring gradient (or forcer gradient) must be maintained constant. Extraneous sources of force become a limiting factor regarding performance capability.

Another example involving torque balance is the pendulous integrating gyro accelerometer. In this case a mass imbalance about the gyro output axis is used to generate a signal torque which is then balanced by a gyroscopic torque proportional to the angular rate about the gyro input axis. The measurement of angular position about the gyro input axis thus provides an indication of the integral of the acceleration along the gyro input axis. (This follows from the fact that angular position is the integral of angular precession

Presented at the ARS 14th Annual Meeting, Washington, D. C.,

Nov. 16-20, 1959.

¹ System Project Engineer, Advance Satellite and Probe Engineering, Missile and Space Vehicle Dept. Member ARS.

² Project Supervisor, Aero-Missile Dept.

³ Numbers in parentheses indicate References at end of paper.

⁴ U. S. Patent no. 2,936,624, granted May 17, 1960, S. Schalkowsky, H. Blazek and I. Tolins

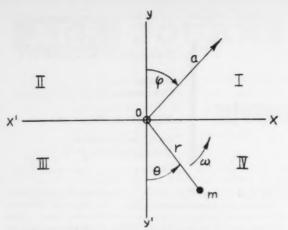


Fig. 1 Idealized configuration of the rotating pendulum

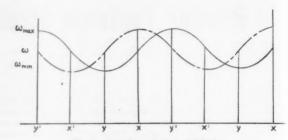


Fig. 2 Angular velocity modulation

rate.) Thus, the balance between inertial torque and gyroscopic torque produces a device which depends upon constant angular momentum to assure linearity, and requires the elimination or reduction of all extraneous torques to assure the desired accuracy.

The principal difference between the foregoing methods and the rotating pendulum approach is that the rotating pendulum accelerometer does not introduce any forces or torques to balance the effect of the signal force or torque. Instead a known, relatively fixed motion is introduced into the device and the acceleration is permitted to alter the nature of this motion. The accelerometer instrumentation then consists of measuring changes of motion. The specific manner in which this is accomplished will be described.

Acceleration-Modulated Angular Rotation

The idealized configuration of the rotating pendulum as shown in Fig. 1 consists of a point mass m suspended from a weightless rigid bar at a distance r from a point 0. The suspension of this bar at 0 is assumed to be frictionless. pendulum is made to rotate at a constant angular velocity ω . In the absence of external forces this idealized configuration will, of course, continue to rotate at a constant rate.

The effect of an acceleration occurring in the plane of the paper will now be considered. With the directions of ω as previously shown and $\varphi = 0$, the mass m will slow down as it goes from y^1 through x to y and, similarly, it will speed up as it proceeds from y through x^1 to y^1 . The manner in which ω is thus modulated is shown in Fig. 2.

The dotted curve shows the modulation which would occur if the applied acceleration were directed along xx^1 . The sensor is thus capable of measuring both the magnitude and direction of acceleration, with the magnitude related to the amplitude of the modulation, and the direction indicated by the phase of the modulation.

Analysis of Pendulum Motion

Undamped Case

Although the condition of zero damping in the bearing is not physically attainable, it is nevertheless useful to study the motion of the undamped pendulum since it represents a limiting condition which can be approximated in practice. The extent of this approximation will be discussed later, along with the introduction of the additional torque needed to overcome losses so as to sustain the constant rotation of the unbalanced mass.

If the undamped pendulum is subjected to an acceleration a, then the equation of motion in terms of torque is as indicated in Equation [1] (see Fig 1, $\varphi = 0$)

$$I(d^2\theta/dt^2) + mar \sin \theta = 0$$
 [1]

wh firs

the

dri

for

as

me

po

ap

the

cu

by

of

tio

the

Although Equation [1] describes the motion of the pendulum for an acceleration input, the same equations apply equally well throughout if a is defined as acceleration minus gravitation. If Equation [1] is multiplied by the identity

$$(d\theta/dt)dt = d\theta$$

and the resulting equation integrated then one obtains the energy form of the equation of motion. Performing these operations yields

$$I\frac{d^2\theta}{dt^2} \cdot \frac{d\theta}{dt} dt + mar \frac{d\theta}{dt} \sin \theta dt = 0$$
 [2]

Integration of Equation [2] with the initial condition as indicated below yields

$$(1/2)I(d\theta/dt)^2 + mar(1 - \cos\theta) = (1/2)I\omega_0^2$$
 [3]

where ω_0 = initial angular velocity at $\theta = 0$ and t = 0.

Equation [3] expresses the principle of the conservation of energy. The first and second terms on the left-hand side of the equation represent the kinetic and potential energy, respectively. As may be seen from Equation [3], the sum of the kinetic and potential energy is equal to a constant.

Solution of Equation [3] for the angular velocity yields

$$\frac{d\theta}{dt} = \sqrt{\omega_0^2 + \frac{2mar}{I} \left[\cos \theta - 1\right]}$$
 [4] Equation [4] may be integrated by separating the vari-

ables; thus

$$dt = \frac{d\theta}{\sqrt{\omega_0^2 + (2mar/I)(\cos\theta - 1)}}$$
 [5]

Equation [5] may now be placed in the standard form of the elliptic integral of the first kind by substitution of the following relations

$$\cos \theta = 1 - 2\sin^2(\theta/2) \qquad \psi = \theta/2 \qquad [6]$$

Thus

$$dt = \frac{2}{\omega_0} \frac{d\psi}{\sqrt{1 - K^2 \sin^2 \psi}}$$

where

$$K^2 = 4mar/I\omega_0^2$$

The solution to Equation [6] for $K^2 < 1$ is therefore

$$t = \frac{2}{\omega_0} F\left(K, \frac{\theta}{2}\right) \tag{7}$$

where $F[K,(\theta/2)]$ represents the elliptic integral of the first kind. The limitation $K^2 < 1$ is satisfied when the pendulum is executing complete revolutions. For $K^2 > 1$ the pendulum will oscillate rather than rotate.

Maximum and minimum values of the angular velocity are given by

$$\omega_{\text{max}} = \omega_0 \qquad \omega_{\text{min}} = \sqrt{\omega_0^2 - 4mar/I}$$

General Case

The equation of motion for a practical accelerometer configuration must include the effects of viscous friction in the bearing of the rotating pendulum as well as the constant driving torque needed to sustain the rotation against the foregoing and related frictional losses. The general equation of motion therefore takes the following form

$$I\frac{d^2\theta}{dt^2} + C\frac{d\theta}{dt} + mar \cdot \sin(\theta + \varphi) = T_d$$
 [8]

where

C = viscous damping coefficient

 T_d = driving torque

Equation [8] does not yield to a closed form solution of θ as a function of time. However, the use of numerical methods in conjunction with digital computations makes possible an analysis to any desired accuracy. This latter approach was successfully used during initial evaluation of the rotating pendulum approach; however, this process is cumbersome. A particularly useful solution which provides good accuracy when the modulation is low may be obtained by considering the signal torque to be a sinusoidal function of time rather than angle of rotation. The modified equation of motion is thus obtained by substituting $\theta = \omega_a t$ in the sinusoidal term of Equation [8].

$$I\frac{d^{2}\theta}{dt^{2}} + C\frac{d\theta}{dt} + mar \cdot \sin(\omega_{a}t + \varphi) = T_{d}$$
 [9]

 ω_a in Equation [9] is related to the period of revolution. Denoting this period by τ

$$\omega_a = \frac{2\pi}{\tau} \approx \frac{T_d}{C}$$
 (angular velocity for $a = 0$)

If the acceleration a is considered constant then Equation [9] is a linear differential equation with constant coefficients.

The steady-state solutions for θ and $\dot{\theta}$ are

$$\theta = \omega_a t + \frac{mra}{I\omega_a^2 \sqrt{1 + C^2/I^2\omega_a^2}} \times \\ \sin\left[\omega_a t + \varphi + \tan^{-1}\frac{C}{I\omega_a}\right] - \frac{mra}{\omega_a C}\cos\varphi \quad [10]$$

$$\dot{\theta} = \omega_a + \frac{mra}{I\omega_a \sqrt{1 + C^2/I^2\omega_a^2}} \times$$

$$cos \left[\omega_a t + \frac{C^2}{I \omega_a} \sqrt{1 + C^2/I^2 \omega_a^2} \right]$$

$$cos \left[\omega_a t + \varphi + \tan^{-1} \frac{C}{I \omega_a} \right]$$
 [11]

As will be shown in the following section on the computation of acceleration, use of the modified equation of motion (Eq. [9]) does not appreciably degrade the accuracy of computation for reasonable modulations of angular velocity. In addition, the modified equation of motion and relationships derived from it are very helpful in presenting the interrelation of pertinent parameters of the rotating pendulum accelerometer. The validity of these interrelationships and conclusions reached from them, has been confirmed by a detailed analysis of the exact equation of motion (Eq. [8]).

Computation of Acceleration

As previously described, the signal acceleration is contained in the modulations of the angular velocity. This information must therefore be extracted from observations of the pendulum motion; there are a number of ways in which this could be accomplished. The direct approach would, of course, be that of measuring angular velocity as a function of angular position. It is felt, however, that neither the present nor the projected state of the art of measuring angular velocity is adequate to exploit fully the potential of the rotating pendulum approach. In contrast, recent advances and continuing developments in the field of precision time measurement make an alternate transducer approach highly desirable. Specifically, it is proposed to transform the angular velocity modulation data into time signals of variable duration, as measured over a fixed angular displacement.

The manner in which the time signals are to be obtained can best be described by referring to Fig. 1. Based upon considerations of symmetry it is readily seen that for C=0 and $\varphi=0$ the pendulum will have its maximum angular velocity as the center of gravity passes through $0y^1$. Similarly the pendulum will have its minimum angular velocity as the center of gravity passes through 0y. It follows, therefore, that the pendulum c.g. will travel through quadrants III and IV in less time than it takes to travel through quadrants I and II, and that the difference in the time Δt will be related to the acceleration.

This refers to time measurements for 180 deg of pendulum rotation. This choice is made so that by measuring the largest suitable angle a fixed angular error will result in the smallest percentage error in the measurement. Practically, however, two signals per revolution will be inadequate to uniquely define both the magnitude and direction of the acceleration. Thus the actual transducer will provide two pairs of such measurements, space-phased 90 deg with respect to each other.

In general, the form of the desired equation relating the acceleration to the measured quantities is

$$\bar{a} = f(\Delta t_1, \ \Delta t_2, \ \tau) \tag{12}$$

where, with reference to Fig. 1

 Δt_1 = time to traverse quadrants II and III minus time to traverse quadrants I and IV

 $\Delta t_2 = ext{time to traverse quadrants I and II minus time to traverse quadrants III and IV}$

= period of rotation

 component of the vector acceleration normal to the axis of rotation

A solution for the acceleration having the form of Equation [12] may be obtained by applying the approximation to the general equation of motion previously described. This yields the following explicit solution for t

$$t = \frac{\theta}{\omega_a} - \frac{mar}{I\omega_a^3 \sqrt{1 + C^2/I^2\omega_2^2}} \times \sin\left[\theta + \varphi + \tan^{-1}\frac{C}{I\omega_a}\right] + \frac{mar}{\omega_a^2 C}\cos\varphi \quad [13]$$

⁵ The authors are indebted to W. Newell for suggesting this approximation and for pointing out the convenience of its use. This suggestion has resulted in the rewriting of the analytical portion of this paper, originally based upon digital computer solutions of Equation [8].

From Equation [13] one may obtain equations for Δt_1 and Δt_2 which may then be solved simultaneously for a and φ . The result is

$$a = \frac{I\omega_{a}^{3} \sqrt{1 + C^{2}/I^{2}\omega_{a}^{2}}}{4mr} \sqrt{\Delta t_{1}^{2} + \Delta t_{2}^{2}}$$
[14]

$$\varphi = \tan^{-1} \frac{\Delta t_2}{\Delta t_1} - \tan^{-1} \frac{C}{I\omega_2}$$
 [15]

where, as previously defined

$$\omega_a = 2\pi/\tau \tag{16}$$

Equations [14–16] are the equations which enable one to compute both the magnitude and phase of the applied acceleration in terms of measurements of time.

To check the validity of the approximate solution, Equation [8] was solved numerically on a general purpose digital computer for a specific design configuration. A table of the per cent errors in the magnitude of the computed acceleration is shown for two different values of modulation as indicated by the ratio $\sqrt{\Delta t_1^2 + \Delta t_2^2/\tau}$

$$\sqrt{\Delta t_1^2 + \Delta t_2^2}/\tau$$
 Per Cent Error 0.05 0.193 0.0023

As may be seen from the errors tabulated, the accuracy of the approximate solution is good even at relatively high modulations, and very good when the modulation is small.

Performance Analysis

It was stated earlier that the rotating pendulum accelerometer departs from conventional methods in that it does not require a null balance between the signal torque and a constraining torque as a condition for obtaining a true indication of the signal acceleration. The balance of torques and the corollary requirement to eliminate all extraneous torques which affect this balance provide definite criteria for the evaluation of different design configurations. Performance of the rotating pendulum accelerometer, on the other hand, must be evaluated by considering all pertinent parameters which constitute its equation of motion. We shall now consider these parameters.

Damping

As may be observed from Equation [11] the effect of damping is to reduce the amplitude of the sinusoidal component of the angular velocity by a factor x, and shift its phase by an angle δ , where

$$x = \frac{1}{\sqrt{1 + C^2/I^2 \omega_a^2}}$$
 [17]

$$\delta = \tan^{-1} C/I\omega_{\rm e} \tag{18}$$

Equations [17 and 18] may be expressed completely in terms of parameters having the dimensions of time by noting that the ratio L/C is equal to the pendulum time constant T in a zero g environment (or the time constant of a balanced cylinder having the same inertia), and by substituting $2\pi/\tau$ for ω_a

$$1/x = 1/\sqrt{1 + (\tau/2\pi T)^2}$$
 [19]

$$\delta = \tan^{-1} \left(\tau / 2\pi T \right) \tag{20}$$

The ratio $\tau/2\pi T$ may be made quite small in any application by selecting the period of rotation τ to be on the order of seconds, and the time constant T to be on the order of minutes. When these conditions are satisfied, the effect of the damping on the amplitude of the modulation is negligible

and the phase shift is on the order of 0.1 deg. The significance of the ratio $\tau/2\pi T$ to performance derives from the fact that if the ratio is small then the errors in the computed acceleration resulting from deviations of the damping from the nominal design value may be made negligible.

Ch

bas

cel

fro

Ho

onl

sta

of

tra

of

lim

211

har

ma

tin

rai

tio

tio

ius

Th

mı

ch

the

no

vio

of

for

no

of

A

The air bearing is one type of suspension in which a time constant of the order of several minutes may be readily obtained with conventional design techniques.

Driving Torque

As may be seen from Equations [14–16] the computation of acceleration does not require a knowledge of the driving torque. This is true because the effect of the driving torque is taken into consideration by using a measured value of the period of rotation τ , obtained by the addition of time measurements over two consecutive 180-deg angles. Because the computed acceleration is not directly determined by the driving torque, it is evident that deviations of the driving torque from its nominal value will not result in the generation of errors.

Period of Rotation

For the condition of low modulation the period of rotation is directly proportional to the damping C and inversely proportional to the driving torque T_d . Inasmuch as the equation for the computed acceleration makes use of a measured period rather than an assumed period, no error is generated as a result of deviations of the period from its nominal value.

Pertinent Design Considerations

In designing a rotating pendulum accelerometer for a specific application the normal type of compromise must be made among the requirements for accuracy, dynamic range, dynamic response and sensitivity. These design parameters and their interrelation will be discussed.

Linearity

Although the rotating pendulum accelerometer is basically a nonlinear device, it does behave in a linear manner when the modulation is small. Its linear properties are most readily seen by resolving the computed acceleration from Equations [14 and 15] into components along the y'y and x'x axes of Fig. 1. Thus, if the small phase shift due to damping is neglected for the moment⁶

$$a_{s's} = a \cos \varphi = a \frac{\Delta t_2}{\sqrt{\Delta t_1^2 + \Delta t_2^2}}$$
 [21]

$$a_{y'y} = a \sin \varphi = a \frac{\Delta t_1}{\sqrt{\Delta t_1^2 + \Delta t_2^2}}$$
 [22]

Substitution of the value of acceleration from Equation [14] into Equations [21 and 22] yields

$$a_{z'z} = (I\omega_a^3/4mr)\Delta t_2$$
 [23]

$$a_{y'y} = (I\omega_a^3/4mr)\Delta t_1$$
 [24]

Thus, within the accuracy of the approximate solution of the equation of motion, acceleration is a linear function of the time measurements. As previously noted, the validity of the approximation, and hence also the above conclusion regarding linearity, is bounded by the requirement that angular velocity modulations be small.

 $^{^6}$ It may be noted that this phase shift could be taken into consideration by a rotation of the transducer which detects the time difference. The magnitude of rotation could be based upon nominal values of C and $a,\,$

Choice of a Suitable Period

For a given configuration and for fixed transducer and time base accuracy the sensitivity of the rotating pendulum accelerometer is determined primarily by the period. Hence, from the point of view of sensitivity a long period is desirable. However, the nature of the device is such that it is suitable only for measuring an acceleration which is essentially constant over a full revolution. If the acceleration is changing, the period must be made small enough so that the acceleration is essentially constant over a full revolution. The choice of period is therefore a compromise between sensitivity and transient response.

Relation Between Dynamic Range and Precision of Measurement

The maximum acceleration input to the accelerometer is limited by the requirement to sustain rotation of the cylinder and considerations of linearity as described. On the other hand, the minimum input is determined only by the precision of the measurement of angular position and time. It may be further noted that the maximum magnitude of the time difference Δt depends also upon the period which is determined by the transient response. The useful dynamic range of the instrument is therefore determined by considerations of linearity, precision of measurement and transient response.

Conclusions

Although the rotating pendulum accelerometer has not been sufficiently developed to permit a comprehensive evaluation of its merits based upon test data, analytical studies justify the following conclusions:

The rotating pendulum accelerometer is particularly suited to the measurement of slowly varying accelerations. This restriction permits the selection of relatively long modulation periods, resulting in a device having a sensitivity much superior to conventional accelerometers.

2 The rotating pendulum accelerometer is not sensitive to changes in torques of a d-c nature. As discussed in the text, the driving torque may change during operation from the nominal design value without affecting the output of the de-This is obviously true for any torque having the form of the driving torque, such as torque due to coulomb friction, for example. The only restriction is that this torque should not have components which vary proportionally to the sine of the angle. The latter torques would, of course, be mistaken for signal torques

3 The rotating pendulum accelerometer is not subject to

the error introduced in conventional accelerometers by the interposition of an intermediate quantity, such as a spring constant or torquer gradient, between the acceleration signal and the measurement which constitutes the output of the device. Associated with this interposed quantity is a calibration requirement, the accuracy of which directly affects overall performance. In the case of the rotating pendulum accelerometer the direct effect of the signal acceleration is to change the time it takes to traverse alternate halves of the pendulum rotation. This time difference is also the direct source for obtaining an output—there is no quantity between these two dependent upon calibration of a physical phenomenon such as a spring or a torquer.

4 Accuracy of the rotating pendulum accelerometer is to a large degree dependent upon the accuracy of the time base and related transducer timing circuitry. Since the state of the art in these latter areas is the subject of considerable attention as a part of efforts in the field of digital computations, it is felt that the rotating pendulum accelerometer is tied to an advancing technology, much in the same manner as null-type devices benefited from the development of servo technology.

In conclusion it is to be noted that the rotating pendulum accelerometer is not necessarily restricted to applications for which the assumption of constant acceleration over the full period of rotation is exactly valid. This assumption simplifies instrumentation and certainly makes possible a more concise analysis. However, more complex configurations should be considered in conjunction with specific application requirements. The principal purpose of this paper has been to point out the basic concepts associated with this new method of accelerometer instrumentation.

Acknowledgments

The authors wish to acknowledge the contribution of the various engineers at the Ford Instrument Co. who participated in the development studies upon which the material presented herein is based. As previously noted, the authors are particularly indebted to W. Newell for suggesting the use of the approximate solution of the general equation of motion.

References

- 1 Crowley, J. C., Kolodkin, S. S. and Schneider, A. M., "Some Properties of the Gravitation Field and Their Possible Application to Space Naviga-
- ties of the Cravitation Field and Their Possible Application to Space Naviga-tion," Fifth Annual Conference Proceedings, East Coast Conference on Aeronautical and Navigational Electronics, 1958.

 2 Streicher, M., Zehr, R. and Arthur, R., "An Inertial Guidance Tech-nique Useable in Free Fall." IRE, Third National Convention on Military Electronics, June 1959.
- Electronics, June 1959.
 3 Carroll, J. J. and Savet, P. H., "Space Navigation and Exploration by Gravity Difference Detection," Aerospace Engng., July 1959, pp. 44-47.
 4 Oberth, M., "A Precise Attitude Control for Artificial Satellites," Vistas in Astronautics (International Series of Monographs on Aeronautical Sciences and Space Flight, Division VII, Astronautics Div. Vol. I); Perganus Percent Levice, 1982.
- TAS 25th Annual Meeting, January 28-31, 1957. Also SMF Fund Paper no. FF-16 published by IAS.

 6 Wyckoff, R. D., "The Gulf Gravimeter," Geophys. vol. 6, 1941, p. 13.

⁷ In instrumenting the computation of the rotating pendulum accelerometer it is possible to include a correction based upon the assumption that the rate of change of the signal acceleration was constant. The correction would utilize differences in the computed accelerations of consecutive periods of rotation

Thermostructural Design-**Entry Vehicles for Mars and Venus**

HENRY T. PONSFORD,2 ROBERT M. WOOD,3 ROBERT E. LOWE⁴ and JAMES F. MADEWELL⁵

(100,000)

tr

228

CC

aı

di

tr

di

su

in

er

hi

62

C

sic

it

A

Douglas Aircraft Co. Santa Monica, Calif.

The objectives of this paper are twofold: to present a general method of designing a minimum weight insulated structure, and to illustrate this method using entry probes for Mars and Venus as examples. These themes are intermingled as follows: the performance and flight mechanics are related to the mission objectives. The thermodynamic environments for the example vehicles are discussed, methods are described for computing transient structural temperatures, and thermal results for different insulations are presented. Material and strength criteria for high temperature structures are considered, promising structural configurations are presented for entry vehicles, and the most suitable types for the example vehicles are evolved. The thermal results are then considered together with the structural results to produce the lowest weight design, and these methods are then generalized for application to any mission with any heating. Finally, the numerical results are presented to yield a typical design for the entry bodies.

The Missions and Their Environment

Interplanetary Transfer Trajectories

THIS STUDY was undertaken using present state of the art booster systems and specific launch dates and velocities (3). The basic ground rules were as follows:

1 The probe will impact the target planet within two times the minimum separation distance between that planet and Earth to simplify communication.

The probe will have a gross weight of 400 lb.

The probe will decelerate to a subsonic terminal velocity high in the atmosphere to maximize data transmission time.

4 The probe will have a midcourse guidance correction system.

5 The design will consider conditions of a system entering the planetary atmosphere with and without terminal guidance.

The entry conditions (4) studied on the individual planets were 29,500 and 38,000 fps, respectively, for Mars and Venus. These entry velocities are greater than the Hohmann minimum energy transfer impact velocities in each case. This increase in impact velocity above the Hohmann transfer condition is necessary in order to be compatible with the "within two times the minimum separational distance" ground rule.

Planetary Atmospheres

It is necessary to estimate the physical and chemical properties of the atmospheres of Mars and Venus in order to determine the trajectories, loading, and thermal environment of the capsule. The assumptions for the atmosphere of Mars (5) are believed to be sound because they are primarily based on direct visual observations. The assumptions for Venus (6), however, are partly founded on a theory of evolution rather than experiment. One of the primary objectives of such a probe will be to verify or disprove atmospheric assumptions.

Of prime importance to the calculation of heat transfer is the assumption of density distribution. The assumption used in this analysis is the classical isothermal atmosphere in which the density varies exponentially with altitude.

The Martian atmosphere is more dense in its upper reaches than is either the Terrestrial or the Venusian. Also, the mass of the atmosphere is more uniformly distributed between the high and low altitudes. Consequently, the deceleration of a descending vehicle on Mars is more gradual and the heat transfer rate less severe during entry into the Martian atmosphere than into the Terrestrial atmosphere. On the other hand, convective heat transfer during Venus entry should be somewhat similar to Earth entry.

Atmospheric Entry Trajectories

Atmospheric entry trajectories were obtained for weight to drag ratios (W/CDA) varying from 10 to 1000 lb per ft2 and for a range of entry angles. Representative trajectories showing velocity vs. altitude for Mars and for Venus are shown in Fig. 1. It can be seen that a probe decelerates at a higher altitude in the Martian atmosphere than in the Venusian for a given W/C_DA .

Ballistic entry trajectories for a point mass were calculated for entry at 29,500 and 38,000 fps for Mars and Venus, respectively. A spherical planet-atmosphere model was

This paper is a condensation of a more complete version presented at the ARS Structural Design of Space Vehicles Conference, Santa Barbara, Calif., April 6-8, 1960, which is available as ARS preprint 1092-60 or Douglas Engineering Paper 976.

¹ The philosophy of the paper is an extension of the method of Ponsford and Wood (1), who presented a technique of thermostructural design using the Nike Zeus structure as an example. To remove security restrictions, this paper has made use of the unclassified work by Lowe on entry vehicles for Mars and Venus (2). To emphasize the required marriage of thermal and structural factors in modern design, the authors have intentionally used the word "thermostructural."

² Chief, Structures Section, Missiles and Space Systems Engineering Department.

neering Department.

Chief, Thermodynamics and Nuclear Science Section,
Missiles and Space Systems Engineering Department. Member

Assistant Supervisor, Thermodynamics and Nuclear Science Section, Missiles and Space Systems Engineering Department.

Formerly, Designer, Structures Section; presently with Chrysler Corp., Huntsville, Ala.

Numbers in parentheses indicate References at end of paper.

474

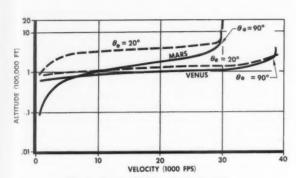


Fig. 1 Atmospheric entry trajectories

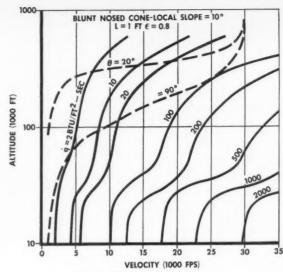


Fig. 2 Mars local heating rates

used rather than the usual flat one because of the low angle trajectories that were considered.

Entry Environment

The prime design considerations for an atmospheric entrance vehicle are the severity of the thermal environment and the magnitude of the pressure and deceleration loadings. These two considerations will be discussed in that order.

Two types of heat transfer to entry bodies predominate: convective heat transfer, which is caused by gaseous compression and viscous skin friction; and radiative heat transfer, caused by electromagnetic radiation from the hot, ionized gases behind the bow shock wave. In order to show a first-order approximation of this environment, lines of constant convective heat flux rate are plotted as a function of altitude and velocity for Mars, in Fig. 2. Radiative heating will be discussed in more detail in the second section. Since the trajectory angle has a large effect on the heat flux rate, two different trajectories with entry angles of 20 and 90 deg are superimposed on the heat rate map.

The pressure and deceleration loading is also greatly influenced by trajectory entry angle. Stagnation pressure histories for a range of entry angles for both Mars and Venus entry are shown in Fig. 3. It can be seen that a 90 deg entry results in stagnation pressures of 9200 and 72,000 lb per ft² for Mars and Venus, respectively. Deceleration histories indicate values of 2000 and 13,800 ft per sec² resulting from 90 deg entry for Mars and Venus, respectively, or 62 and 430 Earth g's.

Configuration

The system of effectiveness of a spacecraft for a given mission is a measure of the weight of the useful payload that it can deliver. An ideal design is possible only after analysis of a variety of vehicles to determine the tradeoffs between varying geometric, stability, loading and thermal environmental conditions.

A configuration having a blunt nose and high form drag was used in this study. The planform configuration with its associated flowfield is shown in Fig. 4. It should be

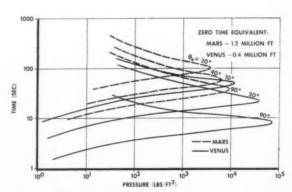


Fig. 3 Mars and Venus entry-stagnation pressure loading

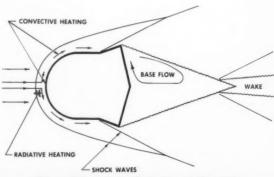


Fig. 4 Entry body configuration and flow field

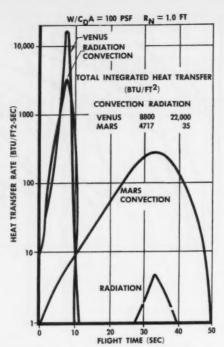


Fig. 5 Heat transfer rate, nose stagnation point

pointed out that this configuration is not necessarily optimum for both Mars and Venus entry conditions because the predominating mode of heat transfer differs for the two planets. However, this configuration is a good compromise choice to illustrate the thermostructural design method.

Thermodynamic Analysis

The overall objective of an entry probe is to receive data from the sensory equipment; thus, the specific objective of the thermostructural design is to keep this equipment functioning, or in other words, to keep the high energy gases out. The thermal protection keeps the structure strong enough and cool enough to do this. If the best structural temperature happens to be high, then additional internal thermal insulation must be provided for the equipment. The additional weight of this insulation should be accounted for in a detailed design study. However, to illustrate the main points of this paper, the thermodynamic considerations will be restricted to a discussion of the methods used to compute the external radiative and convective heat transfer to the surface of the vehicle and the determination of the resulting structural temperatures as a function of time for specific materials.

The thermodynamic analysis proceeds in three main phases: The calculation of the fluid properties outside of the boundary layer from the known atmospheric properties, velocity and altitude of the vehicle as a function of time; the calculation of the net heat flux into the surface of the material, including radiation to and from the surface and mass transfer effects associated with a decomposing insulator; and the calculation of the time histories of temperature distribution in the insulator and structure.

Convective Heat Transfer

Inviscid perfect gas relations are used to get the properties behind the shock wave, using values of γ appropriate for Mars or Venus atmospheres. In spite of these very high apparent temperatures, the enthalpy is correctly computed and the high fictitious temperatures do not cause trouble for convective heating calculations. These values are then used in conjunction with the Crocco-Van Driest solution to the boundary layer equations, according to the treatment of (7 and 8). An alternate method based on real gas assumptions has been presented by Fay and Riddell (9,10). For stagnation point heating, the flow is always laminar and does not depend on any dimension except nose radius. For positions away from the stagnation point, a pressure which depends on local slope is calculated from the modified Newtonian theory. The modified Newtonian pressure is phased into a Prandtl-Meyer expansion when the pressure gradients are equal, as suggested by Lees (11). If the surface material ablates, the mass transfer effect is taken into account at each time increment by correcting the zero mass transfer Stanton number for the instantaneous blowing (or ablation) rate, using the theory of Rubesin and Pappas (12).

Radiative Heat Transfer

It will be seen that radiation during Venus entry is of paramount consideration, whereas for Mars it is less important. This is a result of the greater kinetic energy of the Venus probe at entry. Because of the greater concentration of carbon dioxide and its lower ionization potential, the method utilized to determine the radiative heat transfer is, therefore, illustrated for CO₂. Each step to determine the radiative transport is covered in detail in (2).

From the energy and momentum equations, solved in conjunction with the Hugoniot shock relations, the stagnation pressure and enthalpy can be determined. Thus with the stagnation pressure and enthalpy known, the real gas stagnation temperature can be determined from a Mollier diagram (13). This is necessary if the Stefan-Boltzmann radiation law is used. It is assumed that either the acceleration or capture of an electron by an atom or ion will give off the same amount of average energy whether the process involves an oxygen, nitrogen or carbon species. This assumption permits utilization of the extensive emissivity data for air that are available. The emissivity data for the air must be corrected, however, for use with CO2. This is accomplished by forming the molar ratio of the ion concentration of carbon dioxide (Nco2) to the ion concentration of air (Nair) at a given temperature and pressure. The ion concentration may be found from the ion concentration for carbon dioxide (13) and for air (14). Thus, the carbon dioxide emissivity per unit length can be scaled as follows

$$(\epsilon/L)^* = (\epsilon/L)(N_{\rm CO2}/N_{\rm air})$$

where L is the shock detachment distance, given by

$$L = R_N \frac{\rho_\infty/\rho_s}{1 + \sqrt{2\rho_\infty/\rho_s}}$$

which is suggested by Hayes in (15) and agrees with experimental data. The value of ϵ/L for air (16) can be determined in terms of the temperature in degrees Kelvin and the ratio of local density to stagnation density. From the Stefan-Boltzmann law and the definition of ϵ , $q/L = (\epsilon/L)^*\sigma T_s^4$. The heat flux rate \dot{q} can now be calculated knowing the shock detachment distance L. These calculations were performed for each of the trajectories and result in the radiative heat flux as a function of time.

Comparison and Results

Fig. 5 gives the convective and radiative heat flux rates as a function of time for the stagnation point of the entry bodies for an entry angle of 90 deg. Important points to notice are: The duration of the heat pulse on Venus is one tenth

NOS

that Ven radi vect diffe The com Fig. para T

mate Fig. entry nylo case insulan e anal temp ness nect

N para any dete appl crite a w resu restricted

T appl of b

From

bone

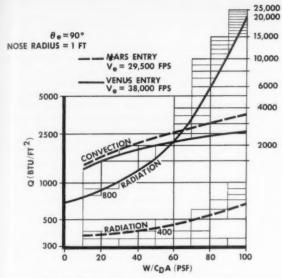


Fig. 6 Stagnation point heat transfer modes

that for Mars (3 sec vs. 30 sec); total radiation input for Venus is about three times as much as convection; total radiation input for Mars is less than $\frac{1}{20}$ as much as convection. This reversal of transport modes could lead to different design solutions for probes for the two planets. The variation of both the radiative and convective heat components for Mars and Venus with W/C_DA are given in Fig. 6, which shows that the radiative heat input becomes paramount on Venus at high W/C_DA .

The end objective of the thermodynamic analysis is a parametric presentation of the thickness of insulation required to keep any selected type and thickness of structural material down to a selected maximum working temperature. Fig. 7 shows the maximum aluminum temperature during entry as a function of aluminum thickness and phenolic nylon thickness for a 90 deg entry angle. The 20 deg entry case is a more difficult thermal problem and results in more insulation for the same structure temperature. Fig. 7 is an example of the final product of a thermodynamic design analysis; it is the parametric connection between structural temperatures, structural thicknesses and insulation thicknesses. These thermodynamic results can now be connected with the structural requirements.

Structural Analysis

Now that methods have been developed to describe parametrically the weight of insulation required to guarantee any arbitrary structural temperature, the next step is to determine the weight of structure required to withstand all applied loads. The structural analysis must consider failure criteria, material properties and structural configurations in a way which can be combined with the thermodynamic results. As in the preceding section, consideration will be restricted to the spherical nose shell as an example of the general principles.

Design Criteria and Material Properties

The nose shell can fail in several modes, but since the applied loads are compressive, all failures result in some type of buckling. The amount of tolerable local skin buckling has been set at zero in order to guarantee the integrity of the bond between the structure and the insulative coating. From a structural standpoint, this criterion may be slightly

conservative for some materials, but any other assumption would open up a number of aerodynamic and thermodynamic problems at only a small possible profit. Therefore, the principal design criterion for the hemispherical nose shell is that it be completely buckle-resistant.

At this point in the design, many materials can be considered. They run the spectrum from such exotics as beryllium and molybdenum to the old standbys, aluminum and steel. The prime material properties affecting the design are the modulus of elasticity, the compressive yield stress and the density. It will be necessary to consider several materials over a large range of temperatures, since the modulus of elasticity varies widely with temperature (17,18). Fig. 8 is an isochronous stress-strain curve which shows the effects of time at a given temperature and various stresses on the properties of 2024-T81 aluminum, with the conventional 0.2 per cent offset indicated. Curves of this type for other temperatures and for other materials are used in calculations to obtain required structural thicknesses.

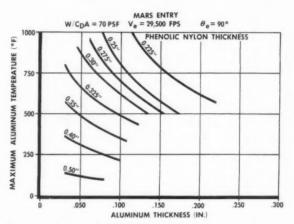


Fig. 7 Effect of insulation thickness on aluminum temperature

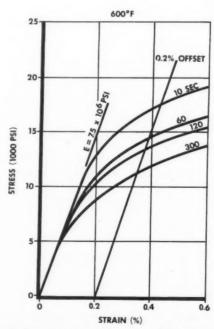


Fig. 8 Isochronous stress-strain curves, 2024-T81 aluminum alloy sheet

SURFACE MATERIAL	SUB-SURFACE MATERIAL	LOAD-BEARING STRUCTURE
METAL	SOLID METAL	MONOCOQUE
TEMPERATURE-RESISTANT INSULATOR	SOLID INSULATOR	SEMI-MONOCOQUE
ABLATING INSULATOR	CELLULAR INSULATOR	HONEYCOMB

Fig. 9 General types of thermostructural configurations

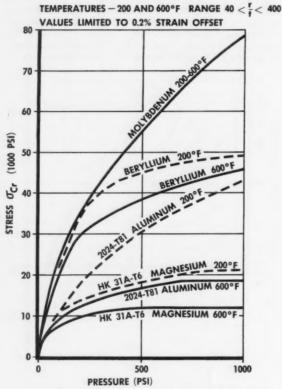


Fig. 10 Spherical shells under external pressure

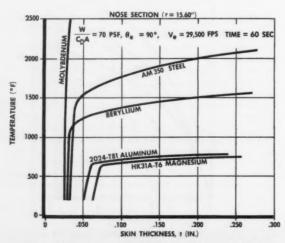


Fig. 11 Mars entry-required structural skin thickness

Possible Structural Configurations

It is apparent that many different combinations of load carrying structure and insulator can be used. Fig. 9 lists a number of possible combinations of configurations, described by outer surface material, subsurface insulating technique and underlying load bearing structure. They each have advantages and disadvantages for particular applications and naturally depend upon the quantitative value of their physical constants. Fig. 9 shows several thermostructural configurations possible for certain areas of the interplanetary probe. They are a monocoque structure covered either with an ablative or a temperature-resistant insulation, or a combination of the two; a semimonocoque structure with similar insulation; and a metal honeycomb covered by an insulator.

The external pressure load on the nose section of the probe is a modified Newtonian distribution. Nevertheless, this distribution has been assumed to be uniform to simplify the calculations. The most reasonable types of construction for the nose section are the monocoque and the honeycomb sandwich. Fig. 10 is a plot of buckling stress σ_{cr} vs. pressure P for a spherical shell under external pressure and in the radius to thickness range shown. These curves were determined from the equation

$$\sigma_{\rm cr} \ = \ 0.6985 P^{0.556} E^{0.444}$$

This equation was derived from the equations and graphs of Gerard and Becker (19), as amplified by Schneider (20). To illustrate the use of Fig. 10, consider the entry to Venus with a maximum pressure of 700 psi. In this application, we could operate at 200 F and select beryllium at a stress of 47,000 psi or magnesium at a stress of 20,000 psi.

Honeycomb was found to weigh about the same as the monocoque because of the high loads and, therefore, was eliminated because of high construction costs.

Structural Results

The nose section of the Mars probe provides an excellent example of the combination of the thermodynamic and the structural analyses. Fig. 11 shows the variation of nose skin thickness with peak temperature for a probe of $W/C_DA=70$ lb per ft² entering the atmosphere of Mars with a peak pressure of about 8000 lb per ft². These curves may be determined by using curves similar to Fig. 10 with proper adjustment of the modulus for both temperature and time effects.

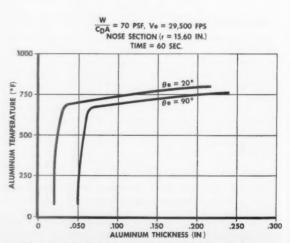


Fig. 12 Mars entry-required structural skin thickness

478

ARS JOURNAL

Ir met tem traje be above spore O tem a cu structure.

T

for strucker required fig. Fig. 90-d there there in N have section weight and

and one Fig. plots This cases On if su 0.050 tion Thus entry

find

Gen Ol quite maxi and

relaz

and very work insig total be c adva cond the para

defin of en The for f is to and first crite

For Apr In order to illustrate this thermostructural optimization method, we will use the familiar 2024-T81 aluminum. The temperature-skin thickness plot is shown in Fig. 12 for trajectories with entry angles of 20 and 90 deg. It should be noted that the modulus of aluminum falls off rapidly above 700 F, and the required thickness increases correspondingly.

Once a curve of required structural skin thickness vs. temperature has been determined, it is possible to determine a curve for total weight vs. temperature. To do this, the structural and thermodynamic analysis will now be combined.

Thermostructural Optimization Example

Thus far, the thermodynamic methods and some results for aluminum and phenolic nylon have been presented, the structural analysis has been discussed, and the structural requirements have been given for aluminum for Mars entry. Fig. 13 shows the superposition of the thermal results of Fig. 7 and the structural requirements of Fig. 12 for the 90-deg Mars entry. Each point of intersection between the thermodynamic and structural curves is an acceptable thermostructural design.

Now that a number of marginally satisfactory designs have been indicated by the several thermostructural intersections, the next problem is to find the lightest one. The weight at each design point can be computed by summing the individual weights of insulator, structural skin and stiffeners, and plotting these weights against a suitable variable to find the minimum. Since aluminum thickness, temperature and phenolic nylon thickness are all interconnected, any one of the three can be used as an independent variable. Fig. 14 shows the combined weight (insulator plus structure) plotted vs. maximum temperature for the two Mars missions. This figure shows that the minimum weight occurs in both cases at approximately 650 F.

On examination, the $\theta=90$ deg designs will surely fail if subjected to the 20 deg environment, since, for example, 0.050 in. of aluminum requires 0.50 in. of insulation for protection at $\theta=90$ deg and 0.83 in. of insulation at $\theta=20$ deg. Thus, the mission trades become clear; one pays a penalty in entry body weight if terminal guidance requirements are relaxed to allow for anything but a bull's-eye, an unlikely occurrence.

Generalized Thermostructural Method

Obtaining the thermal and structural analyses can become quite laborious, especially if factors such as nonsimultaneous maximum load and temperature (the case in this example) and variable missions and materials are considered. A very powerful general method has been evolved from this work which saves computing time and helps one to establish insight to the thermostructural design philosophy. The total problem requires that many different variables must be considered to reach a really efficient design. One of the advantages of the method is that no hard decisions as to what conditions may be critical are required. If doubt exists, carry the particular case along. At some point in the calculation, the doubt will be clarified.

The design parameters include both shape and material parameters. W/C_DA , which is actually a design parameter, defines the degree of bluntness and greatly affects the severity of entry environment.

The optimization is best performed in two major stages. The first is to investigate effects of environmental parameters for fixed values of W/C_DA and material choices; the second is to find the best combination of W/C_DA , material choices and structural configuration for minimum weight. The first stage is essentially an operation to find the most severe criterion; the second is to find the best way to satisfy it. For each combination of the parameters it is necessary to



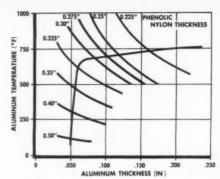


Fig. 13 Mars entry-thermostructural design points

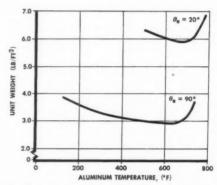


Fig. 14 Mars entry-thermostructural optimization results

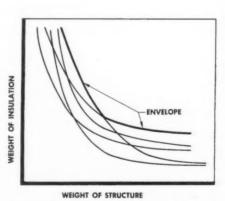


Fig. 15 Envelope of critical design conditions

prepare a graph similar to Fig. 13. The weights can be plotted against each other, as shown in Fig. 15, for a family of constant W/C_DA , material choices and structure configuration. A single line of this figure represents a transposed set of design conditions such as shown in Fig. 13.

For any particular curve, the region to the right and above the curve represents safe over-design, since it has more material than it needs, whereas the region below and to the left is a failure. Therefore, if a particular curve dominates a region which lies below and to the left, it represents a more critical design condition, and the curve below and to the left need not be considered further. The lightest weight design

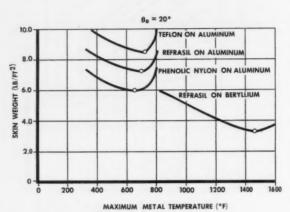


Fig. 16 Mars entry-nose skin unit weight

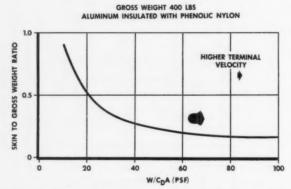


Fig. 17 Mars entry—effect of ballistic coefficient on skin weight

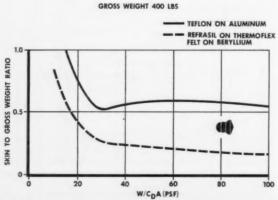


Fig. 18 Venus entry—effect of ballistic coefficient on skin weight

of all those represented in the envelope curve can be found easily by drawing a line with a slope of -1 tangent to the envelope. A line of -1 slope defines a family of designs of constant weight. It can be seen that the various plots shown here enable one to build up an intuitive "feel" for the tradeoffs between combinations of parameters in the thermostructural problem. As this feel improves, fewer cases need be considered in determining the optimum.

See

abl

inte

allo

ten

err

of

str

do

cha

an

on

COL

ine

g L N P \dot{q} Q R

r t T V

 γ

The thermostructural method presented so far is restricted to marginally satisfactory designs, and does not contain factors of safety. Historically, factors of safety are applied only to load, but it is clear that uncertainties may arise in any of the parameters and theories considered in the paper, and to a widely differing degree. What, for example, is the uncertainty in the prediction of the Venusian atmosphere, and how does this uncertainty affect the optimum design? The method can be extended to include considerations like this by means of probability theory.

Conclusions

This paper started with a description of two missions with severe thermal environments and a description of a vehicle which would accomplish them. The thermal and structural analyses were developed and then enmeshed for a particular vehicle design on one part of the vehicle. The basic force of this method of combined thermostructural design was then generalized for any vehicle, any mission and any insulated structure. Although it has been stated that this paper is not intended to present the best overall design for either a Mars or a Venus entry vehicle, it is appropriate to show the results of work related to the sizing, shaping and general design of the probes in connection with two design questions: selection of skin materials, and selection of W/C_DA and size.

The method which has been illustrated here must be applied to many different combinations for each major structural element in order to select the best material combinations and thicknesses. Fig. 16 gives typical weight comparisons for different material combinations at $W/C_DA = 70$ lb per ft², which represents an end result of the thermal structural optimization procedure and puts the designer in a good position to select a material.

Fig. 17 shows the variation of skin to gross weight ratio as a function of W/C_DA for the Mars entry vehicle. The curve represents a family of geometrically similar vehicles of varying size. Skin weight in this figure includes not only the nose section considered thus far, but also the cylindrical section, flare and base. These latter weights were estimated by the method of this study, using appropriate thermal assumptions and structural requirements. The combination of phenolic nylon on aluminum serves as a good example.

For Mars, as W/C_DA approaches zero, the skin to gross weight ratio goes up for two reasons: Although the low W/C_DA has a smaller heat input, the increase in surface area overpowers this favorable effect; and although the loads are lower for lower W/C_DA , buckling is a more severe problem for larger bodies, and the full savings of lower loads cannot be realized.

Fig. 18 gives the same type of information for the Venus entry vehicle. The two curves correspond to two different combinations of materials, Teflon on aluminum and Refrasil on Thermoflex felt on beryllium. The upper curve has a local minimum. This shape is caused by the complicated interaction between opposing effects which have the following trends: As W/C_DA decreases, total surface area goes up, skin gages needed to resist buckling go up, nose insulation thicknesses go down rapidly because of lower radiation input (see Fig. 6), and insulation thicknesses on other areas go down slowly. The lower curve shows no local minimum for a structure of beryllium covered with Thermoflex felt for insulation, and Refrasil for energy absorption by ablation.

See (21) for a definition and discussion of heat protection by ablation.

The application of the forementioned results must take into account the sensitivities of the design parameters to various sources of thermal and structural errors. Since the allowable stress of the structures usually falls off rapidly with temperature increase above the working range, the structure can be completely wiped out by rather moderate thermal errors. The principal defense against this particular type of error, as an example, is to put a safety factor on the insulation thickness rather than to increase the required structural strength. These more generalized safety factors do not change the thermostructural method; they only change the numbers.

The detailed design of probes for Mars and Venus will be an interesting and rewarding task for the future. The work shown in Figs. 16 and 17 demonstrates that the task is not only feasible and economical, but that it can be done with contemporary materials such as aluminum and phenolic nylon. More advanced materials such as beryllium will increase the payload efficiency for more advanced tasks.

Nomenclature

- frontal area, ft3
- drag coefficient, dimensionless
- Emodulus of elasticity, psi
- acceleration of Earth gravity, 32.2 ft/sec2 $\frac{g}{L}$
- shock detachment distance or Reynolds number length
- ion concentration, per cent
- P pressure, psi or psf
- heat flux rate, Btu/ft2-sec
- total heat transferred, Btu/ft²
- nose radius, ft
- radius, in.
- skin thickness, in., or time, sec
- temperature, F
- velocity, fps weight, lb
- Y
- ratio of specific heats, dimensionless emissivity, dimensionless
- θ flight path angle relative to local horizontal, deg
- density, lb per cu ft P
- Stefan-Boltzmann constant (0.48 \times 10⁻¹² Btu/ft²-sec-R⁴), or stress, psi

Subscripts

- = cripping failure mode
- = condition at entry to sensible atmosphere
- = stagnation condition, or pertains to structure = free stream condition

References

- 1 Ponsford, H. T. and Wood, R. M., "Thermo-Structural Design For High Temperature Flight," Douglas Aircraft Co. Engineering Paper no. 664, presented at IAS National Midwestern Meeting, May 1958. (Secret) 2 Lowe, R. E. and Cato, G. A., "Thermodynamic Design of an Interplanetary Probe," Douglas Aircraft Co. Rep. SM-35535, Oct. 1959.
 3 Gunkel, R. J., Laseody, D. N. and Merrilees, D. S., "Impulsive Midcourse Correction of An Interplanetary Transfer," Douglas Aircraft Engineering Paper no. 804, presented at the Tenth International Astronautical Congress Sept. 1959.

- Engineering Paper no. 804, presented at the Tenth International Astronautical Congress, Sept. 1959.
 4 King, O. L., "Maps of Two Dimensional Interplanetary Transits,"
 Douglas Aircraft Co. Rep. SM-35707, April 1959.
 5 Gazley, C., Jr., "Deceleration and Heating of a Body Entering a Planetary Atmosphere from Space," Rand Corp. Rep. P-955, Feb. 1957.
 6 Cole, S. H., "The Atmosphere of Venus," Rand Corp. Rep. P-978,

- Oct. 1956.
 7 Van Driest, E. R., "The Problem of Aerodynamic Heating," Aerodynam. Engag. Rev. Oct. 1956.
 8 Van Driest, E. R., "Turbulent Boundary Layer in Compressible Fluids," J. Aeron. Sci., vol. 17, no. 5, March 1951.
 9 Fay, J. A. and Riddell, F. R., "Theory of Stagnation Point Heat Transfer in Dissociated Air," J. Aeron. Sci., vol. 25, no. 2, February, 1958. pp. 73-85.
- 10 Rose, P. H. and Stark, W. I., "Stagnation Point Heat-Transfer Measurements in Dissociated Air," J. Aeron. Sci., vol. 25, no. 2, Feb., 1958,
- 11 Lees, L., "Laminar Heat Transfer Over Blunt-Nosed Bodies at Hypersonic Flight Speeds," Jet Propulsion, vol. 26, no. 4, 1956, pp. 259-
- 12 Rubesin, M. W. and Pappas, C. C., "A Study of Binary Gas Diffusion in a Turbulent Boundary Layer on a Flat Plate," presented at Rand Corp. Symposium on Mass Transfer, 1957.

 13 Raymond, J. L., "Thermodynamic Properties of the Atmosphere of
- Raymond, J. L., "Thermodynamic Properties of the Atmosphere of Venus," Rand Corp. Rep. RM-2292, Nov. 1958.
 Gilmore, F. R., "Equilibrium Composition and Thermodynamic Properties of Air to 24,000° K," Rand Corp. Rep. RM-1543, Aug. 1955.
 Hayes, W. D., "Some Aspects of Hypersonic Flow," Ramo-Wooldridge Corp., Jan. 1955.
 Kivel, B. and Bailey, K., "Tables of Radiation From High Temperature Air," Avco Research Rep. no. 21, Dec. 1957.
 "Survey of High Temperature Materials for Hypervelocity Models," Douglas Rep. LB-25787, July 1958.
 Hodge, W., "Bervllium for Structural Applications—A Review of

- Douglas Rep. LB-25787, July 1958.

 18 Hodge, W., "Beryllium for Structural Applications—A Review of Unclassified Literature," Defense Metals Information Center Rep. 106, 1958.

 19 Gerard, G. and Becker, H., "Handbook of Structural Stability, Part III—Buckling of Curved Plates and Shells," NACA TN 3783, 1957.

 20 Schneider, M. H., "The Application of Optimum Design Methods to the Thermostructural Optimization of High Speed Missiles," Douglas
- the Thermostructural Optimization of Ingl. Special Advances.

 Engineering Paper no. 902, 1959.

 21 Wood, R. M. and Tagliani, R. J., "Heat Protection by Ablation,"

 Douglas Aircraft Co. Engineering Paper no. 923, presented at IAS National Meeting, Jan. 1960.

Importance of Combustion Chamber Geometry in High Frequency Oscillations in Rocket Motors

J. R. OSBORN² and J. M. BONNELL3

Purdue University, Lafayette, Ind.

The experiments reported herein were concerned with the determination of some of the underlying factors which contribute to the occurrence of transverse modes of combustion pressure oscillation in rocket motors. Two rocket motors having different diameters and several different lengths were employed in the experiments using a gaseous hydrocarbon fuel and air as propellants. The investigation indicated that changes in the aspect ratio and volume of the rocket motor combustion chamber had a profound effect on the incidence and amplitude of the transverse modes. These effects were modified by interactions of the transverse modes with the longitudinal mode. The transverse modes present in the experiments were determined to be the "spinning" and the radial

SERIES of experiments was recently conducted at the A Purdue University Jet Propulsion Center for studying the effects of cylindrical chamber geometry upon the transverse modes of combustion oscillation in a premixed gas rocket motor. The study is part of a research program initiated for studying high frequency combustion pressure oscillations while progressing from a relatively simple premixed gas combustion system through more complicated types of combustion systems and ultimately to high energy liquid bipropellant systems and solid propellant systems. It should be noted that the simple combustion system of the gaseous rocket motor employed in the experiments reported herein is in some respects different from that of either the liquid or the solid rocket motor. By employing such a simple combustion system (1)4 several variables can be eliminated (atomization, vaporization, sublimation, etc.), so that the effect of a single variable can be studied. It should also be noted that several effects observed in the gaseous motor, namely, the critical lengths (2) and an interaction of the longitudinal and transverse modes (3), have occurred in liquid and solid propellant rocket motors.

The study discussed herein employed two low-aspect-ratio rocket motors burning a gaseous hydrocarbon fuel and air which were thoroughly mixed prior to their injection. The experimental rocket motors had inside diameters of 7 and 14 in. The lengths of the combustion chambers of both motors were increased from 2 to 12 in. in 2-in. increments by adding spacers. The 14-in. diameter motor was also operated with two additional lengths of 15 and 18 in. The nozzle throat diameter was 0.500 in. for all the tests reported herein. Instrumentation and other apparatus details may be found in

Experimental Results for Methane and Air

The effects of changes in the combustion chamber diameter

Presented at the ARS Semi-Annual Meeting, Los Angeles,

Calif., May 9-12, 1960.

¹ The results reported herein were obtained during the course of research conducted under Contract N7 onr 39418 sponsored by the Office of Naval Research and Contract AF 49(638)-756 sponsored by the Air Force Office of Scientific Research.

² Associate Professor of Mechanical Engineering. Member

ARS

Research Assistant. Member ARS.
 Numbers in parentheses indicate References at end of paper.

and length are illustrated in Fig. 1 where equivalence ratio is plotted as a function of combustion pressure with combustion chamber length as a parameter. The figure presents a series of typical instability regions for the transverse mode in the 7in. diameter motor. Each curve for a particular length (2 through 12 in.) separates the regions of oscillatory combustion of the transverse mode (to the right of the curve) from either steady combustion or no combustion (to the left of the curve). Thus, it can be seen from Fig. 1 that for a 2-in. long motor burning methane and air at an equivalence ratio of 1.0 the combustion will be unstable in the transverse mode

for any steady chamber pressure over 45 psia.

The curves show that the instability regions for the transverse modes progress steadily toward higher chamber pressure with increasing chamber length. That is, an operating condition that produces transverse oscillations in the 2-in. long motor may produce steady combustion for the 4-in. long and longer motors (see Fig. 1). Basically, the same conclusions apply to the instability regions for the transverse modes of the 14-in. diameter motor configurations, although the toes of the instability regions of the respective lengths occur at higher steady chamber pressures. It should also be pointed out that 14-in. diameter motors having combustion chamber lengths of 15 and 18 in. were operated, but no pressure oscillations of the transverse modes were observed at chamber pressures below 200 psia for either of those lengths.

Fig. 2 is a plot of the maximum peak to peak amplitude of the pressure oscillations of the transverse modes as a function of chamber pressure for each length of the 7-in. diameter motor. This figure illustrates the decrease in amplitude of the oscillations as the motor length increases. In the 14-in. diameter motor the amplitudes are smaller but the trend

Fig. 3 depicts the effect of the length of the combustion chamber upon the amplitudes of the combustion pressure oscillations of the transverse modes at a constant chamber pressure of 160 psia for both diameter motors (7 and 14 in.). The trend of the amplitude curves is the same for both diameter motors.

Experimental Results for Ethylene and Air

Fig. 4 illustrates the relative positions of the instability regions for the transverse modes for chamber lengths 2 through

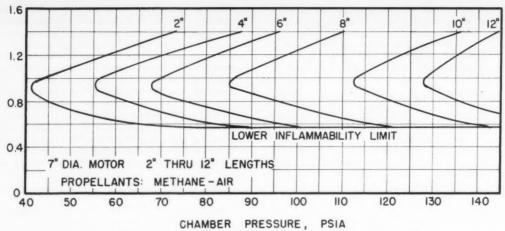


Fig. 1 Transverse mode instability regions for methane-air propellants

12 in. of the 7-in. diameter motor. Fig. 4 is similar to Fig. 1 except that it is drawn from data for the propellants ethylene and air. For the lengths 2 through 8 in., the toes of the instability regions progress toward higher chamber pressures as was noted for the propellant combination of methane and air. At the 10-in. length, however, the toe of the instability region shifts to a lower chamber pressure, but the instability region for the 12-in, length again occurs at a higher chamber pressure.5 The shift of the instability region is also evident for the 14-in. diameter motor. In that case, however, it occurs at the 12-in. length. It should also be noted that the instability regions for ethylene-air (see Fig. 4) are larger than those for methane-air (see Fig. 1).

Fig. 5 illustrates the amplitudes of the pressure oscillations of the transverse modes as a function of the combustion chamber length at a steady chamber pressure of 160 psia. Those curves, plotted for both the 7- and 14-in. diameter motors,

⁵ The shortest chamber length at which the transverse mode instability region shifts to a lower chamber pressure will be referred to as the "shifted length."

LENGTH 7" DIA. MOTOR PSI LENGTHS: 2" THRU 12" PEAK-TO-PEAK PRESSURE AMPLITUDE PROPELLANTS: METHANE-AIR 4" 30 20 8 10

> PRESSURE, PSIA CHAMBER

10

180

Fig. 2 Amplitude of pressure oscillations of the transverse mode vs. steady combustion chamber pressure for methane-air propellants

illustrate the amplitude shifts6 which occur for each of those motors. For the 7-in. diameter motor there is a slight increase in amplitude for the 6-in. chamber length, whereas for the 14-in. diameter motor, a slight amplitude shift occurs at the 8-in. length with a major shift in amplitude at the 12-in. length. It should be noted that no amplitude shift occurred for the methane-air propellant combination (see Fig. 3).

For the longer motors a significant difference was observed between the amplitudes of the pressure oscillations of the transverse modes measured near the injector end of the combustion chamber and those measured near the nozzle end of the motor. Those near the nozzle end are smaller, as one

⁶ The amplitude shifts are changes in the previous trend of decreasing amplitudes of the pressure oscillations with increasing length.

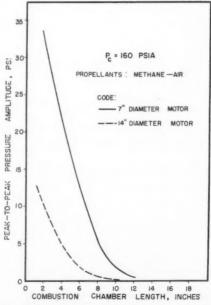


Fig. 3 Amplitude of pressure oscillations of the transverse mode vs. combustion chamber length for methane-air propellants

120

130

140

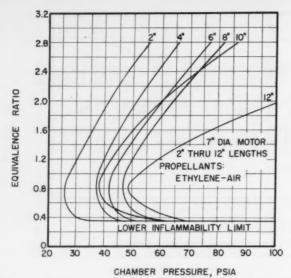


Fig. 4 Transverse mode instability regions for ethylene-air propellants

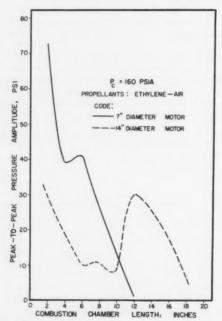


Fig. 5 Amplitude of pressure oscillations of the transverse mode vs. combustion chamber length for ethylene-air propellants

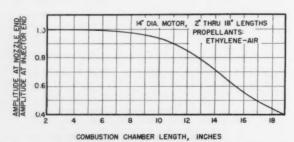


Fig. 6 Relative amplitudes of pressure oscillations of the transverse mode measured at the injector and nozzle ends of the motor vs. combustion chamber length

could expect. Fig. 6 depicts the relative amplitudes of the oscillations at the nozzle end and the injector end versus combustion chamber length as measured in the 14-in. diameter motor. The relationship illustrated in Fig. 6 is approximately the same for the 7-in. diameter motor as well as for the methane-air propellant combination in both motors.

mo

wei

me

eve

for

low

crit

une

hri

(8)

pre

pos

wa

pre

ver

ing

ind

om

tra

oce

mo

8-i

len

att

qu

to

tra

am

AI

Although the instability results presented are for the transverse modes of oscillation, steadily propagating longitudinal modes were also observed in the 7-in. diameter motor at chamber lengths of 8 in. $(L/D=1.14)^7$ and above; they were observed in the 14-in. diameter motor at chamber lengths of 12 in. (L/D=0.86) and above. Transient type longitudinal modes, which will be discussed later, were also observed in shorter lengths of the 14-in. diameter motor.

Discussion of Results

An explanation of some of the results is suggested by the consideration of a possible mechanism for initiating and sustaining the pressure oscillations of the transverse mode. The mechanism was proposed originally for the longitudinal mode in (5), and is supported by the experimental evidence presented in (6). In substance, the proposed mechanism states that in a combustion chamber a pressure wave is initiated by some pressure disturbance and the subsequent passage of the pressure wave through burning and unburned propellants adiabatically compresses these hot gases. The increased temperature and pressure of the gases cause an accelerated chemical reaction rate (or heat release rate) behind the pressure front which drives and sustains the pressure wave. The amount of energy supplied to the pressure wave depends somewhat upon the chemical reactants (7); in this case the ethylene-air combination supplies more than methane-air. As has been stated, that mechanism was employed (5) to explain the existence of the lower critical length and to postulate the probable existence (1) of the upper critical length. The lower critical length of the longitudinal mode was defined in (5) as the combustion chamber length below which a longitudinal mode cannot exist. Above the lower critical length it is possible for a longitudinal mode to exist. As reported in (5), the critical length for ethyleneair propellants is 6 in.; for methane-air propellants, it is 11 in.; these results were obtained using a 33-in. diameter motor.

Whether the initiated longitudinal mode sustains itself or is damped out depends largely upon whether the geometry favors the propagation of that mode. In some cases with large diameter motors, the longitudinal mode triggered a transverse mode. The geometry evidently favored the latter mode; it received the predominant part of the driving energy; and the longitudinal mode was damped out even though the lower critical length had been exceeded. At chamber lengths below the lower critical lengths, however, no longitudinal modes were observed. For ethylene-air propellants at chamber lengths between the lower critical length and a length to diameter (L/D) ratio of approximately 1.0, weak longitudinal modes were initiated but promptly died out; these are referred to as transient-type modes. Above an L/D ratio of approximately 1.0, self-sustaining longitudinal modes were observed. For methane-air propellants, weak, self-sustaining longitudinal modes were observed in the 12-in. long, 7-in. diameter motor; in this case, the lower critical length was exceeded and the L/D ratio was greater than 1.0.

One of the effects of the interaction between longitudinal and transverse modes is the so-called instability region shift, which occurred at the 10-in. length of the 7-in. diameter motor (see Fig. 4) and the 12-in. length of the 14-in. diameter motor when burning ethylene-air propellants. The suggested explanation is based on the fact that, at a motor length only slightly longer than the critical length for the longitudinal

⁷ The L/D ratio is the ratio of the length to diameter.

mode, longitudinal modes (either transient or self-sustaining) were observed. At an increased motor length, the forementioned longitudinal mode increases in amplitude until it eventually "triggers" (supplies an initial pressure disturbance for initiating) the transverse modes at chamber pressures lower than those at which the transverse modes would normally occur.

Another effect influenced by the existence of the lower critical length is the amplitude shift. The mechanism causing the amplification of the peak to peak amplitude of the oscillating pressure waves at a certain length is not completely understood, but it is believed that transient longitudinal modes bring the unburned propellants to a high state of preparation (8) prior to combustion. With the subsequent passage of the transverse mode pressure wave, the local temperature and pressure are raised to higher values than would normally be possible without the prior preparation. This increases the heat release rate above its normal value behind the transverse wave front, thereby supplying additional energy to the wave above that which it ordinarily would receive in passing through a combustion zone without the transient longitudinal mode present. Repeated interactions further amplify the transverse wave until a balance between driving forces and damping forces has been reached once again. It is believed that this effect is primarily a geometry effect although the chemistry of the propellants has an influence (7). Crump and Price (3) indicate that in solid propellant motors the modes interact to give catastrophic changes in the burning rates when the geometry is such that the frequencies of the longitudinal and transverse modes are equal. For the cases reported herein the frequencies are equal when the maximum amplitude shift occurs

In the 14-in. diameter motor burning ethylene and air, the amplitude shifts occurred in lengths where the longitudinal mode occurred repeatedly. The first shift occurred at the 8-in. length, which was only slightly longer than the critical length (6 in.) for the longitudinal mode. Thus, this shift is attributed to the interaction of a weak longitudinal mode with the transverse mode. The major amplitude shift occurred at the 12-in. length where the longitudinal and tangential frequencies are approximately equal.

In the 7-in. diameter motor burning ethylene and air, it so happened that the chamber diameter closely corresponded to the critical length for the longitudinal mode. Thus, the transient longitudinal mode occurred only in the 6-in. length motor with sufficient initial energy content to cause an amplitude shift for the transverse mode. No amplitude shift

was observed when burning the methane-air propellants in either diameter motor. The fact that the instability region and amplitude shifts occurred for ethylene-air propellants and not for methane-air propellants is attributed to the high reactivity of ethylene as compared with methane. This is discussed in (4 and 7); the scope of this paper is limited to the geometrical effects.

It should be observed that a motor having a chamber length smaller than the lower critical length cannot have an interaction between the modes since the longitudinal mode cannot exist.

The other effects were independent of the lower critical length because the lengths employed in the experimental program were either less or greater than the critical length. For all the motor configurations having lengths shorter than the "shifted length" and burning ethylene-air propellants, the instability regions gradually moved to a higher chamber pressure with increasing chamber length (see Fig. 4). Thus, because of the shift to higher pressures (more dense unburned propellants have more available energy per unit volume), it appears that more energy per unit volume is required for sustaining a transverse mode of a given amplitude as the chamber length (or volume) increases. This probably explains the observation that the amplitudes of the pressure oscillations in the motor configurations considered above decrease with increased length (volume) for a fixed steady chamber pressure; that is, for unburned propellants of constant density (see Fig. 3).

For combustion chamber lengths greater than the "shifted length" in motors burning the ethylene-air propellants, the instability regions move toward higher chamber pressure with increasing length because the fixed amount of available energy must be divided between the transverse and longitudinal mode oscillations, both of which exist since the length is greater than the critical length. As a result, more dense unburned propellants must be supplied to drive both modes and, hence, the higher chamber pressure. The longitudinal mode oscillations increase in amplitude with increasing length, because the longitudinal mode is evidently favored by the geometry. Therefore, it receives a greater share of the available energy. It should be noted, however, that the longitudinal mode oscillations eventually reach a limiting amplitude which is to be expected (5).

The local concentrations of available energy within a combustion chamber have a bearing on the distribution of the amplitudes of pressure oscillations. For the longer combustion chambers, the concentration of unburned reactants

1961 ARS Meeting Schedule

Date	Meeting	Location	Abstract Deadline
May 3-5	Space-Nuclear Conference	Gatlinburg, Tenn.	Past
May 22-24	National Telemetering Conference	Chicago, III.	Past
June 13-16	National IAS-ARS Joint Meeting	Los Angeles, Calif.	Past
Aug. 7-9	Guidance and Control Conference	Palo Alto, Calif.	Past
Aug. 16-18	International Hypersonics Conference	Cambridge, Mass.	Past
Aug. 23-25	Biennial Gas Dynamics Symposium	Evanston, III.	Past
Oct. 2-7	XIIth International Astronautical Congress	Washington, D. C.	May 1
Oct. 9-15	ARS SPACE FLIGHT REPORT TO THE NATION	New York, N.Y.	Past

Send all abstracts to Meetings Manager, ARS, 500 Fifth Ave., New York 36, N.Y.

is larger near the injector end of the motor where more energy is available (9) to drive the transverse wave fronts. As the gases move toward the nozzle end of the motor, the concentration of unburned reactants decreases and the concentration of burned combustion products increases. Thus at the nozzle end, the energy released is considerably smaller than at the injector end, and consequently, as one would predict, the amplitudes of the oscillations are smaller (see Fig. 6).

Conclusions

It has been observed that the critical length for the longitudinal mode as reported in (5) plays an important role in determining the length for which the transverse modes will be initiated and amplified. That is, at lengths greater than the critical length, the transverse mode may be initiated at a steady combustion pressure below which it normally occurs. In addition, for existing transverse modes, an interaction between them and the longitudinal mode takes place which causes an increase in the peak-to-peak amplitudes of the transverse mode pressure oscillations over those without the existence of the longitudinal mode. It appears reasonable, therefore, to conclude from these effects and those of (6) that the mechanisms producing the oscillations (5) of the longitudinal and transverse modes are similar.

Acknowledgment

The authors wish to thank Dr. M. J. Zucrow, Atkins Professor of Engineering, Purdue University, for his helpful counsel through the course of the investigation.

of t

but

inc

uni

sho

pro

sho

effe

var

pro

sol

win

for

atta

the

and

the

sim

inte

see mo val ing ing bas

side bee

bod this

refe

Ch

Flo

cha

larg

one

asp

free

may

tha

inve

nan

inte flow mer tere

assi

par

cab

abo

face

exa

API

F tine hyp in t For

References

1 Osborn, J. R. and Schiewe, R. M., "An Experimental Investigation of High Frequency Combustion Pressure Oscillations in a Gaseous Bipropellant Rocket Motor," Purdue University Rep. no. I-58-1, June 1958, p. 40.
2 Crocco, L., Grey, J. and Harrje, D. T., "On the Importance of the Sensitive Time Lag in Longitudinal High-Frequency Rocket Combustion Instability," JET PROPULSION, vol. 28. no. 12, Dec. 1958, p. 841.
3 Crump, J. E. and Price, E. W., "Catastrophic" Changes in Burning Rate of Solid Propellants During Combustion Instability," ARS JOURNAL vol. 30, no. 7, July 1960, p. 705.
4 Bonnell, J. M., "An Experimental Investigation of Transverse Mode Combustion Oscillations in Premixed Gaseous Bipropellant Rocket Motors," Unpublished MSME Thesis, Purdue University, Jan. 1960.
5 Zucrow, M. J. and Osborn, J. R., "An Experimental Study of High Frequency Combustion Pressure Oscillations," JET PROPULSION, vol. 28, no. 10, 0ct. 1958, p. 654.

5 Zucrow, M. J. and Osborn, J. R., "An Experimental Study of High Frequency Combustion Pressure Oscillations," JET PROPULSION, vol. 28 no. 10, Oct. 1953, p. 654.
6 Osborn, J. R. and Pinchak, A. C., "Investigation of Aerothermodynamic Interaction Phenomena in Combustion Pressure Oscillations," Purdue University Rep. no. 1-59-2, June 1959.
7 Osborn, J. R. and Bonnell, J. M., "On the Effect of Fuel Composition on High Frequency Oscillations in Rocket Motors Burning Premixed Hydrocarbon Gases and Air," ARS preprint 1489-60, 1960.
8 Ellis, H. B. and Pickford, R. S., "High-Frequency Combustion Instability," Aerojet-General TN-17, Sept. 1956. (Confidential)
9 Pickford, R. S. and Peoples, R. G., "The Inherent Stability of the Combustion Process," ARS preprint 1490-60, 1960.

Outer Inviscid Hypersonic Flow With Attached Shock Waves

RICHARD A. SCHEUING¹

Grumman Aircraft Engineering Corp. Bethpage, N. Y.

The prediction of pressures in inviscid hypersonic flow with attached shock waves is the subject of the theoretical and experimental investigation which is reviewed herein. Characteristic features of inviscid hypersonic flow are discussed as in introduction to the theoretical methods of interest. Major emphasis is placed on the extension of thin shock layer theory to conical configurations of smooth, but otherwise arbitrary, cross section. In addition, the improvement of the two-dimensional shock expansion method is considered to account for reflection of characteristics from bow shock and vorticity layer. An approximate method for numerically integrating the conical flow equations for flat plate delta wings is also proposed. Very brief mention is made of recent efforts to extend shock expansion theory to three-dimensional flows over planar bodies, and to calculate the flow about conical wing-body combinations.

INCREASING attention to lifting hypersonic configura-tions which have improved aerodynamic efficiencies has provided added impetus to the further development of suitable theoretical solutions for the flow field about such shapes. This paper is devoted primarily to a review of recent progress in several areas of inviscid hypersonic flow theory and related experiments; the characteristic features of hypersonic flow which bear relationship to the theoretical work are also discussed. Although our main interest will be in the prediction of surface pressures under conditions where viscous interaction effects do not play a major role, an important by-product of improved inviscid solutions is that they permit increased accuracy in boundary layer calculations.

The major emphasis in this review is placed on an extension

Presented at the ARS Semi-Annual Meeting, Los Angeles, Calif., May 9-12, 1960.

¹ Head, Fluid Mechanics Section, Research Dept.

of thin shock layer theory to conical configurations of smooth, but otherwise arbitrary, cross section. This presentation includes a discussion of the problems involved in obtaining a uniformly valid solution for the flow properties within the shock layer. In addition, we will briefly consider the improvement of the two-dimensional shock expansion method to account for first reflections of the Mach waves from the bow shock and from the vorticity layer, touching on very recent efforts to extend the shock expansion theory to three-dimensional flows over planar bodies (incorporating effects of local variation in incidence or sweep). We will also indicate an approximate, semi-empirical method for obtaining a numerical solution of the exact conical flow equations for flat plate delta wings, noting some recent progress toward a rational solution for the flow about conical wing-body combinations having a sharp corner at the wing-body juncture.

The basic shapes which we will consider have shock waves attached to the leading edge. Solutions for the flow around these shapes will exhibit most of the characteristic features of flows around similar shapes having slightly blunted apices and leading edges. Indeed, these solutions provide us with the asymptotic result for the blunted leading edge problem. By eliminating the various specific effects of bluntness, we simplify to some extent the theoretical work and the task of interpreting experimental results. Thus, this approach seems a logical first step in the development of theories for more generally shaped bodies. In the absence of a uniformly valid solution, the designer can resort to an empirical matching of a blunted leading edge solution (locally) to a sharp leading edge solution (asymptotically). A logical aim of later investigations would be to put such a matching on a rational basis.

Blunt body problems will not be discussed per se, except to the extent that crossflow stagnation regions must be considered in the attached shock solutions. A great deal has been accomplished by many researchers working on the blunt body problem, and considerable stimulus has been given to this work by such developmental activities as the design of re-entry nose cones. A discussion of many of the available references is presented by Hayes and Probstein (1)².

Characteristic Features of Inviscid Hypersonic Flows

Before proceeding with the theoretical discussion, it is pertinent to review a few of the distinguishing features of inviscid hypersonic flow, since the simplifying assumptions employed in the various hypersonic theories result directly from them. For a flow to be considered hypersonic it must, of course, be characterized by a Mach number which is large; just how large depends on the particular subject of investigation. If one is primarily interested in studying the thermochemical aspects of the flow, for example, it is the total energy of the free stream which is of importance. In this instance, one may require a somewhat higher free stream Mach number than is often considered the lower limit for hypersonic flow in investigations where the hydrodynamic effects are predominant. In either case, the body shape and the flow field of interest play a major role in determining whether or not the flow may be considered to be hypersonic. In the development of the theories discussed here, we are primarily interested in flight Mach numbers in excess of about 5. The assumption that the free stream Mach number is large compared with unity is implicit in all theories specifically applicable to hypersonic flows.

As the free stream Mach number increases, the shock waves about a body are swept increasingly closer to the body surface. That the shock lies close to the body is apparent, for example, in Fig. 1, which is a schlieren photograph taken of a

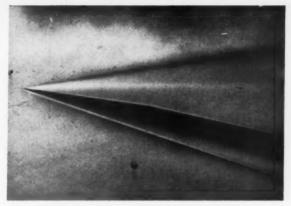


Fig. 1 Schlieren of flow over flat plate at nominal Mach number of 13 at 15-deg angle of attack

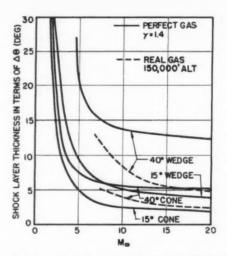


Fig. 2 Variation of shock layer thickness with Mach number

flat plate at Mach ≈13 and 15 deg angle of attack in the Grumman hypersonic shock tunnel (stagnation pressure 1000 psi, stagnation temperature 1650 K). The shock layer thickness measured in terms of $\Delta\theta$, the angle between the shock wave and the body surface (and hence including the boundary layer displacement thickness), is approximately 53 deg (inviscid value ~5 deg). The rapid thinning of the shock layer with increasing Mach number is shown graphically in Fig. 2 for wedges and cones of 15 and 40 deg semivertex angles, assuming a perfect gas with the ratio of specific heats γ equal to 1.4—using NACA tables (2). The influence of real gas effects in diminishing the thickness of the shock layer even further will be discussed shortly. In addition to providing an extremely powerful tool for the development of simplified theories, the existence of the thin shock layer requires modification of the shock expansion method, under certain conditions, to account for the increasing importance of the Mach waves reflected from the bow shock.

In general, the shock layer is noticeably thicker over those portions of the body which are less inclined to the incident flow. For the shapes which we consider here, when the upper surface is wholly at negative incidence, no identifiable shock layer exists. However, in such cases the upper surface pressure coefficients are completely negligible in comparison with those on the lower surface.

Although the shock wave about any given body becomes

³ Numbers in parentheses indicate References at end of paper.

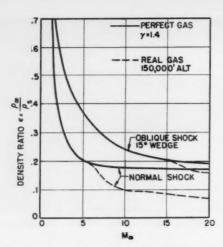


Fig. 3 Variation of density ratio with Mach number

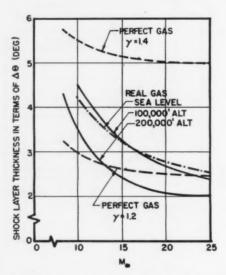


Fig. 4 Real gas effect on shock layer thickness for 40-deg cone

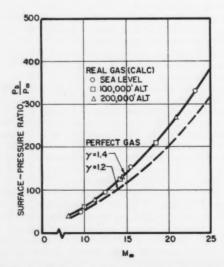


Fig. 5 Real gas effect on surface pressure for 40-deg cone

more oblique to the flow with increasing Mach number, the strength of the shock, which for a perfect gas is a direct function of the Mach number normal to the shock, becomes greater. Associated with this increasing shock strength, we find small values of ϵ , the ratio of the density in front of the shock to the density behind the shock ($\epsilon = \rho_{\infty}/\rho_{\theta}$). This is demonstrated in Fig. 3 for flows through a normal shock and through the oblique shock attached to a 15-deg wedge. The assumption that $\epsilon \to 0$ is basic to the Newtonian theory; the less stringent assumption that ϵ becomes small is basic to the thin shock layer theory. It should be noted that, since the thickness of the shock layer is inversely proportional to the density behind the shock, the shock layer is thin when ϵ is small.

the

wi

me

M

an

en

po

lat

fu

di

pl

ca

no

as

gr

ed

W

le

th

in

li

p

W

ti

n

The influence of the so-called real gas effects resulting from molecular vibrational excitation, dissociation and ionization effects is also shown in Fig. 3 for an assumed flight altitude of 150,000 ft [using Feldman's shock tables (3)]. The general effect is to diminish the value of ϵ noticeably, particularly for the larger shock wave inclination angles. fect results in a marked reduction in the shock layer thickness as indicated in Fig. 2 for the 40-deg wedge and cone and in Fig. 4 for the 40-deg cone at various flight altitudes. Also plotted in Fig. 4 are curves for a perfect gas with constant = 1.4 and 1.2. A reduction in γ from 1.4 to 1.2 results in a thinning of the shock layer by a factor of approximately 50 per cent. Over a major part of the flight envelope of interest here, the "effective" value of γ appears to lie between 1.2 and 1.3. Although the shock layer thickness appears quite sensitive to real gas effects, it does not necessarily follow that the pressure on the surface of the body is equally as sensitive. In fact, for our example of the 40-deg cone, Fig. 5 shows that the pressure changes very little with large changes in γ. In Figs. 2-4, the curves for the "real gas" flow over the cone have been obtained by an approximate theory developed by Brook (4) for cones at hypersonic speeds.

In the shock expansion and the thin shock layer theories discussed here, the equations are formulated to treat a real gas; this results in very little additional complication in the theoretical development, although the additional computational complexity is rather significant. Relaxation times other than zero (thermodynamic equilibrium) or infinity (frozen flow) are not taken into account in this work.

The fact that the perturbed flow field lies quite close to the body and that the Mach lines in this flow field are highly swept means that we must generally deal with gradients of flow properties across the shock layer which are large in comparison with the gradients along the layer. This consideration plays a rather significant role in the development of the hypersonic thin shock layer and the small-disturbance theories. The situation at hypersonic speeds is quite different from that at extremely low supersonic Mach numbers, where we find just the reverse to be true, so far as the relative orders of magnitude of the gradients are concerned. At the lower supersonic speeds, the Mach lines and thus the disturbances propagate in directions which are more nearly normal to the flow.

Another characteristic of the flow associated with the shock lying close to the body is that the shock is frequently highly curved. This curvature results either from curvature of the body (the shock shape at hypersonic speeds being generally quite sensitive to changes in body contour) or indirectly to the interaction effect of the boundary layer (producing effective body curvature). At a point immediately behind the shock, the value of the entropy, which is constant along the streamline from that point, is directly related to the local shock angle. The vorticity in the flow is dependent on the entropy gradient normal to the streamlines, according to Crocco's vorticity law, and is thus a function of shock wave curvature. Consequently, the highly curved hypersonic shocks generate large entropy gradients in the flow behind them, usually in the immediate vicinity of the body, and thus

the flow is frequently highly rotational. We will be concerned with the correction to the two-dimensional shock expansion method required to account for the effect of reflections of Mach lines from the vorticity lines in the entropy layer. In any given problem, this entropy (or vorticity) layer may be generated by curvature of the shock wave in the longitudinal direction (i.e., in the meridional plane). However, we will encounter another geometry where the entropy layer is important, namely, in flows over conical configurations at angle of attack where the shock wave curvature of interest is in the lateral direction (i.e., in the transverse plane). Thus, as fully discussed by Ferri (5), the crossflow streamlines, each of different entropy, create an entropy layer as they wrap around a circular cone converging to a nodal point singularity in the plane of symmetry at the top (e.g., the small angle of attack case shown in Fig. 6). The resulting entropy gradients normal to the conical body occur at lower supersonic speeds as well, although perhaps not quite so strongly. Entropy gradients associated with blunting of the apex or leading edges of the body will obviously not be involved in the present

The simplification of the differential equations of hypersonic flow, by whatever suitable means chosen, invariably leads to a set of equations that are still nonlinear. From the theoretical standpoint this nonlinearity is one of the most important features of hypersonic flows. Because of the nonlinearity of the equations, closed form solutions for the flow properties are unavailable except for a few special cases, and we must thus resort to numerical integration of the simplified equations. In many instances this is not so great an additional inconvenience as it might seem, since the inclusion of real gas effects in the calculations requires a numerical solution in any event. Owing to the increased importance of nonlinear effects, the method of characteristics and the closely related shock expansion method find greater application at hypersonic speeds.

Small-disturbance flow theory is based on the assumption that the maximum inclination of the body surface δ_{10} , relative to the free stream, is exceedingly small. For small to moderate supersonic Mach numbers we are thus able to assume perturbation velocities which are small compared with speed of sound, or that $M_{\infty}\delta_{w}\ll 1$. At hypersonic speeds however, $M_{\infty} \gg 1$, and $M_{\infty} \delta_w = 0$ (1). Thus the linearized flow equations, which result from application of the small disturbance assumption at small to moderate supersonic Mach numbers, no longer apply at hypersonic speeds. Physically, this may be seen by noting, for example, that the free stream Mach lines, along which disturbances propagate according to linear theory, become so highly swept that they penetrate the body; this is true when $M_{\infty}\delta_{\omega} \geq 1$. We note also that, since the flow is rotational as mentioned before, the velocity potential used in the linear equations no longer exists. Nor can we correctly continue to satisfy the body boundary conditions along some mean surface, as is done in linear theory, because of the large gradients in the flow.

Wing-Body "Interference"

With the breakdown of the linear theory, we lose the ability to superimpose solutions of the flow equations. Thus, the concept of the interference effect as developed in the linear supersonic theory, whereby the interference, calculated separately, is simply added to the disturbances generated individually by the configuration components, no longer applies.

We may recall that, at moderate supersonic speeds, interference pressure fields may be employed to reduce zero-lift drag (of the wing) or drag due to lift [e.g., see Ferri (6), Nielsen (7), Lomax and Heaslet (8), or Scheuing, Hopkins and Lang (9)]. At higher Mach numbers, the wing zero-lift wave drag makes a relatively minor contribution to the total configuration drag. Significant zero-lift drag reduction by the use of interference effects can then generally result only by operating on the body drag (for example, by employing a

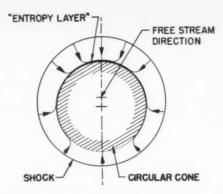


Fig. 6 Sketch of streamline pattern about circular cone at small angle of attack

ring-wing). With more normal wing-body combinations, however, it appears that the only reasonable possibility for improving aerodynamic efficiency by the use of inviscid interference effects is by reducing the drag due to lift.

As Mach number increases, the importance of positive pressure coefficients (which, for a perfect gas, approach a limiting value in the range 1.8 to 2, depending on the value of γ) completely overshadows that of the negative pressure coefficients (which approach zero as $M_{\infty} \to \infty$). Hence at high Mach numbers, inviscid wing-body interference is derived primarily from the interaction of positive pressure fields. In view of the large wing area needed for efficient flight at extreme altitudes, configurations having the body slung under the wing have been considered by various researchers [e.g., see Eggers and Syvertson (10)] with an eye toward using the body generated high pressure field to produce interference lift on the wing.

A simplified configuration of this type consists of a flat plate delta wing with a half-cone slung underneath. It is not our intention here to investigate optimum combinations; indeed, it is pointless to engage in such an investigation unless we also consider viscous effects, since viscous interaction, friction drag and aerodynamic heating will generally play significant roles in the determination of the most efficient shape [e.g., see (11)]. Thus, we consider this particular configuration merely to provide us with a model about which we may make a few pertinent remarks. It should be noted, incidentally, that because of the insignificant pressures on the shielded upper surface of any configuration, a substantial volume may be carried there without large drag penalty.

To simplify the calculations involved, the wing has been set at zero incidence to the free stream; for our purposes, no loss of generality will result. The inviscid interference effect is now simply obtained by integrating the disturbed pressure field about the body, over that portion of the wing which lies within the shock layer. As we have discussed, the shock layer thins noticeably with increasing Mach number, so that the interference effect is considerably reduced. Consequently, except for quite slender bodies (see Fig. 7), the relative importance of the interference effect to the lift on the half-cone is quite small at hypersonic Mach numbers. Even for the slender configurations, however, the inviscid interference effect diminishes rapidly with increasing Mach number. As previously noted, the influence of real gas effects, as reflected in reduced γ , is to produce an even thinner shock layer without appreciably changing the pressures in the shock layer; thus the interference is reduced still further at higher Mach numbers.

There is yet another important factor which should be mentioned in this discussion of hypersonic wing-body interaction—

the importance of boundary layer interaction with the external flow. Reference is made here to some very recently measured, and thus not yet fully explained, pressure distributions. These measurements were made in the AEDC von Kármán Facility at a Mach number of 8. Fig. 8 presents the transverse pressure distributions on a flat plate delta wing of 50-deg sweep with an underslung 12.5-deg half-cone. Pressures measured at two different stations (6.5 and 11.5 in. from the apex) are plotted for the case of zero angle of attack. The abscissa used here is the arc length measured out along the surface from the plane of symmetry, nondimensionalized with respect to the radius of the cone.

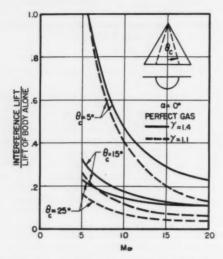


Fig. 7 Variation of interference effect with Mach number

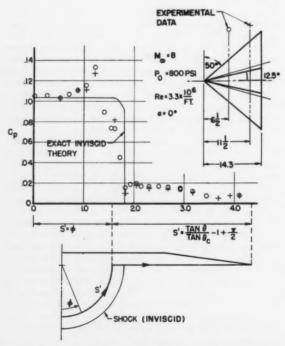


Fig. 8 Pressure distribution on delta wing with half-circularcone body at Mach 8 ($\alpha = 0$ deg)

We note first of all that the flow is quite conical. However, at the wing-body juncture, and for that matter for some distance out on the wing, there is a noticeable difference between the measured pressures and those predicted by inviscid flow theory. This difference is apparently caused by a combination of interaction effects associated with the flow in the corner formed by the wing-body juncture.

If this flow were symmetric with respect to the corner, we would expect a noticeable increase in the boundary layer displacement thickness at the corner and along both walls immediately adjacent to it. The pressure in the vicinity of the corner would then be increased as a result of the symmetrical thickening of the boundary layer and its interaction with the inviscid flow. For the case of the wing-body at zero angle of attack, however, the flow is strongly asymmetric with respect to the corner. The predominant contribution to this asymmetry is the high pressure field neighboring one wall of the corner, namely, the conical body, with the associated shock wave positioned very close by. Secondary contributions to the asymmetry are provided by the curvature of the conical body and the shock wave. The high pressures in the shock layer cause a significant flow in the boundary layer away from the corner and out on to the wing, thickening the wing boundary layer and strengthening the weak compression waves generated by it. Viewed in the plane normal to the body shock, this reverse flow can be likened to the shock induced separation in front of a step in supersonic flow, with the additional complication that the large flow component parallel to the shock causes the reverse flow streamlines to be helical rather than closed loops.

Applying this reasoning to the case of Fig. 8, we observe that, as the corner is approached from the body side, the pressure initially rises considerably above the prediction of inviscid theory, probably as a result of the thickening of the boundary layer. However, the venting effect due to the outflow of the boundary layer, as described previously, predominates in the immediate vicinity of the corner with the result that the shock is weakened and the pressures drop below the inviscid predictions within the shock layer but are higher for several shock layer thicknesses out on the wing.

It should be pointed out that the pressures which we are considering here are quite sensitive to changes in "effective" body shape. For example, estimating local pressures by the tangent-cone method, we find that the 30 per cent increase in pressure which occurs initially as the corner is approached from the body side may be obtained by an increase in the "effective" cone shock angle of about 1½ deg. Similarly, the reduction in pressure in the shock layer could result from a reduction may be brought about by a curving in of the shock toward the corner as a result of the mechanism described above.

Some evidence of the existence of such a shock layer shape is presented in Fig. 9, a vapor screen photograph taken during the course of the experiments at AEDC. The model is at an angle of attack of approximately 5 deg; it has been rolled slightly so that the light screen reflects from the underside of the wing as well as from the side of the body. The light screen for this photograph was located at 50 per cent of the body length from the apex. The free stream is cold, and the condensed particles in it reflect light shining through a slit located at the left (out of the picture). The compression region under the wing is observable as a brighter area because of the greater density of condensed particles. The hotter boundary layer on the wing surface evaporates the particles in the stream with the result that no light is reflected and the region is dark. Similarly, the flow behind the body shock is relatively hot so that the shock layer is dark. However, a finite relaxation time for the particles passing through the body shock is apparent from the brightness immediately behind the shock. At the wing-body juncture we may detect evidence of the cooler air in the shock layer flowing outboard



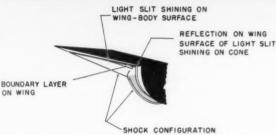


Fig. 9 Vapor screen photograph of flow about delta wing and half-cone body at Mach 8 ($\alpha \approx$ 5 deg)

as part of the reverse flow in the boundary layer. Careful examination also reveals the curving in of the shock toward the body juncture.

Hypersonic Theory Development

In recent years, the rapid advancement in hardware development has tended to outdistance research in certain areas of hypersonic flow theory. The fact that a great deal has been accomplished, nevertheless, is evidenced by the growing number of general treatises on the subject; perhaps the most comprehensive from the standpoint of basic flow theory is the text of Hayes and Probstein (1). Several other discussions of hypersonic flow characteristics, theories and related problems have been presented, e.g., Chernyi (12), Lees (13), Truitt (14), and Kaufman and Scheuing (15).

In view of the great strides in aerospace vehicle development contemplated for the relatively near future, the designer has generally been forced to rely on the use of empirical procedures for predicting pressures and forces on all but the simplest shapes, e.g., using modified, uncorrected Newtonian (see following), tangent-wedge, tangent-cone, and equivalent-cone [Zakkay and Visich (16)] methods. Unfortunately, extensive correlation with experimental data is required before it is possible to define generally the regions of applicability for such empirical methods, and even then they must be applied with some caution.

On the other hand, one of the main advantages in the use of rational theories lies in the ability to estimate errors involved and thus to define proper regions of applicability for each of the various theories. Thus a much higher degree of reliability is associated with predictions of rational theories, and considerable savings can result from the reduction in the cost of wind tunnel tests directed either at developing a particular configuration for a specific mission or at defining the region of applicability of an empirical method as mentioned

previously. Perhaps of even greater importance is the fact that the use of rational theories leads to a fundamental understanding of the phenomena and processes involved, and that with any rational theory is associated a body of valuable concepts. This is only partially true in the case of semi-empirical "theories," and not at all true with purely empirical methods.

A number of rational theories are available to treat flows about bodies with attached shocks; two-dimensional and axisymmetric bodies have usually been considered. We have already briefly mentioned several of these theoretical methods, and, where applicable, the characteristic features of hypersonic flow which are employed in their development. A description of research in progress in a few pertinent theoretical areas is included in the following text; in one instance, a semi-empirical method, which has grown out of the quest for a simplified rational solution for the flat plate delta wing, is presented. The theoretical results and numerical solutions discussed here will be treated in greater detail in the open literature, hopefully in the near future [see also (17)]. The related experimental results have only recently been obtained and have not yet been subjected to thorough critical analysis. However, representative samples of the data are given here to point out certain striking features and to provide the basis for a limited discussion of the correlation of the theoretical work with experiment.

Nothing further will be mentioned about hypersonic small-disturbance theory [see Van Dyke (18) and Hayes and Probstein (1)] or the associated similar solutions [see Mirels (19)], which include strip theory and explosion theory. Higher order solutions for the small-disturbance theory have recently been developed by Waldman (and Probstein), (20), permitting the application of this theory to somewhat thicker bodies at somewhat lower speeds than covered by the first-order small-disturbance theory.

Before proceeding, perhaps a few additional remarks should be made concerning the Newtonian theory, an extensive exposition of which appears in a book by Hayes and Probstein (1). In its proper form, the Newtonian theory [as developed by Busemann (21) provides an expression for the pressure at any point as being equal to the pressure immediately behind the shock plus a term to account for the centrifugal force effects in the shock layer. As pointed out in (1), the ballisticians have for many years employed a pressure law, based on Newton's inelastic-impact model for a rarefied gas, which does not include the centrifugal force correction. A modified sine-squared pressure formula, proposed by Lees (13), has found widespread application as follows: The pressure behind the shock is evaluated using the local body angle in place of the shock angle; the centrifugal force correction is not included, and the result is modified by a multiplicative factor which makes the calculated stagnation pressure equal the actual value. We shall refer to this empirical relation as the

Shock Expansion Method Improvement

modified Newtonian pressure law.

The shock expansion method, as first set forth by Epstein (22), provides for the calculation of the pressure distribution on a two-dimensional airfoil having attached leading edge shock waves. The method accounts for the change in entropy through the shock at the leading edge, and calculates the pressure distribution by assuming a series of Prandtl-Meyer expansion waves emanating from the surface. The effects of reflections of these Mach waves from the shock wave or the vorticity layer are not accounted for. In those instances where these effects may properly be neglected, the shock expansion method finds even greater utility when it may be employed in conjunction with strip theory.

The basic shock expansion method has been extended to the calculation of the flow field about the body by Eggers, Syvertson and Kraus (23). Additional discussion of this problem is presented in the book by Hayes and Probstein (1), and also in (17). The various procedures for obtaining the structure of the flow field itself will not be discussed here in any detail. An approximation to the shock expansion method for thin airfoils at high Mach numbers is also developed in (23).

Under certain conditions (thin shock layer or highly curved forebody), the influence of the reflected characteristics from the shock wave or the vorticity lines in the flow may become quite significant with the result that, in many of these cases, the shock expansion method is seriously in error. However, when the reflections from the vorticity lines are roughly equal in importance to reflections from the bow shock, the uncorrected shock expansion method may continue to give good accuracy simply because the outgoing expansion waves reflect from the bow shock as compressions and from the vorticity lines as expansions with the result that the reflections tend to cancel

As discussed in (1), a significant amount of work devoted to the analytic improvement of the shock expansion method has been reported in the literature [e.g., see Mahoney (24), Mahoney and Skeat (25), Waldman and Probstein (26) and Kogan (27,28)]. What we seek here is a fairly simple numerical method to provide a first-order correction to the basic shock expansion theory by calculating the effect of the shock reflections and vorticity reflections on the surface pressure of a two-dimensional body. The correction is essentially superimposed on the zeroth-order calculation, i.e., the basic shock expansion results. In certain instances, this assumed superposition is not fully valid so that the procedure must be modified in some way. One obvious means is to restart the procedure after it has been carried a distance downstream from the leading edge, with a revised estimate of the assumed zeroth-order flow field. Another is to take into account, in one way or another, the multiple reflections of certain strong wave families.

Reflections From the Shock Wave

We consider here the case where the correction of primary importance is that due to the reflections from the bow shock. A basic parameter which is used here is the reflection coefficient \mathfrak{R}_s , which measures the ratio of the strength (in pressure change) of a reflected wave to an incident wave. The evaluation of this reflection coefficient has been considered by Lighthill (29), Chu (30), Eggers, Savin and Syvertson (31), and Waldman and Probstein (26). We also require a geometrical parameter r which is the ratio of the spacing of incoming waves to the spacing of reflected waves. From Fig. 10, r is given by l_1/l_2 and can be determined as, using the oblique shock relation, $\tan (\sigma - \delta_s) = \epsilon \tan \sigma$

$$r = (1 - \epsilon \sqrt{M_s^2 - 1} \tan \sigma) / (1 + \epsilon \sqrt{M_s^2 - 1} \tan \sigma) \quad [1]$$

where

 σ = shock wave angle

 δ_s = flow deflection angle immediately behind the shock ϵ = ratio of the free stream density ρ_{∞} to the density

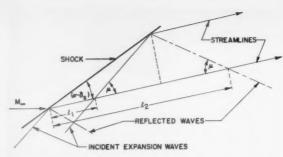
immediately behind the shock ρ_s $M_s = \text{Mach number immediately behind the shock}$

If we let π_+ and π_- represent the strengths of the outgoing and reflected waves in units of pressure gradient, then the condition of reflection at the shock may be written

$$\pi_{-} = r \Re_s \pi_{+} \tag{2}$$

Using the two-dimensional characteristic equations

$$dP = \mp \Gamma P d\delta$$
 on $dy/dx = \tan(\delta \pm \mu)$ [3]



Th

re

[1

of

as

Fig. 10 Geometrical construction for reflection distance ratio r

where

 $\Gamma = \gamma_* M/\sqrt{M^2-1}$ with γ_* the effective adiabatic index (identical to the ratio of specific heats γ for a perfect gas)

M = local Mach number

P = local pressure

 δ = flow deflection angle

 $\mu = local Mach angle$

The boundary condition at the wall provides the following relation

$$\pi_{+} = \pi_{-} + \Gamma P(d\delta_b/ds)$$
 [4]

The subscript b is used to denote conditions at the body surface, and s is distance measured along the body surface. The pressure gradient on the body is

$$dP_b/ds = \pi_+ + \pi_- \tag{5}$$

If we assume that π_+ , π_- and $d\delta_b/ds$ are independent of s, we may combine Equations [2, 4 and 5] to give

$$\frac{dP_b}{ds} = \left[\frac{1 + r\Re_s}{1 - r\Re_s}\right] \Gamma P \frac{d\delta_b}{ds}$$
 [6]

for a plane ogive. Uncorrected shock expansion theory would correspond to $rR_s = 0$. A finite difference method may be used for numerically integrating Equation [6]. It should be pointed out that this expression is valid even if $|rR_s|$ is not small compared with one.

If the body curvature is proportional to s^m instead of being constant (m > -1), we may obtain the result

$$\frac{dP_b}{ds} = \left[\frac{1 + r^{1+m}\Re_s}{1 - r^{1+m}\Re_s}\right] \Gamma P \frac{d\hat{b}_b}{ds}$$
 [7]

If m is small and/or r close to 1, this provides results which are nearly the same as those obtained from the formula with m = 0.

Reflections From the Vorticity Layer

In general, an outgoing wave will pass through a region which has a continuous variation in vorticity. By writing the cross-differentials of the characteristic equations, Equation [3], and combining and integrating [see (17)], it is possible to derive approximately, for small changes, an average reflection coefficient $\overline{\alpha}_{ij}$ which measures the accumulated pressure reflection produced by an outgoing wave

$$\bar{\Re}_{p} = (\Gamma - \Gamma_{b})/(\Gamma + \Gamma_{b})$$
 [8]

This result represents an extension to that given in (1) for the reflection of a wave from a single vorticity line. The quantity Γ in Equation [8] is evaluated outside the distinguishable vorticity layer near the wall; in our example calculation, it was evaluated at the shock.

Thin Shock Layer Approximation

An approximate result for a two-dimensional wing at hypersonic speeds can be obtained with the assumptions that the shock layer is thin and the body shape has only slowly changing curvature. Thus we may write

$$\pi_{+b} = \pi_{-b} + \Gamma_b P_b (d\delta_b/ds)$$
 [9]

$$\pi_{-b} = \Re \pi_{+b} \tag{10}$$

where R is an overall reflection coefficient which will shortly be determined. It follows that the pressure gradient is

$$\frac{dP_b}{ds} = \frac{1+\Re}{1-\Re} \Gamma_b P_b \, \frac{d\delta_b}{ds} \tag{11}$$

using Equations [9, 10 and 5] evaluated at the body. Uncorrected shock expansion theory would correspond to $\Re=0$.

Since δ_b is given, we may obtain a relation between the presently calculated pressure on the body and that obtainable by the uncorrected shock expansion method

$$\int_{0}^{1} \frac{1 - \Re}{1 + \Re} \frac{dP_{b}}{\Gamma_{b}P_{b}} = \left[\int \frac{dP_{b}}{\Gamma_{b}P_{b}} \right]_{\text{shock-expansion}}$$
[12]

We must now evaluate the overall reflection coefficient $\mathfrak R$ for the case where both shock and vorticity reflections must be taken into account. We assume that the average vorticity reflection coefficient $\overline{\mathfrak R}_{\mathfrak p}$ is only slowly varying. By considering the various reflections within the shock layer, the following two equations may be written

$$\pi_{+} = (1 - \overline{\mathfrak{R}}_{v})\pi_{+v} - \overline{\mathfrak{R}}_{v}\pi_{-}$$
 [13]

$$\pi_{-h} = (1 + \overline{R}_{\tau})\pi_{-} + \overline{R}_{\tau}\pi_{+h}$$
 [14]

In addition we have Equations [2 and 9], and by suitable combination of these four equations, together with Equations [11 and 5] evaluated at the body, we obtain [neglecting terms of $O(\overline{\mathfrak{A}}_s^2)$]

$$\Re = (r\Re_s + \overline{\Re}_s)/(1 + r\Re_s \overline{\Re}_s)$$
 [15]

Thus if $\overline{\mathfrak{A}}_v$ is small, \mathfrak{A} is approximately equal to $r\mathfrak{A}_v$; if $r\mathfrak{A}_s$ is small, \mathfrak{A} is approximately equal to $\overline{\mathfrak{A}}_v$.

Thin Shock Layer Approximation (Modified Power Law)

Under certain conditions, an extremely simple relationship accounting for shock and vorticity reflections may be derived from Equation [12]. These conditions are that $\mathfrak R$ is a constant, and that Γ_b is also essentially constant. The latter assumption is valid in a fluid with the thermodynamic coefficient γ_* [see (1)] close to one and the flow locally hypersonic, which is generally consistent with the assumption of a very thin shock layer. We may now simply evaluate the integrals in Equation [12] to obtain

$$\frac{P}{P_0} = \left[\frac{P_{S.E.}}{P_0}\right]^{1+\Re/1-\Re} \tag{16}$$

where

 P_0 = pressure behind the shock at the leading edge P_{S,E_i} = local pressure obtained from the uncorrected shock expansion method

Numerical Applications

The first two examples which we will present here are calculated for a profile which is being tested in our current experimental program. As can be seen from the sketch in Fig. 11, this profile has a rather large amount of curvature near its leading edge. Unfortunately, at the time of this writing, exact calculations by the method of characteristics are not

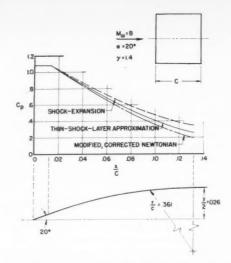


Fig. 11 Calculated pressure distribution on highly curved profile at Mach 8, $\alpha=20$ deg and $\gamma=1.4$

available for comparison with the results of other calculational procedures.

In the first example, we have a Mach number of 8, an angle of attack of 20 deg and $\gamma = 1.4$. In this particular case, the formula given by both Lighthill (29) and Chu (30), for the shock reflection coefficient Rs [see (1), p. 269] was used, and it was determined that R, was negligible in this case. Thus the primary correction to the shock expansion method required here is that due to reflections from the vorticity layer. Results from three different methods are presented in Fig. 11. In this particular case the modified power law version (requiring $\overline{\mathbb{R}}_{v} = \text{constant}$) of the thin shock layer approximation could not be used, since $\overline{\mathbb{R}}_{r}$ varies from 0.02 initially to 0.19 downstream. As might be expected, the effect of the reflections from the vorticity layer is to reduce the pressures calculated by the shock expansion method ($\overline{\mathbb{R}}_{n}$ neglected) as can be seen by comparison with the results of the thin shock layer approximation (Eqs. [11 or 12]). Results of the modified, corrected Newtonian method, based on body shape, are also shown for comparison.

NOTE: PROFILE DIMENSIONS GIVEN IN FIG. II

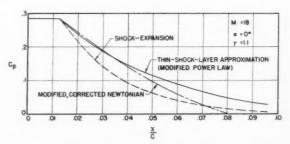


Fig. 12 Calculated pressure distributions on highly curved profile at Mach 18, $\alpha=0$ deg and $\gamma=1.1$

The second example which we consider here is that of the same highly curved profile at Mach number 18, angle of attack of zero deg, and $\gamma = 1.1$. In this particular case, M_h is close to Ms, and reflections from the vorticity layer are insignificant (R, ≈ 0). Because of the high Mach number and the low value of γ , the simple modified power law version of the thin shock layer approximation was employed to obtain the correction to the shock expansion method for the reflections from the shock wave. The value of the shock reflection coefficient R, was calculated from the relation resulting from the strong shock assumption, as given on p. 270 of (1). The effect of incorporating the correction to the shock expansion method is to increase the calculated pressure coefficients, because the expansion waves reflect from the shock as compression waves. The modified, corrected Newtonian, based on body shape, is included for comparison.

Our last example is one which has already been discussed by Eggers, Syvertson and Kraus (23). This example is one of a biconvex airfoil of 10 per cent thickness with Mach number equal to infinity, zero angle of attack and $\gamma = 1.05$. The curves presented in Fig. 13 for the method of characteristics, the shock expansion method, and the modified, corrected Newtonian, based on body shape, are reproduced from (23). Here again, because of the large Mach number and the extremely low value of γ , we have employed the modified power law version of the thin shock layer approximation to calculate the corrections for the shock expansion pressures. As in the previous example, because of the high free stream Mach number the vorticity reflections are not significant but the reflections from the shock are. We see that the calculated slope of the pressure coefficient at the leading edge according to the modified power law is in better agreement with the method of characteristics solution than is the ordinary shock expansion. A noticeable error builds up as the calculation proceeds downstream. This modified power law result can readily be improved by restarting the procedure at some arbitrary point downstream from the leading edge, with a revised estimate of the basic shock expansion solution (making use of the corrected values of the local flow conditions).

Three-Dimensional Flows

For more general geometries having varying sweepback or varying angle of incidence, a more complicated analysis than the standard two-dimensional shock expansion method is required. In our approach to the solution of these three-dimensional flows over flat bodies, a method is being evolved which reduces to the standard shock expansion for two-dimensional flows.

In analogous fashion to the two-dimensional case, a basic

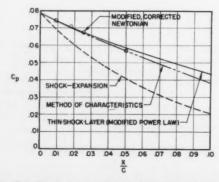


Fig. 13 Calculated pressure distributions on 10 per cent thick biconvex airfoil at Mach $\,\omega$, $\,\alpha=0$ deg and $\,\gamma=1.05$

cylindrical wedge flow is established at the leading edge. The associated planar, strong shock is, in general, disturbed by variations in sweepback or angle of incidence of the body. The perturbations from the cylindrical wedge flow solution are assumed to be infinitesimal, and the problem is linearized in this sense. Hence we are enabled to superimpose elementary conical solutions to obtain the desired result. These small disturbances in the flow field displace the shock, creating entropy and vorticity changes of the first-order in the strength of the disturbances. The perturbation velocity, for which a solution is desired, has been found to be separable into two parts, both conical: The first is irrotational and is chosen to be an arbitrary solution of the classical linearized conical flow theory; the second describes the vorticity in the flow. In this treatment, boundary conditions are satisfied at the undisturbed shock surface, and the conical stream surfaces are replaced by the undisturbed conical stream surfaces.

flo

fla

ty

La

Co

in

(30

fie

Fi

are

fro

str

reg

lin

elli

wi

of

tre

she

ou

Ap

ene

flo

CO

flo

the

fac

A

With the basic reference solution established at the leading edge, the solution is carried downstream by applying the principle of "local linearization." This is done by calculating the effect of small disturbances in terms of the known local conditions in the flow immediately upstream of them. Special consideration must be given in this part of the problem to the interaction between the various disturbances propagating in the flow; this is analogous to the problem in the two-dimensional case of considering the characteristic reflections from the bow shock and the vorticity layer discussed earlier in this section.

Approximate Solution of the Conical Flow Equations

In the section following this, we will discuss the thin shock layer theory and its application to conical configurations with arbitrary cross-sectional shape. We will note that, as presently constituted, the thin shock layer theory is limited in scope to configurations with smooth cross sections (i.e., slope continuous everywhere except perhaps at leading edges). Furthermore, it is restricted to configurations for which the density ratio across the shock, ϵ , is small and is therefore not appropriate at the lower end of the hypersonic Mach number range if the angle of attack is small. For these reasons, we have considered the development of a rational theory for predicting pressures on "distinct," conical, wing-body combinations (such as the flat plate delta wing with underslung cone discussed at the beginning of this paper) at small angle of attack. As a part of this work, we have been concerned with devising an approximate method for calculating pressures on a flat plate delta wing alone. As described briefly in the following, an exact solution requires the determination of the entire flow field about the wing. Since our interest is in surface pressure distributions, our approximate solution is based on a simplified study of the flow in the plane of symmetry and on the surface of the wing. We have been successful to date only in setting up a semi-empirical procedure, which is described in this section.

In this treatment of conical flows, as well as that for the thin shock layer theory, we will be considering projections of the streamlines, or particle trajectories, on a spherical surface r (the distance from the body apex) equal constant. These streamline projections will frequently be referred to simply as streamlines; no confusion should result. It should be noted that the nature of the governing flow equations in any particular region is either elliptic or hyperbolic depending on whether the velocity along the streamline projection is subsonic or supersonic in that region. We will also be considering traces of shock waves and characteristic lines on the spherical surface r = constant. Furthermore, we will be discussing points in the flow, such as singular points, but here also it should be kept in mind that these points represent rays, originating from the body apex, which intersect the spherical surface r = constant at the given point. When we

.

speak of stagnation points, we refer to stagnation of the cross flow velocities only.

A complete solution to the problem of the flow over the flat plate delta wing requires the numerical analysis of mixedtype conical flow fields as discussed in detail by Ferri, Vaglio-Laurin and Ness (32), and Ferri and Vaglio-Laurin (33). Complete solutions have been considered to various degrees in the literature [e.g., Maslen (34), Fowell (35), Bulakh (36) and Brook (37)]. An idea of the structure of the flow field surrounding the wing may be obtained by reference to Fig. 14. On the compression side, the sonic (parabolic) lines are uniquely determined by the two-dimensional flow in the hyperbolic region; the curved shock shape is determined from the solution of the flow in the elliptic region. The flow structure on the expansion side of the wing is characterized by the presence of the curved shock and/or a pseudo-elliptic region (bounded by the limiting characteristic and parabolic line) produced by the interaction between the hyperbolic and elliptic regions. An exact solution to the flow over the delta wing must take into account the properties and boundaries of the various regions delineated in Fig. 14, but except in extreme cases, the entropy gradients produced by the curved shock waves will be small and probably can be neglected without serious error.

Approximate Solution

The conservation equations for mass, momentum and energy for a perfect gas may be combined to produce the following well-known equation of motion governing conical flows [e.g., see Ferri (5)]

where the entropy is singular) has constant entropy.

With the exception of the term involving $\partial v_{\varphi}/\partial \varphi$, our reduced equation of motion, Equation [17b], is identical to the equation for axially symmetric conical flow which may be integrated by simple techniques. Therefore if the behavior of this extra term, as a function of θ , can be deduced in some manner, the determination of the pressure distribution on the surface of the wing is reduced to the integration of an ordinary differential equation (of second-order) in the single independent variable θ , with the term $(1/\sin\theta)\partial v_{\varphi}/\partial \varphi$ representing a correction for lateral effects.

Determination of $\partial v_{\varphi}/\partial \varphi$

We will restrict the remainder of this discussion to the solution for the compression side of the flat plate delta wing. Although we have not yet found a completely rational procedure for determining a first-order solution to the problem, the semi-empirical method which has been devised will hopefully provide results of reasonable accuracy. At the time of writing of this paper, the final IBM 704 program has not been thoroughly checked out and thus numerical solutions are unavailable.

An expression is required for $\partial v_{\varphi}/\partial \varphi$ as a function of θ in the plane of the wing and the plane of symmetry. An earlier attempt at this solution (17) made use of an assumed variation for $\partial v_{\varphi}/\partial \varphi$ based on an approximation to the prediction of linear supersonic theory. This approach unfortunately produced a solution which was physically inconsistent with the actual flow, particularly so far as streamline shapes were

$$v_r \left\{ 2 - \frac{v_{\theta}^2 + v_{\varphi}^2}{a^2} \right\} + v_{\theta} \cos \theta \left\{ 1 + \frac{v_{\varphi}^2}{a^2} \right\} + \frac{\partial v_{\theta}}{\partial \theta} \left\{ 1 - \frac{v_{\theta}^2}{a^2} \right\} + \frac{\partial v_{\varphi}}{\sin \theta \partial \varphi} \left\{ 1 - \frac{v_{\varphi}^2}{a^2} \right\} - \frac{v_{\varphi}v_{\theta}}{a^2} \left[\frac{\partial v_{\theta}}{\sin \theta \partial \varphi} + \frac{\partial v_{\varphi}}{\partial \theta} \right] = 0 \quad [17a]$$

The spherical coordinates and velocity components, r, θ , φ , v_r , v_θ and v_φ are employed here (see Fig. 15); a is the local speed of sound. The entropy equations are expressed as

$$\frac{1}{\sin \theta} \frac{a^2}{\gamma R} \frac{\partial S}{\partial \varphi} = -v_r \left\{ \frac{\partial v_r}{\partial \varphi} \frac{1}{\sin \theta} - v_\varphi \right\} + v_\theta \left\{ \frac{\partial v_\varphi}{\partial \theta} - \frac{1}{\sin \theta} \frac{\partial v_\theta}{\partial \varphi} + v_\varphi \cot \theta \right\} \quad [18a]$$

and

$$\frac{a^2}{\gamma R} \frac{\partial S}{\partial \theta} = -v_r \left\{ \frac{\partial v_r}{\partial \theta} - v_\theta \right\} - v_\varphi \left\{ \frac{\partial v_\varphi}{\partial \theta} - \frac{1}{\sin \theta} \frac{\partial v_\theta}{\partial \omega} + v_\varphi \cot \theta \right\} \quad [19a]$$

We will consider the solution to Equation [17a] in the plane of the delta wing and in its plane of symmetry. Boundary conditions of tangential flow on the wing and of zero crossflow in the plane of symmetry require that v_{φ} must be zero in these planes, and therefore Equation [17a] becomes

$$v_{\tau} \left\{ 2 - \frac{v_{\theta}^2}{a^2} \right\} + v_{\theta} \cot \theta + \frac{\partial v_{\theta}}{\partial \theta} \left\{ 1 - \frac{v_{\theta}^2}{a^2} \right\} + \frac{\partial v_{\varphi}}{\sin \theta \partial \varphi} = 0$$
[17b]

Making use of the appropriate boundary conditions and the fact that $\partial S/\partial\theta$ is equal to zero, Equation [19a] reduces to

$$v_{\theta} = \partial v_{\tau} / \partial \theta$$
 [19b]

in both planes of interest. In the plane of the wing, we obtain the additional relation from Equation [18a] that

$$(\partial/\partial\varphi)(v_{\theta^2} + v_{r^2}) = 0$$
 [18b]

The entropy derivative does not appear here because the entire region adjacent to the wing (except at the wing centerline

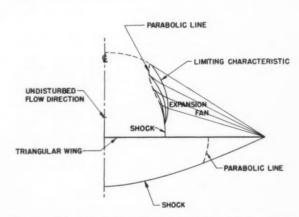


Fig. 14 Schematic of characteristic solution for triangular wing

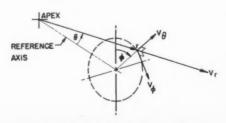


Fig. 15 Spherical polar coordinate system

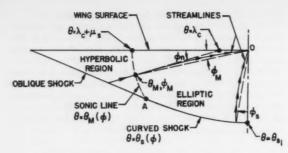


Fig. 16 Shape of streamlines in elliptic region

concerned. As a result, our attack here will be to prescribe a smooth streamline shape and thence derive the desired expression for $\partial v_{\sigma}/\partial \varphi$.

Along any streamline

$$v_{\varphi} = v_{\theta} \sin \theta (\partial \varphi / \partial \theta)$$
 [20]

We will first consider a streamline in the vicinity of the wing surface. In Fig. 16, λ_c is equal to the angle between the wing centerline and the direction of the uniform velocity in the hyperbolic region in the plane of the wing. The sonic line, $\theta = \theta_M(\varphi)$, coincides with the Mach cone of angle μ_s with its axis at $\theta = \lambda_c$. The streamline in the hyperbolic region is normal to the sonic line and thus lies along the radius $\varphi = \varphi_n$ from the point $\theta = \lambda_c$. We consider the streamline which crosses the sonic line at the point θ_M , φ_M , and assume that the nature of the flow pattern is such that the streamlines converge to a single vortical singularity at the centerline along rays $\varphi = \text{constant}$; thus, we have $(\partial \varphi/\partial \theta)_{\theta=0} = 0$. In addition, from conditions in the hyperbolic region, we know $(\partial \varphi/\partial \theta)_{\theta=\theta_M}$.

We make the additional a priori assumption that the slope of the streamline varies monotonically from its value at the sonic line to its value at $\theta=0$. From Fig. 16, we can see that the streamline shape is rather well confined. The choice of expression representing its shape is probably not too critical, particularly in view of the fact that our primary interest is in the calculation of surface pressures. A reasonable choice (satisfying the boundary conditions for $\partial \varphi/\partial \theta$) is

$$\frac{\partial \varphi}{\partial \theta} = \left(\frac{\partial \varphi}{\partial \theta}\right)_{\theta = \theta_M} \left(\frac{\theta}{\theta_M}\right)^m$$
 [21]

where m is arbitrary for the time being.

With φ_M small, $\theta_M \approx \mu_e + \lambda_c$. Integrating Equation [21], we obtain

$$\varphi = \varphi_M \left\{ 1 - \frac{k_1 \theta_M}{m+1} \left[1 - \left(\frac{\theta}{\theta_M} \right)^{m+1} \right] \right\}$$
 [24]

Nur

plan

equi

that

prov

as 0

sma refle of (

rela

tion

terr

gen

rect

plan

refe

plan

sho

line

We

hop

effc

cal

tion

sta

int

Eq

lin Th the cal

dif

A

Substitution of Equation [23] into [21] and then into [20] produces

$$v_{\varphi} = v_{\theta} \sin \theta \, k_1 \varphi_M (\theta/\theta_M)^m \qquad [25]$$

Then, using Equation [24] with [25], we determine the desired equation for $\partial v_{\varphi}/\partial \varphi$ as a function of θ in the plane of the wing

$$\frac{1}{\sin \theta} \frac{\partial v_{\varphi}}{\partial \varphi} = \frac{k_1 v_{\theta} (\theta / \theta_{M_i})^m}{1 - [k_1 \theta_{M_i} / (m+1)][1 - (\theta / \theta_{M_i})^{m+1}]}$$
[26]

with k_1 defined by Equation [23] and $\theta_{Mi} = \mu_{\theta} + \lambda_{\epsilon}$. At $\theta = \theta_{Mi}$, Equation [26] provides the correct relationship between $\partial v_{\varphi}/\partial \varphi$ and v_{θ} [see (37)]

$$\left(\frac{\partial v_{\varphi}}{\partial \varphi}\right)_{\theta=\theta_{Mi}} = k_1(v_{\theta})_{\theta=\theta_{Mi}} \sin \theta_{Mi}$$
 [27]

Applying similar reasoning to the streamlines traversing the elliptic region in the vicinity of the plane of symmetry from the curved shock, $\theta = \theta_{\bullet}(\varphi)$, to the origin, we obtain

$$\frac{1}{\sin \theta} \frac{\partial v_{\varphi}}{\partial \varphi} = \frac{k_2 v_{\theta} (\theta/\theta_{si})^m}{1 - [k_2 \theta_{si}/(m+1)] [1 - (\theta/\theta_{si})^{m+1}]}$$
[28]

where θ_{s_i} is the shock angle in the plane of symmetry and must be determined by the solution. Equation [28], evaluated at $\theta = \theta_{s_i}$, gives

$$k_2 = \frac{1}{(v_\theta)_{\theta=\theta_{gi}} \sin \theta_{gi}} \left(\frac{\partial v_\varphi}{\partial \varphi} \right)_{\theta=\theta_{gi}}$$
 [29]

where $(\partial v_{\varphi}/\partial \varphi)_{\theta=\theta_{s_i}}$ is given in (37) in terms of the angle and curvature of the shock at the plane of symmetry. Using wind axes (reference axis aligned with free stream and passing through the wing apex)

$$\left[\left(\frac{\partial v_{\varphi}}{\partial \varphi} \right)_{\theta = \theta_{si}} = \left(\frac{d^{2}\theta_{s}}{d \varphi^{2}} \right)_{\theta = \theta_{si}} \times \left\{ \frac{\gamma - 1}{\gamma + 1} \frac{1 - V_{\infty}^{2} \cos^{2} \theta_{si}}{V_{\infty} \sin^{2} \theta_{si}} - V_{\infty} \right\} \right]_{\text{wind axes}} [30]$$

where $(\theta_{si})_{\text{wind axes}} = \theta_{si} + \alpha$. It is important to note that here and in Equation [33], the velocities are normalized, as is customary, with respect to the limiting velocity, $V_{\text{max}} = \sqrt{2\gamma RT_0/(\gamma - 1)}$. The result of Equation [30] may be transformed to the centerline-oriented coordinates which we are using by

$$\frac{1}{\sin\theta_{si}} \left(\frac{\partial v_{\varphi}}{\partial \varphi} \right)_{\theta = \theta_{si}} = (v_{\theta})_{\theta = \theta_{si}} \left[\cot \left(\theta_{si} + \alpha \right) - \cot \theta_{si} \right] + \frac{1}{\sin \left(\theta_{si} + \alpha \right)} \left[\left(\frac{\partial v_{\varphi}}{\partial \varphi} \right)_{\theta = \theta_{si}} \right]_{\text{wind axes}}$$
[31]

For streamlines near the wing surface (small φ_M), it may be shown that [using the transformation equations contained in Brook (37)]

$$\varphi_n = \varphi_M[\sin(\mu_s + \lambda_c)/\sin\mu_s]$$
 [22]

and using the expressions in (37) for the velocities in the hyperbolic region

$$\left(\frac{\partial \varphi}{\partial \theta}\right)_{\theta=\theta_M} = \frac{1}{\sin \theta_M} \left(\frac{v_{\varphi}}{v_{\theta}}\right)_{\theta=\theta_M} =$$

$$\varphi_M[\cot \mu_{\theta} - \cot (\mu_{\theta} + \lambda_{\theta})] \equiv k_1 \varphi_M \quad [23]$$

The shock curvature $(d^2\theta_s/d\varphi^2)_{\theta} - \theta_{\theta s}$ is determined in (17) by assuming the shock to be delineated by a cubic equation, the coefficients of which are determined by the fact that we know: the location of point A in Fig. 16; the slope at that point (equal to the oblique shock slope); and the slope at the plane of symmetry (zero). In terms of θ_{ss}

$$\begin{split} \left(\frac{d^2\theta_{ei}}{d\varphi^2}\right)_i &= \frac{1}{2}\sin 2\theta_{ei} \left\{1 - 2\frac{\tan \theta_{ei}}{\cos \varphi_A} \times \right. \\ &\left. \left[\frac{\sin \varphi_A - \tan \alpha \cot \theta_A}{\tan \theta_A \cos \varphi_A - \cot \Lambda} - 3 + \frac{3\tan \theta_{ei}}{\tan^2 \theta_A \cos \varphi_A}\right]\right\} [32] \end{split}$$

Numerical Solution

With $\partial v_{\varphi}/\partial \varphi$ determined in the plane of symmetry and the plane of the wing, we may proceed with the integration of the equation of motion, Equation [17b], in these planes, noting that

$$\lim_{\theta \to 0} v_{\theta} \cot \theta = \partial v_{\theta} / \partial \theta$$

provided that

$$\frac{1}{\sin \theta} \frac{\partial v_{\varphi}}{\partial \varphi} \to 0$$

as $\theta \to 0$ (as assumed). The calculation is initiated by assuming a value for θ_{si} which can be shown to lie within a fairly small allowable range if the curved shock wave is not to have reflex curvature [see (17)]. Using the shock wave relations of (5) to obtain velocities behind the shock, and the derived relation for $\partial v_{\varphi}/\partial \varphi$, Equation [28], we may integrate the equation of motion in the hodograph plane [see (5 and 17)] to determine a solution for v_{τ} and v_{θ} in the plane of symmetry. In general, an iteration procedure will be required before the correct value of θ_{si} is ascertained which permits the boundary condition at the body $(v_{\theta} = 0)$ to be satisfied.

We note that the mass flow which enters the shock through the area bounded by the plane of symmetry and the conical plane, $\varphi = \varphi_s$, must exit through that part of the spherical reference surface (r = constant) which is bounded by the plane of symmetry and the streamline from $\varphi = \varphi_s$ on the shock to the origin (see Fig. 16). The shape of this streamline is fixed by the exponent m, and hence we may employ a balancing of the mass flow to determine the proper value of m. We are thus faced with a double iteration process to solve for θ_{s_i} and m by satisfying the body boundary condition and at the same time balancing the mass flow. In practice it is hoped that the final solution will be relatively insensitive to the choice of m, with a consequent saving in computational effort.

As part of the final solution in the plane of symmetry, we calculate v_r at the centerline ($\theta=0$), $(v_{rc})_{sym}$ and the total pressure ratio across the shock $(P_0/P_{0\infty})_{sym}$. From the solution in the hyperbolic region, we have a different total pressure ratio in the plane of the wing $(P_0/P_{0\infty})_w$ associated with the leading edge oblique shock. With the condition that the static pressure is single-valued at the wing centerline, a jump in v_r results at this point. The value of v_r in the plane of the wing at the centerline is (17)

$$(v_{rc})_w^2 = 1 - [1 - (v_{rc})_{\text{sym}}^2] \left[\frac{(P_0/P_{0\varpi})_{\text{sym}}}{(P_0/P_{0\varpi})_{\text{sym}}} \right]^{(\gamma-1)/\gamma}$$
[33]

Finally, the solution in the plane of the wing is obtained by integrating the equation of motion in the hodograph plane starting with the value of v_r at the centerline, as given by Equation [33]. The solution is carried out to the immediate vicinity of the sonic line where the calculated distributions of velocity components are matched to the values at the sonic line, as prescribed by the solution for the hyperbolic region. This matching procedure will determine (again by iteration) the value of the exponent m in the plane of the wing. A check calculation must now be made to ascertain whether the mass flow in through the shock balances against the radial flow out between the wing surface and an adjacent streamline. If difficulty is encountered in obtaining a mass flow balance, it would then be necessary to replace the assumed equation for the streamline shape on the plane of the wing, Equation [21], with one which employs two unknown parameters to be determined by the solution, rather than just the single parameter m.

Conical Wing-Body Combinations

As pointed out previously, we are primarily concerned in this part of our research program with the development of a

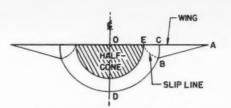


Fig. 17 Shock pattern for conical wing-body at small angle of attack

rational theory for conical wing-body combinations at low angles of attack. Savin (38) has devised a theoretical method for hypersonic flows about slender half-cones (circular cross section) mounted beneath highly swept delta wings. Because of the assumptions on which the method is based, it must, like that described previously for the flat plate delta, be considered as semi-empirical. In light of the importance of the boundary layer interaction with the flow in the vicinity of the corner, and for several shock layer thicknesses out on the wing, the correlation obtained by Savin between his inviscid theoretical method and the experimental results was to a certain extent at least, fortuitous. At zero angle of attack, where we are able to calculate exactly the inviscid flow about the circular cone, there occurs a rather serious error in the results of the approximate solution [of (38)] for the plane of the wing.

Although the method proposed by Savin is of use in filling the gap where no suitable procedure otherwise exists, there is a continuing need for a rational theory treating this problem. The shock pattern for the flow at small angle of attack is shown in Fig. 17. In this figure, AB is the known oblique shock from the wing leading edge; BC and BD are the shock segments bounding the elliptic region, and BE is the slip line generated by the intersection of the shock waves at B. The presence of the slip line introduces extra complication into the solution. We require a means for matching the two regions of different entropy (and velocity) across the slip line while the boundary conditions on the body are satisfied simultaneously. Because of the importance of considering the correct shock layer structure if the proper solution is to be obtained, we are attempting in our experimental program to obtain vapor screen photographs of the flow around the wing-body combinations at a Mach number of 8. Fig. 9 is representative of the results of these efforts to date.

Thin Shock Layer Theory for Conical Flows

As the name implies, thin shock layer theory employs the assumption that the shock layer is thin, and, thus, as previously discussed, that $\epsilon \ll 1$ (see Fig. 3) to provide a means for obtaining an approximate solution to the flow equations. This assumption for the magnitude of ϵ is not nearly so strong as that upon which the Newtonian theory is based, i.e., $\epsilon \to 0$ (infinitesimally thin shock layer). Hence in practice we are able to apply it to a wider range of configuration shapes and flow conditions. However, we find many similarities to the Newtonian solution; indeed, the first-order thin shock layer theory solution has the same form as the solution from the Newtonian theory.

In recent years a number of authors have developed higher-order Newtonian theories, including Hayes (39,40) Chester (41,42), Freeman (43), Fraenkel (44), Chernyi (45), Cole (46), Hayes and Probstein (1), Gonor (47,48), and Cheng (49). All of these investigations, except Gonor's and Cheng's, were concerned with two-dimensional and axisymmetric flows; and all except Hayes', Freeman's, Hayes and Probstein's, and Cheng's considered a perfect gas. Both Gonor

(48) and Cheng (49) treated a circular cone at angle of yaw; Cheng also investigated certain general features of three-

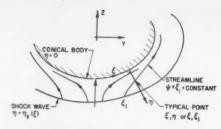
dimensional hypersonic shock layers.

An important part of Gonor's work on the circular cone (47) was the introduction of a stream function transformation which is somewhat similar to the von Mises transformation of viscous boundary layer theory; we make use of this transformation in the following development. In a subsequent publication (48), Gonor extended his initial work to more generally shaped conical bodies at angle of attack and provided two specific examples, i.e., the flat plate delta wing and the elliptic cone. Since this reference was not available for translation until quite recently, the development presented here was carried out independently of Gonor's. Several differences of varying degrees of importance exist between the two treatments. Gonor considers a perfect gas, and his usage of the Lamé coefficients requires separate solution for each case treated; he does not use boundary layer coordinates, and he employs expansions of the flow properties in powers of $\epsilon_l = (\gamma - 1)/(\gamma + 1)$, and thus his procedure for obtaining higher order solutions would be different, and he does not give special consideration to the problem of singularities in the shock layer flow.

In the analysis outlined here for conical configurations of arbitrary cross section, we derive differential equations describing the flow which are parabolic in character. The derivation is based on an order of magnitude analysis which makes use of the thin shock layer assumption mentioned, together with the concept that the flow properties have much greater variation across the shock layer than they do along it. In performing this analysis, we employ a stream function transformation, similar to the von Mises transformation, identical to that introduced by Gonor in (47). For the zeroth-order solution, the shock layer structure is obtained by an iterative procedure using the differential flow equations simplified by neglecting terms of $O(\epsilon)$, but with the exact boundary conditions at the shock. Higher order solutions may be obtained by subsequent iterations of the full differential equations, with the terms of $O(\epsilon)$ evaluated from the results of the previous iteration. Although it has not yet been demonstrated, it is felt that employing the correct boundary conditions at the shock for the zeroth-order calculation might hasten convergence of the higher order solutions. In addition, we obtain a zeroth-order solution that involves a dependence on the free stream Mach number, which seems desirable; use of simplified shock boundary conditions eliminates the influence of Mach number until higher order solutions are calculated [see, for example, Fraenkel (44)]. A discussion is presented of the singular points in the shock layer flow, near which the flow equations can no longer be considered parabolic due to the breakdown of one or more of the basic assumptions. The reader is referred to the introduction of the previous section for a brief review of the use of the spherical projection surface r =constant in depicting the structure of the conical flow field.

Basic Equations and Boundary Conditions

The assumption of a thin shock layer suggests the use of a coordinate system of the boundary layer type with either the shock or body surface as a coordinate surface. We introduce the general conical coordinates r, η , ξ , where r is the distance measured along a ray from the origin, and η and ξ are the curvilinear coordinates of a point, measured across and along the shock layer, respectively, on the sphere r= constant. The curvature of the reference surface selected for the coordinate system must be finite and continuous at every point except, perhaps, at the origin of the conical flow or at a leading edge. Two convenient surfaces that can be used as reference surfaces are the body and the shock. Since we will usually be concerned with the direct problem (body given), we will employ body-oriented coordinates, as the coordinate



the

sym

whe

the

In

sta

len

rela

equ

vel

wh

Th

tai

fu

mi

tr

Fig. 18 Coordinate geometry on a sphere r = constant

system will then not depend on the solution. If the direct problem is formulated in shock-oriented coordinates, the coordinate system is not known beforehand and must be determined by the solution itself.

The form of the equations can be simplified somewhat by taking a plane for one of the coordinate surfaces, in our case the ξ equal constant surfaces (see Fig. 18). We take the scale factor for η equal to r so that $r\eta$ is the distance measured from the body positive in the direction of the shock. The scale factor for the ξ coordinate is $r\chi_1$, where χ_1 is evaluated using the Lamé relations for triply orthogonal surfaces

$$\chi_1 = \cos \eta - K'_b(\xi) \sin \eta \qquad [34]$$

where $K'_{0}(\xi)$ is defined as r times the curvature of the body surface, positive when the surface is concave on the side of positive η . Hence, $r\xi$ corresponds to actual distance on the surface of the body only (i.e., at $\eta = 0$). The metric is

$$(ds)^{2} = (dr)^{2} + (rd\eta)^{2} + (r\chi_{1}d\xi)^{2}$$
 [35]

The coordinate network described here is shown in Fig. 18. The coordinate ξ is defined so that it is equal to zero either in the plane of symmetry or at the leading edges of the configuration; the direction of ξ is defined so that the coordinate system is a right-handed one.

In this coordinate system the equations of motion governing the flow of an arbitrary gas in thermodynamic equilibrium

over a conical body are

$$\frac{\partial \rho v_{\xi}}{\partial \xi} + \frac{\partial \chi_{1} \rho v_{\eta}}{\partial n} + 2\chi_{1} \rho v_{r} = 0$$
 [36a]

$$v_{\xi} \frac{\partial v_r}{\partial \xi} + \chi_1 v_{\eta} \frac{\partial v_r}{\partial \eta} - \chi_1 (v_{\xi}^2 + v_{\eta}^2) = 0$$
 [36b]

$$v_{\xi} \frac{\partial v_{\eta}}{\partial \xi} + \chi_{1} v_{\eta} \frac{\partial v_{\eta}}{\partial \eta} + \chi_{1} v_{\tau} v_{\eta} + v_{\xi}^{2} (\sin \eta + K'_{b} \cos \eta) = -\frac{\chi_{1}}{a} \frac{\partial P}{\partial \eta}$$
 [36c]

$$\begin{split} v_{\xi} \frac{\partial v_{\xi}}{\partial \xi} + \chi_{1} v_{\eta} \frac{\partial v_{\xi}}{\partial \eta} - \chi_{1} v_{r} v_{\xi} - v_{\eta} v_{\xi} (\sin \eta + K'_{b} \cos \eta) &= \\ &- \frac{1}{\rho} \frac{\partial P}{\partial \xi} \end{split} \quad [36d]$$

$$v_{\xi} \frac{\partial S}{\partial \xi} + \chi_1 v_{\eta} \frac{\partial S}{\partial \eta} = 0$$
 [36e]

where v_r , v_η and v_ξ are the velocity components in the r, η and ξ directions, respectively, and P, ρ and S are the pressure, density and entropy. Equation [36a] is the continuity equation, Equations [36b, 36c and 36d] the momentum equations in the r, η and ξ directions, respectively, and Equation [36e]

the entropy equation. The equation of state can be written symbolically for a gas in thermodynamic equilibrium

$$h = h(P, \rho)$$
 [36f]

where h is the specific enthalpy. For an isentropic process, the first law of thermodynamics yields

$$dh = (1/\rho)dP \tag{37}$$

In general, Equation [36f] will be available only in tabular or graphical form. In the special case of a perfect gas with a constant value of the ratio of specific heats γ , a relation equivalent to Equation [36f] is $h = \gamma P/(\gamma - 1)\rho$. Another useful relation, the Bernoulli equation, will serve as one of the basic equations (in place of the ξ -momentum equation) in the development of the theory

$$h + \frac{1}{2}(v_r^2 + v_\eta^2 + v_\xi^2) = h_0$$
 [36g]

where h_0 the stagnation enthalpy is constant throughout the flow.

The boundary conditions at the shock are readily obtained from the shock wave relations in terms of ϵ : at $\eta = \eta_s(\xi)$

$$v_{r_s} = v_{r_m} ag{38a}$$

$$v_{N_s} = \epsilon v_{N_m}$$
 [38b]

$$v_{T_a} = v_{T_m} ag{38c}$$

$$\rho_{\theta} = \frac{1}{4} \rho_{\infty} \qquad [38d]$$

$$P_s = P_{\infty} + \rho_{\infty} v_{N_{\infty}}^2 (1 - \epsilon), \qquad [38e]$$

$$h_z = h_\infty + \frac{1}{2} v_{N_\infty}^2 (1 - \epsilon^2)$$
 [38f]

where the subscripts ∞ and s refer to conditions at the shock wave on the undisturbed and disturbed side, respectively. The velocities V_N and V_T are the components normal and tangential to the shock on the spherical reference surface r= constant; these velocity components are simple algebraic functions of v_η , v_ξ , and the shock wave slope $d\eta_s/\chi_1 d\xi$. In general, ϵ is a function of the free stream conditions and the local flow deflection through the shock and must be determined by iterative procedures. For a perfect gas, ϵ is given explicitly by

$$\epsilon = \frac{\gamma - 1}{\gamma + 1} \frac{M_{N_{\infty}}^2 + 2}{M_{N_{\infty}}^2}$$
 [39]

where $M_{N_{\infty}}$ is the component of free stream Mach number normal to the shock surface. The boundary condition of zero flow through the body surface is given at $\eta = 0$ as

$$v_{\eta} = 0 ag{40}$$

Following Gonor (47) we introduce a "stream function" ψ , which satisfies

$$v_{\xi} \frac{\partial \psi}{\partial \xi} + \chi_{1} v_{\eta} \frac{\partial \psi}{\partial \eta} = 0 \qquad (41)$$

and apply a transformation very much like the von Mises transformation, changing from coordinates η , ξ to coordinates ξ , $\psi(\eta, \xi)$. The stream function ψ is similar to the ordinary stream functions encountered in either two-dimensional or axisymmetric flow in that it is constant along the paths followed by the particles (see Fig. 18); however, in the present case it is impossible to define velocity components in terms of a stream function ψ in such a way that the continuity equation is automatically satisfied, as is the case in two-dimensional or axisymmetric flow. Thus there is a certain arbitrariness in defining ψ , and we shall set it equal to ξ_1 , where ξ_1 is the value of ξ at the intersection of the streamline of interest with the shock (see Fig. 18).

Since the streamline pattern is unknown beforehand, the geometry of the coordinate system must be determined as part of the solution. This disadvantage is offset by the fact that the differential equations take on a particularly simple form, that the stream function serves as a vertical scale in the Newtonian limit where the shock layer thickness approaches zero [see Hayes and Probstein (1), pp. 110–111], and that certain difficulties associated with the entropy layer are generally more easily handled.

With $D/D\xi \equiv (\partial/\partial\xi)_{\xi_1}$, we obtain after transformation

$$\frac{D}{D\xi} \left(\ln \rho v_{\xi} \frac{\partial \eta}{\partial \xi_{1}} \right) + 2\chi_{1} \frac{v_{r}}{v_{\xi}} = 0$$
 [42a]

$$v_{\xi} \frac{Dv_{\tau}}{D\xi} - \chi_{1}(v_{\xi}^{2} + v_{\eta}^{2}) = 0$$
 [42b]

$$v_{\xi} \frac{Dv_{\eta}}{D\xi} + \chi_{i}v_{r}v_{\eta} + v_{\xi^{2}} \left(\sin \eta + K'_{b} \cos \eta \right) = -\frac{\chi_{i}}{\rho} \frac{\partial P/\partial \xi_{i}}{\partial \eta/\partial \xi_{i}} \quad [42c]$$

$$v_{\xi} \frac{Dv_{\xi}}{D\xi} + \chi_{1}v_{\tau}v_{\xi} - v_{\eta}v_{\xi} \left(\sin \eta + K'_{b} \cos \eta\right) =$$

$$-\frac{1}{\rho} \left(\frac{DP}{D\xi} - \frac{\partial P/\partial \xi_{1}}{\partial \eta/\partial \xi_{1}} \frac{D\eta}{D\xi}\right) \quad [42d]$$

$$S = S(\xi_1)$$
 [42e]

$$h = h(P, \xi_1)$$
 [42f]

Equation [42e] is merely a statement of the fact that the entropy along a streamline remains constant. In this system of equations, since η is an additional dependent variable, another equation must be provided to complete the system; from Equation [41]

$$v_{\xi} \frac{D\eta}{D\xi} = \chi_1 v_{\eta}$$
 [42g]

Method of Solution

The transformed system of partial differential equations governing the flow field is nonlinear and is not solvable analytically. In order to derive a consistent solution of specified accuracy, we must first derive an approximate solution that bears some known relation to the exact solution. Then an iteration procedure can be set up which is based on the known relationship between the exact and approximate solutions. We will take as a first-order solution, one which is asymptotic to the exact solution in the limit $\epsilon \to 0$. With the a priori assumption that the shock layer thickness is $0(\epsilon)$, we estimate the order of magnitude of the various terms from the value they take on at the shock surface using Equations [38]

$$\frac{h - h_{\rm I}(\xi_1)}{V_{\infty}^2} = 0(\epsilon) \qquad \frac{\rho}{\rho_{\rm \infty}} = 0\left(\frac{1}{\epsilon}\right) \qquad \frac{P}{\rho_{\rm \infty} V_{\infty}^2} = 0(1)$$

$$\frac{v_{\tau}}{V_{\infty}} = 0(1) \qquad \frac{v_{\eta}}{V_{\infty}} = 0(\epsilon) \qquad \frac{v_{\xi}}{V_{\infty}} = 0(1) \qquad \eta = 0(\epsilon)$$

and from Equation [34], $1 - \chi_1 = 0(\epsilon)$. We note that the introduction of the stream-function transformation has eliminated $\partial/\partial \eta = 0(1/\epsilon)$ from our equations; we have instead $D/D\xi = 0(1)$ so that the derivatives, $\partial/\partial \xi$ and $D/D\xi$, are of the same order. After isolating the terms of lowest order in the equations of motion, we obtain

$$\frac{D}{D\xi} \left(\ln \rho v_{\xi} \frac{\partial \eta}{\partial \xi_{1}} \right) + 2 \frac{v_{r}}{v_{\xi}} = \left\{ 2 \frac{v_{r}}{v_{\xi}} \left(1 - \chi_{1} \right) \right\} = 0(\epsilon) \quad [43a]$$

$$v_{\xi} \frac{Dv_{\tau}}{D^{\xi}} - v_{\xi}^{2} = \{v_{\xi}^{2}(\chi_{1} - 1) + \chi_{1}v_{\eta}^{2}\} = 0(\epsilon)$$
 [43b]

$$K_b'v_{\xi}^2 + \frac{1}{\rho} \frac{\partial P/\partial \xi_1}{\partial \eta/\partial \xi_1} = -\left\{v_{\xi} \frac{Dv_{\eta}}{D\xi} + \chi_1 v_{\eta} v_{\eta} + v_{\xi}^2 \left[\sin \eta + K_b'(\cos \eta - 1)\right] + \frac{1}{\rho} \frac{\partial P/\partial \xi_1}{\partial \eta/\partial \xi_1} \left(\chi_1 - 1\right)\right\} = 0(\epsilon) \quad [43c]$$

In view of Equation [42e], Equation [37] applies as the equation of state along a streamline, and thus

$$h(\xi, \xi_1) - h_s(\xi_1) = \left\{ \int_{\xi_1}^{\xi} \left(\frac{DP}{\rho D \xi} \right) D \xi \right\} = 0(\epsilon)$$
 [43d]

Combining Equation [43d] with the Bernoulli equation

$$[h_{s}(\xi_{1}) - h_{0}] + \frac{1}{2} [v_{r}^{2} + v_{\xi}^{2}] =$$

$$- \left\{ \frac{1}{2} v_{\eta}^{2} + \int_{\xi_{1}}^{\xi} \left(\frac{DP}{\rho D\xi} \right) D\xi \right\} = 0(\epsilon) \quad [43e]$$

Finally, Equation [42g] is written

$$\frac{v_{\xi}}{v_{n}} \frac{D\eta}{D\xi} - 1 = \{(\chi_{1} - 1)\} = 0(\epsilon)$$
 [43f]

To a first approximation, with ϵ small we may neglect the terms appearing in the braces on the right-hand side of Equations [43]. Higher order approximations can be obtained by determining the terms in the braces from the solution of next lower order. This procedure can, in principle, be continued to yield results to any desired degree of accuracy. Since the exact equations are nonlinear, nothing can be said about the convergence of the above procedure; but it is felt that except at, or near, certain singularities, convergence should be obtained for e small enough.

Zeroth-Order Solution

For the "zeroth-order approximation" (differential equations to zeroth order in ϵ , shock boundary conditions exact), we require a solution to the set of differential equations, Equations [43], with the terms on the right-hand side set equal to zero. In the following, the superscript (0) indicates solutions of the zeroth-order equations. For the inverse problem (i.e., shock given) the quantities P_s , h_s and ρ_s are given once and for all, and therefore should not be superscripted in that case.

To this zeroth-order approximation, we see that the enthalpy is constant along streamlines (Eq. [43d]), and that the magnitude of the total velocity is also (from Equation [43e]). Using Equation [43e] in [43f] and integrating, making use of the boundary conditions given by Equation [38a and 38c], we obtain

$$v_r^{(0)} = v'_{\xi_s} \sin(\xi - \xi_1) + v'_{r_{\infty}} \cos(\xi - \xi_1)$$
 [44a]

$$v_{\xi^{(0)}} = v'_{\xi_{\delta}} \cos(\xi - \xi_{1}) - v'_{\tau_{\infty}} \sin(\xi - \xi_{1})$$
 [44b]

where the primed velocity components are to be evaluated at the intersection of streamline ξ_1 with the shock.

Equations [43a, 43b, 43f, 38b and 38c] can be solved to develop a general expression for the pressure at any point in the

$$P^{(0)} = P_s^{(0)} + \rho_w K'_b \int_{\xi_1}^{\xi} Q(\xi_1) (v_{\xi}^{(0)})^3 d\xi_1$$
 [45]

where

$$Q(\xi_1) \equiv \frac{\chi_1}{\epsilon v_{\xi_s}} \left[\frac{d\eta_s}{\chi_1 d\xi} - \frac{v_{\eta_s}}{v_{\xi_s}} \right]$$

As expressed by this equation, the pressure at any point in the shock layer is equal to the pressure at the shock minus the pressure differential across the shock layer due to the lateral curvature of the streamlines. This solution for the pressure is analogous to the solution obtained by Busemann for two-dimensional and axisymmetric bodies in (21) referred to as the "Newton-Busemann" pressure law by Hayes and

Probstein in (1). The integral term appearing in the pressure relation is generally called the centrifugal correction

Similarly, the equation of the streamline can be found after further calculation as

$$\eta^{(0)} = \rho_{\infty} \int_{\xi_{1_h}}^{\xi_1} \frac{Q(\xi_1)v_{\xi}^{(0)}}{\rho^{(0)}} d\xi_1$$
[46]

fac

col

the

(1) rec

sha

ate

the

usi

in

cal

un

acl

[43

lat

on

all

Sin

tac

str

box

sho

In

tha

she

Ta

AP

The third velocity component $v_{\eta}^{(0)}$ may be obtained from Equations [43f and 46]

$$v_{\eta}^{(0)} = v_{\xi}^{(0)} \frac{D\eta^{(0)}}{D\xi}$$
 [47]

The location of the shock surface in ξ, ξ_1 space is determined from the boundary condition at the body, Equation [40] and Equation [47], from which either $v_{\xi}^{(0)} = 0$ or $D\eta^{(0)}/D\xi = 0$ at $\eta = 0$.

The surfaces of the class of bodies with subsonic leading edges (or no leading edges at all) are wetted by streamlines which all originate at the apex. Streamlines in our zerothorder approximation follow paths of zero lateral curvature (geodesics) on the body surface [see Hayes and Probstein (1), pp. 114-115]. Therefore, v_ξ will be zero on the surface of these bodies, since, in this case, the geodesics are straight rays from the origin. Thus, the crossflow streamlines in the shock layer for the zeroth-order approximation will terminate at various points on the body surface as indicated in Fig.

The streamline which intersects the body at a given point in ξ,ξ_1 space is denoted by ξ_{1b} . Using the boundary condition $v_{\xi}^{(0)} = 0$ and an assumed shock shape, we may determine ξ_{1b} for a given value of ξ implicitly from Equation [44b], since v'_{ξ_0} and v'_{τ_0} are then functions of ξ_1 only. However, the flow properties throughout the shock layer will be required for the calculation of the surface pressure and the shock layer thickness, and thus we may conveniently use an alternative calculational approach. For given ξ , $v_{\xi}^{(0)}(\xi_1)$ in the shock layer is calculated proceeding from the shock to the body. When v_{ξ} changes sign we have bracketed the desired value of Ein which may then be readily obtained. These remarks are interpreted graphically in Fig. 19 where the desired ξ_{1b} corresponds to the body location at point A.

Conical configurations having simple convex surfaces with supersonic leading edges are wetted by streamlines that With the body suroriginate at the leading edges (Fig. 20). face coincident with a crossflow streamline, the second result of the application of the flow boundary condition at the body, i.e., $D\eta^{(0)}/D\xi = 0$, is satisfied. In this instance, ξ_{1b} is equal to \$1LE.

BODY

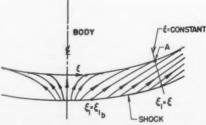


Fig. 19 First-order streamline pattern, with $v_{\xi} = 0$ on body, and determination of \$1,

The desired expressions for the pressure on the cone surface $P_b^{(0)}$ and the shock layer thickness $\Delta \eta^{(0)}$ are obtained directly from Equations [45 and 46], respectively

$$P_{b}^{(0)} = P_{s}^{(0)} + \rho_{\omega} K'_{b} \int_{\xi_{1_{b}}}^{\xi} Q(\xi_{1}) (v_{\xi}^{(0)})^{3} d\xi_{1}$$
 [48]

$$\Delta \eta^{(0)} = \rho_{\infty} \int_{\xi_{1_h}}^{\xi} \frac{Q(\xi_1) v_{\xi}^{(0)}}{\rho^{(0)}} d\xi_1$$
 [49]

where the integrations are carried out along the line ξ = constant (see Fig. 19).

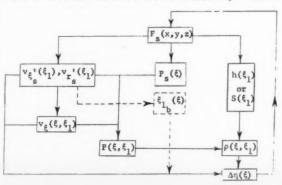
The procedure for calculating the zeroth-order solution for the direct (body given) problem is outlined diagrammatically in Table 1 [similar to the approach of Hayes and Probstein (1)]. With the body shape specified, the iteration procedure required to obtain $\Delta \eta^{(0)}$ is initiated by assuming the shock shape $F_s(x, y, z) = 0$ to be identical to that of the body. The velocities and thermodynamic properties of the fluid immediately behind the shock are determined, and these quantities are used to calculate the lateral component of velocity v_{ξ} , and shapes the pressure P at any point in the $\xi_{\cdot}\xi_{1}$ space. Then thence the pressure P at any point in the ξ, ξ_1 space. using the calculated pressure distribution, together with the energy equation, in the equation of state, we find the density in the ξ, ξ_1 space. Finally, after fixing the value of ξ_{1b} , we may calculate a first approximation to $\Delta \eta^{(0)}$ from which we may obtain an improved shock shape. This process is repeated until the desired accuracy for the zeroth-order solution is achieved. The analysis is simplified if P_s is much greater than the integral (centrifugal correction) term in Equation [45], for then the integral term does not have to be recalculated for each iteration.

In the inverse problem, the shock shape is specified and the computational procedure is relatively straightforward since the flow properties behind the shock are determined once and for all. In this particular case however, it is generally more convenient to use shock-oriented coordinates.

Singularities in the Thin Shock Layer Solution

As indicated in Fig. 19, the zeroth-order solution for detached shock configurations provides us with a pattern of streamlines which terminate at various points around the body surface. Thus, the entropy layer (and the associated nodal point singularity) which occurs in the actual flow, as shown in Fig. 6, does not appear in the zeroth-order solution. In effect, the nodal point singularity has been spread out over the body surface. This inconsistency arises from the fact that while our zeroth-order boundary condition at the body is $v_{\xi}/v_{\infty} = 0$, this velocity ratio is actually $O(\epsilon)$. Cheng has investigated the problem of the entropy layer in hypersonic shock layers at some length (49), with special reference to the

Table 1 Procedure for zeroth-order thin shock layer solution



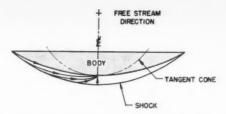


Fig. 20 Streamline pattern sketched for smooth convex conical body—leading edge shock attached

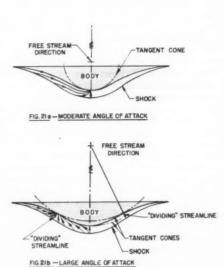


Fig. 21 Streamline pattern sketched for conical body having reverse lateral curvature—leading edge shock attached

proper representation of the entropy layer for a circular cone at small yaw angle. Gonor (47) mentions that the entropy layer appears in the higher order calculations without any special handling in the zeroth-order solution (although he provides very little information concerning his higher order solutions). In any event, whereas the entropy changes very rapidly through the entropy layer and near the nodal point singularity, the pressure does not, so that we may not have to account for the structure of the entropy layer exactly in a theory aimed at predicting surface pressures only [see Ferri (5), and Cheng (49)].

Another feature of the flow about bodies with detached shocks is that, for large enough angles of attack, the pressure becomes zero at some point on the surface. As this point of zero pressure is approached, the shock layer thickens noticeably, and the assumption of a thin shock layer is violated [see Hayes and Probstein (1), pp. 81-92]. This problem has been investigated to some extent by Freeman (43) who found that the solution diverged and that the shock layer thickness became infinite as this pressure singularity was approached. By restricting our present investigation to configurations with supersonic leading edges, we are able to avoid in most cases the possibility of the pressure falling to zero at any point in the shock layer (an advantage alluded to in the beginning of this paper).

Streamline patterns associated with flow around conical shapes with attached leading edge shocks are sketched in Figs. 20 and 21. We note that the dominant feature of these flow patterns is the presence of nodal point singularities, where the streamlines converge to a point. The location of these singularities depends on the cross-sectional shape and angle of attack.

In order to help clarify the following discussion, we introduce a parameter κ which is equal to the radius of curvature of the body at the stagnation point in the plane of symmetry divided by the radius of curvature of a tangent right circular cone, having its apex coincident with that of the body and its axis aligned with the free stream. We note that when $\kappa>1$, the flow in the immediate vicinity of the stagnation point will be converging and thus we will have a nodal point singularity [or more properly, a half-node, see (17), p. 30]; when $\kappa<1$, the flow will be diverging, and we will have a saddle point.

For the case of the smooth, convex conical body with attached shock (shown in Fig. 20), & will always be greater than one and the flow converges from the leading edge to a nodal point singularity in the plane of symmetry [see also Waldman (and Probstein) (20)]. A somewhat more complex conical body shape, having a surface with reverse lateral curvature, is drawn in Fig. 21. For small enough angle of attack, κ is greater than 1, and we will again have a nodal point at the body centerline. As the angle of attack increases, however, κ will become less than one so that a saddle point appears in the plane of symmetry. Two nodal points occur in the shock layer, one on either side of the saddle point. For the type of body shape being considered here, the nodal points generally move outboard with increasing angle of attack, the streamline projections converging to them from each side of the so-called "dividing" streamlines. To the zeroth-order approximation, the dividing streamlines are perpendicular to the shock and body (lying along a line, ξ = constant) and are located at the points of tangency of the inscribed right circular cone having its apex coincident with the body apex and its axis aligned with the free stream.

At the forementioned nodal points, v_{ξ} should equal zero. Since the zeroth-order equations are parabolic, this downstream boundary condition cannot be satisfied in general. Neither will this condition be satisfied by going to higher order iterations, since the higher order equations are also parabolic. This was found to be true for the case of the flat plate delta wing, at least, in the solution obtained by Gonor (48).

The problem of handling the flow in the vicinity of both the saddle and the nodal point stagnation regions is common to the solution for both the detached shock and attached shock configurations. The cause of the local failure of the thin shock layer theory can be traced to the nonuniformity of the approximations involved. In particular, v_{ξ} is not large compared to v_{η} in these stagnation regions; therefore our order of magnitude analysis is no longer correct as it stands, and we must retain many of the terms we previously neglected. If we do this, the system of equations becomes elliptic in nature, and solutions which are locally valid near the stagnation points must be derived and matched with the solution in the remainder of the shock layer if uniformly valid results are to be obtained.

In this paper we have presented the thin shock layer solution, for conical configurations, which should be valid over the major portion of the flow field. Additional solutions which are valid in the stagnation regions are required, particularly for the problem of the nodal point singularity. Procedures for handling the saddle-point stagnation region have been considered by Hayes, Chester and Freeman for two-dimensional and axisymmetric shapes.

In closing, it should be noted that, since pressure changes through the stagnation regions are mild, it is not unreasonable to expect that even without incorporating the local corrections, the zeroth-order thin shock layer theory should be quite useful.

Experiments

In the experimental program currently being run at the AEDC Gas Dynamics Facility, we have included several

conical bodies of identical planform shape but with different cross sections, namely: flat plate, circular arc, and a family of smooth shapes having reverse lateral curvature. All of the pressure data discussed here were taken at a Mach number of 8.1 and are for a planform with 50-deg leading edge sweepback. The programming of the thin shock layer theory for the IBM 704 is currently in the final stages; thus we are presently unable to draw any direct comparisons between theory and experiment. Sample data are exhibited in Figs. 22-24 to provide some indication of the scope of the program and to allow a few brief remarks concerning certain anticipated results.

The main purpose in testing the flat plate delta wing is to provide data for comparison with results of the method outlined in section under "Approximate Solution of The Conical Flow Equations." However, this model is also representative of the simplest case which we can treat with the conical thin shock layer theory, namely, one in which the centrifugal effects are zero. As can be seen from Fig. 22, the pressure reduction in the elliptic region is rather noticeable, particularly at the higher angle of attack, amounting to approximately 10 per cent of the two-dimensional pressure in the hyperbolic region. Gonor has found (48) that with straightforward usage of the thin shock layer theory, the pressure on the flat plate delta is constant, even for higher order solutions; the proper behavior of the equations in the elliptic region must be taken into account if the pressures are to be calculated correctly. The exact theoretical, two-dimensional pressure in the hyperbolic region is plotted in Fig. 22 for $\alpha = 4$ and

Pressure data for the circular-arc cross section are plotted in Fig. 23. The general equation for this cross section is

$$\frac{z}{x} = \left[\frac{\tan^2 \theta_{LE}}{\sin^2 \delta_{LE}} - \left(\frac{y}{x} \right)^2 \right]^{1/2} - \frac{\tan \theta_{LE}}{\tan \delta_{LE}}$$
 [50]

where δ_{LE} is the leading-edge wedge angle in the plane x= constant. In the case considered, $\theta_{LE}=40$ deg and $\delta_{LE}=15.3$ deg (20 deg normal to leading edge). This shape will have moderate centrifugal force effects in the shock layer, and, as indicated in the discussion for Fig. 20, will have a nodal point which is always located on the centerline for the angle

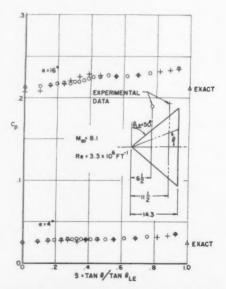


Fig. 22 Experimental pressure distributions on flat plate delta

APR

Fig.

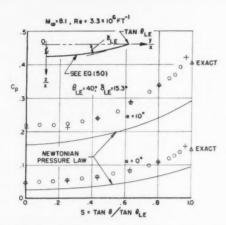


Fig. 23 Experimental pressure distributions on conical body having circular arc cross section

of attack range of interest. Values for the exact the oretical pressure behind the leading-edge shock are plotted in Fig. 23 using the values of α as recorded. As with the flat plate delta wing, we believe that an as yet undetermined α correction must be incorporated in the data reduction. Results from the empirical Newtonian pressure law are also plotted. If these results were modified by matching pressures at the leading edge, the agreement, although still lacking, would be improved.

The cross section for the family of conical bodies having re-

verse lateral curvature (e.g., see Fig. 21) is delineated by the equation

$$\frac{z}{x} = \tan \theta_0 [1 - 3\Omega^2 + 3\Omega^4 - \Omega^6]$$
 [51]

with

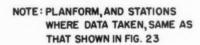
$$\Omega \equiv (y/x/(\tan \theta^*)$$

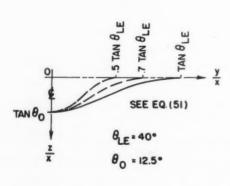
In this expression, $\tan \theta_0$ equals y/x in the plane of symmetry, and $\tan \theta^*$ equals y/x at the point of tangency of the body curve to the plane of the wing. We have selected three basic shapes for study; they are identified by $\tan \theta^* = n \tan \theta_{LE}$ with n = 0.5, 0.7 and 1.0 (see Fig. 24). In all three cases, $\theta_0 = 12.5$ deg and $\theta_{LE} = 40$ deg.

Fig. 24 presents recently obtained pressure data for the shape which has n=1.0, the solid contour in this figure. Since this is the thickest of the three bodies, we should expect the least difficulty in applying the thin shock layer theory to this case. We also expect that the centrifugal force effects will not be quite so strong as for the other two bodies. In the case of the n=1.0 body, the nodal point remains at the centerline throughout the angle of attack range (see Fig. 21a); with the other two bodies we anticipate a movement of the nodal point outboard, as discussed earlier.

The data for the n=1.0 body, shown in Fig. 24, are compared with values at the centerline (where the centrifugal effect is zero) predicted by the empirical tangent-wedge and tangent-cone methods, and with values at the leading edge predicted by exact theory. At the lower angles of attack, significant viscous interaction occurs close to the leading edge, which, at $\alpha=0$, is at zero incidence.

Results of calculations using the Newtonian pressure law are plotted and we note that the trends of the experimental data are only roughly approximated by this empirical method. In this case, the modified Newtonian pressure law is not applicable; matching pressures at the leading edge produces results which are generally at considerable variance with the





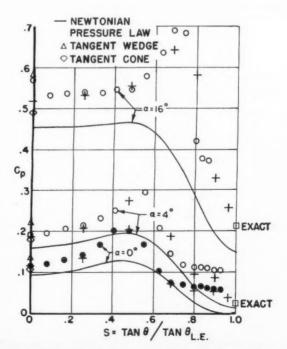


Fig. 24 Experimental pressure distributions on conical body having reverse lateral curvature in cross section

experimental data. The conical thin shock layer theory, as we have developed it, is expected to give improved pressure predictions in that the correct oblique shock relations will be satisfied, and the effect of the centrifugal forces generated by lateral streamline curvature will be in the right sense.

Acknowledgment

The research reported herein was conducted by Grumman Aircraft Engineering Corp. in association with the Aeronautical Research Associates of Princeton. Professor Wallace D. Hayes guided the work at ARAP on the extension of the shock expansion method; his stimulating discussions of the other work reported are also gratefully acknowledged. In addition, special mention should be made of the significant contributions of John W. Brook, Robert E. Melnik and Harold R. Mead of the Grumman Research Department, who worked on the other areas of theoretical research reported and on the execution of the experimental program; and of K. Evan Gray and Roger W. Sullivan of ARAP, who worked on the development of the shock expansion method. A substantial portion of this research was supported by the Flight Control Laboratory of the USAF Wright Air Development Division under Contract no. AF 33(616)-6400. The cognizant Air Force technical representatives are Donald Hoak and H. Max Davis.

Nomenclature

a	=	local speed of sound
C_P	=	pressure coefficient
h	=	specific enthalpy
k	=	thermal conductivity

= r times the curvature of the body surface, positive K_b^1 when surface is concave on side of positive η

M Mach number P pressure

reflection distance ratio defined by Equation [1]

 r, η, ξ conical curvilinear coordinates

r, θ , φ spherical coordinates

specific gas constant in the perfect gas law

R overall reflection coefficient R. shock reflection coefficient

R overall vortical layer reflection coefficient

Re Reynolds number

coordinate measured along a streamline

S specific entropy T

velocity components in the coordinate directions 01 where i indicates the particular coordinate direction (e.g., $i \equiv r, \theta, \varphi \text{ or } r, \eta, \xi$)

magnitude of total velocity

 V_N , $V_T =$ velocity components normal and tangential to the shock on the spherical reference surface r = con-

 $V_{\rm max}$ maximum adiabatic velocity for a perfect gas

x, y, zCartesian coordinates angle of attack

adiabatic index

Mach number parameter $(\gamma_e M/\sqrt{M^2-1})$ Г

local flow deflection angle

maximum inclination of body surface ô

shock layer thickness Δ

density ratio across a shock wave $(\rho_{\infty}/\rho_{\delta})$

= limiting density ratio for a perfect gas $\left(\frac{\gamma-1}{\gamma+1}\right)$ € [

angle between wing centerline and the direction λ_c of velocity in the hyperbolic region on the wing

sweepback angle Δ

= Mach angle

maximum inclination of body surface

 $\Pi_{+}, \Pi_{-} =$ strengths of outgoing and reflected waves in units of pressure gradient

= density

= shock wave angle (equivalent to θ_s in conical flow)

conical scale factor = stream function

Subscripts

conditions at the body surface

"initial" value LE leading edge

M point on sonic line

conditions immediately behind the shock wave

0 = stagnation conditions

conditions in the free stream

Superscripts

= zeroth-order solution (0)

= evaluated at intersection of streamline ξ1 with the

Gener

446.

Shock

Super 32

Witho 264, 1

Polyt

Wing 36

Appre

Mater

Delta

man .

Wing A58F

dridg

hos

lite.

Cal

AP

References

1 Hayes, W. D. and Probstein, R. F., "Hypersonic Flow Theory," Academic Press, N. Y., March 1959. chaps. IV, V and VI.
2 NACA, Ames Research Staff, "Equations, Tables, and Charts for Compressible Flow," NACA Rep. 1135, 1953.
3 Feldman, S., "Hypersonic Gas Dynamic Charts for Equilibrium Air,"

3 Feddman, S., "Hypersonic Cas Dynamic Charts for Equilibrium Air,"
Avoc Research Laboratory, Research Rep. 40, Jan. 1957.

4 Brook, J. W., "An Approximate Method for Calculating the Hypersonic Flow Around Circular Cones at Zero Angle of Attack, Including Real
Gas Effects," Grumman Aircraft Engineering Corp., Research Dept. Rep.
RE-132, March 1960.

5 Ferri, A., "Conical Flow" in "General Theory of High Speed Aero-dynamics," sect. H, chap. 3, pp. 721-747 (Vol. 6 of "High Speed Aero-dynamics and Jet Propulsion"), Princeton University Press, Princeton, N.

J., 1958.

5., 1958.
6 Ferri, A. and Clarke, J. H., "On the Use of Interference Effects for Shock Drag Reduction at Supersonic Speeds," Polytechnic Institute of Brooklyn, PIBAL Rep. 258, July 1954.
7 Nielsen, J. N., "Quasi-Cylindrical Theory of Wing-Body Interference at Supersonic Speeds and Comparison With Experiment," NACA Rep. 1252.

1955.

8 Lomax, H. and Heaslet, M. A., "A Special Method for Finding Body Distortions That Reduce the Wave Drag of Wing and Body Combinations at Supersonic Speeds," NACA Rep. 1282, 1956.

9 Scheuing, R. A., Hopkins, H. B., Jr. and Lang, J., "Contoured Fuselage Sides Producing Maximum Theoretical Drag Reduction for Supersonic Wing-Body Combinations at Any Given Lift Coefficient," Grumman Aircraft Engineering Corp., Research Dept. Rep. RE-101, Nov. 1957.

10 Eggers, A. J., Jr. and Syvertson, C. A., "Aircraft Configurations Developing High Lift-Drag Ratios at High Supersonic Speeds," NACA RM A55LO5, 1956.

11 Butz, J. S., Jr., "Hypersonic Aircraft Will Face Technical Cost."

ABOLUO, 1996.

11 Butz, J. S., Jr., "Hypersonic Aircraft Will Face Technical, Cost Problems," Aviation Weck, vol. 70, no. 25, June 22, 1959, pp. 156 ff.
12 Chernyi, G. G., "Flow of Gas at Hypersonic Speeds," Fizmatgiz, Moscow, 1959 (in Russian). (To be translated by Academic Press, Inc.,

Lees, L., "Hypersonic Flow," Proceedings, 5th International Aeronautical Conference, Los Angeles, the IAS, N. Y., 1955, pp. 241-276.
 Truitt, R. W., "Hypersonic Aerodynamics," Ronald Press Co., N. Y.,

Kaufman, L. G., II and Scheuing, P. A., "An introduction to Hypers," Grumman Aircraft Engineering Corp., Research Dept. Rep. RE-82, Oct. 1956

sonics," Grumman Aircraft Engineering Corp., Research Dept. Rep. RE-82, Oct. 1956.

16 Zakkay, V. and Visich, M., Jr., "Experimental Pressure Distributions on Conical Elliptical Bodies at M &= 3.09 and 6.0," Polytechnic Institute of Brooklyn, PIBAL Rep. 467, March 1959.

17 Scheuing, R. A., Hayes, W. D., Mead, H. R., Brook, J. W., Melnik, R. E. and Gray, K. E., "Theoretical Prediction of Pressures in Hypersonic Flow—Configurations With Attached Leading Edge Shock," Grumman Aircraft Engineering Corp., Research Dept. Rep. RE-124, Nov. 1959.

18 Van Dyke, M. D., "A Study of Hypersonic Small-Disturbance Theory," NACA Rep. 1194, 1954. (Supersedes NACA TN 3173, 1954.)

19 Mirels, H., "Similarity Solutions for Inviscid Hypersonic Flow Over Slender Power Law and Related Bodies," ARS preprint 1111-60, 1960.

20 Waldman, G. D., "Extended Hypersonic Small-Disturbance Theory," Brown University, WADC TN 59-173. (Modified version by Waldman, G. D. and Probstein, R. F., submitted to J. Fluid Mechanics.)

21 Busemann, A., "Flüssigkeits und Gasbewegung," Handwörterbuch der Naturwissenschaften, Zweite Auflage, Band 4, Jeana, Gustav Fischer, 1934, p. 276.

1934, p. 276.

1934, p. 276.

22 Epstein, P. S., "On the Air Resistance of Projectiles," Proc. National Academy of Sciences, U.S.A., vol. 17, 1931, pp. 532-547.

23 Eggers, A. J., Jr., Syvertson, C. A. and Kraus, S., "A Study of Inviscid Flow About Airfoils at High Supersonic Speeds," NACA Rep. 1123, 1953.

24 Mahoney, J. J., "A Critique of Shock-Expansion Theory," J. Aeron. Sci., vol. 22, 1955, pp. 673-680, 720.

25 Mahoney, J. J. and Skeat, P. R., "The Flow Around a Supersonic Airfoil," Aero Note 147, Aeronautical Research Laboratory, Research and Development Branch, Melbourne, Australia, 1955.

26 Waldman, G. D. and Probstein, R. F., "An Analytic Extension of the Shock-Expansion Method," Brown University, Div. Eng., WADC Tech. Note 57-214, 1957.

27 Kogan, A., "On Inviscid Flow Near an Airfoil Leading Edge or an Ogive Tip at High Supersonic Mach Numbers," J. Aeron. Sci., vol. 23, 1956, pp. 794-795.

1956, pp. 794-795.
28 Kogan, A., "An Application of Crocco's Stream Function to the Study of Rotational Supersonic Flow Past Airfoils," Quart. J. Mech. Appl. Math.,

vol. 11, 1958, pp. 1-23.
29 Lighthill, M. J., "The Flow Behind a Stationary Shock," Philosophical Magazine, vol. 40, 1949, pp. 214-220.

30 Chu, B. T., "On Weak Interaction of Strong Shock and Mach Wave Generated Downstream of the Shock," J. Aeron. Sci., vol. 19, 1952, pp. 433-

446. 31 Eggers, A. J., Jr., Savin, R. G. and Syvertson, C. A., "The Generalized Shock-Expansion Method and Its Application to Bodies Traveling at High Supersonic Air Speeds," J. Aeron. Sci., vol. 22, 1955, pp. 231-238, 248. 32 Ferri, A., Vaglio-Laurin, R. and Ness, N., "Mixed-Type Conical Flow Without Axial Symmetry," Polytechnic Institute of Brooklyn, PIBAL Rep.

264. Dec. 1954.

Ferri, A. and Vaglio-Laurin, R., "On Conical Flows of Mixed Type,"
 Polytechnic Institute of Brooklyn, PIBAL Rep. 306, April 1956.
 Maslen, S. A., "Supersonic Conical Flow," NACA TN 2651, March

Fowell, L. R., "An Exact Theory of Supersonic Flow Around a Delta

35 Fowell, L. R., "An Exact Theory of Supersonic Flow Around a Delta Wing," University of Toronto, UTIA Rep. 30, March 1955.
36 Bulakh, B. M., "Remarks on the Paper by L. R. Fowell, 'Exact and Approximate Solutions for the Supersonic Delta Wing'," Zh. Prikladnaya Matematika i melchanika, vol. 22, no. 3, 1958, pp. 404-407.
37 Brook, J. W., "Non-Linear Supersonic Conical Flow Over Flat Plate Delta Wings," Polytechnic Institute of Brooklyn, Dept. of Aeronautical En-

gineering and Applied Mechanics, M.Ae.E. thesis, June 1959. (Also Grumman Aircraft Engineering Corp., Research Dept. Rep. RE-117, May 1959.)

38 Savin, R. C., "Approximate Solutions for the Flow About Flat-Top Wing-Body Configurations at High Supersonic Airspeeds," NACA RM A38F02, Sept. 1958. (Confidential) 39 Hayes. W. D., "Some Aspects of Hypersonic Flow," Ramo-Wooldidge Corp., Rep. STL-1955-1, 1955.

40 Hayes, W. D., "Hypersonic Flow Fields at Small Density Ratio," Ramo-Wooldridge Corp., Rep. STL-1955-5, 1955.
41 Chester, W., "Supersonic Flow Past a Bluff Body with a Detached Shock. Part I. Two-Dimensional Body," J. Fluid Mech., vol. 1, 1956,

"Supersonic Flow Past a Bluff Body With a Detached Chester, W., 42 Part II. Axisymmetrical Body." J. Fluid Mech., vol. 1, 1956, pp.

Shock. Part II. Axisymmetrical Body," J. Fluid Mech., vol. 1, 1956, pp. 490-496.
43 Freeman, N. C., "On the Theory of Hypersonic Flow Past Plane and Axially Symmetric Bluff Bodies," J. Fluid Mech., vol. 1, 1956, pp. 366-387.
44 Freenkel, L. E., "The Hypersonic Flow of a Polyatomic Gas Past Bodies of Finite Thickness," Proceedings, Ninth International Congress of Applied Mechanics, Brussels, vol. 1, 1957, pp. 255-265.
45 Chernyi, G. G., "Hypersonic Flow Around a Body by an Ideal Gas," Izvestiia, AN SSSR, OTN, no. 6, 1957, pp. 77-85.
46 Cole, J. D., "Newtonian Flow Theory for Slender Bodies," J. Aeron. Sci., vol. 24, no. 6, 1957, pp. 448-455.
47 Gonor, A. L., "Hypersonic Flow Around a Cone at an Angle of Attack," Izvestiia, AN SSSR, OTN, no. 7, 1958, pp. 102-105. (Translated by M. D. Friedman, Inc., Needham Heights, Mass.)
48 Gonor, A. L., "The Flow Around Conical Bodies During the Motion of a Gas With Supersonic Velocity," Izvestiia, AN, SSSR, no. 1, 1959. Translated by J. W. Brook, Grumman Aircraft Engineering Corp., Research Translation TR-13, Dec. 1959.
49 Cheng, H. K., "Hypersonic Shock-Layer Theory of a Yawed Cone and Other Three-Dimensional Pointed Bodies," WADC TN 59-335, Oct. 1959.

Error Analysis Considerations for a Satellite Rendezvous

W. M. DUKE1

Space Technology Laboratories, Inc. Los Angeles, Calif.

E. A. GOLDBERG²

Aerospace Corp. Los Angeles, Calif.

I. PFEFFER³

Space Technology Laboratories, Inc. Los Angeles, Calif.

A feasible system for satellite rendezvous with a noncooperative target is described, including both the ascent and the terminal (homing) phases. For the ascent phase, both direct ascent and parking orbit approaches are considered. An error analysis of the ascent phase, employing both analytical and computer techniques, shows that either the direct ascent or parking orbit approach can place the rendezvous vehicle in a favorable position for acquisition of the target and initiation of a simple terminal maneuver to effect the rendezvous. The terminal maneuver, which lasts several minutes, employs a self-contained radar to track the target, and body mounted, non-throttleable engines to provide discrete orbital corrections. An error analysis of the terminal maneuver shows that a rendezvous within 50 ft of the target can be achieved with a terminal relative velocity less than 3 fps.

THE NECESSITY for the achievement of a satellite rendezvous devolves from a variety of military and space technology requirements:

The inspection and possible negation of a potentially hostile satellite.

2 The in-space assembly of subsystems into a large satellite.

3 The supply and maintenance of satellites, including the possibility of personnel, data, equipment or fuel transfer.

4 Interrogation and transfer from interplanetary return vehicles to obviate the necessity for atmospheric re-entry and landing of large vehicles.

For purposes of technical discussion, the overall idea of a rendezvous involves a target and a rendezvous vehicle: the necessity to track the target and thence to compute its ephemeris; a scheme of space kinematics and a corresponding means of implementing this scheme via launching and guidance. A satellite interception system is composed of the following elements: the target and its trajectory; ground

Presented at the ARS Semi-Annual Meeting, Los Angeles, Calif., May 9-12, 1960.

Senior Vice-President.

Member ARS Member of Technical Staff. Member ARS.
 Member of Senior Technical Staff.

tracking for target ephemeris determination; a ground computer; a rendezvous vehicle; a launch system; a scheme of space trajectories; and a guidance concept and its mechaniza-

The Target, Its Trajectory, Target Tracking and Ground Computing

A completely passive target is presumed. In considering the target cross-section area for use in an analytical exercise or in an experimental demonstration, one is concerned with the necessity for properly simulating an operational satellite as well as with the appropriateness of the target for ground tracking and rendezvous vehicle tracking. A nominally circular orbit somewhere in the region 200-1000 nautical miles is similarly reasonable.

The target must be ground tracked to maintain an up to date ephemeris, necessary for exact rendezvous vehicle launch timing and for determination of the parameters of a nominal launch trajectory which will place the rendezvous vehicle in a favorable position for the terminal or homing phase. In considering the magnitude of ground tracking errors, note that, for a passive satellite, skin tracking is mandatory.

The ephemeris determination program is based on a best fit to the actual measured radar data from several radar sites; this best fit expresses the six orbital parameters. These orbital parameters enable prediction of the target's future position as a function of time. It is obvious, in view of radar errors, that the accuracy of the prediction decreases with the prediction time span.

When the radar data starts to come in, an initial determination of target ephemeris is made and constantly improved as more data are received. A launch decision can be made after the target ephemeris is known to an acceptable degree of confidence. After such a decision, the parameters associated with the rendezvous ascent trajectory are calculated. following parameters are of importance:

The position and velocity vector of the launch site.

The position and velocity vector of the target in the region of rendezvous.

The firing azimuth.

A realizable time of flight, which is denoted as \tilde{t} and is determined for a nominal vehicle. In addition, for a direct ascent trajectory it is necessary to compute a rendezvous launch vehicle aiming point vector r_A occurring at $t = \tilde{t}$.

These parameters are computed and transferred to the guidance computer in the rendezvous vehicle.

Space Kinematics and Trajectories

Two types of ascent trajectories have been found promising: After launching, a direct transfer ellipse to target altitude. After launching, a parking orbit plus transfer ellipse to target altitude.

For the direct ascent approach, it is possible to partition the rendezvous vehicle trajectory into four phases:

- 1 Launch: the first period of powered flight plus the transfer ellipse. During the launch phase, the vehicle acquires most of its characteristic velocity.
- 2 Adaptation: a short second period of powered flight near the apogee of the transfer ellipse.
- 3 Search and Acquisition: a period during which the rendezvous payload searches for and acquires the target.

4 Homing: a period of active terminal guidance by the

payload, culminating in rendezvous.

The low-altitude parking orbit, having an angular rate higher than that of the target orbit, permits the rendezvous vehicle to advance upon the target prior to injection into the transfer ellipse which carries the rendezvous vehicle up to target altitude. Thus, unfavorable target in-plane angular position at launch or launch time delays can be made up by remaining in the parking orbit for a greater or lesser time. For the parking orbit approach, the trajectory can be broken into phases: a powered flight phase, during which the rendezvous

vehicle is placed in a circular parking orbit; a parking orbit phase; a boost and yaw phase, to turn into the target plane and achieve enough velocity for transfer (this is a velocity match procedure); a Hohmann transfer ellipse; adaptation (necessary only for high altitude targets); search and acquisition: and homing.

in th

and

at a

ahea

vani

vehi

rend

pha

may

an a

valu

trai

a p

coas

the

targ

vou

incl

ing

this

velo

ing

tion

per

the

At.

abl

me

sis :

ar

fere

clos

ada

the

the

gre

eith

ran

pre

erre

the

vel

ada

ada

poi

ing

poi

the

ren

ada

vel

pro

tisc

thr

ing

gin

AF

A

F

A schematic drawing of the parking and transfer orbits is shown in Fig. 1. From the standpoint of errors, the parking

orbit has two disadvantages:

Launch guidance errors have a varying effect depending upon dwell time in the parking orbit. There is both a periodic and a secular variation. The effect of launch guidance errors increases markedly if the dwell time is greater than, say half an orbit.

The long period of approach allows the error due to target ephemeris prediction to build up.

The rendezvous vehicle is injected into a Hohmann transfer ellipse which carries it to apogee at an altitude very slightly greater than the target altitude. A timer set by the launch guidance system may initiate this injection as a function of

launch time and of the powered-flight thrust history.

The velocity increment for this injection is a fixed magnitude, regardless of launch time (if the target orbit is circular) and is directed essentially along the local horizontal. To produce this velocity increment, one would use a restart capability. The boost vehicle could be carried until target acquisition is obtained, or it could be jettisoned immediately after injection.

The nominal transfer ellipse for the parking orbit case is chosen so that the relative velocity transverse (perpendicular) to the line of sight is zero at a range between bodies appropriate to the acquisition range of the terminal guidance (see Fig. 2). The apogee of this ellipse is slightly above the target altitude. The nominal distance of closest approach,

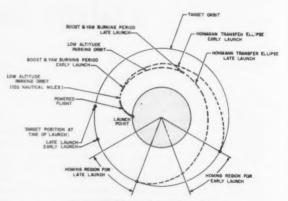
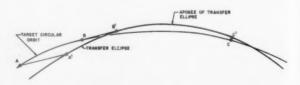


Fig. 1 Parking and transfer orbits



Point of Target Acquisit Point of First Transverse Velocity Correction Maneuver Point of Closest Approach in Absence of any Terminal Maneuver BB' is Tangent to Target Circle and Transfer Ellipse Acquisition Region (acquisition could occur at any range in this region) Nominal Distance of Closest Approach With No Terminal Maneuver

Fig. 2 Geometry of nominal transfer ellipse near apogee

in the absence of any terminal maneuver would be very small and would occur after apogee. The transfer ellipse is initiated at a time such that near apogee the rendezvous vehicle is ahead of the target. The target, however, has a speed advantage, so that it actually closes upon the rendezvous vehicle. Therefore it is not necessary to use propulsion of the rendezvous vehicle to provide closing velocity in the homing phase. Indeed, for very high targets, the closing velocity may be excessive, so that (as for the direct ascent approach) an adaptation increment is needed to reduce this velocity to a value convenient for search, acquisition and homing.

For the direct ascent, a profile of the rendezvous vehicle trajectory is shown in Fig. 3. The launch phase begins with a period of continuous powered flight. A relatively long coast period follows, at the end of which the vehicle arrives at the aiming point. The aiming point is very slightly above the target altitude and is very nearly at the apogee of the rendez-

vous vehicle coast ellipse.

At the aiming point the vehicle will lack a considerable increment of circular orbital velocity. A short second burning period begins, lasting but a few seconds. The function of this adaptation burning period is to add an incremental velocity vector Δv (including a yaw correction), thus changing aiming point velocity to a value convenient for the initiation of the rendezvous phase. Termination of this burning period occurs at a predetermined point in space, referred to as the adaptation point, at a predetermined time. (See Fig. 4.) At the adaptation point, the rendezvous vehicle is considerably ahead of the target but still deliberately lacks an increment (v_e) (fps) of circular orbital velocity.

After adaptation the kinematics and hence the error analysis are essentially the same irrespective of whether a direct or a parking orbit ascent had been used. The velocity differential between target and rendezvous vehicle serves as the closing velocity during the rendezvous phase. The reason for adapting ahead of the target, rather than behind, is seen from the fact that, for a closing velocity of v_c , the vehicle speed at the adaptation point is v_c less than orbital velocity, rather than greater. A saving of $2v_c$ in velocity margin results. (In either case, a v_c velocity increment must later be applied at a range close to the target to complete the rendezvous.)

Although the adaptation point has been referred to as a predetermined point in space, it is clear that certain system errors could affect its position. The nominal trajectory and the guidance philosophy during the launch burning period and the adaptation burning period have been chosen such that:

1 A launch time delay does not affect the position, velocity or time of arrival at the adaptation point.

2 Propulsion dispersions occurring during the launch and adaptation burning periods do not affect the velocity at the adaptation point but do result in small errors in adaptation point position and time of arrival.

3 An error in the time of initiation of the adaptation burning period does not affect the velocity at the adaptation point but does result in a large error in absolute position of the adaptation point. However, the relative position between rendezvous vehicle and target is hardly affected since the adaptation velocity increment is much less than the orbital velocity.

After adaptation, the vehicle is reoriented to face the approaching target, and the boost vehicle is separated and jettisoned in the opposite direction. A profile of rendezvous is shown in Fig. 5.

Launch Guidance

An attractive launch guidance scheme, for the direct ascent approach, operates to force the rendezvous vehicle to pass through a particular point at a particular time, the point being known as the adaptation point. A closely related point, known as the aiming point, at which adaptation burning begins, is computed shortly after launch. (The aiming point

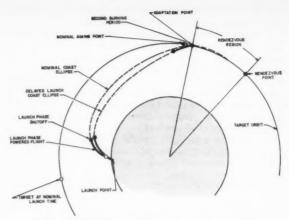


Fig. 3 Profile of rendezvous, coast and burn approach

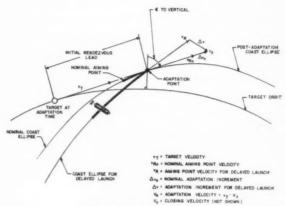


Fig. 4 Adaptation geometry

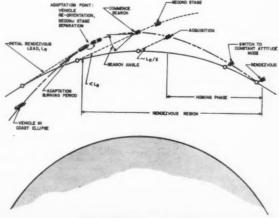


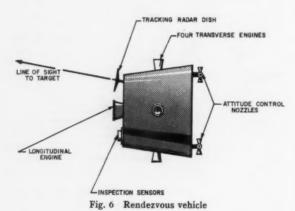
Fig. 5 Rendezvous profile

and the adaptation point would be identical if the second burning were impulsive.) By explicit solution of the orbital equations of motion, the guidance system continuously selects that orbit which causes the rendezvous vehicle to coast from its present position to the aiming point at the correct time. In order to be on such a coast ellipse, the vehicle must have, at any instant, a particular or required velocity. The difference between this required velocity and the vehicle's actual velocity is the velocity to be gained, \bar{v}_{θ} . Appropriate functions of \bar{v}_{θ} are then used to generate attitude commands for the pitch and yaw autopilot channels.

Immediately after launch phase cutoff, the guidance system computes the time of coast, the incremental velocity to be added by the second (adaptation) burning period, and the vehicle attitude required during the second burning period. The vehicle is then reoriented to this attitude under control of the guidance system using torque from the coast attitude control jets. After this maneuver is accomplished, constant

attitude is maintained for the duration of coast.

At the aiming point, the boost vehicle main engine is reignited for a short second burning period. During this burning period, attitude is held constant, and the inertial guidance system measures the incremental velocity added. When this increment equals a precomputed adaptation velocity increment, cutoff is commanded. The vehicle is then at the adaptation point. The rendezvous vehicle is separated from the boost vehicle and is reoriented to point in the direction of the nominal line of sight to the target.



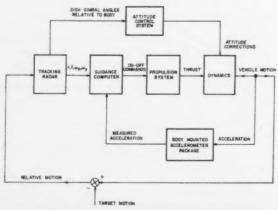


Fig. 7 Block diagram of homing guidance system

Rendezvous Vehicle and Terminal Guidance

Various methods of terminal (homing) guidance (1–4)⁴ may be conceived which lead to different requirements as to sensors, computation, propulsion and payload vehicle configuration. One method which appears attractive for rendezvous with a noncooperative target employs a radar tracker, a small digital computer and a set of moderate size, constant thrust, nongimballed rocket nozzles. Thus the rendezvous vehicle would contain tracking and guidance equipment, a propulsion system including suitable tankage for homing velocity corrections and an attitude control system. The forward face of the vehicle contains the radar dish and the longitudinal correction nozzle (Fig. 6).

tion

ado

Tra

ure

sigl

Ex

of t

is c

ave

rec

giv

vel

exc

init

v. h

eac

one

sine

pul

noi

sine

gui

cor

pro

sun

rec

Lo

unt

tim

veh

a re

to

unl

kno

tion

pul

per

Fig

mit

lon

velo

in t

tion

thr

smo

the

The

API

The attitude control system operates to maintain the body roll axis closely aligned with the radar dish axis during homing. The homing guidance system is based upon an active radar providing data on range, range rate and the two components of the line of sight inertial rate. A digital guidance computer calculates relative velocity perpendicular to the line of sight (using range and line of sight angular rate data). Closing velocity is obtained by differentiation of radar range or else by doppler. A block diagram of the homing guidance

system is shown in Fig. 7.

Shortly after separation a radar search mode is initiated by the rendezvous vehicle computer. A (large) solid angle is searched periodically until target acquisition is obtained. The kinematics after adaptation result in a very long available time for search before the target escapes from the search sector, in order to maximize the probability of acquisition. When detection is accomplished, the search mode is stopped and the tracking mode initiated by locking a tracking gate on the target return and conically scanning the antenna about

an axis always directed toward the target.

After acquisition, the final or homing phase begins. At acquisition, the relative velocity vector will lie generally in the direction of the line of sight, but a substantial error may exist, equivalent to a relative velocity component perpendicular to the line of sight. The range at acquisition and the magnitude of the closing velocity are such that the homing phase duration is several minutes. A reasonably long period is essential to an accurate rendezvous, since sufficient time must be allowed for smoothing of inherently noisy radar tracking data, as well as for correction of the measured errors. A period as great as ten minutes is still short, however, compared with the overall duration of the mission including ascent and the waiting period before launch, and is generally not objectionable. The effect of the differential Earth gravity field (tidal acceleration) has been shown by Hord (5) to be negligible for homing durations not exceeding about ten minutes.

The homing phase may be considered as two successive phases, somewhat independent of each other.

1 A transverse correction phase wherein the relative velocity component perpendicular to the line of sight (transverse velocity) is reduced to zero by application of several transverse pulses of thrust, resulting in a collision course.

2 A longitudinal correction phase wherein, at reasonably close range, the closing velocity is reduced to zero by application of several longitudinal pulses of thrust, resulting in rendezvous. (Actually, additional transverse corrections may occur during this phase to maintain an accurate collision course to very close range.)

Discrete velocity corrections are used in both phases, primarily to avoid the need for proportional thrust engines, but for other reasons as well, e.g., tracking measurements and guidance computations are more easily made during the reasonably long force-free periods between thrust pulses.

After acquisition, the vehicle longitudinal axis is slaved to the direction of the radar axis, using gimbal pick-offs. This procedure maintains the vehicle along the line of sight to the target, automatically pointing all engines in the proper direc-

508

⁴ Numbers in parentheses indicate References at end of paper.

tion for thrust, and eliminating the need for resolvers or an additional platform slaved to the line of sight.

Transverse Correction Phase

In the transverse correction phase, target range r is measured by the radar and the inertial angular rate of the line of sight ω is measured by gyros on the radar tracking head. Except for a negligible gravity effect, the angular momentum of the target, $H = r^2 \omega$ is constant between thrust pulses. H is computed and filtered in an optimum manner by mere time averaging over several seconds. The transverse velocity correction v, required at any instant to yield a collision course is given by \bar{H}/r . After a certain filtering period has elapsed, a velocity correction equal to v_t is commanded provided that v_t exceeds a given threshold function of range. Thrust is then initiated from a transverse engine and is terminated when the integrated output of a body mounted accelerometer indicates v_t has been achieved. The process is iterated as necessary, each succeeding correction tending to be smaller than the last Target tracking data are not used during thrust pulses since the pulses may be too short for accurate measurement of the rapidly varying ω. Tracking is resumed after a thrust

The method described permits accurate homing despite noisy data on r and ω and despite large accelerometer errors, since iteration of corrections provides the effect of closed loop guidance. Moreover, large, reasonably accurate, transverse corrections may be made quite early if the v_t threshold is properly selected. This tends to minimize propellant consumption, since v_t tends to grow inversely with range if uncorrected.

Longitudinal Correction Phase

Longitudinal corrections to reduce r to zero are not begun until the range to the target is reasonably small, by which time the transverse corrections have placed the rendezvous vehicle very nearly on a collision course to the target. Since a rendezvous requires that r and \dot{r} be brought simultaneously to zero, some form of longitudinal thrust control is required unless r \dot{r} , and the thrust acceleration level are all perfectly known at the initiation of longitudinal thrust.

A simple and satisfactory method, not requiring a proportional thrust engine, is to use several successively shorter pulses of constant thrust, separated by reasonably long periods of coasting. A typical closing profile is shown in Fig. 8. (The coast periods shown are sufficiently long to permit additional transverse corrections to be made, should longitudinal thrust misalignment produce any transverse velocity errors.)

The range at which a thrust period is initiated is computed in the vehicle to satisfactory accuracy by the following equation which neglects the effect of mass change during the thrust period.

$$r_{ii} = \frac{v_{ci}^2 - v_{fi}^2}{2a_i} + r_{fi}$$
 $i = 1, 2, 3$ [1]

where

 r_{oi} = range at which to initiate *i*th longitudinal correction

 r_{fi} = desired range at termination of ith correction

 v_{ei} = measured closing velocity before *i*th correction

 v_{fi} = desired closing velocity at termination of ith cor-

rection

 a_i = predicted average acceleration during *i*th correction

 r_{oi} is continually computed during a coast period, using smoothed values for v_{ci} . Thrust is initiated when r_{oi} equals the smoothed value of measured range.

The desired longitudinal velocity correction is

$$\Delta v_i = v_{ei} - v_{fi}$$
 $i = 1, 2, 3$ [2]

The longitudinal engine is shut off when the integrated output

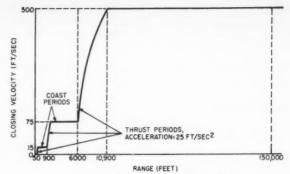


Fig. 8 Nominal closing velocity profile

of a body mounted accelerometer indicates that Δv_i has been achieved.

Launch Guidance Error Analysis

Purpose and Assumptions

The purpose of the launch guidance error analysis is to determine the variations in the acquisition geometry which occur because of errors during the ascent phase. The acquisition geometry parameters which are important to the homing guidance system are: the required acquisition search angle; the transverse velocity of the target relative to the interceptor; and the variation in closing velocity.

Launch guidance errors arise from several sources: during the initial powered flight phase, there are guidance instrument and equation errors, as well as engine shutoff uncertainties. During the ascent trajectory, other errors may be injected by other burning periods, e.g., boost, yaw, and adaptation maneuvers. The actual series of maneuvers is determined by the type of launch trajectory employed for performing the rendezvous. This error analysis will consider two typical schemes, parking orbit and direct ascent.

The burnout errors at the end of the initial powered flight phase determine the ballistic trajectory that is followed thereafter. The error analysis which follows assumes that these burnout errors are available from other analyses and considers how they propagate into acquisition geometry uncertainties for each trajectory. The effect of errors in the powered flight maneuvers peculiar to each trajectory is considered.

The error sources are assumed independent and with normal probability density distributions. For linear situations, an RSS technique is used to find the combined errors. However, the acquisition geometry can be quite nonlinear. To illustrate, consider the line of sight angle between a fixed target and a moving interceptor. Assume that the interceptor moves in a straight line track that does not intercept the target. Even for linear variations in position along this track, the angular variations are quite nonlinear near the point of closest approach. To treat this nonlinear situation, a limited Monte Carlo technique is employed.

Parking Orbit Trajectory

Sources of error

Each phase of the trajectory contains sources of error. The initial powered flight errors cause the parking orbit to be slightly perturbed. Since the attitude reference will drift during the parking orbit phase, the boost and yaw thrusting will also be in an erroneous direction. Moreover, since this

thrusting provides a precomputed velocity increment, position errors can accrue with a nonstandard propulsion system. Finally, position errors cause the adaptation thrusting to be in the wrong direction. An analysis of how these errors propagate through the various phases of the parking orbit is presented in the following. For convenience, this analysis is divided into two parts, in-plane and out-of-plane analyses.

In-plane analysis

This section considers a two-dimensional model, except for the yaw maneuver. Fig. 9 presents the geometry assumed. The subscript i denotes the initial value upon entering the parking orbit, and f denotes the final value at the end of the parking orbit (before boost-yaw) when $\theta = \theta_f$.

Parking orbit phase. For small perturbations about a circular parking orbit, the errors after an Earth angle θ_I are related to the initial errors as shown in the (matrix) equation (3).

Refer to Figure 9 for notation.

erence drift of ϕ_d radians. Since the angle λ is almost 90 deg, angular errors have negligible effect on the thrusting time. Therefore, the errors injected, beyond those already present at the end of the parking orbit, are

$$\delta A_2 = \frac{\Delta V_{\text{in}}}{V_1} \, \phi_d \tag{4}$$

$$\delta V_2 = \Delta V_{\text{out}} \, \phi_d \tag{5}$$

Next, consider a perfect attitude reference, but a thrust acceleration uncertainty δa . The $\Delta V_{\rm in}$ component of velocity can be neglected and the thrust assumed normal to the instantaneous velocity vector ($\psi=90$ deg). Consider the yaw maneuver to be complete after t_y sec, with $A(t_y)=A_2=0$. The position and time uncertainties at the end of thrusting are

$$\delta x(t_y) = V_1 \delta t_y \qquad [6]$$

$$\begin{bmatrix} \delta R_f \\ \delta \theta_f \\ \delta V_f \\ \delta \beta_f \end{bmatrix} = \begin{bmatrix} 2 - \cos \theta_f & 0 & \frac{2R}{V} (1 - \cos \theta_f) & -R \sin \theta_f \\ \frac{1}{R} (2 \sin \theta_f - 3\theta_f) & 1 & \frac{1}{V} (4 \sin \theta_f - 3\theta_f) & 2(1 - \cos \theta_f) \\ \frac{V}{R} (\cos \theta_f - 1) & 0 & 2 \cos \theta_f - 1 & V \sin \theta_f \\ -\frac{1}{R} \sin \theta_f & 0 & -\frac{2}{V} \sin \theta_f & \cos \theta_f \end{bmatrix} \begin{bmatrix} \delta R_i \\ \delta \theta_i \\ \delta V_i \\ \delta \beta_i \end{bmatrix}$$

Notice that δR_f , δV_f and $\delta \beta_f$ are periodic with time spent in the parking orbit (i.e., with θ_f). However, $\delta \theta_f$ contains secular terms which increase with θ_f . The parking orbit, therefore, is limited to some maximum value of θ_f depending upon the initial powered flight errors. Notice also that, in practice, the most important contributors are the burnout velocity errors, δV_f and $\delta \beta_f$.

Boost and yaw phase. The boost and yaw maneuver causes both in-plane and out-of-plane errors. Assume that during this maneuver the velocities to be gained are $\Delta V_{\rm in}$, parallel to the target plane, and $\Delta V_{\rm out}$, normal to the target plane. The worst case is for $\Delta V_{\rm out} \gg \Delta V_{\rm in}$, since with no yaw $(\Delta V_{\rm out}=0)$ the errors injected are small. The simplified geometry assumed is shown in Fig. 10.

Consider first that the thrust acceleration is perfect but that the thrust angle λ is in error because of an attitude ref-

$$\delta y(t_y) = \frac{V_1}{A_1} (1 - \cos A_1) \delta t_y$$
 [7]

$$\delta t_y = -\frac{V_1}{a^2} A_1 \, \delta a \tag{8}$$

sta

di

ex

H

hi

E

in which V_1 and A_1 are the initial velocity and yaw angle at point (1). Also during this maneuver, the target is in error by $V_t \delta t_y$ ft.

Thus the true error caused by thrust uncertainty is

$$\delta\theta_2 = \left(\frac{V_o - V_t}{R}\right) \delta t_y \tag{9}$$

in which V_t is the target's velocity.

Hohmann transfer and adaptation phase. The errors present upon entering the Hohmann transfer ellipse are computed by forming the square root of the sum of the squares of all contributing errors discussed above, i.e., those at the end of parking orbit and boost-yaw period.

With these total errors, a digital computer routine (IBM 704) was used to calculate the resulting transfer trajectory, as

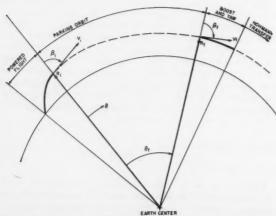


Fig. 9 Parking orbit launch trajectory geometry-vertical plane



Fig. 10 Parking orbit trajectory-boost-yaw phase geometryhorizontal plane

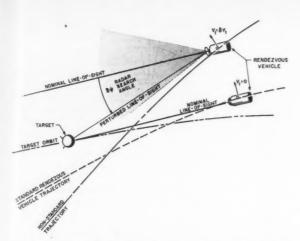


Fig. 11 Typical variation of in-plane acquisition geometry with launch guidance errors

well as the relative geometry between target and rendezvous vehicle. The adaptation thrusting was included in this simulation.

A typical variation in aquisition geometry is shown in Fig. 11. For the errorless case, the rendezvous vehicle follows the standard trajectory. This nominal situation is designed so that, at some predetermined range, the transverse velocity V_t (perpendicular to line of sight) is zero. The line of sight direction is known, and the acquisition radar is directed exactly at the target. Moreover, there is a definite closing rate; i.e., the target is gaining on the rendezvous vehicle. However, with launch guidance errors the rendezvous vehicle's trajectory is perturbed; a typical path is shown in Fig. 11. In this case, the nominal geometry no longer applies. The radar must search for the target through the angle $\delta\psi$. The transverse velocity is no longer zero. The homing guidance system must correct this velocity, δV_t . The closing velocity is also perturbed somewhat.

Fig. 12 shows transverse velocity error δV_i plotted against the error δV , present upon entering the Hohmann transfer ellipse.

The nonlinearity in δV_t (and also in $\delta \psi$) is evident from Fig. 12. With nonlinearities present, it was necessary to compute perturbed transfer trajectories for various *combinations* of errors and dwell times in the parking orbit. The interpretation of these results must consider that some cases will be extreme combinations.

Thus a series of digital computer runs is required to determine the in-plane acquisition geometry, once the errors at the end of boost-yaw are obtained.

Out-of-plane analysis

The analysis of errors effecting the out-of-plane acquisition geometry is straightforward. In the parking orbit, the out-of-plane errors propagate as follows

$$\begin{bmatrix} \delta \epsilon_f \\ \delta A_f \end{bmatrix} = \begin{bmatrix} \cos \theta_f \sin \theta_f \\ -\sin \theta_f \cos \theta_f \end{bmatrix} \begin{bmatrix} \delta \epsilon_i \\ \delta A_i \end{bmatrix}$$
[10]

It was shown in Equation [4] that the positional reference drift causes an azimuthal velocity error. Similarly, from Equation [7] it is seen that the boost-yaw acceleration uncertainty causes an out-of-plane angular position error of

$$\delta \epsilon_2 = \frac{V}{RA} (1 - \cos A) \delta t_y$$
 [11]

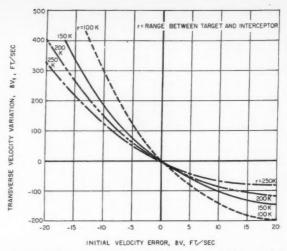


Fig. 12 Transverse velocity variation at acquisition—initial velocity error—parking orbit trajectory—330 n. mi. target altitude

Moreover, since the transfer is Hohmann (180 deg) all of the out-of-plane errors transfer (almost) directly. Therefore, if R_t is the target altitude from Earth-center at acquisition

Out-of-plane velocity error =
$$V \left[\overline{\delta A_1^2} + \overline{\delta A_2^2} \right]^{1/2}$$
 [12]

Out-of-plane search angle
$$=\frac{R_t}{r} \left[\overline{\delta \epsilon_f}^2 + \overline{\delta \epsilon_2}^2 \right]^{1/t}$$
 [13]

in which r is the range between target and interceptor.

Error analysis summary

The error analysis presented above can be summarized as:
The various contributing error sources are used to calculate the errors present upon entering the Hohmann transfer ellipse.

A digital computing routine is used to find the resulting inplane search angle, transverse velocity and closing rate variation for the interceptor-target ranges of interest.

The out-of-plane search angle and velocity requirements are computed using Equations [12 and 13].

Direct Ascent Trajectory

Sources of error

The major sources of error for the direct ascent are those during initial powered flight, as previously described. Other errors are injected during the adaptation (yaw maneuver) because of the position and propulsion system errors.

In-plane analysis

Although the perturbation Equations [3] previously presented apply rigorously about a circular orbit, they can be used to determine the effect of burnout errors upon acquisition geometry for the direct ascent trajectory. Instead of using these equations for a parking orbit, they are used for the complete transfer ellipse; θ_I is 90 deg. However, it was found that the digital computer simulation technique is more convenient for obtaining the relative geometry. Equation [3] is useful in obtaining approximate effects.

An interesting method for presenting the computer results is shown in Fig. 13. This figure presents the tracks of the interceptor relative to the target (at the center) in a vertical plane. Various combinations of boost shutoff errors δV_i and $\delta \beta_i$ were assumed. If positions corresponding to intermedi-

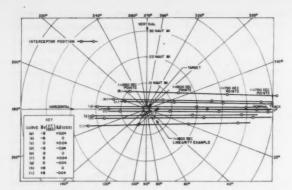
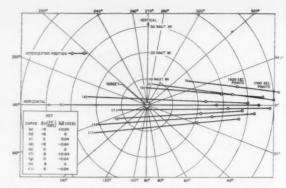


Fig. 13 Interceptor position at acquisition—direct ascent trajectory—1000 n. mi. target (no adaptation)



in F
of ea
purp
for
corr

resu sari sma amo ava U curi of le

Lor

teri

of t

tion

gin

and

ane

rec

sec

per

T

di

Fig. 14 Interceptor position at acquisition—direct ascent trajectory—1000 n. mi. target (with adaptation)

ate times, δV , and $\delta \beta$, are desired, they may be found by interpolation, since the results are approximately linear. An example is shown for t=1800 sec in Fig. 13. At any given target to rendezvous vehicle range, the required search angle can be found directly from these plots.

The inclusion of an impulsive adaptation maneuver is straightforward. If, for example, an in-plane velocity of 1800 fps is added at time 1700 sec in the direction of the nominal line of sight, then the interceptor tracks of Fig. 14 are obtained.

Since this adaptation maneuver can be accompanied by large yaw velocity maneuvers, the propulsion system errors must be included. For a velocity match yaw procedure, the analysis presented in the parking orbit case applies; Equations [4, 5, and 9] apply. The interceptor tracks can be altered accordingly.

Out-of-plane errors

The out-of-plane velocity and position errors at burnout propagate to position and velocity errors, respectively, at acquisition, because of the 90 deg ascent angle. Therefore

$$\delta A_f = \delta \epsilon_i \tag{14}$$

$$\delta \epsilon_i = \delta A_i \tag{15}$$

The yaw maneuver at adaptation will inject an additional out-of-plane position error at adaptation given by equation [11], for a nonstandard thrust acceleration. Thus

out-of-plane velocity error =
$$V\delta\epsilon_i$$

out-of-plane search angle
$$=\frac{R_t}{r}\left[\overline{\delta A_i^2}+\overline{\delta \epsilon_2}^2\right]^{1/2}$$

Error analysis summary

For the direct ascent trajectory, the in-plane acquisition geometry can be found from the burnout errors using the aforementioned digital computer routine. Some additional in-plane errors can be caused by the adaptation maneuver. The out-of-plane errors are given by Equation [16].

Homing Phase Error Analysis

Transverse Errors

Due to the effect of radar tracking noise, accelerometer error, and engine shutoff uncertainty, a transverse velocity error remains at the end of each transverse correction pulse, including the final one. Radar tracking noise arises from: receiver thermal noise; amplitude scintillation of the target; angular scintillation of the target; radar antenna servo jitter; and radar range measurement noise.

The first four sources result in a random error in the measured line of sight angle. This error has a nearly flat spectrum at frequencies below about 1 cps and is heavily attenuated at higher frequencies by action of the radar angle tracking loop. The standard deviations of the angular noise due to these sources varies with range in the following manner: receiver noise with the square of range; amplitude scintillation invariant with range; angular scintillation inversely with range; and servo jitter invariant with range.

Since the computer accepts angular rate data, the angular noise is effectively differentiated before use. The computer then performs an arithmetic averaging of the angle rate noise over a smoothing period T. (Actually, the computer operates on H rather than ω but this is unimportant in the present discussion.) Since T is large compared to the reciprocal of angle noise bandwidth, the resulting angle rate noise after smoothing is given by

$$\omega_{RMS} = \frac{\psi_{RMS}}{T}$$
 [17]

where ψ_{RMS} is the standard deviation of the total angle noise at the radar output due to all four noise sources. The error in measured transverse velocity due to radar tracking noise varies as range times angle rate noise. Thus the velocity error due to radar tracking noise varies with range in the following manner: receiver noise with the cube of range; amplitude scintillation directly with range; angular scintillation invariant with range; and servo jitter directly with range

Fig. 15 shows the transverse velocity error resulting from typical radar errors, plotted against range, with T = 10 sec.

The transverse velocity error due to radar range noise is a second order effect since the error is a product of range error with the small angular rate of the line of sight. The accelerometer error in terminating thrust has a negligible effect for a similar reason. The error due to transverse engine shutoff uncertainty is small and constant for any correction period, and is only important at the end of the last correction. Its value may be held less than 0.6 fps (3 σ) by a reasonable choice of engine thrust level.

Fig. 16 shows a worst possible profile of transverse velocity error. The correction threshold function shown has been chosen empirically and is not necessarily optimum. The 3 σ noise envelope of Fig. 16 is just three times the value of the curve of Fig. 15. The pessimistic assumption has been made

in Fig. 16 that the magnitude of the residual error at the end of each correction period is 3 σ . This has been done for the purpose of sizing the propellant tanks of the homing vehicle for the worst case. The initial transverse error of 250 fps corresponds to a worst case for the launch guidance system.

In determining an acceptable correction threshold function, it must be remembered that too high a threshold will generally result in a propellant penalty since corrections are unnecessarily delayed. Too low a threshold will result in frequent small corrections which are undesirable for several reasons, among them the fact that insufficient smoothing time is available between corrections.

Using typical numbers for a final transverse correction occurring at a range of 200 ft, a 3 σ value of transverse velocity of less than 1.5 fps may be achieved, considering all sources

Longitudinal Errors

The longitudinal error analysis is quite straightforward for the system proposed. The errors in r and \dot{r} (= $-V_c$) at the termination of any but the final longitudinal thrust period are quite unimportant, provided that the nominal closing profile (Fig. 8) has been chosen intelligently. Intelligent choice of this profile, i.e., proper choice of the parameters of Equation [1] permits sufficiently long coast times, so that r and \dot{r} may be adequately smoothed before the next correction begins. If this is done, errors in the radar measurement of rand \dot{r} occurring at the beginning of a prior correction pulse, as well as accelerometer error, thrust acceleration uncertainty, and thrust shutoff uncertainty occurring during the prior correction pulse, only serve to alter the range at which the subsequent correction begins (i.e., lengthen or shorten the coast period before the next correction). No significant accumulation of error results.

The profile is also chosen so that the final correction in closing velocity is small and begins at very close range. The terminal error in r and \dot{r} results from the following sources:

1 Radar measurement error of r at initiation of final longitudinal correction.

Radar measurement error of r at initiation of final longitudinal correction.

Accelerometer error.

Thrust acceleration uncertainty (uncertainty in predicted a.).

5 Thrust shutoff uncertainty.

Sources 1 and 4 produce only a terminal range error. Sources 2, 3 and 5 produce primarily a terminal closing velocity error. For a small final correction, the terminal range error is primarily due to source 1, and for a good radar is surely less than 50 ft (3σ) . The 3σ terminal closing velocity error due to 2 is about 1-2 fps for a good radar. The 3σ error due to 3 may be held to less than 0.4 fps with almost any decent accelerometer. The 3σ error due to 5 may be held to less than 1 fps by proper choice of longitudinal engine size. Thus, the total 3σ error in terminal closing velocity is no more than 2.25 fps.

The total terminal velocity including transverse velocity is therefore, no more than 2.7 fps (3σ) . This velocity defines the quality of rendezvous obtainable with the vehicle described. If desired, a vernier system could be incorporated on the vehicle to effect either a soft contact with the target, or else a standoff position with respect to the target, maintained indefinitely.

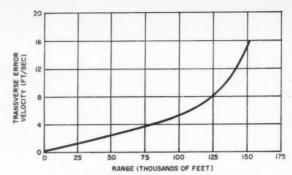


Fig. 15 RMS residual transverse error velocity

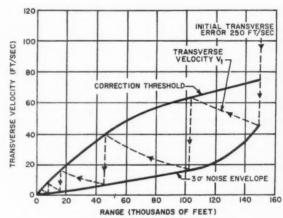


Fig. 16 Homing profile for extreme errors

References

- 1 Sears, N. E., Jr. and Felleman, P. G., "Terminal Guidance for a Satellite Rendezvous," presented at the ARS Controllable Satellites Conference, M.I.T., April 30-May 1, 1959, pp. 778-59.

 2 Cloheasy, W. H. and Wiltshire, R. S., "Terminal Guidance System for Satellite Rendezvous," presented at the IAS National Summer Meeting, Los Angeles, Calif., June 16-19, 1959, IAS Paper no. 59-93.

 3 Swanson, R. S., Petersen, N. V. and Hoover, L. R., "An Astro Vehicle Rendezvous—Guidance Concept," Western Aviation, vol. 40, no. 2, February 1960, np. 12-15 and 31-32.

- Rendezvous—Guidance Concept., Western Artation, Vol. 40, no. 2, February 1960, pp. 12-15 and 31-32.

 4 Wheelon, A. D., "Trajectory Studies of Ballistic Missiles, Satellites, and Space Vehicles, An Introduction to Midcourse and Terminal Guidance," Space Technology Laboratories, Inc., Report GM-TM-0165-00252, June 10,
- 1958. 5 Hord, R. A., NACA, "Relative Motion in the Terminal Phase of Interception of a Satellite or Ballistic Missile," TN 4399, September 1958.

Ignition of Solid Propellant Rocket Motors by Injection of Hypergolic Fluids

CARL C. CIEPLUCH¹ HARRISON ALLEN Jr.¹

NASA Lewis Research Center Cleveland, Ohio

EDWARD A. FLETCHER² University of Minnesota Minneapolis, Minn.

A preliminary experimental investigation was conducted to determine the feasibility of igniting solid propellant motors with hypergolic fluids. Ignition was accomplished by injecting a fluid into the propellant port, which upon contact reacted spontaneously with the fuel component of the propellant, providing sufficient heat for ignition and sustained reaction between the fuel binder and oxidizer. Motors containing composite and double-base propellant were ignited in this manner. Chlorine trifluoride was found to be the most effective ignition fluid; this was a result of its superior reactivity.

This article describes preliminary experiments in which solid propellant rocket motors were ignited by injecting a fluid that reacted hypergolically with the propellant grain. This novel method of igniting solid propellants, which heretofore has been unexplored, may offer advantages over conventional pyrotechnic ignitors for some specific applications. One such application is re-ignition of solid propellant motors during space missions. Of course the problem of the satisfactory quenching of such motors will still remain.

Experiments were conducted with motors containing composite, and in a limited number of cases double-base, solid propellants. Chlorine trifluoride, bromine trifluoride, and bromine pentafluoride were investigated as hypergolic ignition fluids. The effect of altitude on the ability to ignite the motors with hypergolic fluids was determined, and several methods of injecting the fluids were evaluated. Measurements of the ignition delay time and the maximum ignition pressure were made. A comparison of typical pyrotechnic and hypergolic ignition pressure transients is also presented.

Apparatus and Procedure

Composite Rocket Motors

A cutaway view of the composite propellant motor is shown in Fig. 1. The propellant consisted primarily of polysulfide polymer fuel and ammonium perchlorate oxidizer. The ignition fluid injector and chamber pressure taps were located in the steel block at the motor head end. The injection system consisted of the following units: a storage bottle previously filled with the ignition fluid and pressurized with 15-psig helium gas, a control valve operated remotely by an electric-motor-driven mechanical device, a check valve, and the injector. The types of injectors used are shown in Fig. 2. The inside diameter of the open-end injection tube for the pocket injector was 0.104 in. A plasticized polyvinyl chloride and ammonium perchlorate solid propellant disk $\frac{1}{2}$ -in.

thick was added to the propellant core to form the pocket. The radial injector tube inside diameter was 0.104 in., and it contained four radial drilled holes 0.06 in. in diameter. The Y-type injector consisted of two drilled passages of 0.072-in. diameter located at a 90-deg angle to each other. The axial injector consisted of an open-end 0.104-in. ID tube.

Double-Base Rocket Motor

A cutaway view of the double-base propellant motor is shown in Fig. 3. The propellant consisted primarily of a mixture of nitrocellulose, nitroglycerine, and triacetin. The hollow, cylindrical shaped propellant charge was uninhibited,

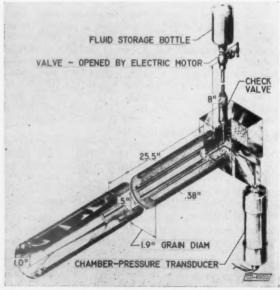


Fig. 1 Cross section of composite propellant motor and injection system details

Received July 7, 1960.

¹ Aeronautical Powerplant Research Engineer, Propulsion Chemistry Division.

² Professor, Mechanical Engineering Department.

Type	Reac-	Ignition	Injector details
injec-	tion	pressure	
tor	time,	ratio,	
	sec	Pc, max	
		Pc, normal	
		C, HOTHAI	
Pocket	0.34	1.71	11/2"
	.31	1.94	30
			1.0" diam.
Radial	0.59	1.64	3"
INCOME	0.00	1.04	-4-
	.55	1.86	
İ			
нүн	0.71	1.77	
_		1	0.313"
			1000 ±
			300
			Visite
			<u>1</u> "
Axial	0.91	1.54	-2-
AXIBI	0.91	1.54	
			N/Par
			-

Fig. 2 Cross-sectional view and performance of several types of injectors—Composite propellant motor; chlorine trifluoride ignition fluid; ambient pressure 1 psia

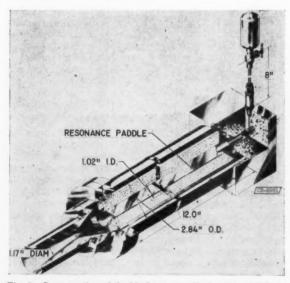


Fig. 3 Cross section of double-base propellant motor with ignition system

and therefore it burned internally and externally. The Y injector (Fig. 2) and chamber-pressure tap were located in the steel block that also held the resonance paddle. The injection system was the same as used for the composite rocket motors.

General

All the experiments were conducted in an altitude facility that was capable of maintaining a pressure of 1.0 psia, equivalent to approximately an 11.7-mile altitude. To obtain lower ambient pressures, some of the rocket motors were mounted in a $2\frac{1}{2}$ -ft diameter by 5-ft long vacuum tank that was installed in the altitude facility. This tank could be pumped down to 100 μ , equivalent to approximately a 50-mile altitude. When the rocket motor was ignited, a 0.002-in. thick aluminum diaphragm (capable of holding a pressure differential of 1 to 2 psi) on the end of the tank was blown out, and the vacuum tank was thus vented to the pressure existing in the altitude facility.

Chamber pressure was measured with a strain gage type of pressure transducer. The pressure side of the transducer and vertical pressure line above the transducer were filled with a high temperature silicone oil for protection from the combustion gas. (This left less than 4 in. of open line between the combustion chamber and oil surface.) The electrical signal from the pressure transducer was recorded on a direct-recording oscillograph.

The direct-recording oscillograph was also used to measure ignition delay for both types of rocket propellant ignitions. This was accomplished by imposing a separate signal (marking time, zero) on the oscillograph record at the moment when electric power was applied to the valve actuator. Ignition delay was the elapsed time from time zero until the chamber pressure rose to 50 per cent of its normal value. Ignition delay consisted of system dead time and reaction time, which was the parameter of interest in these experiments. Dead time was the time required for the fluid to reach the injector after application of electrical power to the valve actuator. The dead time of the fluid system used, which was determined by high speed photography, was approximately 1.1 sec. The reaction time, which was found by subtracting the dead time from the ignition delay, was then the time required, after the fluid had reached the end of the injector, for the chemical reaction to ignite the grain and raise the pressure to 50 per cent of its normal value.

Results and Discussion

Evaluation of Several Hypergolic Fluids

Chlorine trifluoride, bromine trifluoride, and bromine pentafluoride (each 99 per cent pure) were investigated as possible fluids for hypergolic ignition. These interhalogen compounds were chosen because they are highly reactive with the fuel component of the propellant and because they are easily stored as liquids. Ignition and normal combustion of the composite propellant were obtained with each of the fluids. Reaction times for several ignition attempts are listed in Table With the Y-type injector the reaction time for ignition with chlorine trifluoride was 0.71 sec, about half that of either bromine trifluoride or bromine pentafluoride. One ignition attempt with bromine trifluoride was unsuccessful, although there was an indication of some reaction. On the basis of reaction time, chlorine trifluoride appeared to be the more effective hypergolic ignition fluid. The lower reaction time obtained during ignition with chlorine trifluoride is attributed to its higher reactivity. Ignition of the composite propellant motor with chlorine trifluoride exhibited a high degree of reliability; in 15 firings over a wide range of conditions no ignition failure was encountered.

Typical Transient Chamber-Pressure Behavior for Hypergolic Ignition

A typical transient chamber-pressure record for ignition of the composite propellant motor with chlorine trifluoride is shown in Fig. 4. The reaction time (see procedure), which is the time increment from the moment the fluid is injected into the chamber until the chemical reaction ignites the propellant, was of primary interest in this investigation. The data for hyperglolic ignition was therefore presented in terms of the reaction time. The reaction period was characterized, as typically illustrated in Fig. 4, by only a slight increase in chamber pressure, except for occasional small pressure surges, up until ignition was accomplished and the chamber pressure suddenly increased to at least the normal chamber pressure.

During ignition of the composite propellant motor, a

Table 1 Comparison of typical reaction times obtained during ignition with several hypergolic fluids—composite propellant motor; Y injector

Fluid	Reaction time, sec	Ambient pressure, psia	Chamber pressure, psia
 lorine trifluoride	0.71	1.0	600
omine	1.79	1.0	600
trifluoride	no ignition ^b	1.0	600
omine pentafluoride	1.39	1.0	600

^a Reaction time is defined as the time required after the fluid has reached the end of the injector for the chemical reaction to ignite the propellant and raise the chamber pressure to 50 per cent of its normal value.

^b Although ignition was incomplete, an indication of some reaction was observed on the chamber-pressure trace.

Table 2 Reaction time for a range of simulated altitude pressures—composite propellant motor; chlorine tri-fluoride ignition fluid; Y injector

Altitude, mile	Altitude pressure, psia	Reaction time, sec
0.6	13.1	1.16
3.3	7.5	0.51
11.7	1.0	0.71
40.5	0.0035	0.61
45.4	0.0014	0.71

Table 3 Reaction times for double-base propellant motor at several pressure levels—chlorine trifluoride ignition fluid; Y-type injector

Ambient pressure, psia	Fluid injection pressure, psia	Quantity of ClF ₃ ,	Reaction time, sec
13.6	30	5	0.66
13.0	30	10	1.43
13.0	30	10	1.35
7.0	30	10	2.0
7.0	30	10	9.2
7.0	30	10	no ignition
1.0	30	5	no ignition
1.0	• 30	10	no ignition
1.0	65	10	no ignition
1.0	100	10	no ignition

fairly large pressure peak (see Fig. 4) was obtained. Ignition pressure ratio ($P_{e,\max}/P_{e,\text{normal}}$) averaged about 1.7 for ignition with chlorine trifluoride. The high ignition pressure may be due in part to a local increase in burning rate in the vicinity of the propellant surface due to the heat conduction into the propellant during the comparatively long reaction time. It was estimated from the dependence of propellant burning rate on temperature that the burning rate can be about 40 per cent higher (equivalent to a 40 per cent increase in pressure) near its auto-ignition temperature compared with an initial temperature of 70 F. Erosive burning may also have contributed to this pressure peak. The initial motor port to throat area ratio was 1.2, which is in the range where erosive burning is encountered.

The unduly high ignition pressure ratios are probably not inherent to hypergolic ignition. Optimization of design, with its attendant reduction in reaction time, may also reduce this ratio to a more acceptable figure and yet retain the other potential advantages of this ignition approach.

Comparison of Several Injection Techniques

A comparison of the reaction time for several different fluid injectors is given in Fig. 2. The reaction time varied from 0.33 sec for the pocket injector to 0.91 sec for the axial injector. It is interesting to note that the injectors that tend to concentrate the fluid at the head end of the grain core (pocket and radial) have shorter reaction times than those that tend to distribute the fluid over more of the grain surface (Y and axial). Concentration of the ignition fluid at the head end of the core results in a greater probability of reaction with the propellant before escaping through the nozzle. Combustion gases generated at the head end of the core contribute to the heating of the remainder of the propellant surface by convection and radiation during passage to the nozzle.

Fig

ign

de

tin

aff

in

bin

th

nt

ne

Co

E

fu

Although most ignition data were obtained using 5 cc of fluid, the composite propellant motor was also ignited with 2.5 and 10 cc of chlorine trifluoride. The ignition characteristics were roughly similar for this range of fluid quantities.

Effect of Altitude on Ignition Delay

Since the rate of vaporization of the ignition fluid during injection increases as the altitude is increased (decreasing ambient pressure), ignition attempts were made over a range of simulated altitude pressures to determine whether low ambient pressure would affect ignition characteristics. The composite propellant motor was successfully ignited at simulated altitudes from sea level to 50 miles. The effect of altitude on reaction time is shown in Table 2. Except for the data point near sea level which is apparently in error partially as a result of the reduction in fluid pressure drop at lower altitudes which increased dead time, the reaction time was approximately constant with increasing altitude. Since no significant trend of increasing reaction time with altitude was apparent for altitudes up to 50 miles, it is reasonable to assume that no difficulty igniting this motor would be encountered under complete vacuum conditions.

Ignition of Double-Base Propellant

The chemical composition of double-base solid propellants is basically different from that of composites; therefore, a brief study of the ignitability of a motor containing a typical double-base propellant using chlorine trifluoride was made. Reaction time averaged 1.15 sec (see Table 3) for the double-base propellant with a Y-type injector at sea-level ambient pressure. However, at an ambient pressure level of 7.0 psia, reaction time increased significantly and became somewhat erratic. Reaction time varied from 2 to 9 sec, and several ignition failures were obtained. At ambient pressures of 1.0 psia, several ignition attempts were made and all were unsuccessful. In all cases where the propellant failed

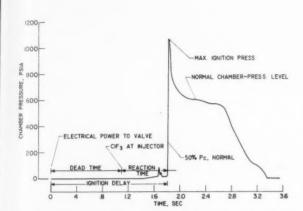


Fig. 4 Typical transient chamber-pressure record for hypergolic ignition of composite propellant motor using chlorine trifluoride with Y-type injector

800 PYROTECHNIC

400 O 2 4 6 8 10 1.2

HYPERGOLIC

400 O 2 14 16 18 2.0 2.2

TIME FROM ELECTRICAL ENERGIZATION, SEC

Fig. 5 Comparison of hypergolic and pyrotechnic ignition chamber-pressure transients

to ignite, a reaction with the propellant surface was evidenced by a gummy surface residue.

It is interesting to note that, while the composite propellant exhibited little or no effect of ambient pressure on reaction time, the ignition of the double-base propellant was severely affected by reduced ambient pressure. Although differences in reactivity between the chlorine trifluoride and the fuel binders of the composite and double-base propellants are a possible explanation for the wide difference in ignitability of these propellants, geometrical factors such as those that affect fluid residence time and distribution may also have contributed to this difference. Further study in these two areas is necessary to determine their relative importance.

Comparison of Hypergolic and Pyrotechnic Ignition

A comparison of typical pyrotechnic and hypergolic ignition transient pressure variation for the composite propellant motor is shown in Fig. 5. The pyrotechnic ignitor was a standard jelly-roll type developed for use with the composite propellant motor. The hypergolic ignition system used chlorine trifluoride with the Y-type injector. The ignition delay with the pyrotechnic ignitor averaged about 0.01 sec compared with a reaction time of 0.71 sec for hypergolic ignition.

This wide difference in ignition delay is a result of the different conditions under which the propellant is ignited. Experimental evidence indicates (1 and 2)³ that the mechanism for ignition of a composite propellant is the pyrolysis of the fuel polymer and oxidizer until a combustible gas mixture is formed and subsequently ignited. With a pyrotechnic ignitor the propellant is suddenly exposed to hot gases at high pressure, which results in a rapid heating of the propellant and consequently short ignition delay. With hypergolic ignition, the heating of the propellant results from a reaction between the fuel polymer and the fluid. An important factor in the ignition delay with this type of ignition is believed to be the absence of high chamber pressure during ignition. Low chamber pressure can result in lower reaction rates, lower

propellant burning rates when ignited, and decreased ability to heat those areas remote from the injection point. Improvement in ignition delay may come from improved injection techniques aimed at maintaining higher chamber pressures during ignition and from adequately exposing more of the propellant surface to the hypergolic reaction.

Ignition pressure ratio with pyrotechnic ignition averaged about 1.3 compared with 1.7 for hypergolic ignition. As mentioned earlier, the high ignition pressure ratio obtained with hypergolic ignition may be reduced by improved techniques. It is possible that reduction in reaction time may help to decrease the ignition peak pressure to a more acceptable value.

Summary of Results

An experimental investigation of the ignition of solid propellent rocket motors by injection of a fluid that reacted hypergolically with the propellant can be summarized as follows:

1 Composite and double-base solid propellant motors were ignited by reaction with a hypergolic fluid.

2 Of the hypergolic fluids investigated, chlorine trifluoride was the most promising because of its superior reactivity. Ignition of the composite propellant motor with chlorine trifluoride exhibited a high degree of reliability over the range of conditions encountered.

3 Reaction time was shortest when the injected hypergolic fluid was concentrated locally at the head end of the propellant port rather than distributed over more of the propellant surface.

4 Ignition characteristics of the composite propellant motor were not affected by extreme altitude. Ignition was obtained at a simulated altitude of 50 miles, the limits of the tests. Although double-base propellant ignition was comparable to the composite propellant at sea-level ambient pressure, ignition was progressively more difficult as ambient pressure was decreased.

5 Longer reaction time was obtained with hypergolic ignition compared with the ignition delay obtained with conventional pyrotechnic ignition. Peak ignition pressure 70 per cent higher than normal chamber pressure was obtained

² Numbers in parentheses indicate References at end of paper.

References

Acknowledgment

The authors wish to acknowledge the cooperation of the Army Rocket and Guided Missile Agency, Redstone Arsenal, Huntsville, Ala., and Picatinny Arsenal, Dover, N. J., in providing the rocket motors used in this investigation.

1 McAlevy, R. F., Cowan, P. L. and Summerfield, M., "The Mechanism of Ignition of Composite Solid Propellants by Hot Gases," ARS Preprint no. 1958, presented at the ARS Meeting on Solid Propellant Rocket Research, Princeton, N. J., Jan. 28, 1960. Published in "Solid Propellant Rocket Research," Summerfield, M. (ed.), Academic Press, N. Y., 1960.
2 Baer, A. D., Ryan, N. W. and Salt, D. L., "Ignition of Composite Propellants," University of Utah, Department of Mechanical Engineering, March 1959. Published in "Solid Propellant Rocket Research," Summerfield, M. (ed.), Academic Press, N. Y., N. Y., 1960.

Optimum Steering Program for the Entry of a Multistage Vehicle Into a Circular Orbit

STEPHEN JUROVICS1

North American Aviation, Inc. Downey, Calif.

The problem of finding the thrust steering program to place a maximum payload into a circular orbit has been investigated by the Mayer formulation of the calculus of variations. The solution of an example problem is discussed, and the mass discontinuity at change of stage is considered. The numerical method of solution is believed to be applicable to a large class of problems. In the sample problem, the boost vehicle is a continuously burning, multistage rocket; atmospheric effects are not considered. Three initial and three final conditions are specified: the velocity, the direction of the velocity and the radius from the center of Earth. For the sample problem, it is found that the optimum trajectory first goes beyond the circular orbit and then enters the orbit from the outside.

THE PROBLEM considered in this study was to find the path along which a vehicle should travel in order to transfer between two points in a minimum time. This is equivalent to maximizing the payload on a vehicle of fixed initial weight, since the rate of fuel consumption is a constant for each stage. The minimum time path is found by obtaining a particular time history, called the optimum, of one or more of the parameters which control a vehicle's flight. In this study the optimized parameter is the thrust direction.

This realm of problems, optimizing trajectories, has been widely treated in the literature. Miele (1)2 lists an extensive bibliography of effort and reviews the general formulation of trajectory optimization problems by the calculus of variations. However, the solution of these problems, once formulated, may be quite cumbersome and no general, systematic approach has yet been reported. A method of solution (acknowledged to be limited to the class of problems considered)

is presented and tested with a sample problem.

Received July 27, 1960.

Dynamics Engineer, Missile Division.
 Numbers in parentheses indicate References at end of paper.

Statement of the Problem

The problem is to place the maximum payload into a circular orbit from a given set of initial conditions on v, γ , r, to a specified set of final conditions on v, γ , and r; v is the velocity, γ is the direction of the velocity vector relative to the local horizontal, and r is the distance from the center of the earth (see Fig. 1). A multistage, continuously burning vehicle is assumed. The following parameters are assumed to be fixed:

- Initial gross weight.
- 2 Number of stages, n.
- Thrust for each stage.
- Time of burning for all but the nth stage.

The maximum payload is placed into the orbit by finding the trajectory corresponding to the minimum time of burning the nth stage. This is achieved by finding the optimum steering program, that is, the time history of the angle α between the thrust vector T and the velocity vector v. Atmospheric effects are not considered.

Equations

Equations [1-4] are dynamic and kinematic relations which apply to the motion of a particle in a plane under the influence of thrust and central gravitational forces

$$\dot{v} = \frac{T \cos \alpha}{m} - \mu \frac{\sin \gamma}{r^2} \tag{1}$$

$$\dot{\gamma} = \frac{T \sin \alpha}{mv} - \mu \frac{\cos \gamma}{vr^2} + \frac{v \cos \gamma}{r}$$
 [2]

$$\dot{r} = v \sin \gamma \tag{3}$$

$$\dot{\sigma} = \frac{v \cos \gamma}{r} \tag{4}$$

where μ is the product of the universal constant of gravity and the mass of Earth.³

The rate of fuel consumption is a constant for each stage, given by

$$\dot{m} = \frac{-T}{g_0 I_{sp}} \tag{5}$$

where g_0 is the acceleration due to gravity at the surface of Earth and I_{sp} is the specific impulse in a vacuum.

Equations [6-8] are the differential equations for the Lagrange multipliers, which arise from the Euler necessary condition in the calculus of variations. Their derivation is given in the Appendix

$$\dot{\lambda}_{v} = -\frac{\lambda_{\gamma}}{r} \left(1 + \frac{\mu}{v^{2}r} \right) \cos \gamma + \lambda_{\gamma} \frac{T \sin \alpha}{mv^{2}} - \lambda_{r} \sin \gamma \quad [6]$$

$$\dot{\lambda}_{\gamma} = \left(\lambda_{\nu} \frac{\mu}{r^{2}} - \lambda_{\nu} v\right) \cos \gamma + \frac{\lambda_{\gamma}}{r} \left(v - \frac{\mu}{vr}\right) \sin \gamma \quad [7]$$

$$\dot{\lambda}_{r} = \frac{-2\mu\lambda_{v}\sin\gamma}{r^{3}} - \frac{\lambda_{\gamma}}{r^{2}} \left(\frac{2\mu}{vr} - v\right)\cos\gamma \qquad [8]$$

The thrust steering angle α is found by

$$\alpha = \tan^{-1} \left(\lambda_{\gamma} / v \lambda_{\nu} \right)$$
 [9]

The conditions to be met upon entry into the circular orbit are

$$\begin{array}{ll} v^1 = \sqrt{\mu/a} & \lambda_{v}^{-1} = (1 - \lambda_{\gamma}^{-1} \dot{\gamma}^{1})/\dot{v}^{1} = f(\lambda_{\gamma}^{-1}, \, t_{n}) \\ \gamma^1 = 0 & \lambda_{\gamma}^{-1} = \text{unspecified} \\ r^1 = a & \lambda_{r}^{-1} = \text{unspecified} \end{array}$$

where a is the radius of the circular orbit. The initial conditions are

$$\begin{array}{lll}
v &= v^0 & \lambda_{v^0} \\
\gamma &= \gamma^0 & \lambda_{\gamma^0} \\
r &= r^0 & \lambda_{r^0}
\end{array} = \text{unspecified}$$
.....[11]

Superscript 0 indicates the value at end boost of stage one, and superscript 1 indicates the value at entry into the orbit.

Method of Solution

The solution of the boundary value problem is obtained when the six first-order differential equations are integrated and satisfy the prescribed conditions at the terminal and initial point. In this study all integrations were backward, i.e., from the terminal to the initial point.

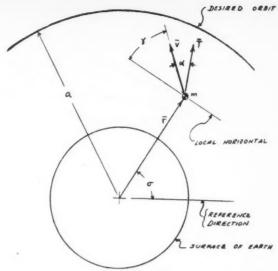


Fig. 1 Geometry

To initiate a backward integration it is necessary to specify the terminal values for the six dependent variables v, γ , r, λ_v , λ_γ , λ_r and the time of burning of the nth stage t_n .⁴

Three of the starting conditions are specified by Equation [10]. Thus values for λ_{γ} , λ_{r} and t_{n} need be assumed before a backward integration may begin. To evolve a method of attack which would mitigate the difficulties inherent in the two-point boundary value problem, it was decided to study the dependence of each of the computed initial values v^0 , γ^0 and r^0 on the variation of the assumed values for λ_{γ} , λ_{τ} , and t_n , taken one at a time. Since an obvious physical meaning is attached to the burning time t_n and to the steering angle a, these two parameters were fixed at arbitrary values while λ_r was varied. As a starting point α was taken as zero. From Equation [9] it follows that $\lambda_{\gamma} = 0$ and from Equation [10] that λ_{r} is a function of t_{n} only.⁵ A first value for t_{n} was selected on the basis of nominal ballistic trajectories. It soon became clear that no conclusions could be drawn from the graphs of λ_r^1 vs. v^0 computed and λ_r^1 vs. γ^0 computed. However, λ_r^1 vs. r^0 computed yielded significant information. The monotonic character of this plot (see Fig. 2) showed that for a wide range of t_n a λ_r^1 could always be found so that the desired value for r^0 could be reached at t^0 . This was the most important find, and, of course, the monotonic character occurs regardless of the initial choice of α ; i.e., a λ_r^1 can always be found so that r^0 occurs at t^0 . The next step taken was to plot t_n vs. v^0 computed (see Fig. 3) for a fixed value of λ, selected from Fig. 2. From Figs. 2 and 3 it was possible to select values for λ_r^1 and t_n for which v^0 and r^0 computed were close to the desired values. The last step is to converge on all three of the initial values v^0 , r^0 , and γ^0 . This is accomplished by varying α^1 along with small changes in

to solve.

⁶ Note from Equation [10] that λ_s at the terminal point is uniquely determined by the choice of λ_γ and t_n .

 $^{^3}$ Equations [1–3] may be solved independently of Equation [4]. In fact, σ as a function of time need not be determined until after the problem has been solved.

⁴ By defining new variables, $\eta = \lambda \gamma / \lambda_v$, $\tau = \lambda_r / \lambda_v$, two equations for $\dot{\eta}$ and $\dot{\tau}$ can be used to replace the three Equations [6–8]. See (2, 3.) However, although it is usually advantageous to reduce the number of dependent variables in a system of equations, it was not done in this report due to the simplicity of solution exhibited by the present system. The monotonic behavior of the plot of λ_r^{-1} vs. τ° (Fig. 2) is the important property which allows a rapid determination of the solution; without that behavior the extremely sensitive variable λ_r^{-1} would take long to determine and the problem would be extremely tedious

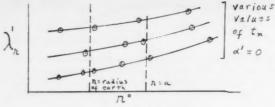


Fig. 2 λr^1 vs. r° computed

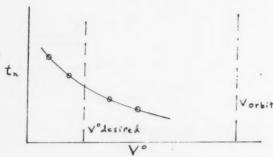


Fig. 3 t_a vs. v° computed

 λ_r^1 and t_n . Convergence in this last step was found to be rapid.

The method of solution is summarized as follows:

- 1 Select t_n on basis of ballistic trajectory and set $\alpha^1 = 0$. This defines $\lambda_{\gamma^1} = 0$ and $\lambda_{\nu^1}(t_n)$.
 - 2 Find r^0 as a function of λ_r^1 with t_n as a parameter.
- 3 Find v^0 as a function of t_n using a value of λ_r^{-1} found from step 2.
- 4 Select λ_r^{-1} and t_n such that convergence on v^0 and r^0 is obtained.
- 5 Vary α^1 while slowly changing λ_r^1 and t_n found in step 4 until convergence on v^0 , r^0 and γ^0 is achieved.

In summary, steps 1 through 4 correspond to satisfying the mechanical energy requirement at the initial point, while step 5 considers the additional constraint upon γ^0 .

Computer Mechanization

The defining equations were mechanized on the Bendix G-15D digital computer using the Intercard system of coding. The details of the program mechanization are not covered in this report; however, a brief description of the integration technique seems appropriate. The terminal conditions, Equations [10], and t_n are the starting values for the backward integration. A predictor-corrector method which allows a variable step size is used to integrate Equations [1, 2, 3, 6, 7, 8] to t^0 . The computed values for v^0 , γ^0 and r^0 are then compared with the desired values, and adjustments in the starting values are made, in accordance with steps 1–5, until the initial conditions are reasonably met.

Sample Problem

In the sample problem considered it was desired to place the maximum payload into a 100-statute-mile orbit with a three-stage vehicle.

Table 1 Data for sample problem

$m_{\rm total} = 31,493.8 \text{ slu}$	g
$T_1 = 1.58 \times 10^6 \text{lb}$	$\dot{m}_1 = -181.8 \text{slug/sec} \ t_1 = 127 \text{sec}$
$T_2 = 8 \times 10^4 \text{lb}$	$\dot{m}_2 = -5.915 \text{slug/sec} \ t_2 = 467 \text{sec}$
$T_2 = 4 \times 10^4 \text{lb}$	$\dot{m}_4 = -2.958 \text{slug/sec} \ t_3 = ?$
$\mu = 14.0775 \times 10^{1}$	$m_{\rm stage \ 1} = 3,510.3 \ {\rm slug}$
a = 21,433,000 ft	$m_{\text{stage 2}} = 334.8 \text{ slug}$
Terminal conditions	Conditions at burnout of stage 1
v = 25,545 fps	v = 9,340 fps
$\gamma = 0$	$\gamma = 25 \deg$
r = 21,433,000 ft	r = 21,105,000 ft
$\lambda_{\nu} = f(t_3, \lambda_{\gamma})$	altitude = $200,000 \text{ ft}$
$\lambda_{\gamma} = ?$	

d

The data used are shown in Table 1. Since atmospheric effects were not mechanized in the digital computer program, it was decided to determine the optimum steering program for only stages 2 and 3 where the atmosphere is negligible, and to assume a ballistic first-stage trajectory. The end burnout conditions v, γ and r for stage 1 form the initial conditions for the variational problem.

About twenty runs were made until values of α , λ_r^1 , and t_n were found which yielded a trajectory, the initial conditions of which reasonably match the end burnout conditions of stage 1. Three of the trajectories' runs are illustrated in Figs. 4 and 5.

In Fig. 4 the distance from the surface of the earth is plotted against the range angle σ . This is a distorted plot since a

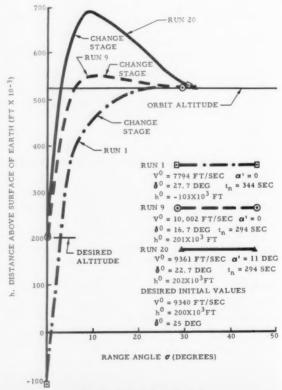


Fig. 4 Sample trajectories

40-deg range angle corresponds to about 1.47×10^7 ft. The computed initial conditions from run 1 are in poor agreement with the end burnout conditions of stage 1. In carrying out step 2 mentioned earlier, that is, varying λ_r^1 until r^0 is met, run 9 finally resulted. Since the computed vo from run 9 was already in good agreement with vo desired, it was decided to jump to step 5 and attempt to bring yo into closer agreement with the desired 25 deg. Such an attempt is shown in run 20 where it may be noted that vo also moved closer to the desired value even though t_n was not changed. Thus the computed initial conditions from run 20 are in fair agreement with the end burnout values of stage 1. By continuing the iterative process as indicated in step 5, any desired agreement with the initial values will be met. As soon as a solution is obtained which yields initial conditions that are in the vicinity of the desired ones, a Taylor series expansion, truncated after first order terms, can be used to achieve rapid convergence.

The time histories of the steering angle α for runs 1, 9 and 20 are shown in Fig. 5. Although the time histories of α do not vary greatly, the resulting trajectories as shown in Fig. 4 appear to be highly sensitive to small changes in α . It is interesting to note that for all three runs the thrust vector points above the flight path.

In all three runs the trajectory path first exceeded the orbital altitude and then entered the orbit from the outside. This somewhat unexpected occurrence may be attributed to the following two facts: 1 The average thrust to weight ratios for the second and third stages are less than unity. 2 The radius of the desired orbit is relatively close to the Earth. Thus the vehicle can not acquire orbital energy in just the flight from the earth to orbital altitude, but must exceed that height and approach the required energy when it is beyond the orbit radius.

Conclusion

A systematic procedure for solving a minimum time problem in which three initial and three final conditions are specified has been presented and successfully tested on a sample problem. The relatively small parameter study involved leads one to expect that other classes of problems also may be solved without an excessive amount of computation time. It is felt that general, systematic techniques must be developed for solving problems formulated by the calculus of variations, if this approach is to become a strong tool for trajectory optimization.

Appendix—Derivation of Equations

The following derivation is based on the Mayer formulation, an approach which has been extensively investigated by Miele (1). It is desired to extremize the difference between the end states of a function G^6 of the dependent variables $x_i = v, \gamma, r, \alpha$ and the independent variable t, subject to the constraints

$$\phi_j(x_i, \dot{x}_i, t) = \dot{x}_j - f_j(x_i, t) = 0 \quad j < i$$
 [A-1]

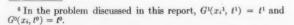
imposed by the equations of motion. The function

$$J = G^{1}(x_{i}^{1}, t^{1}) - G^{0}(x_{i}^{0}, t^{0}) + \int_{t^{0}}^{t^{1}} \lambda_{i} \phi_{i}(x_{i}, \dot{x}_{i}, t)dt \quad [A-2]$$

is to be extremized where the $\lambda_i(t)$ are the undetermined Lagrange multipliers. The superscripts 0 and 1 refer to initial and terminal points, respectively. A repeated subscript in a product indicates summation. For example

$$\lambda_j \phi_j = \lambda_1 \phi_1 + \lambda_2 \phi_2 + \lambda_3 \phi_3 \qquad j = 1 - 3$$

Since the x_i^0 and t^0 are assumed to be specified, variations of



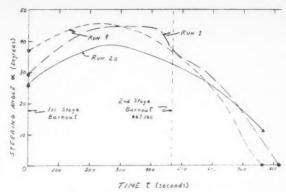


Fig. 5 Steering angle time histories

these quantities do not exist. The requirement that the first variation of J be zero yields

$$\delta J = \delta G^1 + \int_{t^0}^{t^1} \lambda_i \left(\frac{\partial \phi_i}{\partial \dot{x}_i} \, \delta \dot{x}_i + \frac{\partial \phi_j}{\partial x_i} \, \delta x_i \right) dt +$$

$$[\lambda_i \phi_i] \delta t^1 = 0 \quad [\text{A-3}]$$

By Equation [A-1] the last term in Equation [A-3] vanishes. Integration of the first term in the integrand by parts gives

$$\int_{t^0}^{t^1} \lambda_j \frac{\partial \phi_j}{\partial \dot{x}_i} \, \delta \dot{x}_i dt = \lambda_j \frac{\partial \phi_j}{\partial \dot{x}_i} \, \delta x_i \bigg]_{t^0}^{t^1} - \int_{t^0}^{t^1} \frac{d}{dt} \left(\lambda_j \frac{\partial \phi_j}{\partial \dot{x}_i} \right) \delta x_i dt \quad [A-4]$$

The term δG^1 is given by

$$\delta G^{1} = \frac{\partial G^{1}}{\partial x_{i}} \Delta x_{i}^{1} + \frac{\partial G^{1}}{\partial t} \delta t^{1}$$
 [A-5]

where Δx_i is related to a virtual variation δx_i by

$$\Delta x_i = \delta x_i + \dot{x}_i \delta t \qquad [A-6]$$

Substitution of Equations [A-4, A-5 and A-6] into Equation [A-3] provides

$$\delta J = \left(\frac{\partial G^{1}}{\partial x_{i}}\right)^{1} \Delta x_{i}^{1} + \left(\frac{\partial G^{1}}{\partial t}\right)^{1} \delta t^{1} + \left[\lambda_{i} \frac{\partial \phi_{i}}{\partial \dot{x}_{i}} \times \left(\Delta x_{i} - \dot{x}_{i} \delta t\right)\right]_{t^{0}}^{t^{1}} + \int_{t^{0}}^{t^{1}} \left[\lambda_{i} \frac{\partial \phi_{i}}{\partial x_{i}} - \frac{d}{dt} \left(\lambda_{i} \frac{\partial \phi_{i}}{\partial \dot{x}_{i}}\right)\right] \delta x_{i} dt = 0$$

$$(A-7)$$

For the problem considered, $G^1 = t^1$. Thus

$$\left(\frac{\partial G^1}{\partial x_i}\right)^1 \, \Delta x_i^{-1} \, = \, 0 \qquad \left(\frac{\partial G^1}{\partial t}\right) \, \delta t^1 \, = \, \delta t^1$$

The boundary conditions are

$$\delta t^1 \left[1 - \lambda_i \frac{\partial \phi_i}{\partial \dot{x}_i} \dot{x}_i \right]_{\lambda} = 0$$

which reduces to

$$\lambda_i^1 x_i^1 = 1 [A-8]$$

and

$$\lambda_i \frac{\partial \phi_i}{\partial \dot{x}_i} \Delta x_i \bigg]_{t^0}^{t^1} = 0 \tag{A-9}$$

The vanishing of the integral requires

$$\lambda_{i} \frac{\partial \phi_{i}}{\partial x_{i}} - \frac{d}{dt} \left(\lambda_{i} \frac{\partial \phi_{i}}{\partial \dot{x}_{i}} \right) = 0 \quad . \quad [A-10]$$

This formulation is now applied to the particular problem. The explicit form of Equations [A-1] are

$$\phi_1 = \dot{v} - \left(\frac{T\cos\alpha}{m} - \frac{\mu\sin\gamma}{r^2}\right)$$

$$\phi_2 = \dot{\gamma} - \left(\frac{T\sin\alpha}{mv} - \frac{\mu\cos\gamma}{vr^2} + \frac{v\cos\gamma}{r}\right)$$

$$\phi_3 = \dot{r} - v\sin\gamma$$

Equations [A-10] become

$$\begin{split} \dot{\lambda_v} &= -\frac{\lambda_\gamma}{\mu} \cos \gamma \left(1 + \frac{\mu}{v^2 \tau} \right) + \lambda_\gamma \frac{T \sin \alpha}{m v^2} - \lambda_r \sin \gamma \\ \dot{\lambda_\gamma} &= \cos \gamma \left(\lambda_v \frac{\mu}{r^2} - \lambda_r v \right) + \lambda_\gamma \frac{\sin \gamma}{r} \left(v - \frac{\mu}{v \tau} \right) \\ \dot{\lambda_r} &= -2\mu \lambda_v \frac{\sin \gamma}{r^3} - \lambda_\gamma \frac{\cos \gamma}{r^2} \left(\frac{2\mu}{v \tau} - v \right) \\ 0 &= \lambda_v \sin \alpha - \lambda_\gamma \frac{\cos \alpha}{v} \end{split}$$

The boundary condition [A-8] is

$$\lambda_{\nu}^{1}\dot{\nu}^{1} + \lambda_{\gamma}^{1}\dot{\gamma}^{1} + \lambda_{r}^{1}\dot{r}^{1} = 1$$

and in Equation [A-9] v^1 , v^0 , γ^1 , γ^0 , r^1 , r^0 are specified. We now examine the mass discontinuity at change of stage. Consider Equation [1]

$$\dot{v} = \frac{T\cos\alpha}{m} - \frac{\mu\sin\gamma}{r^2}$$

For a given stage, this is explicitly written as

$$\dot{v} = \frac{\cos \alpha}{m_{0-1}/T_1 + \dot{m}_1 t/T_1} - \mu \frac{\sin \gamma}{r^2}$$

$$\dot{v} = \frac{\cos \alpha}{A + Bt} - \mu \frac{\sin \gamma}{r^2}$$

After the change of stage, [A-11] becomes

$$\dot{v} = \frac{\cos \alpha}{C + Dt} - \mu \frac{\sin \gamma}{r^2}$$
 [A-12]

where

$$C = m_{0-2}/T_2$$
 $D = \dot{m}_2/T_2$

 $A,\,B,\,C,\,D$ are, of course, constants for each stage. Therefore, since ϕ_i is different for each stage, the integral in [A-2] should be written

$$\int_{t^{0}}^{tA} \lambda_{j} _{1} \phi_{j}(x_{i}, \dot{x}_{i}, t) dt + \int_{tA}^{tB} \lambda_{j} _{2} \phi_{j}(x_{i}, \dot{x}_{i}, t) dt + \ldots + \int_{tA}^{t} \lambda_{j} _{n+1} \phi_{j}(x_{i}, \dot{x}_{i}, t) dt$$

where t^A , t^B , . . . , t^n are change-of-stage times.

Now, if the first variation of the sum of integrals is sought, the formal parametric procedure explained in (4), p. 9, may be applied, and it will demonstrate that the variational operator δ is distributive. That is

$$\delta J = \delta G^1 + \delta \left[\int_{t^0}^{tA} + \int_{tA}^{tB} + \dots + \int_{tn}^{t^1} \right] = \delta G^1 + \delta \int_{t^0}^{tA} + \delta \int_{tA}^{tB} + \dots + \delta \int_{t^1}^{t^1} dt dt$$

After the operator is applied to the n+1 integrals, a partial integration of the first term of the resulting integrands is performed, and an expression analogous to [A-4] is obtained typical boundary terms are

$$\ldots + \lambda_i \frac{\partial_3 \phi_i}{\partial \dot{x}_i} \, \delta x_i \, \bigg]_{iB}^{iC} + \lambda_i \, \frac{\partial_4 \phi_i}{\partial \dot{x}_i} \, \delta x_i \bigg]_{iC}^{iD} + \lambda_i \, \frac{\partial_4 \phi_i}{\partial \dot{x}_i} \, \delta x_i \bigg]_{iD}^{iB} + \, .$$

At the intermediate times, t^{c} , t^{D} , . . . , we require, in part, for the vanishing of δJ

$$\left[\lambda_{i} \frac{\partial_{3} \phi_{i}}{\partial \dot{x}_{i}} - \lambda_{i} \frac{\partial_{4} \phi_{i}}{\partial \dot{x}_{i}}\right]_{i \in \mathcal{S}} \delta x_{i} = 0$$

Thus, the choice is either to specify x_i at t^c , t^p , . . . , or to require the bracketed part to equal zero.

Now note, however, that specifying the x_i at t^c , t^p , . . . is the more restrictive of the choices, and simply requiring

$$\lambda_i \frac{\partial_a \phi_i}{\partial \dot{x}_i} = \lambda_i \frac{\partial_4 \phi_i}{\partial \dot{x}_i}$$
 [A-13]

will admit a larger set of admissible variations; in fact, the set will include those permissible variations arising from the first choice.

Therefore, [A-13] is the specification at the change of stage times, and it states simply that λ_i is continuous across the change, by dint of [A-1]. At the initial and final time, the end conditions [A-8 and A-9] result.

Acknowledgment

The author wishes to acknowledge the assistance of J. E. McIntyre of the Missile Division, North American Aviation, Inc., and R. Auelmann⁸ of Aeronutronic, a Division of the Ford Motor Company, for their aid and many suggestions which facilitated this study.

Nomenclature

a = radius of the circular orbit

 g_0 = acceleration due to gravity at surface of Earth

 I_{sp} = specific impulse in a vacuum

m = mass

n = number of stages

= radius

T = thrust t = time

v = velocity

α = angle between thrust and velocity vectors

= angle between the local horizontal and the velocity

vector

 $\lambda_{\tau}, \lambda_{\gamma}, \lambda_{\gamma} = \text{Lagrange multipliers}$

⁷ Note, however, that both [A-11 and A-12] may apply over an unlimited range of t; i.e., there is no inherent discontinuity in the equations, as in, say, $\dot{y} = \Omega/t - t_2$ in which case some provision must be made for the point $t = t_2$.

⁸ Formerly with the Missile Division, North American Aviation, Inc.

product of the universal gravitational constant and the mass of Earth

= range angle

structural mass of the ith stage Matage 6 = initial mass of the ith stage

Superscripts

0 = initial time = final time

References

1 Miele, A., "A Survey of the Problem of Optimizing Flight Paths of Aircraft and Missiles," presented at the ARS Semi-Annual Meeting, Los Angeles, May 9-16, 1960.

2 Breakwell, J. V., "The Optimization of Trajectories," J. Soc. Indust. Appl. Math., vol. 7, no. 2, June 1959, pp. 215-247.

3 Kelley, H. J., "An Investigation of Optimum Zoom Climb Techniques," J. Aero/Space Sci., vol. 26, no. 12, Dec. 1959, pp. 794-802.

4 Blisa, G. A., "Lectures on the Calculus of Variations," University of Chicago Press, 1946.

Accuracy of Measuring Ballistic Missile Trajectories

FRANK COOPER¹

Aerospace Corp. Los Angeles, California

Missile propulsion and guidance systems' performance is determined from analysis of the missile's trajectory. During powered flight, the trajectory itself is most accurately determined by radio tracking of a missile-borne beacon. The accuracy of the radio measured trajectory data must in turn be established. The standard used for comparison is the ballistic camera which presently is useful only after powered flight. This paper presents comparisons which establish that, in the low frequency domain, the radio tracking system has the capability of measuring missile position to the same order of accuracy as the ballistic camera standard.

N THE measurement of missile trajectories, the basic question arises as to the accuracy of the values obtained. The precision of the measuring system may be evaluated by statistical methods, which have been developed to describe the so-called random errors. These are errors which are characteristic of precise measuring systems, and are caused by numerous uncontrolled factors such as small temperature changes. In addition to these random errors, there exist the so-called systematic errors. These are errors which might be caused, for example, by incorrectly calibrated scale. Systematic errors may be detected, insofar as detection is possible, by comparison with some other measuring system. This report presents such a comparison between two precise systems-a radio tracking system and a ballistic camera system-using data obtained from the flights of Thor 221 and Thor 238.

In the past, such comparisons have been made only on aircraft flights which differ considerably from missile conditions in the ranges, velocities, accelerations, etc., involved. For example, it is not possible to track an aircraft at a slant range of 100 miles and an elevation angle of 30 deg, because it would require a flight at an altitude of 50 miles above the Earth's surface. (Although special balloons can ascend to this height, they do not simulate the velocities and accelerations with which we are concerned.) Currently, only ballistic missiles are capable of this performance. Consequently, the amount of systematic error, or bias, under such conditions has been

unknown. Since knowledge of this bias is essential in the evaluation of a missile's propulsion and guidance systems, this comparison is of interest to many in the ballistic missile programs.

The Ballistic Camera System(1)²

Ballistic cameras are regarded as the standard for evaluation and calibration of other tracking systems. The basic reason for using ballistic cameras is that the directions of stars may then be computed without errors caused by atmospheric refraction. Since it is above most of the atmosphere, a missile flashing light is affected by refraction to almost the same degree as a background star having the same apparent elevation angle.

The camera itself is simple in construction, similar to a box camera; at the same time, its geometry is precisely known. This characteristic, together with the known directions of the background stars photographed on ultra flat (six fringe) glass plates through lenses calibrated to one micron or better (by means of star recordings), result in a system with the least possible amount of systematic error, hence, the standard for measuring angles.

Fig. 1 is a plate of a ballistic missile taken by a ballistic camera. The bright streak is the flame of the gases, ending at burnout. On board the missile is a light which flashes approximately twice per second. (The timing of these flashes is known to about a millisecond from a telemetry system.) The light flashes are visible after burnout. Shortly before the missile flashes are to be recorded, successive precalibration

Received Aug. 29, 1960.

¹ Member of the Technical Staff, Mercury Program Office.

² Numbers in parentheses indicate References at end of paper.

exposures of 2, 1, $\frac{1}{2}$, and $\frac{1}{4}$ sec are made, separated by 30-sec intervals. Each star thus gives four images of varying size and density, and produces a large selection of stellar images whose photographic characteristics closely match those of the flashing light images. This, in turn, minimizes personal bias in measuring, for personal bias would tend to be the same for both stellar and flashing light images.

After the precalibration, the camera shutter stays closed until just before the missile flashing light is in the camera field of view. Then the shutter is opened and kept open until the light flashes end. Shortly thereafter, a post-calibration is performed with flashes in the sequence of $\frac{1}{4}$, 1, and 2 sec. The final plate shows a series of images of the missile-borne flashing light against a background of stellar images which serve as the standard reference points.

The position of each missile flash is established by triangulation of rays from two or more ballistic camera stations. Because of measuring errors, three or more rays will not meet at a point. The plate coordinates are statistically adjusted by a least squares method to determine the most probable point of intersection of the rays.

D. C. Brown (1) reports that a typical 3 μ standard deviation currently exists in measuring ballistic camera plates because of the combined effect of setting error and emulsion instability. Dividing this figure, i.e., dividing 3 μ by the focal length of the camera, gives the angular accuracy of the measurement. With a pair of ballistic cameras, bias-free positions may be obtained accurate to one part in 10^5 of the range from the cameras.

The Radio Tracking System(2)³

With few exceptions, all missile, satellite and space probe boosters launched on the Atlantic Missile Range are tracked by the well-known Azusa radio tracking system, built by Convair Astronautics and operated by RCA. This is a precision interferometer with a resolution in angle of several parts in a million, and a resolution in range of about 0.1 ft at ranges of 600 miles (or about one part in 30 million). This system is the one that is compared in this report with ballistic camera data.

The Azusa Mark I radio tracking system is used to provide trajectory data in real-time, which consists of measurements in analog form of the slant range and direction cosines from the Azusa ground site to the vehicle being tracked.⁴ These measurements are supplied in digital form to an IBM 704 or IBM 709 computer for real-time impact or orbit prediction. The data are also recorded on magnetic tape for post-flight analysis

The determination of direction cosines is based on measurements of the differences in the phase delay between pairs of antennas receiving the signal from the missile-borne transponder. Slant range is derived from measurements of the phase difference between the transmitted and received modulated signals at one of the ground receivers. Incrementally derived slant range data are obtained from a phase locked loop that enables the Doppler shift to be utilized in measuring slant range increments. (The precision of this measurement is better than one foot in position at a slant range of over 500 miles.)

Figs. 2 and 3 (3) illustrate the Azusa ground station configuration, transponder diagrams, and overall theory.

Ballistic Camera—Azusa Comparisons (4)⁵

Figs. 4 and 5 are graphs of the difference in rectangular coordinates between missile position as determined by ballistic

⁵ The comparisons follow Saastad's method.



Fig. 1 Ballistic camera plate

cameras and by Azusa. (The ballistic camera points were fitted by RCA to an elliptical orbit which was modified to take into account a small residual thrust which occurred after vernier engine cutoff. The ballistic camera positions were then obtained by RCA from this fitted, thrust corrected orbit.) The average differences were

Thor 221 Thor 238
$$\overline{\Delta X} = \frac{1}{N} \sum (X_{BC} - X_A) = 36 \text{ ft} 33 \text{ ft}$$

$$\overline{\Delta Y} = \frac{1}{N} \sum (Y_{BC} - Y_A) = 11 \text{ ft} 21 \text{ ft}$$

$$\overline{\Delta Z} = \frac{1}{N} \sum (Z_{BC} - Z_A) = -56 \text{ ft} -8 \text{ ft}$$

At a point in the data period, the rectangular Azusa position data were transformed back to range and direction cosine measurements as follows

From these values the third direction cosine was computed

Thor 221 Thor 238

$$n = \sqrt{l - (l^2 + m^2)}$$
 +0.606105 +0.598030

The azimuth θ and elevation ϕ angles were obtained from the relations

The above values of r, l, m, n, μ and J are measured by Azusa or computed from Azusa measurements. They contain an unknown amount of bias which is determined by comparison with the ballistic camera data. Since the ballistic cameras measure the position of the optical beacon and the Azusa system tracks the antenna phase center (which is located about 17 ft aft of the optical beacon), correctionsmust be made for the displacement of these two sources.

³ This description is condensed from that given in (2).

⁴ The Mark I Azusa measures position. From these measurements, velocity may be derived. Errors in the derived velocities depend on the derivation method. This report is concerned only with errors in the position measurements.

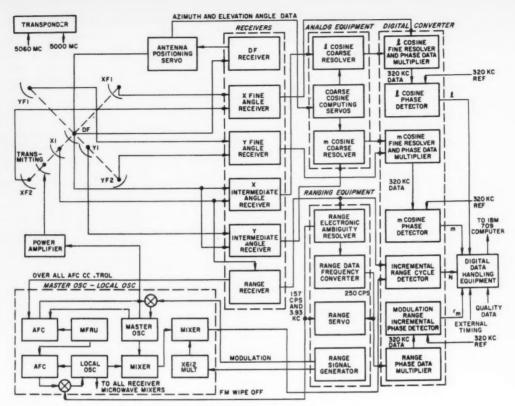
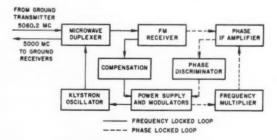
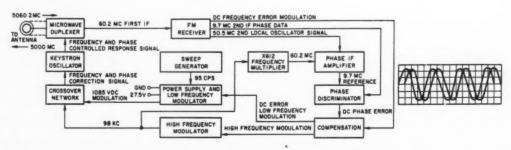


Fig. 2 Azusa ground station

MISSILE - BORNE TRANSPONDER



PHASE AND FREQUENCY CONTROL LOOPS



TRANSPONDER DIAGRAM

Fig. 3 Transponder

Another correction which should be applied adjusts for the second-order Doppler effect, which amounts to about 20 parts per million or about 14 ft at the range under discussion.

Reference (1) indicates that at these ranges, with a twocamera fix, the ballistic cameras are capable of providing positions accurate to the order of one part in 100,000 of the range

from the cameras, approximately 7 ft.

Considering the above factors and the small differences, half the average position differences were attributed to the Azusa system. The initial coordinates were then corrected as

	Thor 221	Thor 238
$x' = x + \frac{\overline{\Delta x}}{2}$	509,500 ft	525,076 ft
$y' = y + \frac{\overline{\Delta y}}{2}$	-195,070 ft	-198,857 ft
$z' = z + \frac{\overline{\Delta z}}{2}$	415,697 ft	418,935 ft

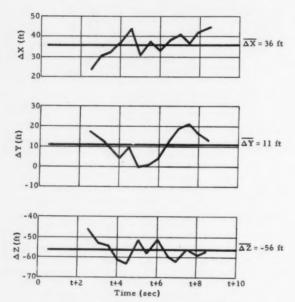


Fig. 4 Position difference-Thor 221

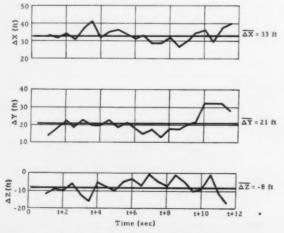


Fig. 5 Position difference-Thor 238

Next the Azusa measurements were recomputed

and similarly

Thor 221 Thor 238
$$n' = \sqrt{l - (l')^2 - (m')^2} \quad 0.606068 \quad 0.598018 \text{ radian} \\ \mu' = \arctan m'/l' \quad -0.365647 \quad -0.362028 \text{ radian} \\ J' = \arccos \sqrt{(l')^2 + (m')^2} \quad 0.651783 \quad 0.641026 \text{ radian}$$

Finally, the biases in the measured Azusa parameters were

$$\begin{array}{cccccc} (r'-r) & & -5 & & +6 \text{ ft} \\ (l'-l) & & +31 \times 10^{-6} & & +17 \times 10^{-6} \\ (m'-m) & & +5 \times 10^{-6} & & +17 \times 10^{-6} \end{array}$$

and also the biases in the computed parameters

Summary of Results

The Azusa system measures two direction cosines, l and m, and range r. The systematic errors in these measurements were determined to be

Expressed in terms of elevation and azimuth bias, the values obtained were

	Elevation $(\Delta \theta)$	Azimuth $(\Delta \phi)$
Thor 238	$+0.01 \ mr$	$-0.01 \ mr$
Thor 221	+0.02 mr	$+0.03 \ mr$

These values may be compared with ballistic camera plate measuring accuracy of 2 sec of arc (based on a standard deviation of 3 μ and a focal length of 300 mm). Two seconds of are in turn represent about 0.01 mr.

The third direction cosine n, which is a computed parameter, was found to have a bias of -12×10^{-6} and $-37 \times$ 10⁻⁶ on Thor 238 and Thor 221, respectively.

Conclusions

The above approach is simple. The results are encouraging and justify a refinement of the procedure. Such a refinement is under way and includes fitting the Azusa data to an elliptical orbit with the same residual thrust modifications that RCA applied to the ballistic camera data. However, it is evident from the above results that under the conditions of the missile tests presented, the Azusa radio tracking system is capable of measuring missile position with only extremely small systematic error.

References

- Brown, D. C., "Precision Photogrammetry in Missile Testing," RCA,
- AFMTC, Fla.

 2 Pepple, R., "The Azusa Tracking System," RCA, AFMTC, Fla.

 3 "Asusa." Report AZN-004, Convair/Astronautics, San Diego, Calif., March 1959.
- 4 Saastad, A., "Three Special Cases of Mark I Asusa Accuracy," Convair/Astronautics, San Diego, Calif.

Escape From Planetary Gravitational Fields by Use of Solar Sails

NORMAN SANDS¹

Radio Corporation of America Moorestown, N. J.

An escape maneuver by use of solar radiation pressure is computed for an initially circular orbit in the plane of the ecliptic of a planetary gravitational field. The flat sail is rotated about its axis at half the revolution rate about the planet. It is assumed that the sun is the only body that provides a flux of radiant energy, and that the sail perfectly reflects this energy specularly from either surface. Effects of extraneous gravitational fields, including that of the sun and moons (if any), are all neglected, as are other perturbing phenomena (such as atmospheric drag, magnetic fields, solar winds, meteoric showers, re-radiation from the planet's surface, etc.). Under these assumptions it is found that for a practical case of escape from Earth's gravitational field, solar sailing could accelerate a payload to escape condition in a period of time of the order of several months, during which time it would pass the vicinity of the moon's orbit about Earth.

TO ESCAPE from a planetary gravitational field by use of solar radiation pressure, the orientation of the sail with respect to both planet and sun must be such as to increase efficiently the total energy of the sail-spaceship system. The method of escape employed in this paper, first suggested by Cotter, was adopted for analysis despite the fact that it does not represent the most efficient escape maneuver. Accordingly, the sail rotates about its own axis at half the rate of revolution about the planet (see Fig. 1).

To simplify the analysis, the following assumptions were made:

The escape maneuver is executed in the equatorial plane of the planet, which is also the plane of the ecliptic.

2 The sail-spaceship system is initially placed in a circular orbit about the planet by means of conventional rocketry.

The sail is assumed flat and perfectly reflecting specularly on both surfaces.

4 The sail-spaceship system is assumed to be under the planet's central force field only, thus neglecting the influence of other gravitational fields (i.e., the planet's moons, if any, and those of other planets, and the sun).

5 Other phenomena that could affect the escape maneuver, such as the planet's atmospheric drag, solar winds, meteoric showers, magnetic fields, re-radiation from the planet's surface, etc., are all neglected.

6 The sun is assumed to be the only body that provides a flux of radiant energy.

The flux of solar energy is constant in the entire region in which the maneuver takes place, even in the region that would normally be the planet's shadow.

Propulsion in a Planetary Gravitational Field by Solar Radiation Pressure

The pressure exerted on a perfectly reflecting flat surface

oriented normally to the incident radiation is

$$P_N = \frac{2S_E}{c} \left(\frac{R_E}{R_P}\right)^2$$
 [1]

When the normal to the surface subtends an angle θ with the sun's rays, the pressure decreases in proportion to $\cos^2 \theta$,

$$P = P_N \cos^2 \theta = \frac{2S_E}{c} \left(\frac{R_E}{R_P}\right)^2 \cos^2 \theta$$
 [2]

Let the reference axis of a polar coordinate system be a line perpendicular to the sun's rays, with origin at the center of the planet, and positive sense in the direction of motion of the planet about the sun as viewed from the north pole (line BB' in Fig. 1). Let ψ be the angular displacement of the sail-spaceship system as measured from this reference axis, and assume that at $\psi = 0$ the reflecting plane is parallel

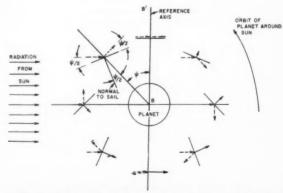


Fig. 1 Orientation of sail with respect to planet and sun

Received Sept. 6, 1960.

Systems Engineer, Physics Group.
 Cotter, T. P., "Solar Sailing," Sandia Corp. Research Colloquium SCR-78, April 1959.

to the sun's rays (i.e., $\theta=\pi/2$). As stated above, the sail is assumed to rotate about its own axis at half the rate of revolution about the planet. Hence $\theta=(\pi/2)-(\psi/2)$, and [2] becomes

$$P = \frac{2S_E}{c} \left(\frac{R_E}{R_P}\right)^2 \sin^2 \frac{\psi}{2}$$
 [3]

The equations of motion of a sail-spaceship system in the central force field of a planet are (radial component)

$$\frac{d^2r}{dt^2} - r\left(\frac{d\psi}{dt}\right)^2 = -\frac{\mu}{r^2} + \frac{F_r}{M}$$
 [4]

(tangential component

$$2\frac{dr}{dt}\frac{d\psi}{dt} + r\frac{d^2\psi}{dt^2} = \frac{F_t}{M}$$
 [5]

where

$$\mu = g_0 r_0^2 \tag{6}$$

and F_r and F_t , the radial and tangential components of the force exerted on the sail by radiation pressure, are given by

$$F_r = -AP \cos \frac{\psi}{2} \left[\frac{\sin \frac{\psi}{2}}{\sin \frac{\psi}{2}} \right] = -\frac{AS_E}{c} \left(\frac{R_E}{R_R} \right)^2 \left| \sin \frac{\psi}{2} \right| \sin \psi \quad [7]$$

and

$$F_{i} = AP \left| \sin \frac{\psi}{2} \right| = \frac{2AS_{E}}{c} \left(\frac{R_{E}}{R_{P}} \right)^{2} \left| \sin^{3} \frac{\psi}{2} \right|$$
 [8]

Substituting [6, 7 and 8] into [4 and 5]

$$\frac{d^2r}{dt^2} - r\left(\frac{d\psi}{dt}\right)^2 + g_0\left(\frac{r_0}{r}\right)^2 = -\frac{AS_E}{Mc}\left(\frac{R_E}{R_P}\right)^2 \left|\sin\frac{\psi}{2}\right| \sin\psi$$

$$2\left(\frac{dr}{dt}\right)\left(\frac{d\psi}{dt}\right) + r\frac{d^2\psi}{dt^2} = \frac{2AS_E}{Mc}\left(\frac{R_E}{R_P}\right)^2 \left|\sin^3\frac{\psi}{2}\right| \quad [10]$$

subject to the following assumed initial condition

at
$$t = 0$$

$$\begin{cases} r = H & \frac{dr}{dt} = \frac{d^2r}{dt^2} = 0\\ \psi = 0 & \frac{d\psi}{dt} = \sqrt{\frac{\mu}{H^3}} \frac{d^2\psi}{dt^2} = 0 \end{cases}$$

The final condition of escape is reached when the total velocity equals the local escape velocity, i.e., when

$$\left(r\frac{d\psi}{dt}\right)^2 + \left(\frac{dr}{dt}\right)^2 = \frac{2\mu}{r}$$
 [12]

Transformation of Coordinates

Let r and t be nondimensionalized with respect to r_0 and $\sqrt{r_0/g_0}$, i.e.

$$\bar{r} = \frac{r}{r_0} \qquad \bar{t} = \sqrt{\frac{g_0}{r_0}} t \qquad [13]$$

and let

$$R = \left(\frac{Q}{g_0}\right)^{1/z} \bar{\tau} \qquad T = \left(\frac{Q}{g_0}\right)^{1/4} \bar{t} \qquad [14]$$

where

$$Q = \frac{2AS_B}{Mc} \left(\frac{R_B}{R_P}\right)^2$$
 [15]

Applying to [9, 10, 11, and 12]

$$\frac{d^2R}{dT^2} - R\left(\frac{d\psi}{dT}\right)^2 + \frac{1}{R^2} = -\frac{1}{2}\left|\sin\frac{\psi}{2}\right|\sin\psi \qquad [16]$$

$$2\left(\frac{dR}{dT}\right)\left(\frac{d\psi}{dT}\right) + R\frac{d^2\psi}{dT^2} = \left|\sin^3\frac{\psi}{2}\right|$$
 [17]

with initial condition

at
$$T = 0$$

$$\begin{cases} R = K & \frac{dR}{dT} = \frac{d^2R}{dT^2} = 0 \\ \psi = 0 \frac{d\psi}{dT} = K^{-3/2} \frac{d^2\psi}{dT^2} = 0 \end{cases}$$

where

$$K = \frac{H}{r_0} \left(\frac{Q}{a_0} \right)^{1/\varrho} \tag{19}$$

and final condition for escape

$$\left(R\frac{d\psi}{dT}\right)^2 + \left(\frac{dR}{dT}\right)^2 = \frac{2}{R}$$
 [20]

Numerical Integration

For numerical integration purposes, the two second-order differential Equations [16 and 17], were transformed into four first-order equations and, for better convergence of the problem, the independent variable was changed from T to ψ . Accordingly, let $R=R(\psi)$ and $T=T(\psi)$, and define

$$\frac{dR}{dx} = V ag{21}$$

$$\frac{dT}{d\mu} = \Omega \tag{22}$$

Then, since

$$\begin{split} \frac{dR}{dT} &= \frac{V}{\Omega} \qquad \frac{d^2R}{dT^2} = \frac{1}{\Omega^3} \left(\Omega \, \frac{dV}{d\psi} - V \, \frac{d\Omega}{d\psi} \right) \\ \frac{d\psi}{dT} &= \frac{1}{\Omega} \qquad \frac{d^2\psi}{dT^2} = -\frac{1}{\Omega^3} \left(\frac{d\Omega}{d\psi} \right) \end{split}$$

Equations [16 and 17] become

$$\frac{d\Omega}{d\psi} = \frac{2V\Omega - \left|\sin^3\frac{\psi}{2}\right|\Omega^3}{2}$$
 [23]

$$\begin{split} \frac{dV}{d\psi} &= R - \left[\frac{1}{R^2} + \frac{1}{2} \left| \sin \frac{\psi}{2} \right| \sin \psi \right] \Omega^2 + \\ &= \underbrace{\frac{2V^2 - \left| \sin^3 \frac{\psi}{2} \right| V \Omega^2}_{P}}_{P} \quad [24] \end{split}$$

with initial and final conditions, corresponding to [18 and 20], respectively

at
$$\psi = 0$$

$$\begin{cases} R = K & V = \frac{dV}{d\psi} = 0 \\ T = 0 & \Omega = K^{2/2} & \frac{d\Omega}{d\psi} = 0 \end{cases}$$
 [25]

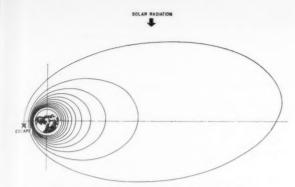


Fig. 2 Solar sail escape trajectory; K = 0.10

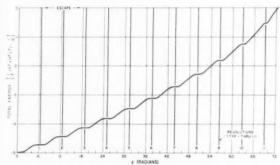


Fig. 3 Relation between gain in total energy and angular displacement; K=0.10

and

51

$$\left(\frac{R}{\Omega}\right)^2 + \left(\frac{V}{\Omega}\right)^2 = \frac{2}{R}$$
 [26]

The Runge Kutta method was used in programming the solution of these equations on an IBM 709 computer.

Results and Discussion

A typical escape trajectory, with K=0.10, is shown in Fig. 2. (The value K=0.10 was chosen to illustrate the nature of the solution merely for convenience, as this value leads to rapid escape (see Figs. 2, 3, 4 and 5). More practical values of K would be in the order of 0.02.) As seen in Fig. 2, apogees and perigees lie along or close to the reference axis BB' of Fig. 1, with the apogees occurring ahead of the planet in its path along the sun. That quasi-symmetry should occur along BB' would be expected from the symmetry of the orientation of the sail with respect to this axis (see Fig. 1), with the resulting energy gain being essentially symmetric about this reference line. Consequently, the integrated energy gain over a complete revolution can, to a close approximation, be regarded as applied impulsively at the perigee, thus vindicating the quasi-symmetry about BB'.

In the particular case shown in Fig. 2, escape occurs near perigee. Although escape can occur at any angular position, it is more likely to take place near $\psi = (2n+1)\pi$, where n= an integer, since most of the energy is gained in this region; this is brought out in a somewhat clearer form in Fig. 3, which is a plot of the total energy at any point along the trajectory versus the angular position ψ . The slopes of E_T vs. ψ are smallest near $\psi = 2\pi n$ and largest near $\psi = (2n+1)\pi$. Hence the chances of crossing the line $E_T = 0$ in Fig. 3, which represents the conditions for escape,

are much better near a perigee than near an apogee. Ratios of kinetic to potential energy for the escape trajectory of Fig. 2 are shown in Fig. 4, where the parameter

$$\frac{T}{K^{1/2}} = \frac{l}{(H/r_0)^{1/2}}$$

rather than T was selected as abscissa, since for a given planet and radius of initial circular orbit, it is directly proportional to t. It should be noted in connection with Fig. 4 that

$$\frac{\left(R\frac{d\psi}{dT}\right)^2 + \left(\frac{dR}{dT}\right)^2}{(2/R)}$$
 [27]

representing the ratio of kinetic to potential energy, is always equal to $\frac{1}{2}$ as $(T/K^{3/2}) \rightarrow 0$, regardless of K, as is immediately seen by substitution from [18]. Likewise, as seen from [20], ratio [27] approaches unity upon reaching escape condition.

The locus at succeeding periges of the ratios of kinetic to potential energy is shown in Fig. 6 for several values of K. As seen in this figure, these loci do not reach unity at the last perigee, since, for the cases shown, escape did not occur at perigee. Escape points corresponding to the respective values of K are, nevertheless, included so that these curves may be used to evaluate the time required for an escape

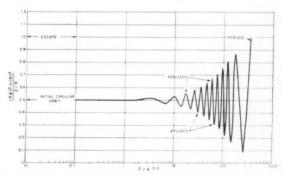


Fig. 4 Ratios of kinetic to potential energy along an escape trajectory; K=0.10

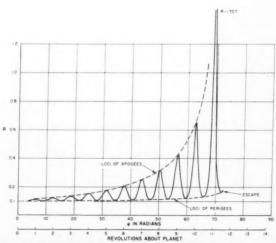


Fig. 5 Variation of R along escape trajectory; K = 0.10

maneuver. A cross plot of the escape times given in Fig. 6 is shown in Fig. 7 as a function of the parameter K. Escape times cannot be predicted accurately, as is seen from the scatter in Fig. 7, since they depend on the angular position of the last cycle in which escape occurs, because of the nonuniform manner in which energy is gained per cycle (see Fig. 3).

The number of revolutions required to escape are given in Fig. 8 as a function of the parameter K. For the range of values of K shown, there is obtained

number of revolutions required to escape $\approx 0.1/K^2$ [28]

The length of time required to complete the nth revolution

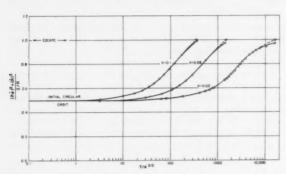


Fig. 6 Locus of the ratios of kinetic to potential energies at perigees

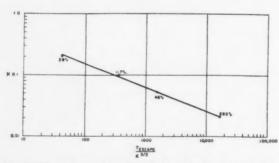


Fig. 7 Effect of parameter K on the length of time required to escape

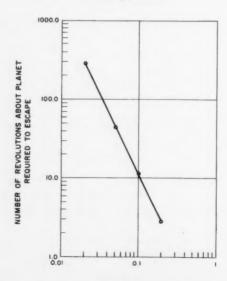
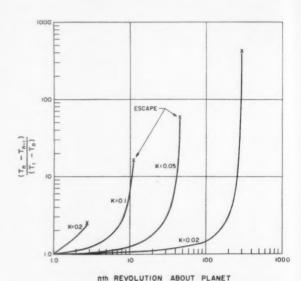


Fig. 8 Effect of parameter K on the number of revolutions about planet required to escape

about the planet compared to the length of time required to complete the first revolution is shown in Fig. 5.

The variation of R along the escape trajectory of Fig. 2 is shown in Fig. 5. For $K=0.20,\ 0.10,\ 0.05$ and 0.02 it was observed, as is also apparent from Fig. 9, firstly, that at any angular position with respect to BB' of Fig. 1, R increases in successive revolutions, and, secondly, that the



an

To (F

th in al

pl

01

th

ar

al fu (I w th

jı

Fig. 9 Comparison of time interval required to complete the nth revolution with the time interval required to complete the first revolution

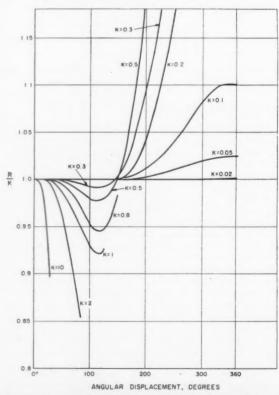


Fig. 10 Normalized radial distance during the first revolution of a planetary satellite propelled by solar radiation pressure

Table 1 Sample calculation for planet Earth

	SIZ	OF SAIL	MASS PER UNIT AREA OF SAIL (gr/cm ²)	MASS OF SPACESHIP EXCLUDING SAIL.	к	TIME REQUIRED TO ESCAPE (BAYS)	DISTANCE TO LAST APOGEE PRIOR TO ESCAPE (MILES)
	AREA (cm²)	DIAMETER OF EQUIVALENT CIRCLE (METERS)					
4500	1010	1130	10"4	108	.0320	54	261,000
4500	1010	1120	2:10-4	109	.0237	112	378,000
4500	1010	1180	3 = 10 0	109	0195	119	473,000
4500	2 46 = 10 ⁸	960	10-4	108	0290	73	297,000
4500	109	356	10-4	109	.0243	105	364,000
4500	109	356	10-4	3 = 10 9	0303	65	288,000
5000	109	396	10-4	3 + 10 8	0365	47	260,000

ratio of apogee to perigee also increases in successive revolutions. These observations can be stated mathematically as

$$\frac{R_{n+1}}{R_n} > 1$$
 at any value of $\psi_{n+1} = \psi_n + 2 \pi$ [29]

and

$$\left(\frac{R_{\text{apogee}}}{R_{\text{perigee}}}\right)_{n+1} > \left(\frac{R_{\text{apogee}}}{R_{\text{perigee}}}\right)_{n}$$
 [30]

where n = number of completed revolutions = 0, 1, 2, . . . To see whether R ever decreases below its initial value K (Equation [18]), several runs were made with unrealistically large values of K. The results, shown in Fig. 10, indicate that R < K can indeed be achieved for sufficiently large K; in these cases, escape conditions were reached in exceptionally short intervals of time, corresponding to angular displacements of the order of one revolution about the planet or less. Such high values of K, almost equivalent to the high thrusts obtainable through conventional chemical rocketry, are obviously unattainable in reality, and were used to compute the data shown in Fig. 10 merely to illustrate the point.

The maximum value of R reached in the last revolution about the planet prior to escape is shown in Fig. 11 as a function of K. As in the case of the time required to escape (Fig. 7), it is not possible to predict R_{max} accurately, as it will depend on whether escape occurs just before reaching the apogee of the nth revolution (in which case R_{max} will be taken to correspond to that of the (n-1)th revolution), or just after reaching the apogee of the nth revolution (in which case R_{max} will, of course, be taken to correspond to that of the nth revolution).

The results of some sample calculations for the planet Earth, for which $r_0 = 6.375 \times 10^8$ cm, $g_0 = 981.5$ cm/sec², and $\mu = 4 \times 10^{20}$ cm³/sec², are given in Table 1. In view of the many assumptions made to simplify the analysis (see above), these results could, at best, be used as a rough estimate of the time involved and span covered in an actual escape maneuver of this kind.3

Concluding Remarks

Placing the sail-spaceship system in an initially circular orbit and rotating it about its own axis at half the rate at which it revolves about the planet does not constitute an efficient escape maneuver. The inefficiency is mainly attributed to the fact that most of the traveling time is spent in

The reviewer pointed out that at an initial orbital radius of 4500 miles, the Earth's atmospheric drag is comparable to solar radiation pressure and would seriously impair the effectiveness of solar sails. The reviewer also noted that at a distance of approximately 160,000 miles from the Earth, solar gravity is equal to the Earth's gravity, thus casting doubt as to the validity of assumption 4.

Assumptions 4 and 5 were introduced to circumvent just such difficulties, and it might perhaps be well, at this point, to draw attention to the restrictive nature of assumptions 1-7. Future work should relax some of these assumptions, which would then make the analysis of an escape maneuver more realistic.

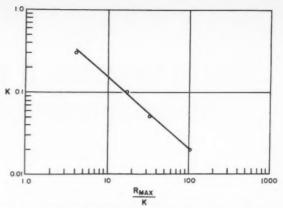


Fig. 11 Effect of parameter K on the maximum radial distance to the last apogee prior to escape

the neighborhood of the apogees where the rate of gain of total energy is small.

A method which would greatly improve the performance (i.e., reduce the time interval required to escape) would be to place the spaceship-sail combination in an elliptic rather than circular initial orbit (but, in order to be fair, of equivalent total energy), with the apogee along BB' extended in the negative direction, so as to have this initial apogee trail behind the planet in its revolution about the sun. The eccentricity of the initial ellipse, as well as the most profitable way of orienting the sail with respect to the sun so as to minimize T escape, will, of course, have to be determined.

Acknowledgment

The author wishes to express his appreciation to Jerome B. Fanucci for his suggestions and advice, and to Gui Saatdjian for his assistance in carrying out the numerical computations.

Nomenclature

= area of sail

c = velocity of light in vacuum $E_T = \text{total energy, } \frac{1}{2} \left[\left(\frac{dR}{dT} \right)^2 + R^2 \left(\frac{d\psi}{dT} \right)^2 \right]$

radial component of force

tangential component of force

planet's gravitational acceleration at sea-level

radius of circular orbit into which the spaceship and sail is initially put by conventional rocketry

= defined by Equation [19]

mass of spaceship including sail $M = M_0 + \rho A$

 M_0 = mass of spaceship excluding sail

= solar radiation pressure on an obliquely oriented re-flecting flat surface

solar radiation pressure on a normally oriented reflecting flat surface

Qdefined by Equation [15]

radial distance in plane polar coordinates

defined by Equation [13]

radius of planet

Rdefined by Equation [14]

 R_P mean distance from Earth to sun

 R_E mean distance from planet to sun

solar energy constant at the Earth's distance from sun; SE $S_{\rm E} = 1.94 \, {\rm cal/cm^2 \, min} = 1.35 \times 10^6 \, {\rm erg/cm^2 \, sec}$

= time

defined by Equation [13] defined by Equation [14] T

V defined by Equation [21]

angle subtended between normal to sail and sun's rays 0

planetary gravitational constant, Equation [6]

mass per unit area of sail

angular displacement of sail-spaceship system relative to axis BB' of Fig. 1.

defined by Equation [22] Ω

= dots denote differentiation with respect to T

Ablation Mechanisms in Plastics With Inorganic Reinforcement

NORMAN BEECHER¹

National Research Corp. Cambridge, Mass.

RONALD E. ROSENSWEIG²

Massachusetts Institute of Technology Cambridge, Mass. E

al T

> pi no

> > u te

n c 1 s o v A d d

Experimental and theoretical studies are described which clarify the nature and importance of the chemical and physical processes that occur in the ablation of these materials. Products and amount of gas from resin pyrolysis are determined from tube furnace tests, the rate of the process is inferred, heat effects are measured by calorimetric methods, and the rate of inorganic reaction between carbon and glass is measured in an induction heated furnace. The heterogeneous silica-carbon reaction is coupled to aerodynamic conditions and this results in a cutoff temperature for such chemical reaction. From an examination of re-entry specimens and order of magnitude calculations of possible carbon-consuming processes a realistic overall picture of the ablation is emerging. Resin decomposition during ablation and further reaction of the high molecular weight species are treated analytically.

WHEN a typical inorganic-reinforced plastic such as Fiberglas-reinforced phenol-formaldehyde resin is subjected to atmospheric re-entry at hypersonic velocity, a complex process occurs which destroys only a thin surface layer of the material and protects the bulk of the material from thermal damage.

Recognition of the effectiveness of ablation in heat protection came first from an evaluation of empirical materials testing programs. A preliminary understanding of the process of ablation soon followed, based in part on examination of materials exposed to a rocket exhaust. The first successful re-entry and recovery of an ablating nose cone, after an intermediate range ballistic missile flight in August 1957, followed months of testing and evaluation at the Army Ballistic Missile Agency (1).³ Although much of the data on military uses is still classified, there is considerable open literature on the results of tests of many different materials thought to be possible candidates for ablation heat shields, e.g. (2,3,4 and 5).

Considerable effort has been expended in attempting to predict the heat transfer to a re-entering vehicle. Because of the backlog of aerodynamic analysis techniques available for its solution and the importance of this part of the problem, most investigators have devoted their attention to the gas dynamics. In re-entry of a blunt body, the shock wave stands off ahead of the nose a distance of some centimeters. Behind the shock the air is hot and compressed with typical temperatures of 5000 to 10,000 K depending on the velocity and air density. Analyses around the stagnation point have been made based on laminar boundary layer theory which include effects such as gas dissociation and chemical reaction (6,7,8). In general, calculations for the turbulent flow regime have been highly empirical (9,10).

Attempts to define the mechanism by which heat is absorbed in the surface layers of the heat shield have, in general, dealt with the simpler materials. Included among the

analyses available are, for glass, Bethe and Adams (11); for carbon, Lees (12); and for Teflon, Scala (13).

The present investigation was undertaken to define the mechanisms of protection in ablation of a thermosetting plastic with inorganic reinforcement. The various heat sinks in general involve decomposition, melting or endothermic chemical reaction.

Ablation Described

At low heat flux reinforced plastics, like many other materials, absorb heat without appreciable ablation. Time is available for deep penetration of energy and the surface temperature is maintained below the decomposition level by removal of heat to the interior of the material.

The heat flux at which ablation begins depends on the plastic but at energy fluxes of 200 to 400 w/cm², under the influence of moderate shear and pressure forces, a practical glass-reinforced phenolic resin loses material at rates up to a millimeter per second. On the surface of the plastic is a layer of molten glass beneath which is a layer of carbonized plastic supported by the glass fibers. Still deeper in the material there is a decomposition zone in which the resin is pyrolyzed to a mixture of light gases and carbonaceous materials. The gases pass through the permeable "char" and the liquid glass into the gas stream. These layers are shown diagrammatically in Fig. 1.

Because of the high energy flux and low conductivity of the plastic, the heat penetrates only to a shallow depth before decomposition temperatures are reached. The layer of pyrolyzed material at the surface is continually and rapidly removed. Therefore, the temperature gradients are extremely steep and the thickness of plastic material affected at any instant is small, of the order of less than one millimeter.

The success of the ablation mechanism in protecting the underlying layers of the nose cone against thermal destruction results from a combination of insulating layers alternating with heat sinks, the latter being defined as processes which absorb energy. To develop new heat shield materials of the ablating type one should understand the mechanism by which the various heat sinks operate and the properties of the insulating layers.

Received Aug. 17, 1960.

¹ Project Manager.

² Assistant Professor of Chemical Engineering; Consultant to National Research Corp.

³ Numbers in parentheses indicate References at end of paper.

Experimental Approach

The approach taken in the present work has been to study the individual reactions and processes occurring during ablation. No attempt at overall simulation was made. The initial decomposition of the plastic has been studied in pyrolyses conducted in tube and arc image furnaces. The products of this reaction consist of volatile material and a nonvolatile residue of glass and carbon. The volatile products have been analyzed and where secondary decomposition or reaction is indicated, as zones of higher temperature are reached, these processes have been studied analytically. The solid residue of glass and carbon was expected to undergo a secondary reaction when it was heated to higher temperatures. The kinetics of these reactions have been determined by separate studies of samples of this material in an induction furnace. The residue was found to be stable up to temperatures of about 1100 C. By 1400 C a rapid reaction occurred which released carbon monoxide as the gaseous product. This could only come from a reduction of the oxides present, by the carbon,

In a typical ablation material of the glass-reinforced phenolic resin type the resin content is of the order of 20-25 per cent by weight. In the initial decomposition reaction about 10-12 per cent by weight of the material is gasified, representing about half of the resin content. The remaining part of the resin, amounting also to 10 to 12 per cent of the original weight of the material, remains as carbon in the glass matrix. A typical analysis of the gaseous products of the original decomposition is shown in Table 1. The gases which actually enter the boundary layer include less large molecules, such as phenols and cresols, and more light gases because of subse-

quent secondary reactions.

The effect of this mass addition to the boundary layer in reducing heat transfer is substantial. Methods of calculation have been treated in detail by others; it has not been the purpose of the present work to consider at length the effects in the gas boundary layer but to study the condensed phases. Nevertheless, the material referred to in Table 1, when injected into the boundary layer, is sufficient to reduce heat transfer by about 20 per cent when surface material is being removed at about one-half millimeter per second.4

⁴ It is of interest to estimate the heat blocking due to this mass addition. In the case of turbulent flow, Mickley (14) found good correlation of flat plate experimental results with film theory in the form $\psi = B/(e^B - 1)$ where ψ is fractional heat unblocked, $B = (m e_p)/h_0$, and \dot{m} is the mass flux of material from the wall, c_p is the heat capacity of gas, and h_0 is the heat transfer coefficient with no mass addition. Conditions for ablation at 0.05 cm/sec are approximately known, and using a heat flux 0.05 cm/sec are approximately known, and using a heat flux calculated by the method of Fay and Riddell (8) and straight temperature driving force, B=0.2 and $\psi=0.9$; i.e., there is 10 per cent heat blockage.

In the case of laminar flow the correlation recommended by Adams (15) reads $\psi = 1 - 0.7 (29/MW)^{1/3}B$. The injected gases have a molecular weight MW = 9.8. For the same value of B as above, $\psi = 0.8$; i.e., there is 20 per cent heat blockage. Characteristically, the laminar flow heat blockage is predicted to

be greater than for turbulence.

Table 1 Gaseous products of pyrolysis of typical glassreinforced phenolic resin

H_2	54 mole %
phenol	2.5 mole %
cresols	2.5 mole %
CO	12 mole %
CH ₄	12 mole %
H_2O	12 mole %
miscellaneous (toluene, benzene, xylene, C ₂ H ₄ , C ₃ H ₆ , C ₄ H ₈)	5 mole %

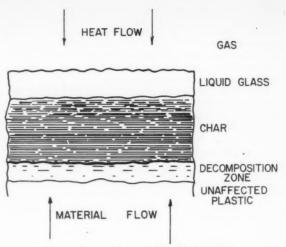


Fig. 1 Layers of material in ablating plastic

Chemical Reactions and Process Zones

The relationship of the liquid, char and decomposition zones in actual re-entry is shown diagrammatically in Fig. 1. As ablation occurs, the heat penetrates deeper into the material as the surface is continuously removed. A quasi-steady state condition is reached wherein the thickness of the affected material is nearly constant. A given layer is very short-lived, as can be seen by considering that the rate of ablation is about one-half millimeter per second and the affected zone about one millimeter thick.

A convenient reference that can be used to describe this quasi-steady process is the liquid-gas interface. The material continuously moves toward and through this reference as ablation occurs. The heat flux, on the other hand, is inward from the interface, countercurrent to the flow of material.

Heating and Decomposition of Plastic

The material in the affected zone farthest from the interface undergoes a process of rapid heating. This is equivalent to one dimensional heat penetration into a semi-infinite moving slab at a uniform surface temperature.

In the decomposition zone the rate of reaction is a function of kinetics and heat transfer into the zone.

Reactions of Gases

From the decomposition zone the gaseous products of the resin flow through the porous matrix of carbon and glass and then pass through the liquid glass. The dimensions of the pores in the char layer are not precisely known, but small size is unquestionable. In the glass there is doubtless some channeling, but again the flow channels appear to be quite small. For approximate calculations, therefore, it is probably a good assumption that these gases reach the temperature of the material through which they are passing.

At such temperatures three types of chemical reaction can occur. First, the gases can thermally decompose. Second, they can react with the solid material; that is, the glass or the carbon. Third, they can react with each other.

The exact specification of all these reactions is difficult, but considerable light can be shed by consideration of the kinetics and thermodynamics of reactions available to each individual component of the gas. It is a tacit assumption that no significant amount of air diffuses back through the glass layer to react with these gases in the char. This view is supported by the consideration of the relatively large mass addition, relative to the rate of oxygen diffusion. It is estimated that the flame front for combustion of these gases lies a small but significant distance above the surface in the boundary layer. In addition, there is the shielding effect due to the physical presence of the glass.

Some of the reactions mentioned above can be dealt with summarily because of minor importance, e.g., if the gaseous component is in small concentration and/or the enthalpy

change on reaction is very small.

Reactions Between Glass and Carbon

At the upper part of the char layer, the Fiberglas softens and eventually forms a liquid layer subject to flow removal. In addition, there are in the glass a number of compounds which can react with the carbon. These reactions are extremely interesting from the aspect of providing heat protection in that they are all highly endothermic. The reaction thermodynamics have been considered with respect to individual components of the glass, as if they were pure compounds. This neglects the effect of solution on activity, but some order of magnitude estimates of relative reaction temperatures are possible. Kinetic data studies have been made with samples of charred plastic and the further reaction between the char and Fiberglas observed. That is to say, the char remaining after substantially complete thermal decomposition of the resin at 1000 C has been subjected to the higher temperatures at which inorganic reactions begin.

Analysis of the Chemical Reactions

In the following sections the chemical reactions described above are analyzed semi-quantitatively. Briefly, they are the thermal decomposition of resin, the reactions of the gaseous products of the decomposition, and the reactions between carbon and molten glass.

Analysis of the Decomposition of the Resin

The model for analysis of the solid is illustrated in Fig. 2. This process is regarded as one of steady state dissipation. The surface temperature of the solid is designated T, and, from the viewpoint of an observer stationed at this surface, the solid material approaches at velocity v. The solid material is removed from the surface by any process capable of doing so; the detailed mechanism is immaterial for this

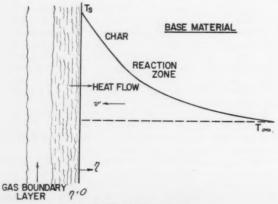


Fig. 2 Steady state ablation

analysis. A continuous temperature gradient exists through the char region, the reaction zone, and the unaffected plastic. The material is initially at T_{∞} and is raised to decomposition temperatures by the influx of heat.

The extent of reaction will be indicated by the variable λ, which equals the fraction of unreacted material. With regard to applying the model represented by this analysis to the ablation behavior of materials of interest, the products of decomposition may be assumed to leave as gases through the char; for this initial analysis the heat transfer between char and gas is assumed negligible.⁵

The material is composed either wholly or in part of a chemically active species which undergoes an irreversible reaction which can be described according to the following overall first-order reaction scheme

$$A \xrightarrow{\Delta H} B$$
 [1]

The reaction rate expression is taken as

$$d\lambda/dt = -k''\lambda \tag{2}$$

It is also assumed that volume changes are negligible.⁶ Accordingly, a material balance on a differential slice for a one-dimensional system gives

$$v(d\lambda/d\eta) + k''\lambda = 0$$
 [3]

where η is the distance from the surface and v is the ablation rate. An energy balance is written assuming constant physical properties of density ρ ; specific heat c_p ; thermal conductivity k; heat of reaction ΔH ; and f is the fraction of reactable species in the initial material

$$\frac{d^2T}{d\eta^2} + \frac{(v\rho c_p)}{k} \frac{dT}{d\eta} - \frac{k''\rho \Delta H \lambda f}{k} = 0$$
 [4]

The solution for a semi-infinite slab is considered for which the boundary conditions are

$$T = T_{\infty}$$
 when $\eta = \infty$
 $\lambda = 1$ when $\eta = \infty$
 $T = T_{*}$ when $\eta = 0$

To take account of the decomposition reaction, a temperature dependent reaction rate expression is introduced

$$k'' = k' \exp\left[-\Delta E/R(T - T_{\infty})\right]$$
 [6]

This is an expression of the Arrhenius type but with one modification: $(T-T_{\infty})$ has replaced the usual T. Some assumption of this nature is necessary to restrain the mathematical model from predicting a completely reacted condition at all finite depths. Hence, T_{∞} plays the role of an ignition temperature for chemical reaction. This is in accord with experience of the sort which says a container of combustible gases does not ignite itself when stored at low temperature for an indefinitely long period. It will become clear that for the problem at hand the composition profiles in the regions of interest are unaffected by this assumption. This artifice would have been unnecessary if instead the problem were set up for a slab with finite thickness, but this would add another variable and, in the end, would contribute nothing of value to the result.

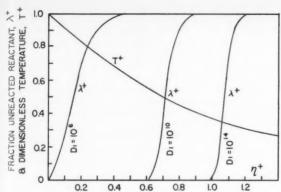
The following dimensionless groups are defined

$$T^{+} = \frac{(T - T_{\infty})}{(T_{\bullet} - T_{\infty})} = \text{reduced temperature}$$

6 In currently used ablation materials, changes on the order of

15 per cent are encountered.

⁵ This is justified because the heat transfer relative to the total heat content of the solid is small. Later, in treating the gas this heat transfer is included, since it is more important relative to the heat content of the gas.



he

of

gh

n

1)

Theoretical analysis of decomposition of solid; effect of D_1 ; $D_2 = 10$

Theoretical analysis of decomposition of solid; effect of D_2 ; $D_1 = 10^{14}$

$$\eta^+ = \frac{\eta v \rho c_p}{k} = \eta v/\alpha = \text{reduced distance}; \text{ ratio of depth}$$
in solid to a characteristic ablation length ($\alpha = \text{thermal diffusivity}$)

$$\lambda^{+} = \lambda$$
 = fractional unreacted reactant $D_{1} = \frac{k \ k'}{v^{2} \rho c_{p}} = \frac{k' \alpha}{v^{2}}$ = ratio of an ablation time to a chemical time

$$D_2 = \frac{\Delta E}{R(T_* - T_{\infty})} = \text{modified Arrhenius group}$$
 $D_3 = \frac{f\Delta H}{c_p(T_* - T_{\infty})} = \text{ratio of chemical enth}$
sensible enthalpy

$$D_3 = \frac{f\Delta H}{c_p(T_s - T_{\infty})}$$
 = ratio of chemical enthalpy to sensible enthalpy

Substituting these groups into the basic Equations [3 and 4] gives the dimensionless equations which describe the process of decomposition in the solid for the model studied

$$\frac{d\lambda^{+}}{dn^{+}} = \lambda^{+}D_{1} \exp\left(-D_{2}/T^{+}\right)$$
 [7]

$$\frac{d^2T^+}{d\eta^{+2}} + \frac{dT^+}{d\eta^+} - D_1D_3\lambda^+ \exp(-D_2/T^+) = 0$$
 [8]

The new boundary conditions are

$$T^{+} = 0$$
 when $\eta^{+} = \infty$
 $\lambda^{+} = 1$ when $\eta^{+} = \infty$
 $T^{+} = 1$ when $\eta^{+} = 0$ [9]

A numerical calculation is necessary to find the most general solution due to the coupling inherent in these equations. However, an important simplification is possible at this point, since the ΔH is expected to be quite small.⁷ This means that a solution for $D_3 = 0$ is of interest. With $D_3 = 0$, Equa-

⁷ The heat of decomposition ΔH , of a glass-reinforced phenolic resin, corresponding to conversion to the products listed in Table I was determined from calorimetric data to be endothermic and about 90 cal/g of resin.

The chemical energy associated with complete reaction of a unit mass of ablating solid = $f\Delta H$; the sensible energy associated with the temperature rise of a unit mass of ablating solid =

$$D_{\rm S} = \frac{f \; \Delta H}{c_{\rm P} \; (T_{\rm S} - T_{\rm \infty})} = \frac{(0.22)(90)}{(0.3)(1600)} = \; 0.04$$

The heat sink effect of reaction amounts to but 4 per cent of the heat sink effect of sensible enthalpy changes. This small the heat sink effect of sensible enthalpy changes. Fraction does not, however, indicate quite such a correspondingly small effect on the composition pattern since the zone of appresmall effect on the composition pattern since the zone of appresmall effect on the composition pattern since the zone of appresmall effect on the composition pattern since the zone of appresmall effect of the composition pattern since the composi ciable reaction extends over a limited temperature range. The effect of an appreciable ΔH would be to broaden the reaction

tions [7 and 8] become uncoupled. The solution of [8] then is given by

$$T^{+} = e^{-\eta^{+}}$$
 [10]

Eliminating T^+ between [10] and [7] gives

$$\lambda^{+} = \exp(-D_1) \int_{\eta^{+}}^{\infty} \exp(-D_2 \exp \eta^{+}) d\eta^{+}$$
 [11]

As it stands, this equation is not convenient for obtaining numerical results due to the unwieldy integration. A convenient equivalent form for the final result is

$$\lambda^{+} = \exp \left[D_1 \, Ei(-D_2 \exp \, \eta^{+}) \right]$$
 [12]

In this equation Ei stands for the exponential integral function, a known function for which tables are available (16).

$$Ei (-z) = \int_{\eta^+}^{\infty} \frac{e^{-z}}{z} dz$$
 [13]

In the above connection $z = D_2 \exp \eta^+$.

The type of solutions obtainable with Equations [10 and 12] are illustrated in Figs. 3 and 4. The curves of λ^+ , the fraction unreacted material, have the anticipated shape, changing more gradually at the beginning of reaction than at the end due to the imposed temperature history of a particular element of solid.

The effect of the constant $D_1 = k k'/v^2 \rho c_p = k'\alpha/v^2$, the ratio of an ablation time to a chemical reaction time, is shown in Fig. 3. When the ablation time is long, relative to chemical reaction time (i.e., ablation slow, the decomposition reaction fast), decomposition occurs farther from the surface. As this ratio becomes smaller, decomposition is nearer the surface and, because of the relative slowness of reaction, is spread over a thicker zone.

The effect of the constant $D_2 = \Delta E/R(T - T_{\infty})$, the modified Arrhenius group, is shown in Fig. 4. As this constant increases, i.e., higher activation energy required, the rate of reaction is reduced. Thus, with large D2 the zone of reaction is closer to the surface where the temperature is higher. The activation energy has little to do with the thickness of the reaction zone, however, which is determined by D_1 . Thus, the form of the curve for $D_2 = 25$ is virtually identical to that for $D_2 = 10$ so long as D_1 is held constant. The two curves are displaced from each other by a considerable distance, however.

A calculation has been made for a point on an IRBM trajectory at which the ablation rate is estimated to be 0.05 cm/sec and the temperature at the outside edge of the char zone approximately 1900 K. The following physical constants apply to a typical glass-reinforced phenolic resin

 $\begin{array}{lll} \alpha & = \text{thermal diffusivity} & = 0.0029 \text{ cm}^2/\text{sec} \\ \Delta E & = \text{activation energy} & = 11 \text{ kcal/mole} \\ k' & = \text{rate constant} & = 10^6 \text{ sec}^{-1} \end{array}$

A base temperature of 300 K is used so that $T_{\bullet} - T_{\infty} = 1600$ K.

The constants ΔE and k' were estimated from the results reported by Madorsky and Straus (17) for decomposition of a phenolic resin. Their value of 18 kcal/mole is equivalent to the 11 kcal/mole value when the latter is used with the modified Arrhenius expression in the reaction temperature range.

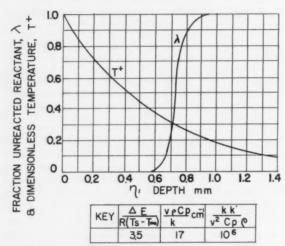


Fig. 5 Theoretical analysis of decomposition of solid; "best" values of constants



Fig. 6 Cross section of ablation test specimen. From top to bottom: glass; char; decomposition zone; heat discolored plastic; unaffected plastic

The exact thickness of the char layer cannot be known either from recovered re-entry nose cones or from ground test specimens, since the transient cooling stage will thicken the pyrolysed layer. However, the indications from both re-entry and ground test specimens are that the curve of "best calculated results" shown in Fig. 5 is close to that anticipated for these conditions.

A comparison of the results in Fig. 5 can be made with an ablation test specimen shown in Fig. 6. The various reaction zones are easily identified, although the char zone and layer of heat-discolored plastic are somewhat thicker than would be expected at the high ablation rate for which calculations were made. This difference is probably due to a lower heating rate occurring at the end of the test period or during cooling.

Reaction of the Gaseous Products of Resin Decomposition

The gaseous products flowing through the char layer will undergo further thermal decomposition of the high molecular weight components such as phenol, cresols, benzene and toluene. An illustrative calculation is presented.

Material and energy balances are taken over a differential slice of the char, dy, infinite in extent in the plane of the surface of the material. The gas and solid are assumed to be in thermal equilibrium. Since the number of moles of gas undergoing reaction is a small fraction of the total gas, the total number of moles present and the m_{g} c_{rg} product are assumed constant.

The energy balance then yields

$$k_{s}(1-\epsilon)\frac{\partial^{2}T}{\partial y^{2}} - k_{g}\epsilon \frac{\partial^{2}T}{\partial y^{2}} + v_{s}(1-\epsilon)\rho_{s}c_{p_{g}}\frac{\partial T}{\partial y} + \dot{m}_{g}c_{p_{g}}\frac{\partial T}{\partial y} + \left[k_{R}\rho_{R}\epsilon \left(\frac{1}{MW}\right)\Delta H \exp\left(-\Delta E/RT\right)\right] = 0 \quad [14]$$

where

 k_{θ} = conductivity of solid or gas

 ϵ = fraction voids in solid

 $v_s, \dot{m}_s, \dot{m}_g$ = velocity and mass rate of flow of solid and gas toward reference plane at surface

T = temperature ρ_s = density of solid

 c_{p_0}, c_{p_0} = heat capacity of solid and gas

The term in brackets is due to heat of decomposition. Because of the low bonding energies of the organic molecules involved and the large sensible enthalpy gradient in gas and solid, this effect can be ignored with small error. Integration of the resulting equation with the boundary conditions of surface temperature, thickness of char, and initial gas composition gives an expression for the temperature as a function of depth in the char

$$\frac{T - T_0}{T_Y - T_0} = \frac{1 - \exp(-yr)}{1 - \exp(-Yr)}$$
 [15]

where

$$r = \frac{\dot{m}_s c_{p_s} + \dot{m}_g c_{p_g}}{\epsilon (k_g - k_s) + k_s}$$

 $T_0 = \text{surface temperature}$

y =distance measured from surface into the char

Y,Y (subscript) = distance to or referring to plane at which the gas enters the char prior to decomposition

The material balance on an element of the reacting gas yields

$$x = x_Y \exp \left[-\frac{P(MW)_{avg}k_R}{\dot{m}_g R} \int_y^Y \frac{1}{T} \exp \left(-\frac{E}{RT} \right) dy \right] \quad [16]$$

where

le

at

d

11

 $\dot{m}_s,\,\dot{m}_g=\max$ flow rate of solid and gas toward the reference plane at surface

 k_R = reaction pre-exponential rate constant x = mole fraction undecomposed reactant gas

Data for the kinetics of o-cresol decomposition have been obtained by extrapolation of the results of Jones and Neuworth (18). Other constants have been estimated from the literature for typical Fiberglas reinforced phenolics. These values have been used in a numerical solution of Equations [15 and 16] with the results shown in Fig. 7

In Fig. 7 the mole fraction of o-cresol remaining unreacted and the temperature are plotted as a function of depth. No reaction occurs over most of the char thickness but when reaction begins, it proceeds rapidly to substantial completion.

The other gaseous components are much more stable than the cyclic compounds like o-cresol. Carbon monoxide, methane, water and hydrogen are unlikely to decompose. Their reactions with inorganic materials in the char are practically ruled out by equilibrium considerations. The most likely reaction of this type is

$$SiO_2(s) + H_2(g) \rightarrow SiO(g) + H_2O(g)$$
 [17]

The free energy change is of the order of 35 kcal (positive) at 2000 K. With this free energy change and assuming a hydrogen partial pressure of one atmosphere, the partial pressures of SiO(g) and $H_2O(g)$ would be about 10 mm Hg.

A likely reaction is that between water and the carbon in the char

$$H_2O(g) + C(s) \rightarrow + CO(g) + H_2(g)$$
 [18]

At 1500 K the free energy change is 19.0 kcal (negative) and at 2000 K, it is 45.9 kcal (negative). Rate data have been investigated (19,20,21,22) and appear to be rather inconsistent.

However, two factors operate to reduce the importance of this reaction. First, the carbon and water have a common source in the phenolic resin, and even if all the oxygen were tied to hydrogen, there would be insufficient water to react with more than one fifth of the carbon. Furthermore, the heat absorption of this reaction is compensated for by the heat absorption of the silica-carbon reaction, which generally would remove any carbon not reacted with water.

Reactions Between Carbon and Fiberglas

Thermodynamic analysis shows that the three reactions of carbon and Fiberglas most likely to occur from the point of view of equilibrium are (23 and 24)

$$SiO_2 + 3C \rightarrow SiC + 2 CO$$

 $\Delta H_{20000^{\circ}K} = 133 \text{ keal}$ [19]

$$SiO_2 + 2C \rightarrow Si(1) + 2 CO$$

 $\Delta H_{20000^{\circ}K} = 157 \text{ keal}$ [20]

$$SiO_2 + C \rightarrow SiO(g) + CO$$

 $\Delta H_{20001} \circ_K = 147 \text{ keal}$ [21]

The equilibria are shown in Fig. 8 and from these data several conclusions can be drawn. At high pressure of carbon

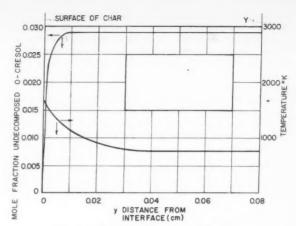


Fig. 7 Decomposition of o-cresol in char

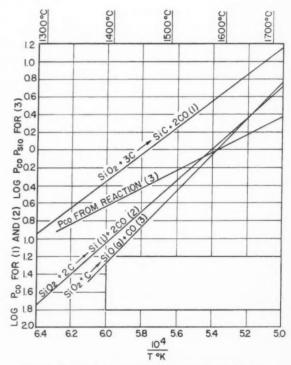


Fig. 8 Equilibria in reactions between silica and carbon

monoxide, reaction [19] can occur at lower temperature than [20 or 21]. For the reaction to proceed vigorously, the equilibrium carbon monoxide pressure would have to be sufficient to force the gas out through the pores of the char against the stagnation pressure of re-entry. The latter is in the neighborhood of 10 atm during the ablation considered here. For reaction at 10 atm the temperature for reaction [19] is 1680 C. This on-off feature of the reaction presents a significant coupling of chemical and aerodynamic processes.

Kinetics were suspected to be controlling rather than equilibrium. Therefore, samples of char from pyrolyzed Fiberglas-reinforced phenolic plastic were held at high temperature to observe the reaction of the carbon and glass.

The apparatus consisted of a modified NRC-912 vacuum fusion apparatus as shown in Fig. 9. Samples were held at 1100 C to drive off residual hydrocarbons or adsorbed gases. They were then dropped into the crucible, held at temperature, and the gas released was pumped to the storage flask and measured by the Alphatron pressure gage connected to a recorder. Reaction temperatures from 1350 to 1700 C were used. After reaction was completed the gas that had been pumped over was analyzed by oxidation and condensation and found to be 100 per cent carbon monoxide or carbon dioxide. Calculations were made on the basis of the monoxide.

Typical data curves are shown in Fig. 10 and initial reaction rates are plotted in Fig. 11. Using an Arrhenius analysis, the activation energy was found to be 92,000 cal/mole. The pre-exponential rate constant was calculated for the fol-

PHATRON PUSH ROD VIEWING **3-TO** GAS PRISM MAGNET RECORDER BULB COLD TRAP SAMPLE OF CHARRED TO GAS PLASTIC **ANALYSIS** APPARATUS ERCURY VALVE INDUCTION COIL CARBON DIFFUSION CRUCIBLE PUMPS

Fig. 9 Diagram of inorganic reaction apparatus

lowing equation, which assumes proportionality to the volume V of reacting mass. It is pictured that the reaction is a heterogeneous one, occurring at interfacial surfaces between carbon and silica, such interfaces being more or less uniformly distributed throughout the volume

$$\frac{dn_c}{dt} = kV \exp\left(-\Delta E/RT\right)$$
 [22]

where $n_a = \text{grams of carbon}$.

The value of k was found to be 2×10^{14} g/cm³ min, based on initial reaction.

It should be noted that these experiments in vacuum do not necessarily measure the rate of reaction [19] in which silicon carbide forms. At pressures of a few microns, thermodynamics does not limit any of the reactions, even at 1300 C, as is evident from Fig. 8. However, as has been pointed out by Fulton and Chipman (25), the slow step is probably either the breaking of SiO bonds or the slow removal of oxygen by carbon at the interface. Both these steps affect the rate of appearance of carbon monoxide in all three reactions almost equally.

In the conditions of re-entry, assumed as 10 atm CO pressure and short reaction time, it appears likely that only reaction [19] occurs. It can be shown that at 1680 C a temperature sufficient to overcome the thermodynamic limitations on reaction [19] but not on [20 or 21], the measured reaction rate would easily produce the observed results. Thus, at the measured initial rate, carbon would be consumed by this reaction at the rate of

$$\frac{-dn_o}{dt} = \frac{2 \times 10^{14} \times 1}{60} \exp \left[-\frac{92000}{(1987)(1680 + 273)} \right]$$
$$= 167 \text{ g/cm}^3 \text{ sec at } 1680 \text{ C}$$

Even if the measured rate is in error by a factor of two or three-fold, and allowing for rate decrease as reaction pro-

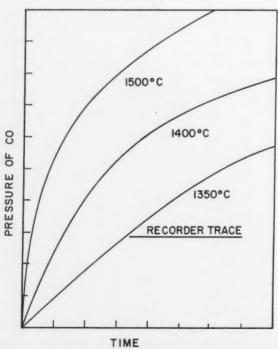


Fig. 10 Typical data on C-SiO₂ reaction

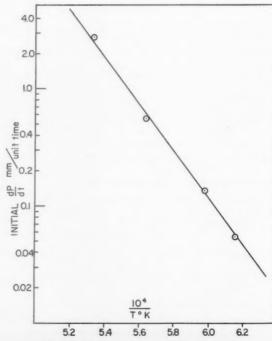


Fig. 11 Arrhenius plot for initial reaction rate

ceeds, all the carbon present would be consumed in less than one second. It would not appear, therefore, that the temperature could reach levels that would permit reactions [20 and 21] to occur, as long as sufficient reactants remained for reaction [19]. It is quite possible, however, that in a zone nearer the surface than the carbon reaction level, the temperature may be sufficient to cause the silicon carbide formed to react further

$$SiC + SiO_2 \rightarrow 2SiO + CO_2$$
 [23]

The question arises whether processes other than the silica-carbon reaction remove carbon. Combustion with air was considered. With the aid of the data of Parker and Hottel (26) it can be shown that diffusion rather than surface reaction limits the combustion, but that it is too slow in comparison with the silica-carbon reaction. Furthermore, there is considerable doubt that a significant amount of oxygen can reach the surface because of shielding in the gas boundary layer by the combustible gaseous products of resin decom-

Sublimation of the carbon is completely impossible under IRBM conditions because thermal radiation would be sufficient to keep the surface below the 3000 C or higher tem-

perature required.

6

n

The carbon can flow off with the glass. We have observed that when a gas-oxygen torch flame is played on the material, it softens and the melt flows under shear carrying along the carbonaceous material with it. However, as is true of the ablation specimen shown in Fig. 6, the surface layer frequently consists of a clear or white glass. Hence, in such areas, there must be some reaction to remove carbon.

Thus, it appears very likely that the silica-carbon reaction is at least partially responsible for removal of carbon, although under certain conditions carbon may flow off with the glass.

Evidently, the rate of ablation is determined by the rate of molten excess glassy material flowing off the surface. This is caused by shear and pressure forces acting on the surface material whose viscosity is lowered by the high temperature. In turn the surface temperature is in large measure determined by the silica-carbon reaction. Thus, in a very real sense, rate of ablation is controlled by the characteristics of this reaction: the amount of heat it absorbs and the reaction temperature.

If a different set of materials with different reaction characteristics were substituted, the material would ablate at a different rate and with a different surface temperature. Reactive materials could, incidentally, be chosen to be most effective at the surface temperature anticipated for a particular re-entry service. Thus, the ablation material could be tailored to the thermal environment to be encountered.

Formation of new char appears to be a secondary process, regulated by a balance between the kinetics of the pyrolysis process and the rate of heat conduction through the char.

Conclusions

It has been shown that an improved understanding of the ablation mechanism in glass-reinforced plastics can be obtained by application of thermodynamic and kinetic analyses. Three processes occurring in the condensed phases have been considered: (a) the thermal decomposition of the resin; (b) the reactions of the gaseous products of this decomposition; (c) the reactions between carbon and Fiberglas. These processes absorb heat: processes (a) and (b) minor amounts, but process (c) about 4 kcal per gram of carbon consumed. Process (c) is thus an important heat sink.

Adams (15) has presented a calculational procedure for estimating heat of ablation for a fiberglass material and finds agreement with arc tunnel and rocket exhaust tests. In those calculations it was found necessary to assume a heat of evaporation of 750 Btu/lb to fit his theory to the facts. Our work serves to better define the source of this heat effect. It is clearly not due to pyrolysis of resin as discussed above. We believe inorganic reactions account for the heat effect in question.

Acknowledgment

The assistance of personnel of the Army Ballistic Missile Agency, E. Braunlich, R. Schulz-Arenstorff, and P. Dyer in the machine computations are gratefully acknowledged. This work was supported by the Army Ballistic Missile Agency under Contract DA-19-020-ORD-4689.

References

1 Lucas, W. R. and Kingsbury, J. E., "A Brief Review of The ABMA Materials Program," Conference on Behavior of Plastics in Advanced Flight Vehicle Environments, WADD Tech. Rept. 60-101, Feb. 1960.
2 Manos, W. T. and Taylor, D. E., "The Effects of Thermal Environmental Parameters on Ablation Characteristics," Conference on Behavior of Plastics in Advanced Flight Vehicle Environments, WADD Tech. Rep. 60-101, Feb. 1960.
WADD Tech. 1960.

60-101, Feb. 1960.

3 King, H. A., "Testing of Materials Under Ablative Conditions,"
Third Pacific Area National Meeting of ASTM, Oct. 1959.

4 Schwartz, H. S. and Farmer, R. W., "Studies on Plastics Exposed to High Mass Flow Thermal Environments," Conference on Behavior of Plastics in Advanced Flight Vehicle Environments, WADD Tech. Rep. 60-101, Feb. 1960.

Feb. 1960.

5 Gill, J. L. et al, "Structural Insulative Characteristics of Ablating Plastics," Conference on Behavior of Plastics in Advanced Flight Vehicle Environments, WADD Tech. Rep. 60-101, Feb. 1960.

6 Scala, S. M. and Baulknight, C. W., "Transport and Thermodynamic Properties in a Hypersonic Laminar Boundary Layer, Part 2, Applications," ARS JOURNAL, vol. 30, no. 4, 1960, pp. 329-336.

7 Hayes, W. D. and Probstein, R. S., "Hypersonic Flow Theory," Academic Press, N. Y., 1959, pp. 292-303.

8 Fay, J. and Riddell, F., "Theory of Stagnation Point Heat Transfer in Dissociated Air," J. Aero/Space Sci., vol. 25, no. 2, 1958, pp. 73-85.

9 Rose, P. H., Probstein, R. S. and Adams, M. C., "Turbulent Heat Transfer Through a Highly Cooled, Dissociated Boundary Layer," J. Aero/Space Sci., vol. 25, no. 12, 1958, pp. 751-760.

Transfer Through a Highly Cooled, Dissociated Boundary Layer," J. Aero'Space Sci., vol. 25, no. 12, 1958, pp. 751-760.

10 van Driest, E. R., "On Mass Transfer Near the Stagnation Point," AFOSR TN-57-458, North American Aviation, Inc., June 1957.

11 Bethe, H. A. and Adams, M. C., "A Theory for the Ablation of Glassy Materials," Avco Research Laboratory, RR 38, Nov. 1958.

12 Lees, L., "Convective Heat Transfer with Mass Addition and Chemical Reactions," Third Combustion and Propulsion Colloquium, AGARD, NATO, Palermo, Sicily, 1958.

13 Scala, S. M., "A Study of Hypersonic Ablation," General Electric MSVD Rep. R-59SD438, Sept. 1959.

14 Mickley, H. S., Ross, R. C., Squyers, A. L. and Stewart, W. E., "Heat, Mass and Momentum Transfer for Flow Over a Flat Plate with Blowing or Suction," NACA TN 3208, 1954.

15 Adams, M. C., "Recent Advances in Ablation," ARS JOURNAL, vol. 29, no. 9, 1959, pp. 625.

15 Adams, M. C., "Recent Advances in Adiauon, And Sydragar, No. 29, no. 9, 1959, p. 625.
16 Jahnke, E. and Emde, F., "Tables of Functions," Dover Publications, N. Y., 1945, pp. 6-9.
17 Madorsky, S. L. and Straus, S., "Measurement of Thermal Stability of High Temperature Polymers," NBS Report 6478, July 1959.
18 Jones, B. W. and Neuworth, M. B., "Thermal Cracking of Alkyl Phenols—Mechanism of Dealkylation," Ind. Eng. Chem., vol. 44, no. 12, 1972, 1972.

1952, pp. 2872–2876.

19 Warner, B. R., "Mechanism of the Steam-carbon Reaction," J. Amer.

Warner, B. R., "Mechanism of the Steam-carbon Reaction," J. Amer. Chem. Soc., vol. 65, no. 8, 1943, p. 1447.
 Gadsby, J., Hinshelwood, C. N. and Sykes, K. W., "The Mechanism of the Steam-carbon Reaction," Proc. Roy. Soc., vol. 187, 1946, p. A129.
 Long, F. J. and Sykes, K. W., "The Kinetics of the Reactions of the Steam-carbon System," Proc. Roy. Soc., vol. 193, 1948, p. A377.
 Ershova, N. M., "On the Order of Reaction in Gasifying Coal with Steam," J. Appl. Chem., (USSR), vol. 27, 1954, pp. 93-94.
 Kubaschewski, O. and Evans, E. L., "Metallurgical Thermochemistry," John Wiley and Sons, Inc., N. Y., 1956, pp. 228-321.
 Rossini, F. D. et al, "Selected Values of Physical and Thermodynamic Properties of Hydrocarbons and Related Compounds," Carnegie Press, Pittsburgh, 1953, p. 704.

Pittsburgh, 1953, p. 704.
25 Fulton, J. C. and Chipman, J., "Kinetic Factors in the Reduction of Silica from Blast-Furnace Type Slags," J. Amer. Inst. Min. Met. Pet. Eng., vol. 215, no. 6, 1959, p. 888.

51. 215, no. 6, 1959, p. 888.
26 Parker, A. S. and Hottel, H. C., "Combustion Rate of Carbon-Study Gas-Film Structure by Microsampling," Ind. Eng. Chem., vol. 28, no. 11, 1936, p. 1334.

Size Distribution and Velocity of Ethanol Drops in a Rocket Combustor Burning Ethanol and Liquid Oxygen

ROBERT D. INGEBO1

Lewis Research Center NASA Cleveland, Ohio

Single jets of ethanol were studied photomicrographically inside a rocket chamber as they broke up into sprays of drops which underwent simultaneous acceleration and vaporization with chemical reaction occurring in the surrounding combustion gas stream. In each rocket test-firing, liquid oxygen was used as the oxidant. Both drop velocity and drop size distribution data were obtained from photomicrographs of the ethanol drops taken with an ultra-high speed tracking camera developed at NASA, Lewis Research Center.

A JET of liquid fuel injected into a relatively high temperature, high pressure, combustion-gas stream very quickly atomizes and ignites into a spray of burning drops. Knowledge of the size distribution and the velocity of burning fuel drops in a combustor is required in order to determine spray vaporization rates which are generally considered to control the rate of the overall combustion process (1).²

The purpose of this investigation was to obtain the size distribution and velocity of ethanol drops in a rocket combustor burning ethanol and liquid oxygen. Other investigations (2) have produced some results in this field by means of photographic technique. From past experience, photographic methods appear to hold the most promise for this type of investigation. For the present study, a high speed tracking camera was developed at NASA, Lewis Research Center [described in (3)] which gave photomicrographs as shown in Fig. 1. A magnification of 15 was used for these pictures.

From the photomicrographs of burning ethanol drops taken at a distance of 4 in. downstream from the injector face, it was possible to determine the size distribution of the drops and analyze the data using the Nukiyama-Tanasawa, log probability, and Rosin-Rammler expressions for size distribution. Also, drop velocities were determined from the speed at which the mirror tracked the drops in stopping their images on the infrared film.

The velocity V_d of a stopped ethanol drop image (as shown in Fig. 1) was calculated from the expression $V_d=4\pi\omega L/M$, where L is the distance from the mirror to the film plane, M is the magnification (M=15), and ω is the mirror speed. A semilog plot of the observed drop velocity against the drop diameter, at a distance 4 in. downstream from the injector face, is shown in Fig. 2. The injection velocity for the ethanol jets was approximately 25 fps, whereas drop velocities were found to be approximately 30 and 70 fps for the 344- and 35- μ diameter drops, respectively, at the camera station.

The volume median drop diameter D_{20} was found to be 152 μ as calculated by direct integration of the experimental drop



Fig. 1 Photomicrograph of burning ethanol drops

Presented at the ARS Propellants, Combustion and Liquid Rockets Conference, Columbus, Ohio, July 18–19, 1960.

Aeronautical Research Scientist.

Numbers in parentheses indicate References at end of paper.

size data. This agrees with the value of 154 μ obtained for D₃₀ from Fig. 3, which shows a plot of the following Nukiyama-Tanasawa expression

$$\frac{dR}{dD} = \frac{b^6}{120} D^5 e^{-bD}$$
 [1]

which may be rewritten as

$$\log \frac{\Delta R}{(\Delta D)D^{5}} = -1.7 \frac{D}{D^{30}} + \log \left[\frac{3.915}{D^{30}} \right]^{6} / 120$$
 [2]

since integration of Equation [1] gives $D_{30} = 3.915/b =$ -1.7/slope.

The drop size data were also plotted, as shown in Fig. 4, using the log probability expression

$$R = \frac{\delta}{\sqrt{\pi}} \int_{-\infty}^{\delta y} e^{-\delta^3 y^2} dy$$
 [3]

where $y = \ln (D/D^*)$. Integration of Equation [3] and the slope of the plot in Fig. 4 gives a value of D_{30} of 158 μ , which also agrees fairly well with the value obtained by direct integration of the drop size data.

A plot of the Rosin-Rammler expression

$$1 - R = e^{-(D/D)^q}$$
 [4]

shown in Fig. 5, gives a D_{30} value of 116 μ . This is considerably below the value of 152 μ obtained by direct integration of the drop size data. Thus, the Rosin-Rammler expression appeared to give the poorest results. However, more experimental drop size data for fuel sprays burning in rocket combustors are needed to establish the general applicability of the Nukiyama-Tanasawa and log probability expressions to burning sprays.

Concluding Remarks

The most difficult problem encountered in photographing the fuel spray was that of providing sufficient light to penetrate the relatively opaque flame without scattering appreciably and still operate on an extremely short time scale (ten billionths of a second for a $10-\mu$ diameter drop traveling 100 fps and magnified 15 times). However, with the tracking camera it was possible to have an exposure time of approximately 8 microsec. Also, since long wave length light gave less light scattering, it was found that infrared film used in conjunction with a red filter on the light source gave the best

Nomenclature

= constant Equation [1]

= drop diameter, cm

= size parameter in Equation [4], cm

 $D^* = \text{drop diameter at } R = 0.50, \text{ cm}$ $D_{30} = \text{volume median drop diameter, defined by the general ex-}$ pression $(D_{el})^{s-f} = \frac{\Sigma n D^s}{\Sigma n D^f}$ which gives $D_{bb} = \begin{bmatrix} \Sigma n D^b \\ \Sigma n \end{bmatrix}^{1/s}$

$$D_{30} = \begin{bmatrix} \Sigma n D^3 \end{bmatrix}^{1/s}$$

mean diameter notation

mean diameter notation

distance from tracking mirror to film plane, cm

M = magnification

= number of drops n

= constant Equation [4]

= volume fraction of drops having diameters < D

 $\Delta R = n D^3/\Sigma n D^3$

 V_d = drop velocity, fps

 $= ln (D/D^*)$ u

constant Equation [3]

tracking mirror speed, rps

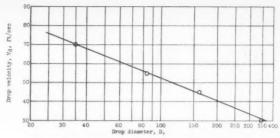
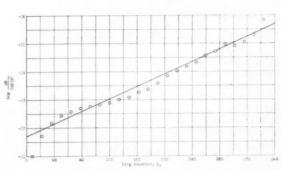


Fig. 2 Drop size and velocity data



Nukiyama-Tanasawa analysis of experimental drop size data; b = 0.0254, $D_{30} = 154 \mu$

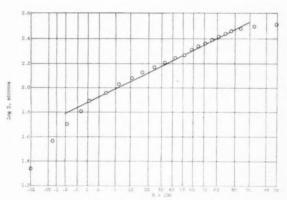


Fig. 4 Log probability analysis; $D^* = 187 \mu$, $D_{30} = 158 \mu$

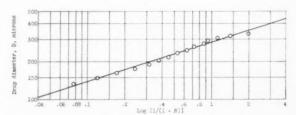


Fig. 5 Rosin-Rammler analysis; $q=3.2, \overline{D}=288 \mu, D_{30}=$

References

1 Priem, R. J. and Heidmann, M. F., "Vaporization of Propellants in Rocket Engines," ARS JOURNAL, vol. 29, no. 11, Nov. 1959, pp. 836-842.
2 Rossmann, T. G., "A High-Speed and High-Resolution Photographic Technique for the Observation of Propellants Injected into a Firing Combustion Chamber," Rep. 8007-981-008, Bell Aircraft Corp., May 1959.
3 Ingebo, R. D., "Photomicrographic Tracking of Ethanol Drops in a Rocket Chamber Burning Ethanol and Liquid Oxygen," NASA TN

D-290, June 1960.

APRIL 1961

Technical Notes

Some Comparisons of Sloshing **Behavior in Cylindrical Tanks** With Flat and Conical Bottoms1

H. NORMAN ABRAMSON² and GUIDO E. RANSLEBEN Jr.3 Southwest Research Institute, San Antonio, Texas

Some results obtained from sloshing experiments with rigid model cylindrical tanks in translation, and having both flat and conical bottoms, are discussed and compared. On the basis of both total force and wall pressure distribution measurements, it is concluded that sloshing behavior in tanks with conical bottoms can be represented quite adequately by an "equivalent" flat bottom (based on equal liquid volumes).

THE PRACTICALLY important problem of sloshing behavior in a cylindrical tank of circular cross section and having a conical bottom has recently been studied theoretically (1).4 This analysis is, however, limited to free oscillations, although the designer more frequently desires information applicable to forced oscillations. Because the sloshing characteristics of tanks with flat bottoms undergoing forced oscillations are readily available from theory (2-5). the question arises as to the possibility of utilizing theoretical flat bottom sloshing characteristics for tanks with nonflat bottoms. Of course, it is recognized that for extremely shallow liquid depths the bottom shape must govern the fluid motion, and that for relatively great liquid depths the bottom shape will not influence the fluid motion to any appreciable extent. In view of the latter fact, the question then becomes one of investigating sloshing behavior at moderately shallow depths to explore the possibility of utilizing theoretical results for the flat bottom case for problems involving nonflat bottoms, on the basis of an "equivalent" flat bottom tank having an equal liquid volume.

Using the notation of Fig. 1 we may define a tank with an equivalent flat bottom depth h_{rg} such that the liquid volumes are equal. Thus, assuming the liquid surface to be at the junction of the cylindrical wall and conical bottom

$$\frac{h_{eq}}{d} = \frac{h_0}{3d} = \frac{h_0}{6r_0} \tag{1}$$

Received May 23, 1960.

¹ The results presented in this paper were obtained during the course of research carried out under the sponsorship of the Army Ballistic Missile Agency, Contract no. DA-23-072-ORD-1251. Appreciation is expressed to the ABMA for permission to publish this paper, and to Luis R. Garza for his valuable assistance in the experimental work. experimental work.

Director, Department of Mechanical Sciences. Member ARS.

³ Senior Research Engineer, Department of Mechanical Sci-

⁴ Numbers in parentheses indicate References at end of paper.

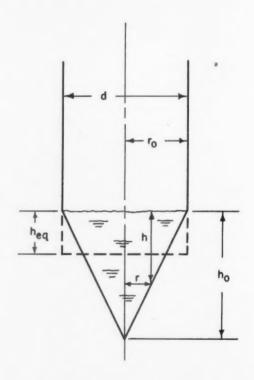
At higher surface levels, the equivalent flat bottom depth

$$\frac{h_{eq}}{d} = \frac{h_0}{6r_0} + \frac{h_1}{d}$$
 [2]

where h_1 is the height of the liquid surface above the junction of the cylindrical wall and conical bottom. On this basis. the natural frequencies for the conical bottom given in (1 are compared with corresponding values for the flat bottom given in (2), in Fig. 2. $d \omega_n^2/a$ is a dimensionless frequency parameter, where ω_n is the natural frequency and a is the acceleration in the direction of the tank longitudinal axis. The difference between the two theories is slight in the first, and generally the most important, mode, but increases somewhat in the higher modes, particularly at very shallow

Experimental Results

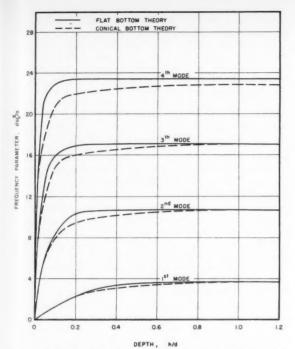
The test facility and measurement techniques employed to obtain the data reported here have been described elsewhere



$$h = h_0 (1 - r/r_0)$$

Fig. 1 Conical bottom and equivalent flat bottom

EDITOR'S NOTE: The Technical Notes and Technical Comments sections of ARS JOURNAL are open to short manuscripts describing new developments or offering comments on papers previously published. Such manuscripts are usually published without editorial review within a few months of the date of receipt. Requirements as to style are the same as for regular contributions (see masthead page).



th

2

n

t

Fig. 2 Comparison of flat and conical bottom natural frequencies

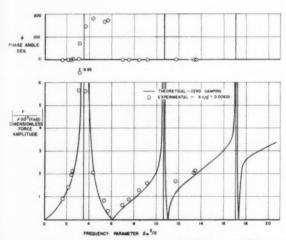


Fig. 3 Total force measurements for flat bottom model with $h/d\,=\,0.50$

(6). The models were mounted vertically and oscillated in the transverse direction. Two different sizes of tank models and two different liquids were employed in these experiments (6).

The results of total fluid sloshing force measurements are shown in Figs. 3–6, in terms of amplitude and phase angle ϕ , with ρ the fluid density and X_0 the excitation amplitude. The theoretical curves shown in each of these figures correspond to those for an equivalent flat bottom tank. Note that the liquid depth of h/d=0.25 (Fig. 6) corresponds to the liquid surface being approximately at the juncture of the conical bottom and the cylindrical wall, and thus represents a rather shallow condition (approximating the condition assumed in Fig. 1).

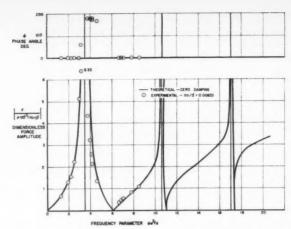


Fig. 4 Total force measurements for conical bottom model with $h/d\,=\,0.50$

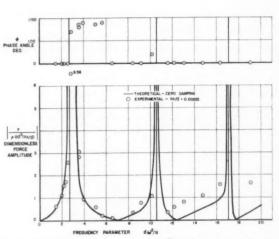


Fig. 5 Total force measurements for flat bottom model with h/d=0.25

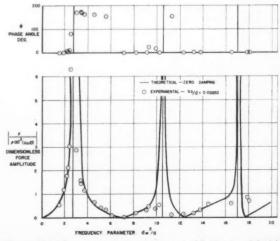


Fig. 6 Total force measurements for conical bottom model with $h/d\,=\,$ 0.25

The results of wall pressure distributions for both flat and conical bottoms at h/d = 0.50 are shown in Figs. 7 and 8 for two values of the frequency parameter.5 h' represents the

⁵ A more detailed study of pressure distributions during sloshing is given in a separate paper in this issue of ARS JOURNAL (pp. 545-547).

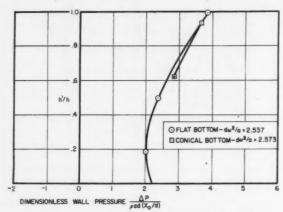


Fig. 7 Comparison of wall pressure distributions for flat and conical bottoms at $d\omega^2/a \approx 2.5$, h/d = 0.50

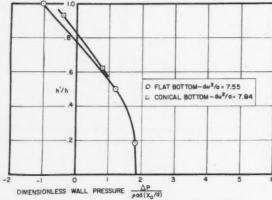


Fig. 8 Comparison of wall pressure distributions for flat and conical bottoms at $d\omega^2/a \approx$ 7.7, h/d= 0.50

height from the equivalent flat bottom to the point at which the pressure is measured.

The data presented in Figs. 3-8 are intended to be only representative examples of a vast amount of data collected as part of a more general research program. However, no data were collected for h/d values less than 0.25, and no reliable pressure distribution data were obtained for h/dless than 0.50. It may be of interest to note that the comparisons between measured total force and integrated pressure distributions almost invariably showed agreement within less than 10%, and usually within only a very few per cent.

The total force data of Figs. 3-6 show generally excellent agreement with the equivalent flat bottom theory, at least through the second mode. It is clear that even at the rather shallow depth of h/d = 0.25, the agreement between the measured total force and the flat bottom theory is quite good.

The wall pressure distribution data of Figs. 7 and 8 show that the conical bottom data are virtually identical to the flat bottom data, at least to the depth of the lowest pressure cell (h'/h = 0.620). It is unfortunate that no pressure data are available for h/d < 0.50; however, on the basis of the total force measurements there is no reason to expect that the agreement would not continue to be quite good, at least down $t_0 h/d = 0.25$.

Conclusions

It appears from the experimental data presented here and obtained under the test conditions described, that there is ample justification for the use of an equivalent flat bottom theory to describe sloshing behavior in tanks with nonflat bottoms, except for relatively shallow fluid depths $(h/d \ll$ 0.50). This conclusion appears to be valid at least through the second mode, and possibly through the third. This knowledge should be of extreme value during the design stage of new configurations.

References

- 1 Lawrence, H. R., Wang, C. J. and Reddy, R. B., "Variational Solution Fuel Sloshing Modes." Jet Propulsion, vol. 28, no. 11, Nov. 1958, pp. 729-736.

- 729-736.

 Bauer, H. F., "Fluid Oscillations in a Circular Cylindrical Tank," ABMA Rep. no. DA-TR-1-58, April 1958.

 Miles, J. W., "On the Sloshing of Liquid in a Cylindrical Tank," Rano-Wooldridge Corp., Rep. AM 6-5, April 1956.

 Kachigan, K., "Forced Oscillations of a Fluid in a Cylindrical Tank," Convair Rep. ZU-7-046, Oct. 1956.

 Schmitt, A. F., "Forced Oscillations of a Fluid in a Cylindrical Tank Undergoing Both Translation and Rotation," Convair Rep. ZU-7-069, Oct. 1958.
- 6 Abramson, H. N. and Ransleben, G. E., Jr., "Simulation of Fuel Sloshing Characteristics in Missile Tanks by Use of Small Models," ARS JOURNAL, vol. 30, no. 7, July 1960, pp. 603–612.
- ⁰ At h/d = 1.00, similarly excellent agreement was obtained, with the location of the lowest pressure cell at h'/h = 0.30.

Wall Pressure Distributions During Sloshing in Rigid Tanks¹

H. NORMAN ABRAMSON² and GUIDO E. RANSLEBEN Jr.³ Southwest Research Institute, San Antonio, Texas

Some measurements of wall pressure distributions obtained during sloshing experiments with rigid model cylindrical tanks having flat bottoms and excited in translation are presented and discussed. Total force and moment, obtained by integration of the measured pressures, and the pressure distributions themselves are compared with theoretical predictions.

Pressure Distributions

hich

only

no

no

h/d ari-

ure

him

ent

ast ler he

od.

he

r

to

a

10

n

KNOWLEDGE of wall pressure distributions resulting from fuel sloshing in missile tanks is important for understanding the flow mechanisms involved and for structural design studies. It does not appear that measured pressure distributions have previously been reported in the literature.

The test facility and measurement techniques employed to obtain the data reported here have been described elsewhere (1).4 The models were mounted vertically and oscillated in the transverse direction.

The results of wall pressure measurements are shown in Figs. 1–4. Fig. 1 is a plot of pressure distributions on the wall and flat bottom at various frequencies, and Fig. 2 is a cross plot showing pressure vs. frequency at various depths in the liquid. Figs. 3 and 4 present similar data for a different liquid level. Pressures and frequencies are given in non-dimensional form (1), where a is the acceleration in the direction of the tank longitudinal axis and other symbols are defined on the figures. It may be mentioned in passing that the bottom shape has little influence on wall pressures, except possibly at extremely small liquid depths (2) (h/d < 0.25).

Some interesting observations may be made from the results shown in Figs. 1–4. It appears that approximately the lower third of the liquid behaves essentially as a rigid mass, while most of the sloshing effects occur near the surface, as has been predicted theoretically, and qualitatively observed experimentally. This is, in fact, the basis upon which some of the various mechanical analogies involving spring-mass or pendulum systems are founded (3). It may be possible to employ such pressure distributions to assist in arriving at the optimum arrangement of, and parametric values for, such analogous systems.

Figs. 1 and 2 may also help to explain a peculiarity observed during the test program, which occurred in the frequency range from the resonant frequency of the first mode to the frequency at which the total force passes through zero, between the first and second modes $(d\omega^2/a \approx 3.7-4.7$ for h/d=1.00, Fig. 1). Just below the latter frequency the pressure traces all showed a distortion of the peaks in one direction only. As the frequency was decreased to the first resonance, this distortion grew to the point that the pressure-

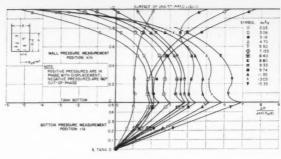


Fig. 1 Wall pressure distributions (h/d = 1.00)

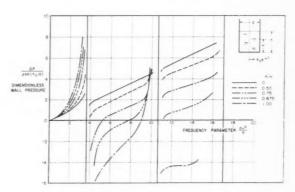


Fig. 2 Wall pressure distributions (h/d = 1.00)

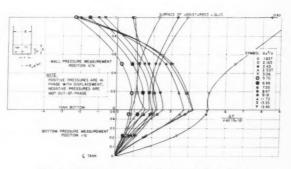


Fig. 3 Wall pressure distributions (h/d=0.50)

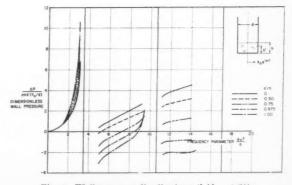


Fig. 4 Wall pressure distributions (h/d=0.50)

Received May 26, 1960.

¹ The results presented in this paper were obtained during the course of research carried out under the sponsorship of the Army Ballistic Missile Agency, Contract no. DA-23-072-ORD-1251. Appreciation is expressed to the ABMA for permission to publish this paper, and to Luis R. Garza for his valuable assistance in the experimental work.

experimental work.

² Director, Department of Mechanical Sciences. Member ARS.

Senior Research Engineer, Department of Mechanical Sciences.
 Numbers in parentheses indicate References at end of paper.

time traces appeared to be almost sinusoidal, but of twice the exciting frequency. Examination of the pressure distributions at frequencies between the first and second modes (Fig. 1) shows that pressures near the surface are 180 deg out of phase with those near the bottom (which are in phase with the displacement) over a significant portion of this range. Indeed, the distribution at $d\omega^2/a = 4.70$ shows such a balance of the in- and out-of-phase portions and that the re-

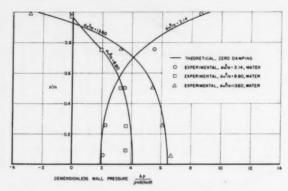


Fig. 5 Comparison of theoretical and experimental wall pressure distributions (h/d=1.00)

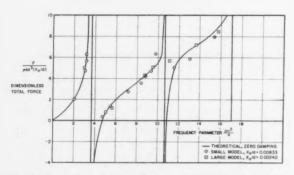


Fig. 6 Force from integrated pressure distribution (h/d=1.00)

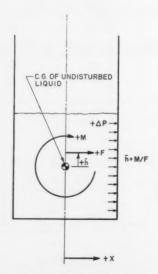


Fig. 7 Sign convention

sulting total force is near zero, although actual pressure magnitudes, near the surface especially, are relatively high-A similar situation exists betwen the higher modes. It ie probable that shearing action between the layers of liquiss which are moving in opposite directions introduces the distortion noted in the range where the out-of-phase portion dilarger in magnitude than the in-phase portion.

The distortion of the pressure signals previously discussed was reflected by only a slight distortion of the total force signal, which, when reduced, provided very good correlation with theory, even in this frequency range.

A comparison of theoretical (4) and experimental (Figs. 1 and 2) wall pressure distributions is given in Fig. 5 for h/d = 1.00; the agreement is excellent. Similar agreement was obtained for a fluid depth corresponding to h/d = 0.50.

Total Force and Moment

For the purpose of integrating the pressures from bottom to surface, it was assumed that the shapes of the radial pressure distributions remain constant from bottom to surface. This was justified by the fact that measured variation of bottom pressures and radial wall pressures at one height indi-

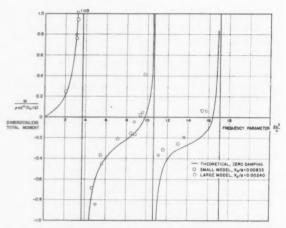


Fig. 8 Moment about c.g. of undisturbed liquid from integrated pressure distributions (h/d = 1.00)

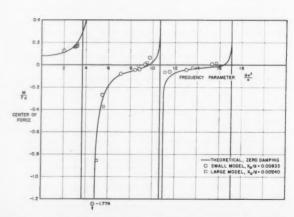


Fig. 9 Center of force from pressure distributions (h/d = 1.00)

cated the same shape. The total forces obtained by integration were compared with measured total force over a wide frequency range: agreement was consistently within 10%. A comparison of total force obtained by integration of the data of Fig. 1 with theoretical predictions (4) is given in Fig. 6.

re

h-

ie

22

di

d

e

n

A similar comparison between integrated experimental values and theory for moment about the center of gravity of the undisturbed liquid, with the notation of Fig. 7, is given in Fig. 8, and shows agreement with theory equally as good as that for force. Dividing moment by force to obtain the location of the force center (Fig. 9) shows, in turn, equally good agreement with theory.

Results obtained from a similar study of data corresponding to h/d = 0.50 showed essentially the same agreement with theory for both force and moment.

References

1 Abramson, H. N. and Ransleben, G. E., Jr., "Simulation of Fuel Sloshing Characteristics in Missile Tanks by Use of Small Models," ARS JOURNAL, vol. 30, no. 7, July 1960, pp. 603-612.

2 Abramson, H. N. and Ransleben, G. E., Jr., "Some Comparisons of Sloshing Behavior in Cylindrical Tanks With Flat and Conical Bottoms," ARS JOURNAL, vol. 31, no. 4, April 1961, pp. 542-544.

3 Abramson, H. N., Chu, W. H. and Ransleben, G. E., Jr., "Representation of Fuel Sloshing by Means of an Equivalent Mechanical Model," Tech. Rep. no. 8, Contract no. DA-23-072-ORD-1251, Southwest Research Institute. June 1960. tute, June 1960.

4 Bauer, H. F., "Fluid Oscillations in a Circular Cylindrical Tank," ABMA Rep. no. DA-TR-1-58, April 1958.

Fluidized Solids as a Nuclear Fuel for Rocket Propulsion

L. P. HATCH, W. H. REGAN² and J. R. POWELL³

Brookhaven National Laboratory, Upton, N. Y.

THE APPLICATION of the energy of atomic fission to high thrust rocket propulsion systems may well require nuclear reactor capabilities in excess of 15,000 megawatts. This power level is more than an order of magnitude higher than the design capacities of the largest reactors presently contemplated for use in the production of electrical energy. The transfer of heat, at the very high rates and fluxes, from the nuclear fuel to the propellant gas at temperatures bordering on 6000 F and without serious loss of fuel to the propellant poses one of the most challenging problems in the design of nuclear rocket propulsion systems (1).4

Use of the more conventional type of rigid solid fuels has the great advantage of simplicity but presents the difficulty of providing sufficient heat transfer surface while maintaining structural integrity in the fuel element assemblies. Use of the gaseous form of nuclear fuel with provision for thorough admixing of fuel and propellant would give outstanding advantages in that heat transfer would be virtully instantaneous and temperature limitations would be imposed by the conditions at the container walls and not by those existing in the reactor core. A major difficulty in the use of the gaseous fuel, however, would be to obtain efficient separation of the fuel and the propellant and, thus, to restrain the fuel in the reactor core. With the inherent problems of these two types of reactor systems in mind, it is proposed to consider the possibility of using fuel in the form of solid granular particles maintained as a fluidized bed wherein very high surface area would be available for heat transfer and structural strength problems would be eliminated.

Normally a fluidized bed is established by passing a fluid through a bed of solid particles in a direction opposite to that of the force of gravity and at such velocities that the entire bed of particles is expanded and held in a state of suspension while the fluid passes on. The rate of flow of the fluid in this system is limited to velocities such that the drag forces do not exceed the normal weight of the particles. However, if the unit should be rotated in a circular path about an external point lying downstream on the axis, the velocity required to maintain the bed in a fluidized state would be increased in re-

lation to the number of g's imposed on the system. Thus, it would seem possible to have the propellant flowing through such a rotating bed of fuel particles with sufficient velocities to meet the requirements for high thrust rocket propulsion systems. A practical arrangement would be to establish a continuous bed in the form of a rotating cylindrical annulus. Two ways in which such a bed of fuel particles could be maintained are by tangential flow of propellant into a cavity reactor core and by having a rotating core vessel and radial flow of propellant through the porous walls.

Very small scale experiments have been carried out to determine some of the simple performance characteristics of fluidized beds rotating at speeds up to 2000 rpm. With a 2-in. diameter chamber as shown in Figs. 1, wherein the gas enters the bed radially through the porous walls of the inner chamber, about 100 g's were imposed on the system. The three views show the apparatus in various stages of operation: Fig. 1a, at rest; 1b, rotation at 2000 rpm with the particle bed already established but without gas flow; and 1c, rotation with gas flow and the bed in the expanded fluidized state.

Under the alternative concept in which the bed of particles would be rotated by means of tangential entry of propellant to the core chamber, the system would be greatly simplified mechanically since no rotating core vessel would be required. However, in this design the problem of establishing and maintaining a uniform and stable bed is a crucial one.

From the standpoint of mechanical performance, at least, the rotating fluidized bed concept appears to be useful in the development of nuclear rocket propulsion. Advantages to be gained through the use of fluidized particulate fuels include the following:

Large surface to volume ratio, thus providing for the transfer of heat to the propellant under the very high fluxes with relatively low temperature differentials and consequently with higher exit propellant temperatures.

2 Requirements for the fuel bearing material would be centered mainly on high temperature stability factors without serious concern for structural strength and fabrication problems.

3 Feasibility of fuel addition during operation to make up for such losses as might be incurred because of volatilization and reaction between fuel particles and propellant.

4 High degrees of separation between fuel particles and propellant under high velocity flow.

If one were to think in terms of a specific impulse of 1000 sec with a corresponding exit temperature for hydrogen of about 5400 F, using the particulate form of fuel, the choice of uranium bearing material would appear to be limited to solid solutions of uranium carbide in the carbides of tantalum, zirconium and columbium. Of the three materials, zirconium carbide (mp 6400 F) is the most suitable for a thermal reactor because of its low neutron capture cross section and, therefore, has been selected for purposes of this discussion.

Presented at the ARS Semi-Annual Meeting, Los Angeles,

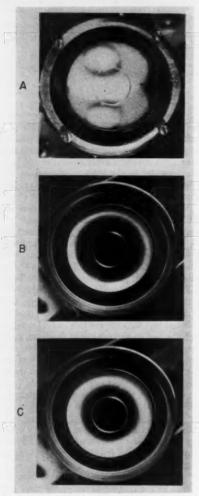
Calif., May 9–12, 1960.

¹ Sanitary Engineer.

² Associate Chemical Engineer.

Associate Nuclear Engineer ⁴ Numbers in parentheses indicate References at end of paper.

Let us assume a system capable of producing a thrust of 1,000,000 lb. This would require a propellant (hydrogen) flow rate of 1000 lb per sec and a reactor power of 25,000 megawatts, or, a heat transfer rate of 8.5×10^{10} Btu per hr. Assuming a heat transfer coefficient of 1000 Btu per ft² × hr × deg F and a Δt of 500 F, the required heat transfer area is on the order of 170,000 ft2. This amount of surface area would be available in a bed of 100 µ particles making up a 7-ft -long



Figs. 1a, 1b, 1c Rotating fluidized bed

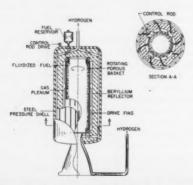


Fig. 2 Illustration of rotating chamber concept

cylindrical annulus with an outer diameter of 3 ft and 6 in. and an inner diameter of 2 ft and 11 in. (bed depth = $3\frac{1}{2}$ in.). A bed of these dimensions was used as a basis of analysis of the nuclear, fluid flow and heat transfer aspects of the two conceptual designs, one of which is shown in Fig. 2. The maximum radial component of velocity in the core for the propellant flow of 1000 lb per sec would be on the order of 450 fps. Drag forces of the 100μ particles would be such as to require some 2000 g's in order to prevent entrainment in the exit gas which would be achieved by rotation of the bed at the rate of 2000 rpm.

These reactors are of the "cavity" type; i.e., the fuel is in a nonmoderated core surrounded by an external moderatorreflector. Calculation techniques are based on those developed by Safonov (2). These are satisfactory for a preliminary survey, but better methods are needed for a detailed

Critical masses and neutron lifetimes were calculated for the rotating core vessel and tangential inlet cases.

The fuel was chosen to be U238 (100%). Its high value of (2.28) substantially reduced fuel inventory. In fact, it is doubtful whether the rotating core vessel design could be made thermally critical on U235.

The moderator-reflector is beryllium metal. The thickness of the reflector was chosen to be 18 in., a reasonable compromise between the wish to save reflector weight, and to keep critical mass low. The total reactor weight neglecting the pressure shell is approximately that of the reflector plus 2200 lb of UC-ZrC fuel mixture. This is about 21,000 lb for both

The following assumptions had to be made in carrying out the calculations:

- Neutron spectrum is thermal-there wili be some epithermal fission, which should tend to reduce the required critical mass.
- 2 The actual cylindrical core is nuclearly equivalent to a spherical reactor of the same bare buckling.
- 3 The neutron poisoning effect of the steel and ZrC can be included in a modified η (fast neutrons produced per thermal neutron absorbed) of the fuel.
- 4 The fuel is distributed uniformly through the cavity instead of in an annular ring. This will tend to slightly overestimate critical mass.
- 5 The rocket operates for such a short time that there is no fission product poisoning or depletion of fuel by burnout.
- 6 Neutron streaming in the void channels of the reflector will increase the calculated critical mass by the ratio of reflector area plus void area to reflector area minus void area. This should be adequate for small void areas.

The results are:

Rotating vessel Tangential inlet Critical mass U233, kg 66 33 2.9×10^{-4} Neutron lifetime, sec 1.3×10^{-4}

The critical masses and lifetimes are reasonable. It would be economically desirable to have a very low critical mass since the fuel is not recoverable, but these values, though high, are satisfactory. The uranium accounts for about 5% of the fuel bed weight.

Theoretically one would need no excess reactivity, since fission product poisoning and fuel burnup are negligible, but, since the fuel is in a mobile state, some should be included to keep the reactor critical in configurations slightly off the optimum.

Control will be by means of control rods in the reflector, probably of the rotating drum type.

References

- 1 Rom, F. E., "Advanced Reactor Concepts for Nuclear Propulsion," ASTRONAUTICS, vol. 4, no. 10, 1959, p. 20.
 2 Safonov, G., "The Criticality and Some Potentialities of 'Cavity' Reactors," RM-1520, Rand Corp., Santa Monica, Calif., July 1955.

Optical Refraction With Emphasis on Corrections for Points Outside the Atmosphere1

DUANE C. BROWN²

Instrument Corp. of Florida, Melbourne, Fla.

NA RECENT paper Wasel (1)3 presented a theory of atmospheric refraction which parallels in some respects that developed by the present writer (2) and employed at the Atlantic Missile Range since 1956 for the reduction of ballistic camera plates. The object of this note is to point out a major simplification, not considered in Wasel's treatment, which becomes possible for points sensibly outside Earth's atmosphere (as far as optical refraction is concerned, the atmosphere may be considered to end at an altitude of about 50 km). This simplified theory is particularly applicable to satellite observations. The problem of refraction for observations made at the satellite is also considered.

Statement of the Problem

in.

1.).

of

wo

he

he

of

28

ed

The effect of atmospheric refraction is illustrated in Fig. 1. Earth is regarded as a sphere with center at C, the geocentric radius to a terrestrial observer at 0 is r_0 ; the broken curve 0Prepresents the trajectory of light between 0 and a point P at an altitude h' above 0. The density of the atmosphere is assumed to be a function of altitude only and is therefore independent of azimuth; it follows that the ray path 0P lies in the plane OCP. The following quantities are defined in the

= angle subtended at center of Earth by 0 and P

= true zenith distance of P from 0

= apparent zenith distance of P from 0

= true nadir distance of 0 from P

= apparent nadir distance of 0 from P

= angle between zenith at 0 and tangent to ray path

The refraction for a terrestrial observer at 0 is

$$\delta \zeta_0 = z - \zeta_0 \tag{1}$$

and that for an aerial observer at P is

$$\delta \zeta_0' = z' - \zeta_0'$$

The problem of refraction for a terrestrial observer may be stated as follows: Given the apparent zenith distance ζ_0 of P, the altitude h' of P, and the index of refraction μ as a function of altitude, determine the true zenith distance z. It will be shown that the solution to the corresponding problem for an aerial observer can be obtained from the solution for the terrestrial observer.

Refraction Corrections for Terrestrial Observer

Smart (3) has shown that the astronomical refraction $R(\zeta)$ corresponding to an apparent zenith distance \(\zeta_0 \) is given by

$$R(\zeta_0) = r_0 \mu_0 \sin \zeta_0 \int_1^{\mu_0} \frac{d\mu}{\mu [(r_0 + h)^2 \mu^2 - (r_0 \mu_0 \sin \zeta_0)^2]^{1/2}}$$
[3]

in which μ_0 is the index of refraction at 0. It follows from Smart's derivation that the angle \(\zeta_0^* \) may be expressed as

$$\zeta_0^* = \zeta_0 + r_0 \mu_0 \sin \zeta_0 \int_{\mu \omega'}^{\mu \omega} \frac{d\mu}{\mu [(r_0 + h)^2 \mu^2 - (r_0 \mu_0 \sin \zeta_0)^2]^{1/2}}$$
[4]

Received July 25, 1960.

¹ This research was supported by the Air Force Research and Development Command under Contract AF 08(606)-3413.

Associate Director, Research and Analysis.
 Numbers in parentheses indicate References at end of paper.

in which μ_0 is the index of refraction at P. From Fig. 1 it is seen that

$$\zeta_0^* = \theta + \zeta_0' \tag{5}$$

and from Snell's law for spherical refraction [Smart (3)] it follows that

$$(r_0 + h')\mu_0' \sin \zeta_0' = r_0\mu_0 \sin \zeta_0$$
 [6]

As a consequence of the last three equations

$$\theta = \zeta_0 - \sin^{-1} \left[\frac{r_0 \mu_0}{(r_0 + h') \mu_0'} \sin \zeta_0 \right] +$$

$$r_0 \mu_0 \sin \zeta_0 \int_{\mu_0'}^{\mu_0} \frac{d\mu}{\mu [(r_0 + h)^2 \mu^2 - (r_0 \mu_0 \sin \zeta_0)^2]^{1/2}}$$
[7]

With θ thus determined, triangle 0CP in Fig. 1 may be solved for the true zenith distance z

$$\tan z = \frac{(r_0 + h')\sin \theta}{(r_0 + h')\cos \theta - r_0}$$
 [8]

If P is outside the atmosphere, $\mu_0' = 1$ and the integral term in Equation [7] becomes equivalent to the astronomical refraction Equation [3]; θ may then be expressed

$$\theta = \zeta_0 + R(\zeta_0) - \sin^{-1} \left[\frac{r_0 \mu_0}{(r_0 + h')} \sin \zeta_0 \right] \qquad (h' > 50 \text{ km})$$
[9]

As is shown in (2) this result may also be derived from the alternative integral expression for θ employed by Wasel (1).

Determination of Astronomical Refraction

Equation [9] is of particular significance in missile and satellite photogrammetry, because it shows that refraction for points outside the effective atmosphere can be expressed in terms of astronomical refraction which, in turn, can be determined to a high degree of accuracy (2). In many applications a standard formula such as that suggested by Wasel (1) may be entirely adequate. When the utmost accuracy is re-

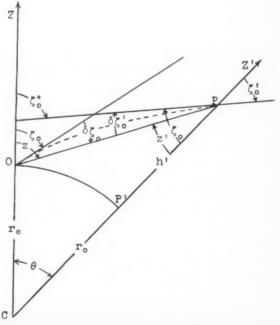


Fig. 1 Geometry of atmospheric refraction

quired, one may employ photogrammetric observations of background stars for an accurate determination of the coefficients of astronomical refraction; alternatively, the method described by Smart (3) of observing zenith distances of selected stars at upper and lower culmination may be employed. When a profile of the index of refraction is available from meteorological soundings, Equation [3] may be integrated numerically to produce a refraction table for selected zenith distances; accurate coefficients of refraction may then be extracted from the table by means of a least squares fit of a suitable expansion of astronomical refraction. It is shown in (2) that four terms of an expansion derived by Garfinkel (4) are sufficient to provide accuracies (in the sense of agreement with the results of ray tracing by numerical integration) of 0,2" of arc or better for zenith distances as great as 90 deg; the expansion, in fact, retains its validity even for zenith distances in excess of 90 deg. It is noteworthy that Equations [7, 8 and 9] are valid for all zenith distances and thus may be employed for points near the horizon.

Refraction Corrections for Aerial Observer

Fig. 1 illustrates that the true nadir distance of 0, as observed at P, is given by

$$z' = z - \theta \tag{10}$$

Since it has been established that if ζ_0 is known θ and z may be determined from Equations [7 and 8], the problem of refraction for an aerial observer may be reduced to one of determining 50 from the apparent nadir distance 50' observed at This is immediately accomplished by the application of Snell's law (Eq. [6]) which gives

$$\zeta_0 = \sin^{-1} \left[\frac{(r_0 + h')\mu_0'}{r_0\mu_0} \sin \zeta_0' \right]$$
 [11]

It follows, then, that except for the additional steps, Equations [10 and 11], the computations for aerial refraction reduce to those for terrestrial refraction. Again, if P is outside the atmosphere so that $\mu_0'=1$, Equation [9] may be used to compute θ ; in this case the formula for θ reduces to

$$\theta = \zeta_0 + R(\zeta_0) - \zeta_0'$$
 $(h' > 50 \text{ km})$ [12]

The simplicity of these results together with their validity for all zenith (or nadir) distances makes them well suited to the reduction of photographs taken from a satellite.

Final Considerations

It is pointed out in (2) that inasmuch as the true altitude h' is required in the foregoing formulas it is necessary to perform an iterative cycle of computations in applying refraction corrections. First, an approximate value of h' is employed in the formulation to obtain initial corrections for refraction; these are applied, and the resulting improved directions are used in a fresh determination of h' (e.g., by triangulation from two or more stations). The new h', in turn, is used to produce second approximations to the refraction corrections. The iteration is continued until sufficiently stable corrections are attained. For zenith distances less than 70 deg the initial corrections usually require no further improvement; however, with increasing zenith distances the process of iteration becomes increasingly important.

Conclusions

The differential refraction between points outside the effective atmosphere and corresponding occluded stars is essentially parallactic. Accordingly, the problem of correcting such points for atmospheric refraction reduces fundamentally to one of determining astronomical refraction. The accuracy of the corrections therefore depends primarily upon the accuracy of the determination of astronomical refraction. Sophisticated observational and reductional techniques permit astronomical refraction, even for very low elevation angles, to be determined to a degree of accuracy wholly sufficient for whatever optical system is used in its determination.

References

1 Wasel, A. D., "Refraction Correction Techniques in Earth Satellite Optical Tracking for Precision Prediction," ARS JOURNAL, vol. 30, no. 3, March 1960, pp. 282-284.

2 Brown, D. C., "A Treatment of Analytical Photogrammetry with Emphasis on Ballistic Camera Applications," RCA Data Reduction Technical Rep. no. 39, Aug. 1957, ASTIA Document no. 124144, pp. 33-51.

3 Smart, W. M., "Textbook on Spherical Astronomy," Cambridge University Press, N. Y., 1956, 4th ed., pp. 62-65, 68, 69.

4 Garfinkel, B., "An Investigation in the Theory of Astronomical Refraction," Astron. J., vol. 50, no. 8, Feb. 1944, pp. 169-179.

Simple Method for Estimating First-Stage Boost Thrust and Specific Impulse

ROBERT L. DOEBLER¹

Los Angeles Div., North American Aviation, Inc., Los Angeles, Calif.

In preliminary design work, where detailed studies are not required, it is often sufficient to use methods which give reasonably accurate results rapidly. Based upon the basic rocket thrust equation, a simple method is derived to produce the thrust or specific impulse vs. altitude characteristic of a liquid propellant or neutral burning solid propellant rocket engine. This method has much utility in preliminary design trajectory studies on high speed digital or analog computers. The method has accuracy well within the range quoted for performance by rocket engine manufacturers, and predicts performance independent of knowledge of propellants, thrust chamber pressure, or nozzle area ratio.

Assumptions and Notation

The basic rocket thrust equation is

$$F_{\text{alt}} = (W_p/g)Vel_s + A_s(P_s - P_{\text{alt}})$$
[1]

where

 $F_{\text{alt}} = \text{thrust at any altitude, lb}$

 W_p propellant flow rate, lb per sec

gravitational constant, ft per sec2

Vel_e = nozzle exit velocity, fps

 $A_{\mathfrak{e}} = \text{nozzle exit area, ft}^2$

 P_s nozzle exit static pressure, lb per ft2

 P_{alt} = ambient pressure at any altitude, lb per ft²

For rocket engines used for first-stage boost, the nozzle is usually fully expanded at some low altitude. If the assumption is made that this full expansion occurs at sea level, then $P_a = P_{SL}$ and Equation [1] for sea level becomes

$$F_{SL} = (W_p/g)Vel_e$$
 [2]

Substituting this expression into the basic rocket thrust equation

$$F_{\text{alt}} = F_{SL} + A_s(P_{SL} - P_{\text{alt}}) \tag{3}$$

This equation can be written for thrust in vacuum, noting that

Received May 26, 1960. ¹ Senior Engineer, Advance Design.

ambient pressure in vacuum is approximately zero, therefore

$$F_{\infty} = F_{SL} + A_{\epsilon}(P_{SL}) \tag{4}$$

where $F \infty$ is the thrust in vacuum, in pounds.

or

1e

18

0

Equation [4] may be subtracted from Equation [3] leaving

$$F_{\rm alt} = F_{\infty} - P_{\rm alt} A_{\rm e}$$

If Equations [4 and 5] are solved simultaneously, A. is eliminated. After some algebraic manipulation the resulting equation is

$$F_{\rm alt} = (1 - P_{\rm alt}/P_{SL})(F_{\infty} - F_{SL}) + F_{SL}$$
 [6]

For liquid propellant or neutral burning solid propellant boost rocket engines, propellant flow rate is approximately constant for all altitudes. Propellant flow rate may be ex-

$$W_p = \frac{F_{\text{alt}}}{I_{s,u}} \tag{7}$$

where I_{alt} is the specific impulse at any altitude, in seconds.

Equation [7] indicates that for constant propellant flow rate, specific impulse varies with altitude in the same way that thrust varies or

$$I_{s_{\text{alt}}} = (1 - P_{\text{alt}}/P_{SL})(I_{s_{\infty}} - I_{s_{SL}}) + I_{s_{SL}}$$
 [8]

Application of Equations

For use in computing equipment, it is convenient to curve-fit the parameter $(1-P_{\rm alt}/P_{SL})$ vs. altitude. To utilize Equations [6 and 7], the only input data required is the sea level static and vacuum thrust and specific impulse, which are the performance data points most readily available from rocket engine manufacturers.

As an illustration of the use of the foregoing equations, assume the following hypothetical rocket engine. Given:

$$\begin{array}{ll} F_{sL} = 200{,}000 \;\; {\rm lb} \\ F_{\infty} = 232{,}000 \;\; {\rm lb} \\ I_{^sSL} = 260 \; {\rm sec} \end{array}$$

Find: $F_{40,000'}$ and $I_{^{8}40,000'}.$ Applying Equations [6 and 7] $F_{40,000'} = (1-391.68/2116.22)(232,000-200,000) + 200,000$

 $F_{40,000'} = (0.8149)(32,000) + 200,000 \text{ lb}$

 $F_{40,000'} = 226,077 \text{ lb}$ $W_p = 200,000/26$ = 200,000/260 = 769.2 lb per sec

 $I_{s_{40,000}} = F_{40,000}/W_p = 226,077/769.2 = 293.9 \text{ sec}$

Conclusion

For preliminary design studies on boost trajectories, the preceding method may be used to predict thrust or specific impulse vs. altitude performance without any knowledge of propellants, thrust chamber pressure or nozzle area ratio. The value of this method lies in its utility, its simplicity and its accuracy. In studies utilizing this method the performance produced has been within $\pm 1\%$ of engine manufacturers data.

Acknowledgment

The author wishes to acknowledge the assistance of Charles Price and George Fair of the Los Angeles Division of North American Aviation, Inc.

An Approach to Problem of Optimum Rocket Trajectories¹

SAMUEL E. MOSKOWITZ² and LU TING³

Polytechnic Institute of Brooklyn, Freeport, N. Y.

N APPLICATION to questions of minimum time and maximum altitude, for which some technique of numerical integration is employed, the problem is usually converted into an initial value problem with two families of an infinite number of parameters $\lambda_1(x_1)$ and $\lambda_2(x_1)$. The computations, however, can be simplified considerably if zero is used as the initial value for the multiplier associated with a kinematic condition; i.e., $\lambda_2(x_1) = 0$, with the assumption that the aerodynamic forces are small only in a finite interval at the beginning of the optimum flight duration, and if the terms of $O(\epsilon)$ in the entire flight interval are neglected in the Euler-Lagrange equations. The resulting governing equations will not only be less complicated but there will be only one family of infinite parameters with which to deal. Using these approximations, the result will differ from the exact value by $O(\epsilon^2)$.

Problems Defined

In the field of space mechanics, it is frequently necessary to minimize or maximize some arbitrary function of the problem variables. Space flight problems, in particular, involve

such questions as: What are the performance characteristics of a class of solutions typifying the shortest time of powered flights or maximum altitude? These problems have their principal variables in common which, in the time-description of the extremizing path, satisfy certain constraints in the form of equations of motion and kinematic conditions. They consequently belong to the class of problems known as multidimensional, nonlinear boundary value problems of a variational nature (1).4

Formulation

We seek, in general, to extremize the definite integral

$$J = \int_{1}^{2} F(v, \gamma, h) dx$$
 [1]

with respect to continuously differentiable functions v = v(x), $\gamma = \gamma(x), h = h(x)$ which are subject to the constraints

$$G = G(v, \gamma, h, v', \gamma', h', x) = 0$$
 [2]

$$H = H(v, \gamma, h, v', \gamma', h', x) = 0$$
 [3]

where the prime denotes differentiation with respect to x.

It would be advantageous to arrange the governing equations in a form such that the problem is essentially one of rendering stationary the integral

$$I = \int_{1}^{2} (F + \lambda_{1}G + \lambda_{2}H)dx \qquad [4]$$

An explicit representation of these problems is

$$F \equiv \frac{R_1 + h(\vartheta)}{v(\vartheta) \cos \gamma(\vartheta)} \quad \text{with } x = \vartheta$$
 [5]

⁴ Numbers in parentheses indicate References at end of paper.

Received Nov. 29, 1960. ¹ This research was supported by the United States Air Force through the Air Force Office of Scientific Research, Air Research and Development Command, under Contract no. AF 49(638)-445, Project no. 9781.

Research Associate.
 Research Professor, Aeronautical Engineering.

$$H \equiv [R_1 + h(\vartheta)] \tan \gamma(\vartheta) - h'(\vartheta) = 0$$
 [6]

for the problem of minimum time and

$$F \equiv v(t) \sin \gamma(t)$$
 with $x = t$ [7]

$$H \equiv v(t) \sin \gamma(t) - h'(t) = 0$$
 [8]

for one of maximum altitude. The constraint G is formed by combining equations of motion and auxiliary relations with a kinematic condition, whereas H is equivalent to the remaining kinematic condition.

The extremizing functions $v^*(x)$, $\gamma^*(x)$, $h^*(x)$, $\lambda_1^*(x)$ and $\lambda_2^*(x)$ must identically satisfy the system of Equations [see (2)]

$$E_{\nu}(F + \lambda_1 G + \lambda_2 H) = 0$$
 [9]

$$E_{\gamma}(F + \lambda_1 G + \lambda_2 H) = 0$$
 [10]

$$E_{h}(F + \lambda_{1}H + \lambda_{2}H) = 0$$
 [11]

$$G = 0 ag{12}$$

$$H = 0 ag{13}$$

The Approximate Method

A scrutiny of G would reveal some measure of significance, for we would find that some terms remain relatively small in magnitude throughout their time histories. Viewed in a light of engineering precision, it would appear reasonable to assume that any justifiable simplification would not significantly affect the value of the extremum. Indeed, it has been proved (3) that if terms $O(\epsilon)$, $\epsilon \ll 1$, are omitted from the Euler-Lagrange differential equations, but retained in the accompanying constraint equations, the resulting error in extremum would be of $O(\epsilon^2)$. Therefore we may, with some confidence, neglect the smaller terms if they remain unimportant throughout the time interval. The effect of Earth's curvature, Coriolis and centrifugal inertia forces due to Earth's rotation, angle of sideslip, and dependence of the polar-angular rate on altitude are examples of effects that remain relatively unimportant. On the other hand, lift and drag forces may at times be significant, e.g., during first stage. In these cases their effects cannot be neglected in the entire flight duration.

In principle, therefore, we can analyze constraint G in a manner such that these minor effects are separated from the principal constituents. This is accomplished by converting G to the scales, in which case

$$G = G_0 + \epsilon_1 G^{(1)} + \epsilon_2 G^{(2)} + \epsilon_3 G^{(3)}$$
 [14]

The functions $\epsilon_1G^{(1)}$, $\epsilon_2G^{(2)}$ and $\epsilon_dG^{(3)}$ represent the insignificant quantities mentioned previously. Although a similar decomposition of G into functions with and without aerodynamic forces is, in this case, not valid, one characteristic is evident: these forces are definitely small in most cases for a considerable initial portion of the powered flight duration. It is possible, therefore, to modify Equation [14] in the finite interval $[x_1, x_1 + \xi]$ so that the aerodynamic effects are denoted as being small. In this case we may say that

$$G = G^{(0)} + \epsilon_1 G^{(1)} + \epsilon_2 G^{(2)} + \epsilon_3 G^{(3)} + \epsilon_4 G^{(4)}$$
 [15]

Equation [15] is valid for x contained in $[x_1, x_1 + \xi]$ and Equation [14] is valid for $[x_1 + \xi, x_2]$. An interesting feature is that G_0 in Equation [14] is dependent upon h, whereas $G^{(0)}$ in Equation [15] is independent of h.

The assertion that the forces are small for a finite interval $[x_1, x_1 + \xi]$ is equivalent to the assertion that $\lambda_2(x) = O(\epsilon)$ where x is contained in $[x_1, x_1 + \xi]$. We can prove this statement by examining the relative orders of magnitude indicated in Equation [11]. It is assumed that if G, H, v, γ, h and x are converted to the scales, $G^{(i)}$ i = 1,..., 4, H and all their derivatives will be of O(1).

Equation [11] states that

$$E_b F + E_b(\lambda_1 G) + E_b(\lambda_2 H) = 0$$
 [16]

In the problem of minimum time, Equation [5] leads to

$$E_h F = E_h [(R_1 + h)/(v \cos \gamma)]$$
 [17]

Converting to the scales, Equation [17] is revealed as $O(\epsilon)$, since $h(\vartheta)/R_1 = O(\epsilon)$ throughout the interval of flight. If we now restrict our discussion to the interval $[x_1, x_1 + \xi]$, Equation [15] is applicable with $G^{(0)}$ independent of h and h'. Consequently the orders of magnitude of Equation [16] are disclosed as

$$O(\epsilon) + \epsilon_1 E_h(\lambda_1 G^{(1)}) + \epsilon_2 E_h(\lambda_1 G^{(2)}) + \epsilon_3 E_h(\lambda_1 G^{(3)}) + \epsilon_4 E_h(\lambda_1 G^{(4)}) + E_h(\lambda_2 H) = 0 \quad [18]$$

Briefly, since $G^{(1)}$, $G^{(2)}$, $G^{(3)}$, $G^{(4)}$ are of O(1)

$$E_h(\lambda_2 H) = 0(\epsilon) \tag{19}$$

The problem of maximum altitude can be analyzed in a similar manner. The function F, however, is independent of h and h', for $F = v(t) \sin \gamma(t)$. In this case Equation [16] also reduces to Equation [19].

Equation [19] is valid for x contained in the finite interval $[x_1, x_1 + \xi]$. It implies that $\lambda_2 = O(\epsilon)$ since H and its derivatives are of O(1).

On the basis of the preceding proof that $\lambda_2(x_1) = O(\epsilon)$ and Equation [14], we are suggesting the following approximate method of analysis: Retain only zero-order terms in the Euler-Lagrange differential equations; i.e., replace G by G_0 of Equation [14] and choose zero as the initial value of λ_2 ; i.e., $\lambda_2(x_1) = 0$, regardless of the actual maximum magnitude of aerodynamic forces during flight. It is now necessary to prove that the resulting error in the stationary value is of $O(\epsilon^2)$.

Proof of Validity

The resulting approximate solutions $\bar{\lambda}_1$, $\bar{\lambda}_2$, \bar{v} , $\bar{\gamma}$, and \bar{h} must satisfy

$$E_{\hat{v}}(\bar{F} + \bar{\lambda}_1 \tilde{G}_0 + \bar{\lambda}_2 \bar{H}) \equiv 0$$
 [20]

$$E_{\bar{\tau}}(\bar{F} + \bar{\lambda}_1 \bar{G}_0 + \bar{\lambda}_2 \bar{H}) \equiv 0$$
 [21]

$$E_{k}(\bar{F} + \bar{\lambda}_{1}\bar{G}_{0} + \bar{\lambda}_{2}\bar{H}) \equiv 0 \qquad [22]$$

$$\tilde{G} \equiv 0$$
 [23]

$$\bar{H} \equiv 0$$
 [24]

Given $G = G_0(v, \gamma, h, v', \gamma', h')$ [maximum aerodynamic effects may be significant] and $\bar{\lambda}_2(x_1) = 0$, we want to show that the approximate extreme \bar{I} differs from the exact extreme I^* by an $O(\epsilon^2)$.

Comparing Equations [9, 10 and 11] with Equations [20, 21 and 22], we note that terms in the differential equations for the exact solutions differ from those for the approximate solutions by $O(\epsilon)$. Moreover, if the initial value of $\lambda_2^*(x_1) = O(\epsilon)$ is replaced by $\bar{\lambda}_2(x_1) = 0$, it can be shown by means of formal expansions that the solutions differ as

$$\lambda_2^*(x) = \bar{\lambda}_2(x) + \epsilon \tilde{\lambda}_2(x)$$
 [25]

$$v^*(x) = \bar{v}(x) + \epsilon \bar{v}(x)$$
 [26]

$$\gamma^*(x) = \gamma(x) + \epsilon \tilde{\gamma}(x)$$
 [27]

$$h^*(x) = \tilde{h}(x) + \tilde{\epsilon h}(x)$$
 [28]

For the purpose of comparing the exact extremum with its approximation, we form

$$I^* - \bar{I} = \int_{1}^{2} [(F^* - \bar{F}) + \bar{\lambda}_1 (G^* - \bar{G}) + \bar{\lambda}_2 (H^* - \bar{H})] dx = \epsilon \int_{1}^{2} \{\bar{F}_v + \bar{\lambda}_1 \bar{G}_v + \bar{\lambda}_2 \bar{H}_v] v + [\bar{F}_{\gamma} + \bar{\lambda}_1 \bar{G}_{\gamma} + \bar{\lambda}_2 \bar{H}_{\gamma}] \tilde{\gamma} + [\bar{F}_{h} + \bar{\lambda}_1 \bar{G}_{h} + \bar{\lambda}_2 \bar{H}_{h}] \tilde{h} \} dx + \epsilon \int_{1}^{2} \{ [\bar{\lambda}_1 \bar{G}_{v'} + \bar{\lambda}_2 \bar{H}_{v'}] v' + [\bar{\lambda}_1 \bar{G}_{\gamma'} + \bar{\lambda}_2 H_{\gamma'}] \tilde{\gamma}' + [\bar{\lambda}_1 \bar{G}_{h'} + \bar{\lambda}_2 \bar{H}_{h'}] \tilde{h}' \} dx + O(\epsilon^2)$$
 [29]

Integrating the second term by parts and using Equations [14, 20, 21 and 22], we obtain

$$I^* - \bar{I} = \epsilon \{ v(\bar{\lambda}_1 \tilde{G}_{v'} + \bar{\lambda}_2 \bar{H}_{v'}) + \tilde{\gamma}(\bar{\lambda}_1 \bar{G}_{v'} + \bar{\lambda}_2 \bar{H}_{\gamma'}) + \tilde{h}(\bar{\lambda}_1 \tilde{G}_{h'} + \bar{\lambda}_2 \bar{H}_{h'}) \} |_1^2 + O(\epsilon^2) = O(\epsilon^2)$$
 [30]

The boundary term vanishes because of either prescribed or

Nomenclature

p(x)

16] to

If ξ],

are

8]

9]

50

te

of ıť

t

E_{τ}	= operator defined as $(d/dt)(\partial/\partial i) - (\partial/\partial v)$
F, G, H	= given functions of v, γ, h
h(x)	= change in altitude from initial station
I	= functional
J	= definite integral
R_1	= radial distance from Earth's center to initial station
$(R_1 + h)$	= radial distance from Earth's center to vehicle
t, 9	 specific independent variables of time and polar angle, respectively

velocity

x	=	generalized independent variable
x_1, x_2	=	limits of x
$\gamma(x)$	=	flight path inclination
ξ	==	finite parameter
€, €;	=	small parameters, $i = 1, 2, 3, 4$.
λ_1, λ_2		Lagrange multipliers

Subscripts

(')	=	differentiation with respect to x
(*)	=	related to exact extremum
(-)	=	related to approximate extremum
(~)	=	related to a perturbation
$(\)_{v},\ (\)_{\gamma},\ (\)_{h}$ $(\)_{v'},\ (\)_{\gamma'},\ (\)_{h'},$	=	partial derivatives

References

- 1 Breakwell, J. V., "The Optimization of Trajectories," J. Soc. Indust. Appl. Math., vol. 7, no. 2, June 1959.
 2 Courant, R. and Hilbert, D., "Methods of Mathematical Physics, vol. I," Interscience Publishers, Inc., N. Y., 1953.
 3 Ting, L., "Approximations in Variational Problems," Polytechnic Institute of Brooklyn, PIBAL Rep. no. 610, AFOSR TN 60-789, July 1960. also in Aero/Space Engng., Jan. 1961.

Application of the Mangler Transformation in Boundary Layer Flow

S. deSOTO1 and H. WOLF2

Rocketdyne Div., North American Aviation, Inc., Canoga Park, Calif.

IN CONTEMPLATING the problems associated with convective heat transfer from hot gases in rocket nozzles, or for any axisymmetric configuration with internal or external flow, a correlation with flat plate data through the use of the Mangler transformation (1)3 immediately comes to mind. The forementioned transformation transforms the boundary layer equations for axisymmetric flow to those for two-dimensional flow; for example, the integral momentum boundary layer equation for flow over a cone may be transformed to flow over a wedge. Schlichting (2) discusses the transformation briefly. Eckert (5) shows for the case of a laminar boundary layer in supersonic flow over a cone (with an attached shock wave), that the heat transfer coefficient is $\sqrt{3}$ times the value of that for a point on a flat plate with the same Reynolds number.

It has been determined that the Mangler transformation is not valid for the case of the turbulent boundary layer.

It should be noted that the transformation appears, on the surface, to be purely geometric in nature and hence it is not immediately obvious that it does not apply to the case of the

turbulent boundary layer. The Mangler transformation consists of a clever set of geometric substitutions that converts the continuity equation in axisymmetric form to the twodimensional form. If the coordinate system for both the two-dimensional and axisymmetric cases is taken such that xis parallel to the surface of the body and y is perpendicular to the surface, then the axisymmetric form of the momentum and energy differential equations is identical to the two-dimensional forms of the respective equations. Hence, one of the properties of the Mangler transformation must consist of its ability to change the form of the continuity equation from the axisymmetric to the two-dimensional form without affecting the form of either the momentum equation or the energy equation. The transformation equations are

$$\bar{x} = (1/L^2) \int_0^x r^2 dx$$
 [1]

$$\bar{y} = (r/L)y \tag{2}$$

where

L = constant reference lengthr = local radius of revolution

The barred variables represent the two-dimensional case and the unbarred variables represent the axisymmetric case.

Laminar Boundary Layer

The equation for the heat transfer coefficient h, for the laminar boundary layer over a flat plate (or a wedge in supersonic flow with an attached shock) in continuum flow with no mass transfer through the surface and no streamwise temperature gradients, is given by

$$\bar{h} = \frac{k}{\bar{x}} \, 0.33 \left(\frac{\rho \bar{x} U}{\mu} \right)^{1/2} (P_r)^{1/3} = \frac{k}{T_{ow} - T_w} \left(\frac{\partial T}{\partial y} \right)_u \quad [3]$$

¹ Formerly Technical Specialist, Research, Rocketdyne; presently Associate in Engineering, UCLA, Los Angeles, Calif.

² Principal Scientist. Member ARS.

³ Numbers in parentheses indicate References at end of paper.

k =thermal conductivity

T = temperature

 $\mu = \text{viscosity}$

 $T_w = \text{wall temperature}$

 $\rho = \text{density}$

 T_{aw} = adiabatic wall temperature

U =free stream velocity

 $P_r = \text{Prandtl number}$

For the case of the cone in supersonic flow with attached shock the pressure and velocity downstream from the shock are constant over the surface of the cone as for a flat plate. Therefore, according to the geometry of the cone, $r = x \sin(a)$, where a = cone half angle, a constant. Equation [1] thus gives

$$\bar{x} = \sin^2 a(x^3)/3L^2 = r^2x/3L^2$$
 [4]

Substituting Equations [2 and 4] into Equation [3] yields

$$h = \sqrt{3} \frac{k}{x} 0.33 \left(\frac{\rho x U}{\mu} \right)^{1/2} (P_r)^{1/3} = \frac{k}{T_{aw} - T_w} \left(\frac{\partial T}{\partial y} \right)_w$$
 [5]

It may be seen that Equation [5] is identical to Equation [3] except that all barred variables have been eliminated and an

added term, $\sqrt{3}$, has emerged in Equation [5].

The significance of Equation [5] is as follows: if the flat plate equation for the heat transfer coefficient through a laminar boundary layer is applied to a cone no change need be made in the variables of the flat plate equation. However, the result must be multiplied by $\sqrt{3}$ indicating that the heat transfer coefficient for the laminar boundary layer over a supersonic cone with attached shock is greater than that for flat plate conditions (for the same Reynolds number, Prandtl number and distance from the leading edge) by the constant factor $\sqrt{3}$.

Turbulent Boundary Layer

The very same procedure as used above will now be applied to the case of the turbulent boundary layer. The equation for the heat transfer coefficient for the turbulent boundary layer over a flat plate or a wedge with an attached shock (i.e., no streamwise pressure or temperature gradients) is given by

$$\bar{h} = \frac{k}{\bar{x}} (0.0296) \left(\frac{\rho \bar{x} U}{\mu} \right)^{0.8} (P_r)^{1/3} = \frac{k}{T_{aw} - T_w} \left(\frac{\partial T}{\partial y} \right)_w \quad [6]$$

where, again, the barred values represent the two-dimensional case. Now if, as was done before for the case of the laminar boundary layer, Equations [2 and 4] are substituted into Equation [6], we get

$$\begin{split} h &= \left(\frac{r}{L}\right)^{0.6} (3)^{0.2} \frac{k}{x} \left(0.0296\right) \left(\frac{\rho x U}{\mu}\right)^{0.8} (P_r)^{1/3} = \\ &\qquad \qquad \frac{k}{T_{aw} + T_w} \left(\frac{\partial T}{\partial y}\right)_w \end{split} \ \ [7] \end{split}$$

It is seen that Equation [7] would be identical in form to Equation [6] if it were not for the term $(r/L)^{0.6}(3)^{0.2}$. It can be seen that these terms do not appear in Equation [5] for the laminar boundary layer simply because in that case the Reynolds number (which contains an x term) is taken to the 0.5 power thereby canceling out both the r and the L terms in the transformation from Equations [3–5]. For the case of the turbulent boundary layer, however, the Reynolds number is raised to the 0.8 power and hence the transformation given by Equations [1 and 2] cannot entirely eliminate the r/L term.

It appears that this difficulty can be alleviated by changing Equation [1] to read

$$\bar{x} = (1/L^5) \int_0^x r^5 dx$$
 [8]

so that for the cone in supersonic flow with a turbulent boundary layer Equation [4] becomes

$$\bar{x} = r^5 x / 6L^5 \tag{9}$$

Upon transformation of Equation [6] the r/L term is completely eliminated so that Equation [6] becomes

$$h = (6)^{0.2} \frac{k}{x} (0.0296) \left(\frac{\rho xv}{\mu}\right)^{0.8} (P_r)^{1/3} = \frac{k}{T_{av} - T_v} \left(\frac{\partial T}{\partial y}\right)_v$$

It should be noted that Equation [8] is not the Mangler transformation. It must now be shown whether Equation [8] can transform the momentum, continuity, and energy equation for the turbulent axisymmetric boundary layer to the two-dimensional case in order for Equation [10] to hold. That this does not happen is shown in the following section.

Transformation Attempt

For purposes of comparison the momentum and continuity equations for the two-dimensional laminar boundary layer are written (utilizing Mangler's notation).

$$\bar{\rho}\left(\bar{u}\frac{\partial\bar{u}}{\partial\bar{x}} + \bar{v}\frac{\partial\bar{u}}{\partial\bar{v}}\right) = -\frac{d\bar{P}}{d\bar{x}} + \frac{\partial}{\partial\bar{v}}\left(\bar{u}\frac{\partial\bar{u}}{\partial\bar{v}}\right)$$
 [11]

$$\frac{\partial(\overline{\rho u})}{\partial \overline{v}} + \frac{\partial(\overline{\rho v})}{\partial \overline{v}} = 0$$
 [12]

The continuity equation for the two-dimensional axisymmetric laminar boundary layer is given by

$$\frac{\partial(\rho ur)}{\partial x} + \frac{\partial(\rho vr)}{\partial y} = 0$$
 [13]

The equations for the proposed transformation are

$$\bar{x} = \frac{1}{L^5} \int_0^x r^{\xi}(x) dx \text{ and } \bar{y} = \frac{r(x)}{L} y$$
 [14]

$$\bar{P}(\bar{x}) = P(x)$$
 $\bar{\rho}(\bar{x}, \bar{y}) = \rho(x, y)$ $\bar{\mu}(\bar{x}, \bar{y}) = \mu(x, y)$

$$\bar{h}(\bar{x}, \bar{y}) = h(x, y)$$
 $\bar{\psi}(\bar{x}, \bar{y}) = \frac{1}{L} \psi(x, y)$ [15]

Therefore

$$\bar{x} = \bar{x}(x)$$
 $\bar{u}(\bar{x}, \bar{y}) = u(x, y) \times$

$$\bar{v} = \frac{L}{r} \left(v + \frac{r'}{r} y u \right) \qquad r' = \frac{dr}{dx}$$

For the turbulent axisymmetric boundary layer the momentum and continuity equations can be written as follows with notation according to Shapiro (4)

$$\widetilde{\rho u} \frac{\partial^{2}}{\partial \overline{v}} + \widetilde{\rho v} \frac{\partial \widetilde{u}}{\partial \overline{v}} = -\frac{d\widetilde{P}}{dx} + \frac{\partial}{\partial \overline{v}} \left[(\epsilon + \widetilde{\mu}) \frac{\partial \widetilde{u}}{\partial \overline{v}} \right]$$
[17]

$$\frac{\partial}{\partial \bar{x}} (r \rho u) + \frac{\partial}{\partial \bar{y}} (r \rho v) = 0$$
 [18]

where the tilde (\sim) signifies a time mean value for the turbulent flow. The energy equations have not been written, but the discussion that follows is also applicable to them. The transformation of Equations [17 and 18] to a form similar to Equations [11 and 12] will now be attempted; note that the term $(\epsilon + \tilde{\mu})$ corresponds to $\bar{\mu}$. In the following equations the tildes are omitted for convenience.

A stream function in axisymmetric flow may be defined as

$$\rho u = \frac{1}{r} \frac{\partial \psi}{\partial y} \qquad \rho v = -\frac{1}{r} \frac{\partial \psi}{\partial x} \qquad [19]$$

The stream function in two-dimensional flow may be defined

$$\overline{\rho u} = \frac{\partial \overline{\psi}}{\partial \overline{u}} \qquad \overline{\rho v} = -\frac{\partial \overline{\psi}}{\partial \overline{v}} \qquad [20]$$

But from Equations [14-16], $\bar{x} \neq \bar{x}(y)$, and $\partial \bar{y}/\partial y = r/L$; also $\psi = L\overline{\psi}$.

$$\frac{\partial \psi}{\partial y} = L \frac{\partial \bar{\psi}}{\partial \bar{y}} \frac{\partial \bar{y}}{\partial y} + L \frac{\partial \bar{\psi}}{\partial \bar{x}} \frac{\partial \bar{x}}{\partial y} = \frac{\partial \bar{\psi}}{\partial \bar{y}} r$$
 [21]

and from Equations [19-21]

$$\rho u = \frac{1}{r} \frac{\partial \psi}{\partial y} = \frac{\partial \overline{\psi}}{\partial \overline{y}} = \overline{\rho \mu}$$
 [22]

Now from Equation [19] and from Equations [8, 14-16]

$$-\rho v = \frac{1}{r} \frac{\partial \psi}{\partial x} = \frac{L}{r} \left[\frac{\partial \bar{\psi}}{\partial \bar{x}} \frac{r^5}{L^5} + \frac{\partial \bar{\psi}}{\partial \bar{y}} \frac{\bar{y}}{r} r' \right]$$

so that

nt

91

1

$$\rho v = \overline{\rho v} (r^4/L^4) - \overline{\rho} \overline{u} \overline{y} r' L/r^2$$
 [23]

Now from Equations [22, 23, 15, 16 and 14]

$$\rho u \frac{\partial u}{\partial x} = \overline{\rho} \overline{\mu} \left[\frac{r^5}{L^5} \frac{\partial \overline{u}}{\partial \overline{x}} + \frac{r'}{r} \overline{y} \frac{\partial \overline{u}}{\partial \overline{v}} \right]$$
 [24]

$$\rho v \frac{\partial u}{\partial v} = \left[\overline{\rho v} \frac{r^4}{L^4} - \overline{\rho} \frac{\overline{\mu y}}{r^2} r' L \right] \left[\frac{r}{L} \frac{\partial \overline{u}}{\partial \overline{v}} \right]$$
 [25]

Now the sum of Equations [24 and 25] represents the transformation of the left-hand side of the momentum equation. Summing, we get

$$\rho u \frac{\partial u}{\partial x} + \rho v \frac{\partial u}{\partial y} = \frac{r^5}{L^5} \left[\overline{\rho_u} \frac{\partial \bar{u}}{\partial \bar{x}} + \overline{\rho v} \frac{\partial \bar{u}}{\partial \bar{y}} \right]$$
 [26]

And from Equations [8 and 15] we have

$$-\frac{dp}{dx} = -\frac{r^5}{L^5} \frac{d\bar{p}}{d\bar{x}}$$
 [27]

For the right-hand side of the momentum equation, from Equation [14] one obtains

$$\frac{\partial}{\partial y} \left(\epsilon_M \frac{\partial u}{\partial y} \right) = \frac{r^2}{L^2} \frac{\partial}{\partial \bar{y}} \left(\bar{\epsilon}_M \frac{\partial \bar{u}}{\partial \bar{y}} \right)$$
 [28]

by letting $\epsilon_M = (\epsilon + \hat{\mu})$, the turbulent eddy viscosity. Consequently, by combining Equations [26-28] we have

$$\frac{r^{\delta}}{L^{\delta}} \left[\overline{\rho \mu} \frac{\partial \tilde{u}}{\partial \bar{x}} + \rho v \frac{\partial \tilde{u}}{\partial \bar{y}} \right] = - \frac{r^{\delta}}{L^{\delta}} \frac{d\overline{p}}{d\bar{x}} + \frac{r^{2}}{L^{2}} \left[\frac{\partial}{\partial \bar{y}} \left(\bar{\epsilon} \frac{\partial \tilde{u}}{\partial y} \right) \right]$$
[29]

Comparison of Equation [29] with Equation [17] shows the transformation, as proposed, cannot be carried out for the turbulent momentum equation. The above explanation of the inadequacy of the transformation for the turbulent case is based simply on the mechanics of the mathematics involved. Physically, the explanation might be found by examining Equations [11 and 17].

These equations imply a mean value concept (indicated by tilde) which is really statistical in nature. Hence the treatment of this statistical concept with a mathematics that is essentially valid for a continuum is questionable. Further, the terms ϵ and $\tilde{\mu}$ that appear in Equation [17] in the concept of "eddy viscosity" are really an oversimplification of an involved phenomenon, i.e., turbulent transport and vorticity, which is again statistical in nature. Equation [17] has been "forced" to appear as it does, so that it is of the same form as the more exact equation used for laminar flows.

It appears, then, that the power of the Mangler transformation cannot be applied to the turbulent boundary layer in spite of the fact that it might seem to be nothing more than a geometric transformation of the space variables. However, it is assumed in Equation [15] that the viscosity remains invariant in the transformation. Although this may be true for the case of the laminar boundary layer, the transport properties such as viscosity and thermal conductivity would appear to be affected by the transformation in the turbulent case. This implies that a physical difference exists between the transport properties of two-dimensional and axisymmetric flows for the case of turbulent flows.

A simple extrapolation procedure for the determination of heat transfer coefficients for axisymmetric flows from twodimensional flows is therefore not available for the turbulent boundary layer.

1 Mangler, W., "Zusammenhang Zwischen Ebenen und Rotationssymmetrischen Grenzschichten in Kompressiblen Flussigkerten," ZAMM, vol. 29, 1958, p. 97.

2 Schlichting, H., "Boundary Layer Theory," McGraw-Hill Book Co., Inc., N. Y., 1955.

3 Shapira A. H. (1977)

3 Shapiro, A. H., "The Dynamics and Thermodynamics of Compressible Fluid Flow," Ronald Press Co., N. Y., 1955.

4 Ibid., pp. 1085, 1086. 5 Eckert, E. R. G. and Drake, R. M., "Heat and Mass Transfer," McGraw-Hill Book Co., Inc., N. Y., 1959.

Small MHD Power Generator Using Combustion Gases as an Energy Source

G. J. MULLANEY¹ and N. R. DIBELIUS²

General Electric Co., Schenectady, N. Y.

A small MHD channel was used to investigate the fundamental principles of this method of power generation. In the experiments described in this report, the potassium concentration was varied from 1 to 6% by weight of the combustible mixture. The power output of the generator increased as the square root of the potassium concentra-

tion, following the trend established in conductivity experiments made earlier. The output power was 55% of the calculated value. Power extraction was transverse to both magnetic field and gas flow, and continuous electrodes were employed.

WE RECENTLY investigated the conductivity of par-tially ionized flame gases seeded with potassium.³ With this background of experimental data on electrical conductivity of seeded flames, we were in a favorable position to investigate the principles of operation of an MHD generator. A small continuous electrode power channel was used which could be operated for several minutes per run, and the results obtained are described in this note.

³ Mullaney, G. J., Kydd, P. H. and Dibelius, N. R., "Electrical Conductivity in Flame Gases with Large Concentrations of Potassium," J. Appl. Phys., April 1961.

Received Oct. 20, 1960.

Mechanical Engineer, Research Laboratory.

Mechanical Engineer, General Engineering Laboratory.

MHD POWER GENERATION UNIT USING SEEDED FLAME GASES

c d d

The same burner for mixing of propane and oxygen as used for the electrical conductivity experiments mentioned was used in the MHD tests. A 30-cc hypodermic syringe, the piston of which was driven by a rack and pinion from an electrical motor, provided the injection of a water solution of potassium carbonate. A cutaway of the burner and MHD channel is shown in Fig. 1. The experiments were limited to about 5 min chiefly because of the loss of graphite (0.00227 gm per cm²-sec) at 2300 K owing to the chemical attack of the flame gases and erosion. For such short intervals of operation it is very important to use a low density furnace material, such as 150 lb per ft³ zirconia to provide a high degree of thermal insulation. On the other hand, the high electrical conductivity of zirconia makes it a poor choice for the insulating walls of the MHD power extraction channel. Ninety seven per cent purity MgO blocks provided satisfactory electrial insulation. Operating conditions for the experiments described in this paper are given in Table 1. The method of operation was as follows: The fuel valve was cracked, and the propane ignited by a Telsa coil downstream of the MHD channel test section; oxygen and propane flow then were gradually increased until the required flows were obtained. The starting process took about 30 sec. After the full flows were established, both inner channel wall temperature and elapsed time were monitored. An optical pyrometer focused through a slit in the zirconia furnace was used to observe a zirconia chip exposed to the flame gases on the side of the channel away from the observer. In earlier experiments using the same combustion system and a comparable channel crosssectional area, we had established that gas temperature and the temperature of a zirconia chip at the wall surface were identical. Usually the required gas temperature (and surface temperature) were reached in the same elapsed time in each test. However, this time interval (about 2 min) was shortened when experiments were set up and run before the apparatus had cooled to ambient temperature.

After the required gas temperature was reached, the additive injection was started and the magnetic field applied. A voltmeter and ammeter were used to determine the power output from the MHD channel as the external load was changed.

Fig. 2 shows voltage-current data for constant gas temperature and magnetic field but with various amounts of potassium additive. Power output increased as the square root of the additive concentration for the range of concentrations studied. The open circuit voltage is given by

$$V = vaB ag{1}$$

Table 1 Operating conditions

Fuel-propane

Oxidizer—oxygen

Additive-K2CO2 (1 to 6% potassium by weight of com-

bustible mixture)

Channel dimensions

length (l) = 4.9 cmheight (h) = 2.8 cm

distance between electrodes (a) = 2.9 cm

Magnetic characteristics

magnetic current density (B) = $0.425 \times 10^{-4} \text{ v-sec/cm}^2$

4-in. diameter pole pieces gap 4.75 in.

250 v d-c and 30 amp input

Electrodes

graphite (continuous) 13.7 cm² each

Channel insulating wall-97% MgO

Flame gas temperature—2300 K

Gas conductivity in absence of magnetic field (σ)-10

mhos per m for 1% potassium by weight

Ratio of electron cyclotron radian frequency to electron collision frequency (β) = 0.67

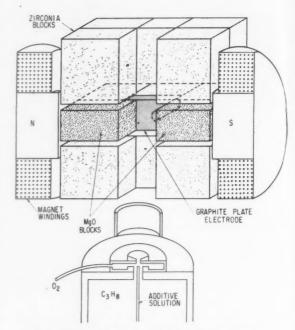


Fig. 1 Cutaway view of the MHD channel and burner

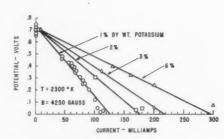


Fig. 2 Voltage-current data for constant gas temperature and magnetic field

where

V = potential, v

v = average gas velocity, cm per sec

a =distance between electrodes, cm

 $B = \text{magnetic current density, v-sec per cm}^2$

Since the open circuit voltage does not depend on the degree of conductivity of the gas, all additive concentrations produce the same open circuit voltage. From the measured open circuit voltage, the average gas velocity is calculated to be 5680 cm per sec.

The short circuit current is given by

$$I_{ss} = \left[\sigma_{0e}/(1+\beta^2)\right]vBhl$$
 [2]

where

= short circuit current, amp

 σ_{0e} = electronic conductivity with no magnetic field, mhos per cm

= channel length, cm

B = ratio of electron cyclotron radian frequency to electron collision frequency

= channel height, cm

For 1% potassium and our experimental conditions, the calculated short circuit current is 0.237 amp. This is nearly double the measured short circuit current (Fig. 2). β is independent of the additive concentration, and, therefore, the short circuit current should be proportional to the electrical conductivity of the gas. The increase in short circuit currents with additive concentration are consistent with earlier conductivity measurements which showed that the electrical conductivity increased as the square root of the additive concentration. Power output for transverse power extraction and continuous electrodes is expressed by

$$P = [\sigma_{0e}/(1 + \beta^2)]v^2B^2n(1 - n)hal$$
 [3]

where

P = power output,

n = ratio of operation load voltage to open circuit loadvoltage

In a series of tests using 1% potassium, the output power was determined from current-voltage measurements at various external resistance and then calculated using Equation [3]. As shown (Fig. 3), the maximum power output was about 55% of the theoretical power. This may be a result of velocity and temperature gradients in the

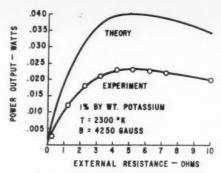


Fig. 3 Output power vs. external resistance

power extraction channel. Aside from the losses believed to be associated with velocity and temperature gradients, the theoretical maximum power should be approached because the magnetic field has been extended considerably beyond the electrodes to minimize end electrical losses.

Acknowledgments

The authors are grateful for the skillful assistance of C. W. Moon in the design and construction of many components of the apparatus used in this work. We also wish to thank G. E. Moore, R. A. Alpher, J. D. Cobine and L. P. Harris for many stimulating discussions and suggestions.

Similar Solutions of the Free **Convection Boundary Layer Equations** for an Electrically Conducting Fluid¹

BARRY L. REEVES²

California Institute of Technology, Pasadena, Calif.

RECENTLY Lykoudis (1)³ presented a solution of the problem of the free convection boundary layer adjacent to a vertical plate with a uniform surface temperature. The model proposed by Lykoudis differs from the classical problem solved by Pohlhausen (2) by the fact that the surrounding medium is an electrically conducting fluid and an applied magnetic field is normal to the direction of fluid motion.

Since for nonconducting fluids it is known that the case of constant wall temperature is one of an entire class of similar solutions (3, 4), the purpose of this note is to demonstrate that a class of similar solutions also exists for an electrically

conducting fluid.

Using the standard two-dimensional boundary layer coordinates, x is taken as the coordinate parallel to the plate and y the coordinate perpendicular to the plate. A magnetic field acts transversally to the fluid motion, and the field is as-

sumed to be independent of y. Thus, the retarding force per unit volume $\mathbf{J} \times \mathbf{B}$, which acts in the x direction, is $-\sigma u B^2$. Here, σ is the electrical conductivity (assumed constant), u is the fluid velocity component in the x direction, and B is the magnetic inductance. Furthermore, if the fluid properties are constant, the boundary layer equations of motion and energy may be written

$$\frac{\partial u}{\partial x} + \frac{\partial v}{\partial y} = 0 ag{1}$$

$$u\frac{\partial u}{\partial x} + v\frac{\partial u}{\partial y} = g\beta\theta - \frac{\sigma uB^2}{\rho} + v\frac{\partial^2 u}{\partial y^2}$$
 [2]

$$u\frac{\partial\theta}{\partial x} + v\frac{\partial\theta}{\partial y} = \frac{k}{\rho c_p}\frac{\partial^2\theta}{\partial y^2}$$
 [3]

where

 $\theta = T - T_{\infty}$

 β = coefficient of thermal expansion

Now introduce the stream function

$$u = \partial \psi / \partial y$$
 $v = -\partial \psi / \partial x$

and the following similarity transformations

$$\psi = ax^p f(\eta) \tag{4}$$

$$\theta = bx^m \varphi(\eta) \tag{5}$$

$$\eta = cy/x^n \tag{6}$$

where a, b and c are constants.

Research Fellow, Guggenheim Aeronautical Laboratory.
 Numbers in parentheses indicate References at end of paper.

Received Oct. 18, 1960.

This work was supported by the Air Force Office of Scientific Research, ARDC, Fluid Mechanics Division under Contract AF 49(638)-916.

The velocity components become

$$u = acx^{(p-n)}f'$$

$$v = ax^{(p-1)}[n\eta f' - pf]$$

Similarly, expressions for the derivatives of u, v and θ can be found, and the momentum and energy equations become, respectively

$$\begin{split} [(p-n)(f')^2 - pff''] x^{(2p-2n-1)} &= \frac{c}{a} \ \nu x^{(p-3n)} f''' + \\ &\frac{g\beta b}{a^2 c^2} x^m \varphi - \frac{\sigma B^2}{a c \rho} \ x^{(p-n)} f' \end{split} \ \ [7]$$

$$[mf'\varphi - pf\varphi']x^{(p-n+m-1)} = \frac{k}{\rho c_p} \frac{c}{a} x^{(m-2n)}\varphi''$$
 [8]

Since similar solutions exist if Equations [7 and 8] are independent of x, we obtain

$$p = 1 - n \qquad m = 1 - 4n$$

Furthermore, Equations [7 and 8] are dimensionally homogeneous so that we can let $a/c = \nu$. Hence, the momentum and energy equations become

$$(1-2n)(f')^2 - (1-n)ff'' = f''' + \frac{g\beta b}{c^4\nu^2} \varphi - \frac{\sigma B^2}{\rho c^2\nu} x^{2n}f'$$
 [9]

$$\varphi'' + (1 - n)Prf\varphi' + (4n - 1)Prf'\varphi = 0$$
 [10]

where $Pr = Prandtl number = \rho c_p \nu / k$.

It is apparent from the last term of Equation [9] that the magnetic inductance must vary with x according to the re-

$$B = \text{constant}/x^n$$
 [11]

If we arbitrarily set $\varphi(0) = 1$ where $\eta = 0$ represents the plate surface, from Equation [5]

$$\theta_w = T_w - T_\infty = bx^{(1-4n)}$$
 [12]

The constant c is found by equating the coefficient of φ equal to unity in Equation [9]

$$c = (g\beta\theta_w/\nu^2x^{1-4n})^{1/4} = (Gr)^{1/4}/x^{1-n}$$

where

$$Gr = Grashof number = g\beta x^3\theta_w/v^2$$

Thus, Equation [9] becomes

$$f''' + (1-n)ff'' + (2n-1)(f')^2 + \varphi - Zf' = 0 \quad [13]$$

where Z is a magnetic parameter given by

$$Z = \frac{\sigma B^2}{\rho c^2 \nu} x^{2n} = (Gr)^{-1/2} \left(\frac{\sigma B^2 x^2}{\rho \nu} \right)$$
 [14]

Hence Z is actually the ratio of the square of the Hartmann number (defined as the ratio of magnetic to viscous forces) to the square root of the Grashof number.

The boundary conditions to Equations [10 and 13] are

$$\begin{array}{ll} \eta = 0 \colon f = f' = 0, \quad \varphi = 1 \\ \eta = \omega \colon f' = 0, \quad \varphi = 0 \end{array}$$

It is desirable to point out several specific cases for which subsequent machine calculations and experiments could be used for comparison with results for nonconducting fluids (Z = 0). First, it is apparent from Equations [11 and 12] that if $n = \frac{1}{4}$, B varies as $x^{-1/4}$ and T_w is a constant. This is the case which was studied in some detail in (1) and has received extensive study for nonconducting fluids.

If n = 0, B is a constant and T_w varies linearly with x. Since there is no singularity in either B or T at the leading edge of the plate, this case would probably be the most de-

sirable for experiments.

Finally, it was demonstrated in (4) that for a nonconducting fluid and for $n > \frac{2}{5}$, a portion of the fluid in the boundary layer attains a higher temperature than that of the plate even though $T_w > T_{\infty}$, and it was also shown that solutions which are physically meaningful do not exist for $n \ge 1$. Thus, calculations for finite Z could be used to determine the effects of the singularities in B and T at the leading edge on the downstream velocity and temperature profiles.

1 Lykoudis, P., "Natural Convection of an Electrically Conducting Fluid in the Presence of a Magnetic Field," Purdue Univ., Lafayette, Ind., Rep. no. A-60-1, Aug. 1960.
2 Schlichting, H., "Boundary Layer Theory," McGraw-Hill Book Co., N. Y., 1955, p. 275.
3 Finston, M., "Free Convection Past a Vertical Plate," Zeitechrift fur Angewondte Mathematic und Physik, vol. 7, 1956, p. 527.
4 Reeves, B. and Kippenhan, C., "On a Particular Class of Similar Solutions of the Equations of Motion and Energy of a Viscous Fluid," J. Aero/Space Sci. (to be published).

Stability Problem of the Flow With **Combustion in Variable Area Duct**

ANDRZEJ KOWALEWICZ¹

Warsaw Institute of Technology, Warsaw, Poland

The method of investigation of the nonlinear pressure oscillations in a combustion field presented by Rosen is extended for the flow in a variable area duct. Necessary conditions for damping are presented, and the order of magnitude of the terms describing the generation and the damping of the pressure oscillations are analyzed. The problem has a practical application in jet engines, especially ramjets.

Received Sept. 19, 1960.

¹ Research Engineer.

THE PROBLEM of nonlinear pressure oscillations in a combustion field was described by Rosen (1)2 for the case of flows in constant area ducts. The present paper attempts to extend the problem to flows in variable area ducts.

Let us consider one-dimensional flow of compressible, inviscid, nonconducting fluid in a duct, in which area is a function of axial coordinate A = A(x). The flow parameters, velocity in x direction u, pressure P, density ρ are the functions of coordinate x and time t. The rate of combustion (production of burned gas) is determined by $d\omega/dt = f(\omega, P, \theta)$ fluid element), where ω is the weight fraction of the burned gas. This relation does not predetermine the character of combustion; it may as well be heterogeneous as homogeneous. Other assumptions, among which the entropy of burned gas is assumed to be constant, are the same as in Rosen's paper.

² Numbers in parentheses indicate References at end of paper.

This model may be described by the equations

13]

[4]

nn

2]

e

18

$$\begin{split} \frac{\partial \rho}{\partial t} + u \, \frac{\partial \rho}{\partial x} + \rho \, \frac{\partial u}{\partial x} + \rho \, u \, \frac{\partial \ln A}{\partial x} &= 0 \\ \frac{\partial u}{\partial t} + u \, \frac{\partial u}{\partial x} + \frac{1}{\rho} \, \frac{\partial P}{\partial x} &= 0 \\ \frac{d\omega}{dt} &= f \, (\omega, P, \text{fluid element}) \\ \omega \rho &= a \, P^{1/\gamma} \end{split}$$

which are almost the same as in the case A = constant except for the term $\rho u(\partial \ln A/\partial x)$ in the continuity equation.

The transformation from Euler's coordinate system to Lagrange's may be made by introducing the stream function $\psi(x,t)$ which satisfies the equations (2)

$$\frac{\partial \psi}{\partial x} = \rho A \qquad \frac{\partial \psi}{\partial t} = -\rho u A \qquad [2]$$

Any function F(x,t) may be expressed in the new coordinate system by the relation

$$F(x,t) = \hat{F}[\psi(x,t),t]$$
 [3]

and its derivatives take the form

$$\frac{\partial F}{\partial x} = \frac{\partial \hat{F}}{\partial \psi} \cdot \frac{\partial \psi}{\partial x} = \frac{\partial \hat{F}}{\partial \psi} \rho A$$

$$\frac{\partial F}{\partial t} = \frac{\partial \hat{F}}{\partial t} + \frac{\partial \hat{F}}{\partial \psi} \cdot \frac{\partial \psi}{\partial t} = \frac{\partial \hat{F}}{\partial t} - \frac{\partial \hat{F}}{\partial \psi} \cdot \rho u A$$

$$(4)$$

Equations [1] expressed in terms of ψ ,t according to Equations [3 and 4] take the form

$$\begin{split} \frac{\partial}{\partial t} \left(\frac{1}{\rho} \right) - A \frac{\partial u}{\partial \psi} - u \frac{\partial A}{\partial \psi} &= 0 \\ \frac{\partial u}{\partial t} + A \frac{\partial P}{\partial \psi} &= 0 \\ \frac{\partial \omega}{\partial t} &= f(\omega, P; \psi) \\ \omega_P &= a P^{1/\gamma} \end{split}$$

where for simplicity the sign " $^{"}$ " by functions P, ρ , u, A and ω is omitted

After combination of Equations [5] and elimination of u and ρ , the system reduces to the single equation

$$\begin{split} \omega \, \frac{\partial^2 P}{\partial t^2} - \, a \gamma P \, \frac{\gamma + 1}{\gamma} \, A^2 \frac{\partial^2 P}{\partial \psi^2} &= \left(\gamma P \, \frac{\partial f}{\partial P} - 2 f \right) \frac{\gamma P}{\partial t} \, + \\ \frac{\gamma + 1}{\gamma} \, \frac{\omega}{P} \left(\frac{\partial P}{\partial t} \right)^2 &+ \, \gamma P f \, \frac{\partial f}{\partial \omega} + 2 \gamma a P \, \frac{1 + \gamma}{\gamma} \, A \, \frac{\partial P}{\partial \psi} \cdot \frac{\partial A}{\partial \psi} \quad [6] \end{split}$$

Equation [6] differs from the equation which may be obtained in the case of A = constant, because of the term

$$2\gamma aP^{\frac{\gamma+1}{\gamma}}A(\partial P/\partial \psi)\cdot \partial A/\partial \psi$$

Physical interpretation of Equation [6] is similar to that in the case of A = constant.

The pressure disturbances propagate with the velocity

$$\partial \psi/\partial t = \pm \sqrt{\gamma A^2 P \rho}$$

which in the x,t coordinate system has the form

$$\frac{dx}{dt} = u \pm \sqrt{\gamma(P/\rho)}$$

It means that the variable area of the duct does not influence the velocity of disturbances (the same as the presence of combustion).

The last term in Equation [6] converted into $x,\,t$ coordinate system takes the form

$$2\gamma P \frac{\omega}{\rho} \frac{\partial \ln A}{\partial x} \frac{\partial P}{\partial x}$$

which is more convenient for physical interpretation. This term describes the influence of variability of duct area on low frequency pressure oscillations. This influence is damping or amplifying according to the positive or negative value of the term (the same as for the first term of the right side of Equation [6]).

In case $\partial \ln A/\partial x > 0$ ($\partial \ln A/\partial x < 0$) the necessary condition for damping is

$$\partial P/\partial x < 0 \qquad (\partial P/\partial x > 0)$$
 [7]

The necessary condition for damping coming from the interaction of combustion processes with pressure waves is the relation (1), [Eq. 13]

$$\partial \ln f / \partial \ln P < 2/\gamma$$
 [8]

The conditions [Eqs. 7 and 8] are necessary for damping, but cannot be considered as sufficient conditions for stability of the flow. In order to analyze the problem of stability it is necessary to estimate the order of magnitude of the terms of Equation [6].

The derivative $\partial f/\partial P$ in the first term on the right side of the equation determines the influence of the pressure on the rate of combustion. In the general case, however, the order of magnitude of $\partial f/\partial P$ cannot be estimated because it depends on the function of fuel-air ratio (3,4). In particular, in some range of concentration, which is only partly actual in technical application (i.e., c=1.5-2.4% for gasoline), the flame velocity is expressed by the relation

$$U \sim P^{-n}$$
 $n = 0.25-0.30$

which is satisfied by the majority of hydrocarbon-air mixtures (4). On the basis of this data, the order of magnitude of $\partial f/\partial P$ may be estimated.

Similarly, the order of magnitude of the combustion rate f cannot be estimated in a general case; in actual technical problems it may be estimated only in some ranges of pressure and concentration. According to the foregoing, the order of magnitude of the terms $P(\partial f/\partial P)$ and f are not the same as Rosen has assumed, and the assumption that the order of magnitude of the first term of the right side of the equation is equal to $f \cdot |P/\partial t|$ does not seem to be justified.

In the same way the orders of magnitude of combustion rate f and derivative $\partial f/\partial \omega$ cannot be considered to be the same in the general case, as Rosen has done. The order of magnitude of the derivative $\partial f/\partial \omega$ in the case of hydrocarbonair mixtures and other gaseous mixtures varies in a wide range, because the curve $f = f(\omega, P = \text{constant})$ has an explicit maximum and is steep (3). Hence the order of magnitude of the term $\gamma f P(\partial f/\partial \omega)$ changes in a wide range also.

The order of magnitude of the term

$$\frac{\gamma+1}{\gamma}\frac{\omega}{P}\cdot\left(\frac{\partial P}{\partial t}\right)^2$$

is determined by the order of

$$\frac{1}{P} \left| \frac{\partial P}{\partial t} \right|^2$$

Similarly, the order of magnitude of the term

$$2\gamma P \frac{\omega}{\rho} \frac{\partial \ln A}{\partial x} \frac{\partial P}{\partial x}$$

is expressed by the order of

$$\frac{P}{a} \left| \frac{\partial \ln A}{\partial x} \right| \cdot \left| \frac{\partial P}{\partial x} \right|$$

References

1 Rosen, G., "Nonlinear Pressure Oscillations in a Combustion Field," ARS JOURNAL, vol. 30, no. 4, April 1960, pp. 422-423.
2 Sauer, R., "Fluides Compressibles," Paris et Liéqes, 1951.
3 Hitrin, "Physics of Combustion and Detonation," Moscow, 1957.
4 Goldenberg, S. A. and Pelevin, V. S., "Influence of Pressure on Rate of Flame Propagation in Turbulent Flow," Seventh Symposium (International) on Combustion, London 1959.

Rapid Method for Plug Nozzle Design

H. GREER¹

Northrop Corp., Hawthorne, Calif.

An approximate method is presented for determining the contour of a plug nozzle for a given design expansion ratio and ratio of specific heats. This procedure is based on centered isentropic wave expansion and geometric considerations.

THERE has been considerable interest recently in plug nozzles. In preliminary studies the precise layout of the plug contour is quite time-consuming. This paper develops an approximate method of obtaining the geometry of a plug

A centered wave, or isentropic Prandtl-Meyer expansion fan, is assumed to occur at the lip of the plug nozzle, as shown in Fig. 1. To obtain the isentropic plug contours, the streamlines are replaced by surfaces. At design conditions the flow in the immediate vicinity of the lip is assumed to undergo a corner expansion through the angle 90 - ψ (see Fig. 2) becoming parallel to the plug centerline. The flow area at any point along the plug is approximated by the surface area of an annular conic frustrum formed by rotating L_1 , the line perpendicular to the plug surface and extending to its intersection with the lip streamline, about the plug centerline. The flow area is

$$A = \pi L_1 (r_1 + r_2)$$
 [1]

The Mach number of the flow just inside the nozzle lip at the throat is unity and increases along the plug to its final value at the plug tip where the flow is assumed to be uniform and axially parallel. The relationship between the Mach number and the flow area along the plug is

$$\epsilon_{f} = \frac{A}{A_{t}} = \frac{1}{M} \left\{ \left[\frac{2}{\gamma + 1} \left(1 + \frac{\gamma - 1}{2} M^{2} \right) \right]^{\gamma + 1/\gamma - 1} \right\}^{1/2}$$
[2

Associated with each Mach number along the plug is the Mach angle

$$\alpha = \sin^{-1} 1/M$$
 [3]

and the Prandtl-Meyer function

$$\omega = \left(\frac{\gamma + 1}{\gamma - 1}\right)^{1/2} \tan^{-1} \left[\frac{\gamma - 1}{\gamma + 1} \left(M^2 - 1\right)\right]^{1/2} - \tan^{-1} \left(M^2 - 1\right)^{1/2}$$
 [4]

¹ Senior Engineer, Advanced Systems Section. Presently, Member Technical Staff, Systems Research and Planning Div., Aerospace Corp., El Segundo, Calif. Member ARS.

The contour of the plug is different for each design expansion ratio ϵ_{ϵ} . For a given ϵ_{ϵ} , Eqs. 2 and 4 define ω_{ϵ} and the nozzle lip inclination

$$\psi = 90 - \omega_{\rm e} \tag{5}$$

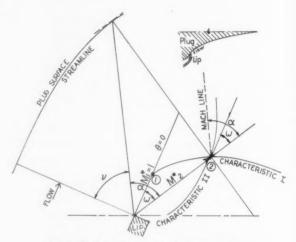


Fig. 1 Hodograph diagram of plug nozzle flow

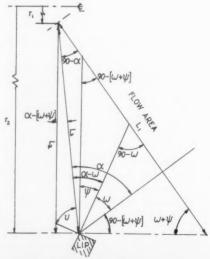


Fig. 2 Plug nozzle flow geometry

The plug contour is now determined. In Fig. 2, the following geometrical relations are obtained for any point along the plug surface

$$\phi = 90 + \alpha - (\psi + \omega) \tag{6}$$

$$L_2 = L_1 \sin \left(\psi + \omega \right) \tag{7}$$

$$L_3 = L_2/\cos(\alpha - \psi - \omega)$$
 [8]

$$r_1 = r_2 - L_2$$
 [9]

By substituting Eqs. 7 and 9 into Eq. 1

Rate

ion zle

$$A = \pi L_1 [2r_2 - L_1 \sin (\psi + \omega)]$$
 [10]

is obtained. By solving Eq. 10 for L_1

$$L_{1} = \frac{r_{2}}{\sin(\psi + \omega)} - \left\{ \left[\frac{r_{2}}{\sin(\psi + \omega)} \right]^{2} - \frac{A}{\pi \sin(\psi + \omega)} \right\}^{1/2}$$
[11]

and substituting this result and Eq. 7 in Eq. 8, the following

$$L_{3} = \frac{\sin(\psi + \omega)}{\cos(\alpha - \psi - \omega)} \left\{ \frac{r_{2}}{\sin(\psi + \omega)} - \left\{ \left[\frac{r_{2}}{\sin(\psi + \omega)} \right]^{2} - \frac{A}{\pi \sin(\psi + \omega)} \right\}^{1/2} \right\}$$
[12]

Upon dividing this espression by r_2 and simplifying, the dimensionless radial length λ is

$$\lambda = \frac{L_3}{r_2} = \frac{1}{\cos(\alpha - \psi - \omega)} \times \left\{ 1 - \left[1 - \frac{A \sin(\psi + \omega)}{\pi r_2^2} \right]^{1/2} \right\}$$
[13]

Of course, the design flow area at the plug tip is

$$A_s = \pi r_2^2 \tag{14}$$

and the ratio of the nozzle expansion ratio at any point to the design expansion ratio is

$$\xi = \frac{\epsilon_f}{\epsilon_e} = \frac{A}{A_e} \tag{15}$$

Using these relations, the radial length becomes

$$\lambda = \frac{1}{\cos (\alpha - \psi - \omega)} \times \{1 - [1 - \xi \sin (\psi + \omega)]^{1/2}\}$$
 [16]

Using Eqs. 6 and 16 it is, therefore, possible to lay out an approximate plug nozzle contour for any desired expansion ratio and ratio of specific heats. In Fig. 3, the generalized nozzle contours for various design expansion ratios using a constant ratio of specific heat of 1.17 are presented.

Nomenclature

A = flow area

L = length

M = Mach number

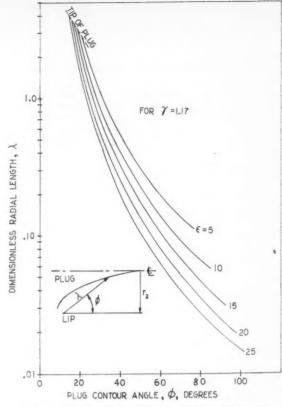


Fig. 3 Radial length vs. contour angle for a plug nozzle

r = radius

= Mach angle

 γ = ratio of specific heats

= expansion ratio

= inclination of velocity vector

 λ = dimensionless radial length

 ν = angle in flow geometry ξ = ratio of expansion ratios

 ϕ = plug contour angle

 ψ = inclination of nozzle lip

 ω = Prandtl-Meyer function

Subscripts

= critical Mach number for isentropic flow

1, 2, 3 = positions in flow geometry

= nozzle exit

= nozzle throat

Growth of Magnetohydrodynamic **Boundary Layers**

J. C. WU

Douglas Aircraft Co., Inc., Santa Monica, Calif.

NUMBER of papers appeared during the past three years on the flow of electrically conducting fluids over flat plates or curved walls, in the presence of transverse magnetic fields (1-4).2 In many of the publications, the conditions of similarity are either assumed or implied. It is demonstrated in the following paragraphs that in the presence of uniform transverse magnetic fields, laminar boundary layers grow in an approximately exponential fashion rather than parabolically as would exist in the similarity cases. Although the first three analyses given here are heuristic and do not constitute a proof, the fourth one is more rigorous and is further supported by numerical results obtained through the use of a finite difference technique (5). It is further demonstrated that for cases where the magnetic interaction parameter mx exceeds unity, the growth of the boundary layer becomes very rapid. The possible re-entry applications of this rapid boundary layer growth are discussed. The differences between electromagnetic forces and adverse pressure forces are also discussed briefly.

One of the cases studied by Rossow in (1) is the steady flow of an incompressible fluid over a flat plate in the presence of a uniform transverse magnetic field, with the electrical conductivity of the fluid given by the expression

$$\sigma = \sigma_0[(u_{\infty} - u)/u_{\infty}]$$
 [1]

Rossow's analysis resulted in the following expression for the displacement thickness

$$\delta^* = (1.73 + 0.93 \, mx + \dots) \sqrt{\nu x/u_{\infty}}$$
 [2]

In another case (1), the electrical conductivity was considered constant throughout the entire flow field and flow separation was calculated to exist at mx = 0.5.

It should be noted that in Rossow's analysis, the velocity is assumed to be of the form

$$u = u_{\infty}[f_0' + (mx)f_2' + (mx)^2f_4' + \dots]$$
 [3]

where f_i 's are functions of η only.

Only the first two or three terms in Eq. 3 were considered in (1). As pointed out by Rossow in his original analysis, "The velocity profiles shown . . . indicate that the flow separation at mx = 0.5 for the constant electrical conductivity case will probably not be predicted if a sufficient number of terms are taken in series [3]. The first three terms describe the velocity in the boundary layer quite well up to at least mx = 0.2." In fact, it should be noted that there is no a priori justification in assuming that the series in Eq. 3 will converge for all values of mx. Also, comparison of the expression in Eq. 2 with Taylor series for e^{mx} reveals some formal resemblance. It is not impossible that if enough terms in the expression for u are considered, one will reach the conclusion that the boundary layer thickness follows the form

$$\delta \cong Ke^{mx} \sqrt{\nu x/u_{\infty}}$$

where K is some constant.

Consider a layer of inviscid incompressible fluid flowing over a flat plate in the presence of a uniform transverse magnetic field. Let the pressure gradient be zero everywhere within the layer and let the initial velocity U_{∞} in the layer be uniform. The momentum equation for this "one-dimensional" flow geometry, neglecting the gravitational forces, can be written as

$$u(\partial u/\partial x) = -muu_{\infty}$$
 [4]

which gives

$$u = u_{\infty} (1 - mx) \tag{5}$$

The thickness of the layer δ is governed by the continuity equation. Using the expression for u in Eq. 5, one has

equation. Using the expression for
$$u$$
 in Eq. 5, one has
$$\delta = \delta_0 [1 + (mx) + (mx)^2 + (mx)^3 + \dots (mx)^n + \dots]$$
[6]

where δ_0 is the initial thickness of the layer.

Evidently, when mx approaches 1, the expression for δ diverges and the boundary layer thickness becomes very large. This equation also indicates that when mx is larger than 1, the boundary layer growth becomes extremely rapid. This statement agrees with previous prediction of Meyer (6) for the stagnation point flow. If the maximum temperature in the boundary layers of a re-entry body is comparable to the stagnation region temperature, the results of (6) can be used directly in estimating the magnetic field strength required to produce a rapid growth in boundary layer. Thus, for x =1 m and a re-entry speed of 10,000 m per sec, the field strength required is 10,000 Gauss at 10,000-m altitude and only 1000 Gauss at 50,000-m altitude.

Following the usual method of estimating the boundary layer thickness by considering the terms in the momentum equation, we state that the sum of the viscous and the Lorentz forces should be approximately equal to the inertia force.

$$\frac{\mu u}{\delta^2} + \sigma B^2 u \cong \frac{\rho u^2}{r} \tag{7}$$

or

$$\delta^2 \cong \frac{\mu x}{\rho u} \left(\frac{1}{1 - mx} \right) \tag{8}$$

Again, we conclude that the boundary layer growth will be large at mx = 1.

A more rigorous way of showing this conclusion is to make use of the boundary layer integral equations. The continuity and momentum equations for an incompressible flat plate flow are

$$\frac{\partial u}{\partial x} + \frac{\partial v}{\partial y} = 0 ag{9}$$

$$u\frac{\partial u}{\partial x} + v\frac{\partial u}{\partial y} = -\frac{\sigma B^2 u}{\rho} + v\frac{\partial^2 u}{\partial y^2}$$
 [10]

Integrating the momentum equation with respect to y from 0 to h, where the line y = h is everywhere outside the boundary layer, and subsequently substituting the integral expression for v obtained from the continuity equation, yields

$$\int_0^h \left(u \frac{\partial u}{\partial x} - \frac{\partial u}{\partial y} \int_0^y \frac{\partial u}{\partial x} dy + \frac{\sigma B^2 u}{\rho} \right) dy = -\frac{\tau_0}{\rho} \quad [11]$$

Integrating the second term in the integral by parts and using the relationship assumed by Rossow for electrical conductivity, Eq. 1, we have

$$\int_0^h \left\{ \frac{\partial}{\partial x} \left[u(u_{\infty} - u) \right] - \frac{\sigma B^2}{\rho u_{\infty}} u(u_{\infty} - u) \right\} dy = \frac{\tau_0}{\rho} \quad [12$$

For the first term in Eq. 12, differentiation with respect to x and integration with respect to y may be interchanged, since the upper limit of integration h is independent of x. Introducing the momentum thickness θ then yields

$$\frac{d\theta}{dx} - m_0\theta = -\frac{\tau_0}{\rho} \tag{13}$$

Received Nov. 4, 1960.

Specialist of Research, Thermodynamics Section.

Numbers in parentheses indicate References at end of paper.

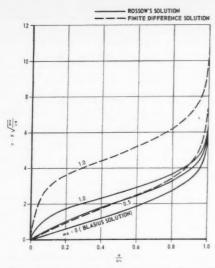


Fig. 1 Comparison between Rossow's and finite difference solutions-variable electrical conductivity

where $m_0 = \sigma_0 B^2 / \rho u_{\infty}$ is a constant.

[4]

uity

[6]

di-

rge.

the

his

for

in

the

sed

red

th

100

ry

ım

tz

7]

8]

The solution of the differential equation is

$$\theta = e^{m_0 x} \left[\int \frac{\tau_0}{\rho u_{\infty}^2} e^{-m_0 x} dx + C \right]$$
 [14]

where C is a constant to be determined from the initial condition. Note that the first term inside the bracket is not a definite integral and does not, in general, vanish for x = 0. For larger values of mx, the first term in the bracket becomes relatively unimportant and the term Ce^{m_0x} dominates the behavior of the momentum thickness. Thus, for larger values of m_0x , the momentum thickness grows approximately in an exponential fashion.

To verify the discussion, Rossow's problem involving variable electrical conductivity was solved using a finite difference method developed by this author (5). The results are expressed in Figs. 1 and 2. The following conclusions are clearly indicated:

1 For smaller values of mx (mx < 0.5), the results obtained, using the finite difference method, agree with Rossow's results.

2 For values of mx larger than 0.5, Rossow's solution, as expected, is not valid.

The boundary layer grows very rapidly near mx = 1 as predicted by the analyses given.

It should be noted that for values of mx greater than unity, the growth of the boundary layer will be so rapid that the interaction between the boundary layer and the main stream becomes important. Investigations by this author, concerning this problem and the problem of the hypersonic flow of a compressible fluid where fluid properties, including the electrical conductivity of the fluid, are functions of the temperature and the pressure of the fluid, are in progress.

In (7) Bleviss, studying magnetogasdynamic Couette flow, pointed out that relatively weak magnetic fields (500 Gauss) produce large increases in the total drag, large reductions in the skin friction, and at the same time have relatively little effect on the heat transfer. It was pointed out (7 and 8) that the increase in total drag due to magnetic drag contribution may be desirable from the energy dissipation point of view. The increased drag can be used as a brake to further alleviate the portion of dissipated energy eventually transferred back to a re-entry body. On the basis of the same total drag, the heat transfer for the magnetic force will be much less than for the nonmagnetic case. It should be noted that the magnetic drag not only provides a possible method of reducing heat transfer for a re-entry body but also offers a possibility of controlling a body traveling at hypersonic speed.

In (3), Lykoudis showed that general "similarity" solutions exist for the boundary layer, if the intensity of the magnetic field acting perpendicular to the direction of flow varies according to a power law with respect to the distance from the forward stagnation point. Bush extended Lykoudis' work to the case of compressible, flat plate, similar boundary layer (4) in which the intensity of the magnetic field acting normal to the direction of flow is assumed to be inversely proportional to the square root of the distance from the leading edge. His result demonstrated that the skin friction and heat transfer can be reduced with the application of an external magnetic field. The rapid growth of boundary layer associated with larger values of mx as demonstrated in the present analysis places a new importance on the possibility of the forementioned applications. It may be concluded from Bush's analysis that one can hardly hope for similarity to exist for a uniform external magnetic field. In fact, since the magnetic force is proportional to the thickness of the boundary layer (the thickness of the layer which is electrically conducting), one may conclude that the magnetic effect is important only when the boundary layer thickness has reached a certain value. In the application of the magnetic fields as drag producing devices, it may be advantageous to apply the fields only at the downstream section of a body where the boundary layer is relatively thick.

It should also be mentioned that although the electromagnetic force is similar to an adverse pressure gradient in slowing down the flow in the boundary layer, it differs essentially from ordinary pressure gradient in that the electromagnetic forces are proportional to the flow velocity. The magnetic force ceases to exist once the fluid in the layer comes to rest. Furthermore, the magnetic force resists backflow and makes it possible to have boundary layer flow with zero skin friction but no flow separation. A different type of flow separation may occur through the presence of the induced magnetic field. If the free stream pressure is small in comparison to this "induced magnetic pressure," the fluid can be virtually lifted from the solid surface.

Nomenclature

B = magnetic field strength

 $m = \sigma B^2/\rho u_{\infty}$

x, y =space coordinates along and normal to the wall

u, v = x and y components of the fluid velocity

 U_{∞} = free stream velocity

 $= y\sqrt{u_{\infty}/\nu x}$

= boundary layer thickness

= displacement thickness

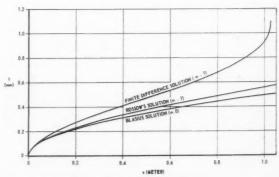


Fig. 2 Boundary layer growth

momentum thickness = $(1/u_{\infty}^2) \int_0^{\infty} u(u_{\infty} - u) dy$ θ

absolute viscosity βŝ kimematic viscosity

mass density

electrical conductivity

electrical conductivity of the fluid at the wall er o

shear stress

shear stress at the wall m

1 Rossow, V. J., "On Flow of Electrically Conducting Fluids Over a Flat Plate in the Presence of a Transverse Magnetic Field," NACA Rep. 1358 1958

2 Sears, W. R., "Some Solutions of the Microscopic Equations of Magnetohydrodynamics," paper presented at the ARS-Northwestern Gas Dypaper presented at the ARS-Northwestern Gas Dy-

namics Symposium, Aug. 1959.
3 Lykoudis, R. P., "On A Class of Magnetic Laminar Boundary Layers,"
Heat Transfer and Fluid Mechanics Institute Preprint, June 1958, pp. 176-186

176-186.

4 Bush, W. B., "Compressible Flat Plate Boundary Layer Flow With an Applied Magnetic Field," J. Aeron. Sci., vol. 27, no. 1, Jan. 1960, pp. 49-58.

5 Wu, J. C., "The Solution of Laminar Boundary Layer Problems by the Finite Difference Method," Douglas Rep. no. SM-37484, April 1960.

6 Meyer, R. X., "Magnetohydrodynamics and Aerodynamic Heating," ARS JOURNAL, vol. 29, no. 3, March 1959, pp. 187-192.

7 Bleviss, Z. O., "Magnetogasdynamics of Hypersonic Couette Flow," J. Aeron. Sci.; vol. 25, no. 10, Oct. 1958, pp. 601-615.

8 Liepmann, H. W., "Magnetic Effects on High Speed Boundary Layers," comments presented at Third Combustion and Propulsion Colloquium, AGARD, NATO, Palermo, Sicily, March 1958.

Experimental Study of Combustion Instability in Solid Rocket Propellants'

LELAND A. WATERMEIER²

Ballistic Research Labs., Aberdeen Proving Ground, Md.

Double-base rocket propellant slabs were burned in a transparent walled chamber which was vented to the atmosphere through a nozzle. The slabs were ignited at ambient nitrogen pressures of 200 to 800 psi. Pressure waves were produced normal to the burning surface by a siren operating at frequencies of 100 to 1400 cps. Photographs revealed an increased burning rate as the siren approached the resonant frequency of the chamber. Large pressure variations recorded during this process present evidence of possible acoustic interaction with the burning surface.

OMBUSTION instability in solid rocket propellants Combustion instanting in some continues to be the subject of much research effort (1). The Interior Ballistics Laboratory has been engaged in a laboratory scale experimental study of this phenomenon for

Received Dec. 9, 1960.

¹ This work is being conducted under Army Ordnance Research and Development Project no. TB5-20. ² Combustion Section Chief, Physics Branch, Interior Ballistics

Lab. Member ARS.

³ Numbers in parentheses indicate References at end of paper.

Fig. 1 View of the siren assembly attached to the top of the test chamber

some time (2,3). This report gives some of our most recent

Apparatus and Procedure

The experiment consists of burning a $\frac{1}{4}$ in. $\times \frac{3}{4}$ in. $\times 1\frac{1}{4}$ in. slab of propellant, cigarette fashion, in a windowed chamber that is vented to the atmosphere through a siren or slotted wheel, Fig. 1. The sides of the slab are inhibited by a coating of Duco cement and a flow of nitrogen directed upward past the propellant. The nitrogen also provides the means of pressurizing the chamber for any desired ignition pressure up to 900 psi. The nozzle dimensions are altered for each pressure range investigated, so that the mean chamber pressure does not rise more than 100 to 150 psi during a run, independent of the ambient condition. The propellant surface is maintained at a certain level in the chamber during a run by means of an elevator mechanism. The siren is turned on at a set time after ignition and introduces pressure waves normal to the propellant surface. The siren frequency range is approximately 100 to 1400 cps.

Dynamic Instrument Corporation pressure transducers and a Consolidated Electrodynamics Corporation oscillograph recorder are used to record the chamber pressure. A Fairchild Motion Analysis 16-mm camera is used to photograph

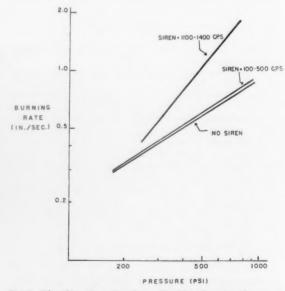


Fig. 2 Plot of burning rates of propellant A as function of pressure and siren frequency

a

P

B

fla

fo

A

the burning slabs. Since the framing rate of this camera is high, several measurements for burning rates can be made while the chamber pressure remains essentially constant. The burning rate of the propellant is determined by measuring the normal regression rate of the surface as a function of time.

Data

Approximately 175 experimental runs were made with a cast double base propellant-propellant A-which was a plateau-type containing lead salts. All runs were made below the plateau pressure region. First, the burning rate was determined at various pressure levels without the siren induced oscillations. These rates were somewhat lower than comparative strand burner results. Second, the burning rates were determined as the burning surface underwent pressure pulses from the siren. Fig. 2 shows a plot of some of the data. Approximately 75 runs were made using various frequencies from 100 to 1400 cps. The burning rate was not appreciably affected by the pressure pulses until the 1100 to 1400 cps range was reached. This is the approximate resonant frequency range of the test chamber. The burning rate was based on 11 to 2 sec of burning under the influence of the siren. In the resonant range of siren operation, the burning rate was much higher than normal at the same pressure level. No attempts were made to determine variations in the rate. Approximately 2 sec after the siren came on, the flame would usually start burning down the sides of the slab. In the 600-800 psi and 1100-1400 cps ranges, this phenomena was exaggerated and the entire slab would suddenly burst into flame.

Large amplitude chamber pressure variations (20–25% of mean pressure) were recorded when the siren frequency was 1100–1400 cps, only if a burning propellant surface was present. This observation, together with indications of impedance matching in some instances, lends some support to the Hart-McClure theory of acoustic interaction with the burning surface.

Photographic Observations

Motion pictures revealed what appeared to be a molten surface layer during the burning of propellant A. This layer seemed to move about like "lava" and contained bubbles or bumps which had dimensions of the same order as those of the casting powder. The flame was characterized by cone-like projections which reached down to the surface at various points.

In the low frequency range (100–500 cps) of siren operation, the propellant flame zone was moved alternately toward and away from the burning surface. This movement was rather large considering that the amplitude of the pressure pulses was generally not greater than 5–8% of the mean chamber pressure. By contrast, the flame zone was compressed and almost extinguished by siren pulses in the 1100–1400 cps frequency range, Fig. 3.

Two other lots of modified propellant A (propellants B and C) were investigated to learn more about the nature of the burning surface and to note changes in the flame zone. B and C were of the same composition as A except that B did not contain the lead salts and C contained approximately 3% aluminum.

Motion pictures of burning propellant B showed that the liquid surface layer was no longer evident as it was with A. Propellant C was burned both with and without the siren pulses. No appreciable change in burning rate was measured under these conditions. Fig. 4 shows a comparison of three runs using these propellants. Notice that in comparing A and B, the most evident difference is the loss of the cones of flame projecting to the surface when the lead salts are absent. Propellant C shows that with the addition of aluminum, the flame zone loses its homogeneous appearance and appears to be a zone of burning globules and particles of aluminum. These particles may also be acting as individual flame holders for the burning gases. It is conceivable that this zone could

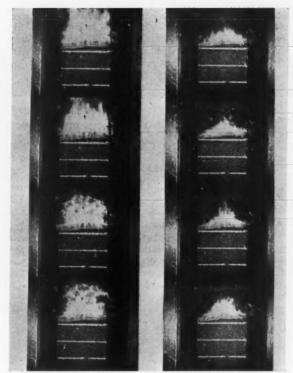


Fig. 3 Frames from movie (~1800 fps) of propellant A burning at chamber pressure of 550 psi and undergoing siren pulses of 1350 cps. The first two frames on the left are prior to siren

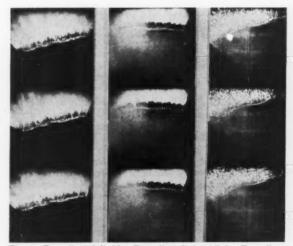


Fig. 4 Propellant A (left). Propellant B (middle). Propellant C (right). Comparative frames from movies of three cast double-base propellants. Chamber pressure = 500 psi. Notice change in flame zone

break up wave motion and provide a heterogeneous medium through which a wave would need to propagate if unstable conditions were to be encouraged. The characteristic dark zone of double-base propellant was still evident in burning slabs of C. Very little aluminum was seen burning on the surface at the lower pressures, but as the pressure increased (600-800 psi range) more aluminum tended to burn on the surface. Wood (4) has made significant observations of this type of phenomenon, also.

References

1 Summerfield, M., Solid Propellant Rocket Research, Academic Press, N. Y., 1960, pp. 295-619.
2 Watermeier, L., Satkowski, T. and Mifflin, T., Experimental Study of Combustion Instablity in Solid Rocket Propellants—Part I, Memo Rep. no. 1172, Ballistic Research Labs., Aberdeen Proving Ground, Md., Oct.,

1958. Watermeier, L., An Experimental Study of Combustion Instability in Solid Rocket Propellants—Part II, Rep. no. 1116, Ballistic Research Labs., Aberdeen Proving Ground, Md., Sept., 1960.
4 Wood, W. A., Rohm and Haas Report No. P-59-1, Jan. 15, 1959. (Confidential)

Optimal Powered Arcs in an Inverse **Square Law Field**

D. F. LAWDEN¹

University of Canterbury, Christchurch, New Zealand

GENERAL theory of optimal trajectories for a rocket vehicle moving under the actions of an arbitrary gravitational field, and its motor thrust, has been developed by the author of this note in earlier papers (1,2).2 Assuming the motion to lie in the plane of rectangular axes Oxy, if V(x, y)is the gravitational potential function, it was shown that a vector quantity termed the primer can be defined, whose components (λ, μ) parallel to the axes satisfy the equations

$$\frac{d^2\lambda}{dt^2} + \lambda \frac{\partial^2 V}{\partial x^2} + \mu \frac{\partial^2 V}{\partial x \partial y} = 0$$

$$\frac{d^2\mu}{dt^2} + \lambda \frac{\partial^2 V}{\partial x \partial y} + \mu \frac{\partial^2 V}{\partial y^2} = 0$$

along an optimal trajectory and which are direction ratios for the thrust at any instant the rocket motor is operating. The complete optimal trajectory was taken to comprise a number of arcs each belonging to one of the three following

1 Coasting arcs for which the motor is closed down.

2 Arcs along which the motor operates at maximum thrust; if this maximum is sufficiently great, the thrust may be treated as being impulsive.

3 Powered arcs along which the motor thrust is not maximal.

It was shown that the condition

$$\lambda^2 + \mu^2 = \text{constant}$$
 [2]

must be satisfied along an arc of type 3 and it was believed that, by expanding V in a Taylor series and neglecting all but second-order terms, it could be demonstrated (3) that Eqs. 1 possessed no first integral in the form of Eq. 2, and hence that type 3 arcs were not admissible. Leitmann (4) has expressed doubts regarding the validity of this argument, and upon further investigation it has been found that the existence of such powered arcs can be demonstrated for a general field. It accordingly becomes necessary to extend the theory to include such arcs, and this will be done in a later paper. However, the purpose of this note is to prove that these powered arcs exist in the inverse square law field due to a single attracting body, and to calculate their

Let γ/r^2 be the attraction per unit mass at a distance r from the body which is supposed fixed at the origin O. Let r, θ be the polar coordinates of the rocket at any instant t, θ being measured counterclockwise from Ox. If ξ , η are the respective components of the primer along and perpendicular to (in the direction of θ increasing) the radius r, then from Eq. 2

$$\xi^2 + \eta^2 = 1/\alpha^2$$
 [3]

where α is constant, and $\alpha \xi$, $\alpha \eta$ are the cosines of the angles made by the primer with these two directions. Since the thrust is always parallel to the primer, if f is the vehicle acceleration due to its motor, the equations of motion can now be written

$$\ddot{r} - r\dot{\theta}^2 = -\gamma/r^2 + \alpha f \xi$$

$$r\ddot{\theta} + 2\dot{r}\dot{\theta} = \frac{1}{r}\frac{d}{dt}(r^2\dot{\theta}) = \alpha f \eta$$
[4]

where dots denote differentiations with respect to t.

By resolving along Ox and Oy, it will be found that

$$\lambda = \xi \cos \theta - \eta \sin \theta \qquad \mu = \xi \sin \theta + \eta \cos \theta \quad [5]$$

Also

$$V = -\gamma/r = -\gamma(x^2 + y^2)^{-1/2}$$

and hence

$$\frac{\partial^2 V}{\partial x^2} = \frac{\gamma}{r^3} (1 - 3\cos^2 \theta)$$

$$\frac{\partial^2 V}{\partial u^2} = \frac{\gamma}{r^3} (1 - 3\sin^2 \theta)$$

$$\frac{\partial^2 V}{\partial x \partial y} = -\frac{3\gamma}{r^3} \sin \theta \cos \theta$$

Substituting from Eqs. 5 and 6 into Eqs. 1 and subsequently solving for ξ , $\ddot{\eta}$, it will be found that

$$\ddot{\xi} = 2\dot{\eta}\dot{\theta} + \eta\ddot{\theta} + (\dot{\theta}^2 + 2\gamma/r^3)\xi$$

$$\ddot{\eta} = -2\dot{\xi}\dot{\theta} - \xi\ddot{\theta} + (\dot{\theta}^2 - \gamma/r^3)\eta$$
[7]

We now put

$$\xi = rp \qquad \eta = rq \qquad [8]$$

in Eqs. 7, to obtain

$$r\ddot{p} + 2\dot{r}\dot{p} + (\ddot{r} - r\dot{\theta}^2 - 2\gamma/r^2)p - 2r\dot{\theta}\dot{q} - (r\ddot{\theta} + 2\dot{r}\dot{\theta})q = 0$$

 $r\ddot{q} + 2\dot{r}\dot{q} + (\ddot{r} - r\dot{\theta}^2 + \gamma/r^2)q + 2r\dot{\theta}\dot{p} + (r\ddot{\theta} + 2\dot{r}\dot{\theta})p = 0$

which, with the aid of Eqs. 4, can be reduced immediately to

$$r\hat{p} + 2\hat{r}\hat{p} + \alpha fr(p^2 - q^2) - 2r\dot{\theta}\dot{q} - 3\gamma p/r^2 = 0$$

 $r\ddot{q} + 2\hat{r}\dot{q} + 2\alpha frpq + 2r\dot{\theta}\dot{p} = 0$ [10]

Received Dec. 8, 1960.

¹ Professor of Mathematics.

² Numbers in parentheses indicate References at end of paper.

Employing dashes to denote differentiations with respect to A it follows that

$$\dot{p} = p'\dot{\theta} \qquad \hat{p} = p''\dot{\theta}^2 + p'\ddot{\theta} \qquad [11]$$

and similarly for q. Eqs. 10 can accordingly be written in

$$r\dot{ heta}^2p'' + (r\ddot{ heta} + 2\dot{r}\dot{ heta})p' + \alpha fr(p^2 - q^2) - 2r\dot{ heta}^2q' - 3\gamma p/r^2 = 0$$

$$r\dot{\theta}^2q'' + (r\ddot{\theta} + 2\dot{r}\dot{\theta})q' + 2\alpha frpq + 2r\dot{\theta}^2p' = 0$$
[12]

Now let $h = r^2 \dot{\theta}$, so that

$$\alpha frq = r\ddot{\theta} + 2\dot{r}\dot{\theta} = hh'/r^3$$
 [13]

Then Eqs. 12 will be seen to be equivalent to

$$h^2p'' + hh'p' + (hh'/q)(p^2 - q^2) - 2h^2q' - 3\gamma rp = 0$$

$$hq'' + h'q' + 2h'p + 2hp' = 0$$
 [14]

Also, writing r = 1/s, it follows that

$$\dot{r} = -\frac{1}{s^2} \dot{s} = -r^2 \dot{\theta} \frac{ds}{d\theta} = -hs'$$
 [15]

and then that

$$\hat{r} = -\dot{\theta}(d/d\theta)(hs') = -hs^2(hs'' + h's')$$
 [16]

The equations of motion, Eq. 4, can now be expressed in the following form

$$hs^{2}(hs'' + h's') + h^{2}s^{3} - \gamma s^{2} = -\alpha fp/s$$
 [17]

$$hh's^3 = \alpha fq/s \tag{18}$$

Elimination of α between Eq. 17 and 18 now yields the equation

$$s'' + s = \frac{\gamma}{h^2} - \frac{h'}{h} \left(s' + \frac{sp}{q} \right)$$
 [19]

It also follows from Eqs. 3 and 8 that

$$(\alpha p)^2 + (\alpha q)^2 = s^2$$
 [20]

Eqs. 14, 19 and 20 determine the quantities p, q, h, sas functions of θ along an optimal powered arc. The equa-

$$\frac{dt}{d\theta} = \frac{1}{hs^2}$$
 [21]

then determines t and Eq. 18 yields f. We proceed to solve these equations.

The second of Eqs. 14 possesses an immediate first integral

$$h(q' + 2p) = \frac{A}{\alpha} (a \text{ constant})$$
 [22]

Also, from the general theory, it is known that the Eqs. [1] possess a first integral in the form

$$\lambda \frac{\partial V}{\partial x} + \mu \frac{\partial V}{\partial y} + \lambda \dot{x} + \mu \dot{y} = \frac{C}{\alpha} \text{(a constant)}$$
 [23]

Substituting from Eqs. 5 and setting $x = r \cos \theta$, $y = r \sin \theta$, Eq. 23 is written as

$$\dot{r}\dot{\xi} + r\dot{\theta}\dot{\eta} + \left(r\dot{\theta}^2 + \frac{\gamma}{r^2}\right)\dot{\xi} - \dot{r}\dot{\theta}\eta = \frac{C}{\alpha}$$
 [24]

Employing Eqs. 8, this is shown to be equivalent to the equation

$$r\dot{r}\dot{p} + r^2\dot{\theta}\dot{q} + \left(\dot{r}^2 + r^2\dot{\theta}^2 + \frac{\gamma}{r}\right)p = \frac{C}{\alpha}$$
 [25]

which then leads to the equation

$$ss'p' - s^2q' - \left(s^2 + s'^2 + \frac{\gamma s}{h^2}\right)p = -\frac{C}{\alpha h^2}$$
 [26]

If ψ is the angle made by the thrust and primer vectors with the perpendicular to the radius vector, then by Eq. 3

$$\xi = \frac{1}{\alpha} \sin \psi \qquad \eta = \frac{1}{\alpha} \cos \psi$$
 [27]

and hence

$$\alpha p = s \sin \psi \qquad \alpha q = s \cos \psi \qquad [28]$$

Substituting for p and q from these latter equations into Eqs. 19, 22, and 26, we obtain the following set of equations

$$s'' + s = \frac{\gamma}{h^2} - \frac{h'}{h} (s' + s \tan \psi)$$
 [29]

$$s' \cos \psi + s \sin \psi - (\psi' - 1)s \sin \psi = A/h$$
 [30]

$$h^{2}(\psi'-1)(s'\cos\psi+s\sin\psi)=\gamma\sin\psi-C/s^{2}$$
 [31]

determining s, h, ψ as functions of θ .

We now introduce a quantity w defined by the equation

$$w = h(s'\cos\psi + s\sin\psi)$$
 [32]

Since $h = r^2 \dot{\theta}$ and s = 1/r

$$w = r\dot{\theta}\sin\psi - \dot{r}\cos\psi \tag{33}$$

indicating that w is the component of the rocket's velocity perpendicular to the direction of the thrust. In terms of w, Eqs. 29-31 will be found to take the form

$$w' + h(\psi' - 1)(s'\sin\psi - s\cos\psi) = (\gamma/h)\cos\psi$$
 [34]

$$w - h(\psi' - 1) \cdot \sin \psi = A, \tag{35}$$

$$hw(\psi' - 1) = \gamma \sin \psi - C/s^2$$
 [36]

Employing Eq. 36 to eliminate $h(\psi' - 1)$ from Eqs. 34 and 35, this pair of equations can be written

$$ww' + \left(\gamma \sin \psi - \frac{C}{s^2}\right) (s' \sin \psi - s \cos \psi) = \frac{\gamma w}{h} \cos \psi,$$
[37]

$$w^2 - (\gamma \sin \psi - C/s^2)s \sin \psi = Aw$$
 [38]

h is now eliminated from the set of Eqs. 36-38 by reference to Eq. 32. The resulting set of equations can be expressed

$$w^{2}(\psi'-1) = [(\gamma/r^{2})\sin\psi - C](r\sin\psi - r'\cos\psi) \quad [39]$$

$$ww' + C(r'\sin\psi + r\cos\psi) = (\gamma/r^2)\{r'(\sin^2\psi - \cos^2\psi) + 2r\sin\psi\cos\psi\}$$
 [40]

$$w + \frac{1}{w} \left(Cr - \frac{\gamma}{r} \sin \psi \right) \sin \psi = A \tag{41}$$

This set of equations determines r, w, ψ as functions of θ . If Eq. 41 is differentiated with respect to θ and if ψ', w' are eliminated between the resulting equation and Eqs. 39 and 40, the result will be found to reduce to

$$w^{2}(\cos^{2}\psi - 2\sin^{2}\psi) = \frac{r}{\gamma}\left(Cr - \frac{\gamma}{r}\sin\psi\right)^{2} \quad [42]$$

This equation and Eq. 41 now determine r and w as functions of ψ without further integration. Substitution of these functions in Eq. 39, solution for $d\theta/d\psi$ as a function of ψ and an integration, yields θ as a function of ψ . The family of optimal powered ares is then known and depends upon three parameters, i.e., A, C and the constant of integration for θ .

It has been proved in the general theory that, if the times

of departure and arrival are not assigned and the propellant expenditure is to be minimized with respect to the time of transit, then the constant C is zero over the whole optimal trajectory. In this, the usual case, Eqs. 39, 41 and 42 are easily solved to yield

$$w = (\gamma/a)^{1/2} \csc^2 \psi \tag{43}$$

$$r = a \sin^6 \psi / (1 - 3 \sin^2 \psi)$$
 [44]

$$\theta = \theta_0 - 4\psi - 3\cot\psi \qquad [45]$$

where $a = 9\gamma/A^2$ and θ_0 is an arbitrary constant. All questions concerning the nature of a powered arc can now be decided without difficulty. Eqs. 44 and 45 indicate that

such an arc is part of a spiral unwinding from the center of attraction and this trajectory presumably enters into the solution to the problem of optimal escape from a circular orbit which has already received attention elsewhere (5,6).

References

1 Lawden, D. F., Advances in Space Science I, chap. 1, Academic Press, N. Y., 1959.
2 Lawden, D. F., "Necessary Conditions for Optimal Rocket Trajectories," Quart. J. Mech. Appl. Math., vol. 12, 1959, p. 476.
3 Lawden, D. F., "Inter-Orbital Transfer of a Rocket," J. Brit. Interplanet. Soc., vol. 11, 1952, p. 321.

4 Leitmann, G., private communication, Nov. 1960.
5 Michielsen, H. F., "The Case for the Low Acceleration Space Ship,"
Astronautica Acta, vol. 3, 1957, p. 130.
6 Lawden, D. F., "Optimal Escape from a Circular Orbit," Astronautica
Acta, vol. 4, 1958, p. 218.

Technical Comments

Magnetic Compensation of Satellites

ROY G. BRERETON¹

Aerojet-General Corp., Azusa, Calif.

A discussion of a technique for increasing the compatibility of magnetic experiments with other types of experiments and equipment in a satellite is presented.

WITH THE advent of larger Earth satellites, and the desirability of incorporating many types of scientific space experiments into each satellite, ways must be found to enhance the compatibility of individual experiments. For example, measurements of planetary, solar and cosmic magnetic fields must be made to an accuracy of approximately one gamma (1 gamma = 10⁻⁵ Gauss), in order to be of scientific value; however, magnetic measurements are easily influenced by other experiments, telemetry equipment, power supplies, and even the satellite itself. Thus, ways must be developed to compensate the immediate space around the magnetometer sensor for these anomalous effects, or they must be reduced by proper design of the carrier vehicle and careful placement of its components. In the event that proper design and careful placement of components is not a practical solution for eliminating all of the undesirable magnetic effects, compensation of the magnetometer sensor must be considered.

The compensation process consists of creating in the immediate space around the sensing element of the magnetometer a magnetic field that accurately balances the disturbing field produced by the satellite. These disturbing fields are due to both induced and permanent magnetism. Permanent magnetism results from d-c circuits and ferromagnetic components in the satellite, whereas induced magnetic effects are caused by the action of ambient magnetic fields on components of the satellite, and the satellite shell itself, and are thus more variable and difficult to compensate

Permanent Magnetism

As indicated earlier, these effects are caused by d-c circuits and ferromagnetic components in the circuitry and structure of the satellite. Magnetic effects from d-c circuits are easily eliminated by providing a dual current path consisting of twin leads loosely twisted together, whereas the perm resulting from current effects on coils and other such components and from the effect of magnetized structures must be reduced by a so-called system of Helmholtz coils. These can be formed from a fraction of an ounce of wire arranged into three orthogonal loops (axial, vertical and transverse) about the sensing head of the magnetometer. The magnitude of the compensating current in the Helmholtz coils would depend on the perm of the satellite.

Induced Fields

These fields can be effectively reduced by placing ferrous compensators of a computed shape and effect, contiguous to the sensing element of the magnetometer. Thus, from knowledge of the shape and position of induced fields in and around the satellite, the shape and location of a single ferrous compensator can be determined that will produce the same induced magnetic field as all of the induced fields of the satellite. When the shape and location of the primary compensator has been determined, two similar compensators can be added to the system to cancel the induced fields produced by the first. The fact that three similarly shaped compensators would produce zero field at the magnetometer element can be demonstrated by observing that any field applied to the system can be resolved along three perpendicular axes (x, y, z), and that each of these components produces an effective magnetic dipole at each of the three compensators. If these dipoles are all equal and equally spaced from the detector, the sum of their fields at the magnetometer sensor must be

Received Nov. 14, 1960.

¹ Senior Geophysicist, Advanced Research Division.

Compensation Procedure

of

it

-

11

d

ts

ie

h

28

s.

r-

d

г.

lS

0

d

IS

e

1-

ŀ

e

y

n

e

),

e

r,

A procedure for adjusting the magnetic compensation of the satellite follows. This compensation process must be carried out in a test area offering a known and very smooth magnetic field gradient and equipped with sensitive magnetic field monitoring equipment. Such facilities can be prepared at any test site; however, they are presently available at Fredericksburg, Va. under the sponsorship of the U. S. Coast and Geodetic Survey, or near Bedford, Mass., under the direction of the Air Force Cambridge Research Center.

In a practical design, the magnetometer sensor would be located at the end of a boom or appendage projecting from the main body of the satellite. The axial Helmholtz coil would be arranged to produce a magnetic field along the axis of the boom, the transverse coil would produce a magnetic field along the lateral or horizontal axis of the satellite, and the third coil would function in the vertical direction.

The first step is to place the satellite in the test area on a north and then on a south heading, taking special care to locate the sensing head of the magnetometer over the same point on each heading. The total field intensity (F_N) and

 F_S) should be read from the magnetometer for each heading. The current in the axial Helmholtz coil should now be adjusted to change F by $1/2(F_N-F_S)$. The direction of the current should be such as to make the F indication equal the average value of F_N and F_S . The satellite should next be placed on an east and then on a west heading and the transverse coil current adjusted to produce a change in F equal to $1/2(F_E-F_F)$.

This procedure should be repeated until $(F_N - F_S)$ and $(F_E - F_W)$ are reduced to approximately one gamma. If this cannot be accomplished, the current in the vertical coil must be adjusted by rolling the satellite about its axial axis.

The difference of $(F_N + F_s)/2 - (F_E + F_w)/2$ is a measure of the induced field produced at the magnetometer by ferrous parts of the satellite; however, it should be realized that the total induced field will be a function of this value plus induced magnetic effects from eddy currents caused by the motion of the satellite.

Where an accuracy of the order of one or two gammas is desired for satellite magnetic studies, ferrous induction compensators will be required.

Book Notes

Mechanics of Solids and Fluids, Long, Robert R. (Professor, Department of Mechanics, The Johns Hopkins University), Prentice-Hall, Inc., Englewood Cliffs, N. J., 1961, 145 pp. \$9.

Chapters: 1. Vectors and Tensors; 2. Stress in a Continuous Medium; 3. Deformation and Flow; 4. Materials and Their Mechanical Properties; 5. The Equations of Elastic Solids; 6. Problems in Linear Elasticity; 7. Equations of Fluid Mechanics; 8. Problems of Fluid Statistics and Dynamics.

This book places primary emphasis on the rigorous, but plausible, development of the equations of motion of elastic solids and Newtonian fluids. Providing a detailed treatment of vector operations and an intensive coverage of Cartesian tensors, the book gives the reader important and valuable tools for dealing with fundamental concepts in the statics and dynamics of solids and fluids.

Progress in Combustion Science and Technology, Volume 1, edited by Ducarme, J., Gerstein, Melvin and

The books listed here are those recently received by the ARS from various publishers who wish to announce their current offerings in the field of astronautics. The order of listing does not necessarily indicate the editors' opinion of their relative importance or competence.

Lefebvre, A. H., Pergamon Press, New York, 1960, 226 pp. \$10

York, 1960, 226 pp. \$10.

Contents: "Flow Visualization Techniques," by E. F. Winter; "Chemical Analysis in Combustion Chamber Development," by B. Toone; "Aerodynamic Influences on Flame Stability," by M. V. Herbert; "Geometric-Optical Techniques in Combustion Research," by F. J. Weinberg; "Flame Quenching," by A. E. Potter Jr.; "Ignition in Liquid Propellant Rocket Engines," by E. A. Fletcher and G. Morrell.

This volume is the first of a series of annual volumes that will contain review articles specially commissioned covering the whole field of propulsion and combustion as related to aeronautics.

Spaceflight Technology, edited by Gatland, Kenneth W., Academic Press, New York, 1960, 365 pp. \$11.

Contents: Programs and Economics, papers by John E. Allen, Derek Wragge Moreley, T. R. F. Nonweiler, P. A. Lapp and A. E. Maine; Launching Vehicles, papers by W. T. Fisher, H. J. Higgs, G. K. C. Pardoe, O. H. Wyatt; Aero/Space Vehicles and Re-Entry, papers by H. R. Watson, D. J. Shapland, D. E. Bailey; Propulsion Systems, paper by W. F. Hiton; Space Vehicle Cabins, paper by George Beardshall and Peter W. Fitt; Instrumentation, papers by P. Barratt, D. Rothwell and B. V. Somes-Charlton;

Tracking and Communication, papers by J. H. Thomson and A. P. Willmore; Navigation, paper by P. R. Wyke; Exploration of the Moon, paper by D. S. Carton.

This volume contains the proceedings of the first Commonwealth Spaceflight Symposium organized by the British Interplanetary Society and held in London in 1959.

Aeronautics and Astronautics, edited by Hoff, Nicholas J. and Vincenti, Walter G., Pergamon Press, New York, 1960, 460 pp. \$12.

Contents: Papers by Sir Jeffrey Taylor, Richard R. Heldenfels, Luigi Broglio, W. F. Thielemann, G. N. Patterson, H. W. Liepmann, Leslie S. G. Kovásznay, H. de L'Estoile and L. Rosenthal, Von R. Eshleman, Jan Hult, J. F. Besseling, Wilfred H. Dukes, J. M. Burgers, Francis H. Clauser, Antonio Ferri, H. Julian Allen, Samuel Herrick and W. B. Klemperer. Also contained are introductory remarks by Theodore Von Kármán, Hugh L. Dryden, Frederick E. Terman and Colonel Raymond A. Gilbert.

This volume contains the scientific proceedings of the conference held at Stanford University in 1959 to celebrate the 100th anniversary of the birth of William Frederick Durand.

Thermal Reactor Theory, Galanin, A. D. (translated from Russian by J. B. Sykes). Pergamon Press, New York, 1960, 412 pp.

\$15.

Chapters: 1. Diffusion and Slowing Down of Neutrons; 2. The Critical Size of a Reactor on One-Group Theory; 3. Multiplication, Slowing-Down and Diffusion in a Homogeneous Medium; 4. Heterogeneous Reactors; 5. The Critical Size of a Reactor; 6. Perturbation Theory; 7. The Time Variation in the Isotopic Composition of Nuclear Fuel; 8. Delayed-Neutron Kinetics, the Temperature Coefficient, and Control; 9. The Use of the Boltzmann Equation; 10. The Theory of Heterogeneous Reactors.

This book is intended for use by scientists working in, or learning, the subject of reactor physics: it fills the need for a practical volume that will be valuable to all reactor physicists and technologists. The mathematical physics of the various aspects of the subject is discussed in the first part of the book, the detailed mathematical arguments being left to the second

Propulsion Systems for Space Flight, Corliss, William R. (Nuclear Division, The Martin Company), McGraw-Hill Book Company, Inc., New York, 1960,

300 pp. \$10.

Chapters: 1. Introduction; 2. Propulsion-System Performance and Space Missions: 3. The Environment of Space; 4. Power Generation in Space; 5. Thermal Propulsion Systems; 6. Electrical Propulsion Systems; 7. Nuclear-Particle Generators; 8. Photonic Propulsion Systems; 9. Propulsion Systems Using Natural Force Fields; 10. Summary and Evaluation.

This book offers a survey and an evaluation of the manifold schemes that have been proposed for transportation in space. Largely nonmathematical, it originated in a course on advanced propulsion concepts that the author presented at the General Electric Company in 1958, and has since been brought up to date.

Boolean Algebra and Its Applications, Whitesitt, J. Eldon (Associate Professor of Mathematics, Montana State College), Publishing Company, Addison-Wesley Inc., Reading, Mass., 1961, 182 pp. \$6.75.

Chapters: 1. The Algebra of Sets; 2. Boolean Algebra; 3. Symbolic Logic and the Algebra of Propositions; 4. Switching Algebra; 5. Relay Circuits and Control Problems; 6. Circuits for Arithmetic Computation; 7. Introduction to Probability in Finite Sample Spaces.

The purpose of this book is to introduce Boolean algebra on a level which will make it available even to those with rather limited mathematical background, and to examine each of its applications and give the reader an appreciation of the scope and usefulness of the subject. Developed out of notes used in the past two years in a course at Montana State College, it is especially designed to be used in a one-semester course for students of mathematics and engineering; it may also serve as a reference for scientists and engineers concerned with computer design, control systems or electronic circuitry.

Radio Waves in the Ionosphere: The Mathematical Theory of the Reflection of Radio Waves from Stratified Ionised Layers, Budden, K. G. (Fellow of St. John's College and Lecturer in Physics, University of Cambridge), Cambridge University Press, London, England, 1961,

542 pp. \$18.50.

Chapters: 1. Introduction; 2. The Basic Equations; 3. The Constitutive Relations; 4. Propagation in a Homogeneous Isotropic Medium; 5. Propagation in a Homogeneous Anisotropic Medium. Magnetoionic Theory; 6. Properties of the Appleton-Hartree Formula; 7. Definition of the Reflection and Transmission Coefficients; 8. Reflection at a 9. Slowly Varying Sharp Boundary; Medium. The W.K.B. Solutions; Ray Theory for Vertical Incidence When the Earth's Magnetic Field Is Neglected; 11. Ray Theory for Oblique Incidence When the Earth's Magnetic Field Is Neglected; 12. Ray Theory for Vertical Incidence When the Earth's Magnetic Field Is Included; 13. Ray Theory for Oblique Incidence When the Earth's Magnetic Field Is Included; 14. The General Problem of Ray Tracing; 15. The Airy Integral Function, and the Stokes Phenomenon; 16. Linear Gradient of Electron Density; 17. Various Electron Density Profiles When the Earth's Magnetic Field Is Neglected; 18. Anisotropic Media. Coupled Wave-Equations and W.K.B. Solutions: 19. Applications of Coupled Wave-Equations; 20. The Phase Integral Method: 21. Full Wave Solutions When the Earth's Magnetic Field Is Included; 22. Numerical Methods for Finding Reflection Coefficients; 23. Reciprocity.

Based on a course of lectures given annually in Cambridge since 1956, and repeated in 1957 at the U.S. National Bureau of Standards Laboratories, Boulder, Colo., the book is designed to be used both as a text-book, for those comparatively new to the subject, and as a reference book for more experienced readers. (Some of the more advanced topics are printed in smaller type and could be omitted on a first reading.) Throughout the book the stress is on the understanding of the mathematical methods rather than on their immediate practical use. The reader is assumed to be familiar with calculus, the theory of complex variables, vectors including the operators div, curl, grad, and electromagnetic theory as far

as Maxwell's equations.

Electro-Erosion Machining of Metals Livshits, A. L. (Cand. Tech. Sc.), translated by E. Bishop, edited by R. S. Bennet, Butterworth Inc., London, in association with the Department of Scientific and Industrial Research, 1960 (orig. publ. in Russian, Moskow, 1957), 115 pp. \$5.75.

Chapters: 1. Physical Conditions for Cutting by the Electro-Erosion Process; 2. The Generation of Current Pulses; 3. Automatic Control of the Machining Process; 4. Electrotechnological Characteristics; 5. Machine Tools for Dimensional Electro-Erosion Machining of

The information given in this book constitutes a complete and up-to-date descrip-

tion of the state of the technique, technology and industrial uses of electro-erosion machining. Importance has been placed on electropulse methods rather than electro-spark methods. The book is intended for use by engineering and technical workers in industry, scientific research institutes and laboratories

Sequential Decoding, Wozencraft, John M. (Associate Professor of Electrical Engineering, Massachusetts Institute of Technology) and Reiffen, Barney (Lincoln Laboratory, Massachusetts Institute of Technology, Technology Press of MIT and John Wiley & Sons, Inc., N.Y., 1961, 74 pp. \$3.75.

Chapters: Coding and Communication; 2. Block Codes: 3. Sequential Decoding: 4. Convolutional Encoding; 5. Simulation; 6. Extensions and Applications. Appendix: Bounds on Sums of Random

Variables

One of a series of Technology Press "Research Monographs," this book is essentially a report on research done by the authors. It will interest communications systems engineers, data processing engineers and information theorists.

Rocket Development: Liquid-Fuel Rocket Research, 1929-1941, Goddard, Robert H., edited by Esther C. Goddard and G. Edward Pendray, Prentice-Hall, Inc., Englewood Cliffs, N. J., 1961, 222 pp. Spectrum paperback edition, \$2.45; cloth edition. \$3.95.

Originally published in 1945, the year of Dr. Goddard's death, the book contains Dr. Goddard's own condensations of his experimental notebooks for the period from 1929 to 1941. This edition includes, as an introduction, Dr. Pendray's biographical essay on Dr. Goddard entitled, "The Man Who Ushered in the Space

The Mathematical Theory of Non-Uniform Gases: An Account of the Kinetic Theory of Viscosity, Thermal Conduction, and Diffusion in Gases, Chapman, Sidney and Cowling, T. G., Cambridge University Press, London, England, 1960 (orig. publ. 1939), 431 pp. Paperback reprint,

Physics, the Pioneer Science, Taylor, Lloyd William, Dover Publications, Inc., N. Y., 1959 (orig. publ. 1941). Paperback reprint in two volumes: Vol. 1, Mechanics, Heat, Sound, pp. 1-395, \$2. Vol. 2, Light, Electricity, pp. 396-847, \$2.

The Life and Death of Cells, Hoffman, Joseph G., Doubleday & Company, Inc., Garden City, N. Y., 1961 (orig. publ. 1957), 354 pp. Dolphin paperback reprint, \$0.95.

The Origin of Species by Means of Natural Selection, or the Preservation of Favored Races in the Struggle for Life, Darwin, Charles, Doubleday & Company, Inc., Garden City, N. Y., 1961, 517 pp. Dolphin paperback reprint, \$0.95.

n

n

n

(F)

George F. McLaughlin, Associate Editor

Gondola used in high altitude research (2,952,378). L. C. Renslow, St. Paul, Minn.

Pair of concave body portions with outwardly extending flanges about their marginal edges. Made with laminations of glass cloth impregnated with a resin.

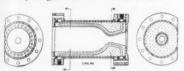
Missile gyro alignment system (2,952,-779). R. M. Talley, Santa Barbara, Calif., assignor to the U. S. Navy.

Synchro transmitter and receiver connecting a missile gyro and a remote master gyro. An electro optical system directs collimated light to a detector to show misalignment.

Missile velocity indicating system (2,-952,846). J. D. Tear, J. V. D'Onofrio, H. F. McKenney, R. D. Gross and F. J. McKeown, Brooklyn, N. Y., assignors to Ford Instrument Co., Div. of Sperry Rand Corp. (ARS corporate member).

Radar at a ground station for providing the range, elevation angle and azimuth angle of an oscillator on an airborne missile. Computing equipment shows the velocity of the oscillator.

Fluid cooled homogeneous ceramic rocket motor wall structure (2,956,399). C. M. Beighley (ARS member), Fair Oaks, Calif., assignor to the U. S. Air Force.



Cast wall structure utilizing a specially selected ceramic or refractory material of high thermal conductivity and near zero coefficient of expansion.

Fuel for and method of operating a jet engine (2,959,915). K. L. Dille and H. E. Vermillion, Wappingers Falls, N. Y., assignors to Texaco Inc.

Engine lubricant cooled by indirect heat exchange with a composition of hydrocarbon stock, and then using the hydrocarbon for fuel.

Supersonic inlet (2,959,916). W. W. Carlton and G. A. Sears, Encino, Calif., assignors to the Marquardt Corp. (ARS corporate member).

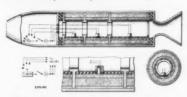
Spike means in fixed relationship to a cowl for imparting to the oncoming air a velocity of flow parallel to the spike and transverse to the original direction of the oncoming air.

Sound suppressor for jet engine (2,959,-917). R. L. McGehee, Derby, Kans., assignor to Boeing Airplane Co. (ARS corporate member).

Outside air injects and is mixed with exhaust gas, producing oblique shock waves, part of which interact at the center of the body, thereby effecting sound reduction.

EDITOR'S NOTE: Patents listed above were selected from the Official Gazette of the U. S. Patent Office. Printed copies of patents may be obtained from the Commissioner of Patents, Washington 25, D. C., at a cost of 25 cents each; design patents, 10 cents.

Variable thrust rocket motor (2,956,401). E. M. Kane, Oxnard, Calif.



Solid propellant motor, the thrust of which can be adjusted to desired value before firing. Adjustment is controlled from a remote station.

Gas impingement starter nozzle for turbines (2,959,919). J. A. Chiera and B. J. Gedrewicz, Lynnfield Center, Mass., assignors to General Electric Co. (ARS corporate member).

Pair of radially inclined walls extending from an outer nozzle diaphragm to form a chute. Gas flow under pressure is directed into nozzle spaces on the chute.

Launcher (2,960,009). R. F. Hereth, R. S. Chamberlin, and J. F. Sample, Bremerton, Wash., assignors to the U. S. Navy.

Shipboard launcher for rocket propelled missiles mounted on a gun turret whereby the gun firing axis may be disposed of at a desired elevation.

Rocket cluster (2,960,033). L. D. Jackson, Alexandria, Va.

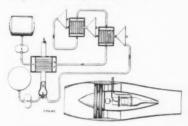
Auxiliary casings having opposite ends adaptable to be releasibly secured to the main casing. Impact of the rocket with the target fires explosives in predetermined time delay relation.

Balloon seal having load bearing element (2,960,282). O. C. Winzen (ARS member), Minneapolis, Minn., assignor to Winzen Research, Inc.

Adjacent edges of gores extending from the apex to the appendix are externally positioned to produce a finned juncture. Linear load bearing assemblies extend through substantial portions of the juncLaunching carriage for jet propelled missiles (2,960,034). C. W. Besserer Jr.. Silver Spring, Md., assignor to the U. S. Navy.

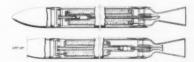
Plurality of rockets with their axes parallel to that of the missile. A centering member releasably engages the rear end of the missile.

Multistage high altitude engine (2,956,-402). R. S. Rae (ARS member), Los Angeles, Calif., assignor to the Garrett Corp. (ARS corporate member).



Hydrogen on its way to the engine stages is passed through a first heat exchanger which is also connected to the single combustion chamber. The hydrogen is heated to a temperature higher than that which could be withstood by any stage of the engine.

Powder propellant rocket motors (2,957,307). E. M. Brandenberger (ARS member) and E. Tanner, Asheville, N. C., assignors to Amcel Propulsion, Inc.



A charge contracts or expands in length in response to changing ambient temperature. Changing length causes an associated member to move, varying the effective exhaust area of the nozzle.

CHANGE-OF-ADDRESS NOTICE

In the event of a change of address, it is necessary to include both your old and new addresses, as well as your membership number and coding, when notifying ARS headquarters, in order to insure prompt service. If you are moving or have moved, send the following form to Membership Dept., American Rocket Society, 500 Fifth Ave., New York 36, N. Y.:

Membership Card No.	Coding	
New Address		

Technical Literature Digest

M. H. Smith, Associate Editor

The James Forrestal Research Center, Princeton University

Propulsion and Power (Combustion Systems)

Measured Base Pressures on Several Rocket-Nozzle Configurations at Mach Numbers of 0.6 to 1.4 with Effects Due to Nozzle Canting and Stabilizing Fins, by James M. Cubbage and Earl H. Andrews Jr., NASA TN D-544, Oct. 1960, 19 pp.

Conference on Aviation and Astronautics, 2nd, February 9-10, 1960, Tel-Aviv and Haifa, Proceedings, (Reprint from Bull. Res. Council of Israel, vol. 8c, Feb. 1960, no. 1), 57 pp.

A Hypersonic Ramjet Using Normal

Detonation Wave, by M. Arens, pp. 25-35.

Measurements of the Accuracy of a Data Acquisition System, by W. A. Hendricks and William Bernard Jr., JANAF Solid Propellant Rocket State Test Panel, 9th Meeting, Oct. 1960, Bull. Addendum, (Solid Propellant Info. Agency, Pub. no. SPSTP/9A), Oct. 1960, 7 pp., 6 fee.

A Further Report on the Westcott Digital Recording and Analysis System, by W. R. Beakley and D. S. Dean, JANAF Solid Propellant Rocket Static Test Panel, 9th Meeting, Oct. 1960, Bull. Addendum, (Solid Propellant Info. Agency, Pub. no. SPSTP/9A), Oct. 1960, 12 pp.

Static Testing Instrumentation Accuracy Capabilities, by B. V. Diercks and L. L. Hart, JANAF Solid Propellant Rocket Static Test Panel, 9th Meeting, Oct. 1960, Bull. Addendum, (Solid Propellant Info. Agency, Pub. no. SPSTP/9A), Oct. 1960, 14 pp.

The Reliability of Multiple Rocket Engines, by Gillian Ruston, Aeron. Qtly., vol. 9, part 4, Nov. 1960, pp. 371–386.

Effect of Nozzle Convergence Length on

Effect of Nozzle Convergence Length on Performance of a Heptane-Oxygen Combustor, by Marshall C. Burrows, NASA TN D-579, Dec. 1960, 22 pp.
Internal-Performance Evaluation of Two Fixed-Divergent-Shroud Ejectors, by James R. Mihaloew, NASA TN D-763, Jan. 1961, 30 pp.

Internal-Performance Evaluation of a Two-Position-Divergent Shroud Ejector, by James R. Mihaloew and Andrew J. Stofan, NASA TN D-762, Jan. 1961, 19

Manned Space Stations Symposium, Los Angeles, April 20-22, 1960, N. Y Inst. Aeron. Sciences, 1960, 322 pp. The Use of Chemical Power Systems in the Construction, Servicing and Operation of Manned Space Stations, by H. J. Howard and R. M. Laugh-lin, pp. 254-258.

Some Aspects of Underwater Jet Propulsion Systems, by C. A. Gongwer, ARS JOURNAL vol. 30, no. 12, Dec. 1960, pp. 1148-1151.

EDITOR'S NOTE: Contributions from Professors E. R. G. Eckert, E. M. Sparrow and W. E. Ibele of the Heat Transfer Laboratory, University of Minnesota, are gratefully acknowledged.

The Optimum Size of a Rocket Engine, by J. E. P. Dunning, Royal Aeron. Soc., vol. 64, no. 600, Dec. 1960, pp. 717-735.

Propulsion and Power (Non-Combustion)

Analytical Investigation of Cycle Characteristics for Advanced Turboelectric Space Power Systems, by Thomas P. Moffitt and Frederick W. Klag, NASA TN D-472, Oct. 1960, 29 pp.

Power Supply Design Parameter Study for Electromagnetic Detonations (Phase I), by K. M. Forman, Republic Aviation Corp., Plasma Propulsion Lab., PPL-Tech. Rep. 60-3, (AFOSR TN 60-1198), Aug. 1960, 17 pp.

Zur Mathematischen Theorie der Nichtgleichgewichtsvorgange in Plasma, by A. Koller, Forschungsinstitut für Physik der Strahlantriebe, Stüttgart, Mitteilungen no. 22, May 1960, 161 pp., 59 refs.

Thermoelectricity, including the Proceedings of the Conferences on Thermoelectricity sponsored by the Naval Re-search Lab., Sept. 1958, Paul H. Egli, ed., N. Y., John Wiley & Sons, 1960, 407 pp.

The Impact of Thermoelectricity upon Science and Technology, by C. Zener, pp. 3-22.

Some Considerations of the Basic Physics of Thermoelectric Effects, by Werner B. Teutsch, pp. 23–29.

Thermoelectric Device Design, by Gerhard C. Stoll, Robert L. Eichorn and Richard G. Sickert, pp. 30–46.

Some Considerations of the Problems of Minimizing the Weight of Thermopile Generators in Space Applications, by D. L. Kerr and R. L. Gessner, pp. 47-76.

Experimental Investigations of the Cesium Plasma Cell, by W. A. Ranken, G. M. Grover and E. W. Salmi, J. Appl. Phys., vol. 31, no. 12, Dec. 1960, pp. 2140-2153.

Atoms and Space, by H. L. Dryden, Spaceflight, vol. 2, no. 8, Oct. 1960, pp. 226-229.

Electric Power Generation Systems for Use in Space, by Henry O. Slone and Seymour Lieblein, Internat. Council Aeron. Sci., Second Internat. Congress, Zurich, Sept. 12-16, 1960, 25 pp., 9 figs.

The Linear Acceleration of Large Masses by Electrical Means, by Knox Millsaps and Karl Pohlhausen, Air Force Missile Dev. Center, TR-60-11, June 1960, 27 pp., 6 refs.

An Ion Rocket with an Electron Bombardment Ion Source, by Harold R. Kaufman, NASA TN D-585, Jan. 1961,

Fundamental Investigation of Electrical Power- Sources for Electric Thrust De-vices, by Helen Fife, Plasmadyne Corp. TN no. E-2TNO98-332 (AFOSR TN 58-791) (ASTIA AD 202,224), Sept. 1958,

The U. S. Ion Propulsion Program, by Capt. Richard Hayes, ARS JOURNAL, vol. 30, no. 12, Dec. 1960, p. 30.

Advances in Electrostatic Propulsion, by A. T. Forrester and J. M. Teem, ARS JOURNAL, vol. 30, no. 12, Dec. 1960, p. 34.

Measurement of Ion Currents in Ion-Acceleration Systems, by V. A. Egorov, D. V. Karetnikov and S. N. Popov, *Electronics*, vol. 34, no. 1, Jan. 6, 1961, pp. 331–333.

Device for Generating a Low Temperature, Highly Ionized Cesium Plasma, by Nathan Rynn and Nicola D'Angelo, Rev. Scientific Instruments, vol. 31, no. 12, Dec. 1960, pp. 1326-1335.

Manned Space Stations Symposium, Los Angeles, April 20-22, 1960, N. Y. Inst. Aeron. Sciences, 1960, 322 pp.

A Comparison of Nuclear and Solar Power Systems for Manned Space Sta-tions, by W. C. Cooley, pp. 207-213. Integrated Thermodynamic Systems for Manned Space Stations, by M. G. Del Duca, A. D. Babinsky and F. D. Mir-

aldi, pp. 214-230.

Utilization of Plasma Cell Energy Conversion in Nuclear Reactors, by W. A. Ranken and T. G. Frank, pp. 231-240. A Circulating Dust-Fueled, Radiation Cooled Space Power Reactor, by W. R. Corliss, pp. 241–253.

Propellants and Combustion

Solid Propellant Detonability, by Adolph B. Amster, Evan C. Noonan and George J. Bryan, ARS JOURNAL, vol. 20, Oct. 1960, pp. 960–963.

Methane-Oxygen Flame Structure. I. Characteristic Profiles in a Low-pressure, Laminar, Lean Premixed Methane-Oxygen Flame, by R. M. Fristrom, C. Grunfelder and S. Favin. J. Phys. Chem., vol. 64, Oct. 1960, pp. 1386–1392.

Methane-Oxygen Flame Structure. II. Conservation of Matter and Energy in the One-tenth Atmosphere Flame, by A. A. Westenberg and R. M. Fristrom, J. Phys. Chem., vol. 64, Oct. 1960, pp. 1393–1406.

The Reaction Between Oxygen Atoms and Diborane, by Francis P. Fehlner and Robert L. Strong, J. Phys. Chem., vol. 64, Oct. 1960, pp. 1522–1529.

Determination of Flame Velocities in Gaseous Predetonation, by G. J. Hecht, A. J. Laderman, and R. A. Stern, et al., Rev. Sci. Instr., vol. 31, Oct. 1960, pp. 1107-1111.

A Method for Detecting Hydrogen in Gas Mixtures, by J. R. Young and N. R. Whetten, Rev. Sci. Instr., vol. 31, Oct. 1960, рр. 1112-1113.

The Laws of Thermal Emission of a Flame, by B. I. Plyukhin, Soviet Physics: Doklady, vol. 5, Sept.-Oct. 1960, pp. 279-

Structure of Gaseous Detonation in Tubes, by Yu. N. Denisov and Ya. K. Troshin, Soviet Physics; Tech. Physics, vol. 5, no. 4, Oct. 1960, pp. 419-431.

Charge Transfer Between Atomic Hydrogen and N⁺ and O⁺, by R. F. Stebbings, Wade L. Fite and David G. Hummer, J. Chem. Phys., vol. 33, Oct. 1960, pp. 1226High Temperature Equilibria Involving Metallic Halides, by L. J. Gordon, ARS JOURNAL, vol. 20, Oct. 1960, p. 978.

A Nomograph for Boiling Temperature by the Meissner Method, by R. J. Sieraski and G. M. Machwart, Ind. Engng. Chem., vol. 52, Oct. 1960, pp. 869–872.

A Relativistic Transport Equation for a Plasma, II, by Yu. L. Klimontovich, Soviet Physics: Doklady, vol. 5, Sept.-Oct. 1960, pp. 876-882.

r

1

.

).

١,

Cryogenics—A Survey, by A. Juster and P. K. Shizume, *IRE Trans. on Component Parts*, vol. CP-7, no. 1, March 1960, pp. 26-33.

Application of Molecular Beam Techniques to the Study of Inelastic Molecular Collision Phenomena in Gases, by John E. Scott Jr., *Project Squid, Tech. Rep* UVA-1-P, June 1960, 16 pp.

On the Structure of Plane Detonation Waves, by T. C. Adamson Jr., Project Squid, Tech. Rep. MICH-6-P, June 1960, 38 pp. (also Phys. Fluids, vol. 9, Sept.-Oct. 1960, pp. 706-719).

The Interaction of Atoms with Solid Surfaces, by Bernard J. Wood and Henry Wise, *Project Squid*, *Tech. Rep.* SRI-8-P, Aug. 1960, 15 pp.

The Structure of Gaseous Detonation Waves, by James A. Fay, Project Squid, Tech. Rep. MIT-23-P, Aug. 1960, 34 pp.

Ignition by Hot Gases, by M. Vanpee and H. G. Wolfgard, *Project Squid, Tech. Rep.* BUM-30-R, Aug. 1960, 12 pp.

A Research Study to Advance the State of the Art of Solid Propellant Grain Design, by Thiokol Chemical Corp, Rep. no. E132-60 (Quarterly Progress Rep. no. 4), July 1960, 28 pp. (E132-60)

Burning Velocities of the Hydrogen Peroxide Decomposition Flame, by Charles N. Satterfield and Ephraim Kehat, MIT, Dept. of Chem. Engng., Rep. no. 56, Sept. 1960, 26 pp.

Storage Distribution, and Dispersing of Aircraft and Vehicular Fuels, Army Corps of Engineers, EM 1110-345-332, July 1960.

A Study of the Encapsulation of High Energy Substances, by Ernest F. Hare, National Cash Register Co., Fundamental Res. Dept., Interim Rep. no. 1, July 1960, 13 pp.

Diffusion and Heterogeneous Reaction. V. Measurement of the Kinetics of Hydrogen Atom Recombination on Surfaces, by Bernard Wood and Henry Wise, *Project Squid, Tech. Rep.* SR 1-7-P, July 1960, 37 pp.

Contact Surface Tailoring in a Chemical Shock Tube, by H. B. Palmer and B. E. Knox, Project Squid, Tech. Rep. PSU-7-P, Aug. 1960, 6 pp.

International Astronautical Congress, 10th, London, 1959, Proceedings, F. Hecht, ed., Springer-Verlag, Vienna, 1960, 2 vols., pp. 1–504 and 505–946.

Theoretical and Experimental Study of Fuel Mixtures; Measurement of Combustion Products, by Lucien Reingold, vol. 1, pp. 352-369. (In French.)

Symposium on Detonation, 3rd, Princeton, 1960, James Forrestal Research Center, Princeton University, Sept. 26–28, 1960, co-sponsored by Naval Ordnance Laboratory, White Oak, and Office of Naval Research. *ONR Symposium Report* ACR-52, Oct. 1960, 2 vols. incl., 659 pp.

A Colliding Ball High Explosive Impact Sensitivity Testing Machine, by C. M. Bean, pp. 1–9. A Photographic Study of Explosions Initiated by Impact, by J. Wenograd, pp. 10-23.

Pure Environmental Shock Testing of Condensed Phases, by T. A. Erikson, pp. 24-41.

On the Memory Effect in the Thermal Initiation of Explosives, by W. R. Hess and R. C. Ling, pp. 42–49.

The Thermal Decomposition of [CO $(NH_4)_4$] $(N_3)_3$, by T. B. Joyner and F. H. Verhoek, pp. 50–59.

The Behavior of Explosives at Very High Temperature, by J. Wenograd, pp. 60-76.

The Rapid Burning of Secondary Explosives by a Convective Mechanism, by J. W. Taylor, pp. 77-87.

Electrical Initiation of RDX, by G. M. Muller, D. B. Moore and D. Bernstein, pp. 88-111.

Detonation Studies in Electric and Magnetic Fields, by F. E. Allison, pp. 112-119.

Electrical Measurements in Detonating Pentolite and Composition B, by R. L. Jameson, pp. 120-138.

On the Electrical Conductivity of Detonating High Explosives, by G. Hayes, pp. 139-149.

Ionization in the Shock Initiation of Detonation, by R. B. Clay, M. A. Cook, R. T. Keyes, O. K. Shupe and L. L. Udy, pp. 150–183.

Chemical Factors in External Detonation-generated Plasmas, by M. A. Cook, A. G. Funk and R. T. Keyes, pp. 184– 201.

Energy Transfer to a Rigid Piston Under Detonation Loading, by A. K. Axiz, H. Hurwitz and H. M. Sternberg, pp. 205-225

Detonation Plasma, by E. L. Kendrew and E. G. Whitbread, pp. 202–204.

A Computer Program for the Analysis of Transient Axially Symmetric Explosion and Shock Dynamics Problems, by T. Orlow, D. Piacesi and H. M. Sternberg, pp. 226–240.

Pressure Profiles in Detonating Solid Explosive, by G. E. Hauver, pp. 241-252.

Decay of Explosively-induced Shock Waves in Solids and Spallings of Aluminum, by J. O. Erkman, pp. 253-266.

Effects of Boundary Rarefactions on Impulse Delivered by Explosive Charge, by B. C. Taylor, pp. 267–284.

Experimental Determination of Stresses Generated by an Electric Detonator, by J. S. Rinehart, pp. 285–303.

The Shock Initiation of Detonation in Liquid Explosives, by A. Gay and Karl Kinaga, 9 pp. (between vol. 1 and vol. 2).

Comments on Hypervelocity Wave Phenomena in Condensed Explosives, by R. F. Chaiken, pp. 304–308.

Non Ideal Detonation of Ammonium Nitrate-Fuel Mixtures, by L. D. Sadwin, R. H. Stresau and J. Savitt, pp. 309-325.

The Detonation Velocity of Pressed TNT, by M. J. Urizar Jr. and L. C. Smith, pp. 327-356.

Measurements of Detonation, Shock and Impact Pressures, by R. T. Keyes and W. O. Ursenbach, pp. 357-385.

Low Pressure Points on the Isentropes of Several High Explosives, by W. E. Deal, pp. 386-395.

Strong Shocks in Porous Media, by J. L. Austing, H. S. Napadensky, R. H. Stresau and J. Savitt, pp. 396–419. The Behavior of Explosives at Impulsively Induced High Rates of Strain, by M. S. Napadensky, R. H. Stresau and J. Savitt, pp. 420–435.

Initiation and Growth of Detonation in Liquid Explosives, by F. C. Gibson, C.R. Summers, C. M. Mason and R. W. Van Dolah, pp. 436–454.

Initiation Characteristics of Mildly Confined, Bubble-free Nitroglycerin, by C. H. Winning and E. I. du Pont, pp. 455–468.

Shock Initiation of Detonation in Liquid Explosives, by A. W. Campbell, W. C. Davis and J. R. Travis, pp. 469–498.

Shock Initiation of Solid Explosives, by A. W. Campbell, W. C. Davis, J. B. Ramsay and J. R. Travis, pp. 499-519.

Shock Induced Sympathetic Detonation in Solid Explosive Charges, by M. Sultanoff, V. M. Boyle and J. Paszek, pp. 520-533.

Growth of Detonation from an Initiating Shock, by J. W. Enig, pp. 534-561.

Initiation of a Low-density PETN Pressing by a Plane Shock Wave, by G. E. Seay and L. G. Seely Jr., pp. 562–573.

The Transition from Shock Wave to Detonation in 60/40 RDX TNT, by E. L. Kendrew and E. G. Whitbread, pp. 574-583

Determination of the Shock Pressure Required to Initiate Detonation of an Acceptor in the Shock Sensitivity Test, by I. Jaffe, R. Beauregard and A. Amster, pp. 584–605.

A Computational Treatment of the Transition from Deflagration to Detonation in Solids, by C. T. Zovko and A. Macek, pp. 606–634.

A Method for Determination of Detonability of Propellants and Explosives, by S. Wachtell and C. E. McKnight, pp. 635-658

Materials and Structures

Structural Behavior of Pressurized, Ring-stiffened, Thin-wall Cylinders Subjected to Axial Compression, by James P. Peterson and Marvin B. Dow, NASA TN D-506, Oct. 1960, 24 pp.

Correlation of the Buckling Strength of Pressurized Cylinders in Compression of Bending with Structural Parameters, by James P. Peterson, NASA TN D-526, Oct. 1960, 21 pp.

Use of Subsonic Kernel Function in an Influence-coefficient Method of Aeroelastic Analysis and Some Comparisons with Experiment, by John L. Sewall, Robert W. Herr and Charles E. Watkins, NASA TN D-515, Oct. 1960, 86 pp.

Membrane Theory of Large Spherical Radomes, by A. L. M. Grzedzielski, (National Research Council, Canada, National Aeronautical Establishment) NRC LR-278, May 1960, 76 pp.

Decay of Explosively Induced Shock Waves in Solids and Spalling of Aluminum, by John O. Erkman, Stanford Res. Inst., Poulter Labs., Tech. Rep. 008-60, Aug. 1960, 16 pp.

Halogen-containing Gases as Lubricants for Crystallized-glass-ceramic-metal Combinations at Temperatures to 1500°F., by Donald H. Buckley and Robert L. Johnson, NASA TN D-295, Oct. 1960, 19 pp.

The Metal Beryllium, D. W. White and J. E. Burke, eds., American Society for Metals, Cleveland, 1955, 703 pp.

The Physical and Mechanical Proper-

ties of Beryllium Metal, by D. W. White Jr. and J. E. Burke, eds., pp. 304–327.

The Nuclear Properties of Beryllium, by J. R. Stehn, pp. 328–366.

Refractory Compounds and Cermets of Beryllium, by W. W. Beaver, pp. 570-598

The Refractory Properties of Beryllium Oxide, by J. F. White, pp. 599-619. Health Hazards from Beryllium, by M.

Eisenbud, pp. 620-640.

Aluminum Alloys. Materials of Construction Review, by F. B. Murphy, I/EC, Ind. Engng. Chem., vol. 52, Nov. 1960, pp.

The Mechanical Strength of Ceramic Materials, by V. G. Bravinskii, Soviet Physics: Doklady, vol. 5, Sept.-Oct. 1960, pp. 217-455, pp. 368-370.

Saturn Booster Bulkheads Pose Fabrication Problems, by F. G. McGuire, Missiles and Rockets, vol. 6, no. 18, May 2, 1960,

Space Age from the Metallurgist's Point of View, by W. H. Steurer, Metals Review, vol. 33, no. 4, April 1960, p. 12.

Supersonic Flutter of Cylindrical Shells, by D. J. Johns, Cranfield College Aeron., CoA Note no. 104, July 1960, 17 pp.

Survey of Materials Problems Resulting from Low-Pressure and Radiation Environment in Space, by Robert A. Lad, NASA TN D-477, Nov. 1960, 18 pp.

Lubricating Properties of Some Bonded Fluoride and Oxide Coatings for Temperature to 1500°F, by Harold E. Sliney, NASA TN D-478, Oct. 1960, 26 pp.

Compatibility of Various Metals and Carbon in Liquid Fluorine, by C. J. Sterner and A. H. Singleton, Air Products Inc., Allentown, Pa. (WADD TR 60-436), Aug. 1960, 110 pp., 162 refs.

On the Dynamics of Plastic Spherical Shells, by R. Sankaranarayanan, Brooklyn Polytechnic Inst., Dept. of Aerospace Engag. Appl. Mech., PIBAL Rep. no. 580, Sept. 1960, 15 pp. (AFOSR TN 60-1165.)

NASA-Industry Program Plans Conferences, 1st Proceedings, July 28–29, 1960, 23 pp.

Structures and Materials Research Programs, by Richard V. Rhode, pp. 23-28.

Structures and Materials, by George Gerard, Astronautics, vol. 5, Nov. 1960, p. 47.

Dynamic Measurement of Elasticity Using Resonance Methods, by G. Bradfield, British J. Appl. Phys., vol. 11, Oct. 1960, p. 478.

Structural Weight Approximation for a Bell-nozzle Divergent Section, by G. D. Brewer and E. Levin, J. Engng. Ind. (ASME Trans.), vol. 82B, no. 4, pp. 359-

Optimum Tolerances of Sheet Materials for Flight Vehicles, by G. A. Hoffman, J. Engng. Ind. (ASME Trans.), vol. 82B, no. 4, pp. 363–368.

Mechanical Vibration Filters with Non-linear Characteristics, by W. J. Worley, J. Engng. Ind. (ASME Trans.), vol. 82B, no. 4, pp. 369-376.

Electrical Properties of Crystal Compounds of Graphite, II Acid Salts of Graphite, by L. C. F. Blackman, J. F. Mathews and A. R. Ubbelohde, Royal Society, London, Proceedings, vol. 258A, no. 1294, Oct. 25, 1960, pp. 329–338.

Electrical Properties of Crystal Com-pounds of Graphite, III. The Role of Elec-tron Donors, by L. C. F. Blackman, J. F. Mathews and A. R. Ubbelohde, Royal

Society, London, Proceedings, vol. 258A, no. 1294, Oct. 25, 1960, pp. 339–349.

Fatigue Damage Under Varying Stress Amplitudes, by H. W. Liu and H. T. Corten, NASA TN D-647, Nov. 1960, 68 pp.

International Astronautical Congress, 10th, London, 1959, Proceedings, F. Hecht, ed., Springer-Verlag, Vienna, 1959, 2 vols., 946 pp.

Effects of a Meteoroid Impact on Steel and Aluminum in Space, by R. J. Bjork, vol. 2, pp. 505-514, 10 figs.

Industrial Carbon and Graphite (papers, read at the conference held in London Sept. 24-26, 1957), Society of Chemical Industry, London, 1958, 630 pp.

A Kinetic Study of the Deposition of Pyrolytic Carbon Films, by D. B. Murphy, H. B. Palmer and C. R. Kinney, pp. 77–85.

The Preparation and Properties of High-temperature Pyrolytic Carbon, by A. R. G. Brown and W. Watt, pp. 86-100.

The Dependence of Structure and Prop erties of Carbon Mixtures on Their Composition, by A. S. Fialkov, pp. 101-

The Rates of Reactions of Carbon and Graphite Materials with Combustion Gases at High Temperatures, by J. A. Graham, A. R. G. Brown, A. R. Hall Graham, A. R. G. Brown and W. Wati, pp. 309-320.

Some Physical Properties of Graphite as Affected by High Temperature and Irradiation, by John E. Hove, pp. 501-

The Effects of Neutron Irradiation on the Physical Properties of Graphite, by J. H. W. Simmons, pp. 511-518.

Thermal Expansion of Aluminum at Low Temperatures, by P. G. Klemens, Phys. Rev., vol. 120, Nov. 1, 1960, pp. 843-844.

A Type of Solution for Thin Shells in the Form of an Hyperbolic Paraboloid, by G. H. Beguin, Zeitschrift fur Angewandte Mathematick und Physik, vol. 11, Sept. 25, 1960, pp. 356-367.

The Minimum Weight Design of Circular Sandwich Plates, by G. Eason, Zeitschrift fur Angewandte Mathematik und Physik, vol. 11, Sept. 25, 1960, pp. 368-

Super Plastic Builds a Better Nose Cone, American Machinist, vol. 104, no. 19, Sept. 1960, pp. 95–96.

Fluids Dynamics, Heat Transfer, and MHD

On the Linear Behavior of Large-amplitude Magnetohydrodynamic Waves, by J. Shmoys and E. Mishkin, *Phys.* Fluids, vol. 3, July-Aug. 1960, p. 661.

Energy Analysis of Shock Wave Structure, by Maurice Roy, La Recherche Aeronautique, no. 78, Sept.-Oct. 1960, pp. 3-6. (In French.)

Rapid Method of Calculating the Parameters of Hypersonic Flow of a Real Gas in Equilibrium, by F. Bounsol, *La Re-*cherche Aeronautique, no. 78, Sept.-Oct. 1960, pp. 21-22. (In French.)

Quantum Corrections for Transport Coefficients, by Sang-II Choi and John Ross, J. Chem. Phys., vol. 33, Nov. 1960, pp. 1324-1331.

Structure of Transport Equations, by Tamor, J. Chem. Phys., vol. 33, Nov. 1960, pp. 1421-1425.

Statistical Mechanics of the Nonuniform Gas, by P. L. Auer and S. Tamor, J. Chem. Phys., vol. 33, Nov. 1960, pp. 1426-1431

Derivation of Thermodynamic Relations for Three-dimensional Systems, by Francis S. Manning and William P. Manning, J. Chem. Phys., vol. 33, Nov. Manning, J. Chem. 1960, pp. 1554-1557.

Statistical Mechanics for the Nonideal Bose Gas, by A. E. Glassgold, A. N. Kaufman and K. M. Watson, Phys. Rev., vol. 120, Nov. 1, 1960, pp. 660-674.

Statistical Mechanics of Transport in Fluids, by James A. McLennan Jr., Ph Fluids, vol. 3, July-Aug. 1960, pp. 493-

Shear and Heat Flow for Maxwellian Molecules, by S. Ziering, *Phys. Fluids*, vol. 3, July-Aug. 1960, pp. 503-509.

Intermolecular Forces from Diffusion and Thermal Diffusion Measurements, by S. Weissman, S. C. Saxena and E. A. Mason, *Phys. Fluids*, vol. 3, July-Aug. 1960, pp. 510-518.

Turbulence Theory and Functional Integration, by Gerald Rosen, Phys. Fluids, vol. 3, July-Aug. 1960, pp. 519-

Energy Transfer in a Turbulent Fluid, by B. Samuel Tanenbaum and David Mintzer, Phys. Fluids, vol. 3, July-Aug. 1960, pp. 529-538.

International Astronautical Congress, 10th, London, 1959, Proceedings, F. Hecht, ed., Springer-Verlag, Vienna, 1959, 2 vols., 946 pp.

Compressible Flat Plate Boundary Layer of an Electrically Conducting Fluid in the Presence of Magnetic Fields, by L. G. Napolitano and A. Pozzi, vol. 2, pp. 576-603, 8 figs.

Unsteady Compressible Magnetic Laminar Boundary Layers in Hypersonic Flow, by P. S. Lykoudis and J. P. Schmitt, vol. 2, pp. 604-624, 8 figs.

Jet Orbital Lift in Hypervelocity Flight, by D. Cunsolo and C. E. Cremona, vol. 2, pp. 515-525. (In Italian.)

Laboratory Experimental Studies Re-entry Aerothermodynamics, by W. R. Warren, vol. 2, pp. 683-704, 22 figs. A Study of Hypersonic Ablation, by S. M. Scala, vol. 2, pp. 709–827, 21 figs.

Industrial Carbon and Graphite (papers read at the Conference held in London, Sept. 24–26, 1957), London, Society of Sept. 24–26, 1957), London, Sc Chemical Industry, 1958, 630 pp.

The Thermal Conductivity of Carbons and Graphites at High Temperatures, by R. W. Powell, pp. 46-51.

Statistical Mechanics of Transport Processes, XIV. Linear Relations in Multicomponent Systems, by John G. Kirkwood and Donald D. Fitts, J. Chem. Phys., vol. 33, Nov. 1960, pp. 1317-1323.

A Theoretical Study of Annular Supersonic Nozzles, by W. T. Lord, Great Britain, Royal Aircraft Establishment Rep. no. Aero. 2627, Oct. 1959.

It's Time to Add a New Dimension: Unsteady-State Heat Transfer—I, by S. H. Davis and W. W. Akers, Chem. Engng., vol. 67, no. 8, April 18, 1960, pp. 187–192. Some Radiator Design Criteria for Space Vehicles, by J. P. Callinan and W. P. Berggren, J. Heat Transfer (ASME Trans, Series C), vol. 81, no. 3, Aug. 1959, np. 237–244. pp. 237-244.

A Certain Class of Exact Solutions of the A Certain class of Exact Solutions of the Equations of Magneto-gasdynamics, by D. V. Sharikadze, PMM: Applied Math. and Mech., vol. 23, no. 5, 1959 (transl. from Prikladnaia Matematika i Mekhanika, vol. 23, no. 5, 1959) pp. 1356-1357.

Analysis of the Aerodynamic Heating

for a Re-entrant Space Vehicle, by M. J. Brunner, J. Heat Transfer, (ASME Trans., Series C) vol. 81, no. 3, Aug. 1959, pp. 223-220

Einstein's Equations and Classical Hydrodynamics, by J. Blankfield and G. C. McVittie, Archive for Rational Me-chanics and Analysis, vol. 2, 1958/1959, pp. 337-354.

Blunt Body Viscous Layer with and Without a Magnetic Field, by Hakuro Oguchi, Wright Air Development Center, Tech. Note 60-57, Feb. 1960, 41 pp., 4 figs. (Also Phys. Fluids, vol. 3, no. 4, July-Aug. 1960.)

Transition Stimulation for Terminal Velocity Reduction in Water-exit Studies, by J. M. Robertson, J. C. F. Chow and M. E. Clark, Illinois University, Dept. Theoret. and Appl. Mech., T & AM Rep. no. 152, Nov. 1959, 28 pp.

Investigation of Internal Film Cooling of Exhaust Nozzle of a 1000-pound-thrust Liquid-ammonia Liquid-oxygen Rocket, by Andrew E. Abramson, NACA Research Memorandum E52C26, June 1952, 18 pp. (Declassified by authority of NASA Tech Pubs. Announcement, no. 33, Nov. 111669.

Two Heat Diffusion Problems with Shock Tube Applications, by D. A. Spence, Great Britain, Royal Aircraft Establishment, TN no. Aero. 2637, July 1959, 16 pp.

Free-flight Aerodynamic-heating Data to Mach Number 10.4 for a Modified von Karmán Nose Shape, by William M. Bland Jr. and Katherine A. Collie, NACA Res. Mem L56D25, July 1956, 28 pp. (Declassified by authority of NASA Tech. Pubs. Announcement no. 33, Nov. 24, 1960.)

Measurements of Free Molecule Heat Transfer in Air at Mach Numbers from 10-18, by R. L. Warwig, Space Tech. Labs. STL/TR-60-0000-94324, Oct. 1960,

Interaction Effects of Side Jets Issuing from Flat Plates and Cylinders Aligned with a Supersonic Stream, by James L. Amick and Paul B. Hays, Wright Air Development Center TR 60-329, May 1960, 57 pp.

The Mechanism of Sound Field Effects on Heat Transfer, by J. P. Holman, J. Heat Transfer (ASME Trans.), vol. 82c, no. 4, Nov. 1960, pp. 393-395.

Uber die berechnung der schallgeschwindigkeit in gasmischungen, by V. S. Vrkljan, Nuovo Cimento, vol. 17, no, 6, Sept. 1960, pp. 845–849. (In German.)

Plasma Oscillations in a Magnetic Field, by Ikuo Kaji and Masfumi Kito, Physical Soc. of Japan J., vol. 15, Oct. 1960, pp. 1851–1861.

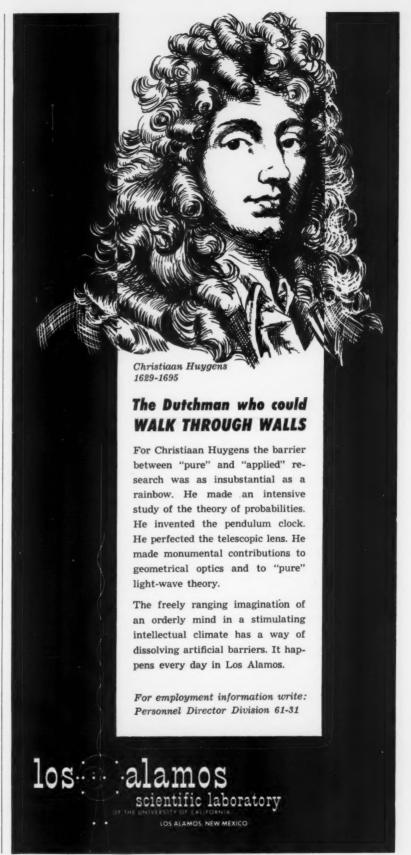
Radiation of Plasma Oscillation, by Shoji Kojima and Shigeo Hagiwara, Physical Soc. of Japan J., vol. 15, Oct. 1960, p. 1904.

Similarity Methods in Radiation Hydrodynamics, by L. A. Elliott, Royal Society, London, Proceedings, vol. 258A, no. 1294, Oct. 25, 1960, pp. 287–318.

Nonlinear Phenomena in a Plasma Located in an Alternating Electronic Field, by V. L. Ginzburg and A. V. Gurevich, Soviet Physics: Uspekhi, vol. 3, no. 2, Sept.—Oct. 1960, pp. 175—194.

Heating of Blunt Forms in Hypersonic Flight, by L. D. Wing, *Space/Aeron.*, vol. 34, no. 4, Oct. 1960, pp. 187–196.

The Three-Dimensional Turbulent Boundary Layer, by D. R. Blackman and P. N. Joubert, J. Royal Aeron. Soc., vol. 64, Nov. 1960, pp. 692–693. Observation of Ion Oscillations in a



Plasma, by M. D. Gabovich, L. L. Pase-chnik, and V. G. Yazeva, Soviet Physics; JETP, vol. 11, no. 5, Nov. 1960, pp. 1033-

The Motion of a Piston in a Conducting Medium, by R. V. Polovin, Soviet Physics; JETP, vol. 11, no. 5, Nov. 1960, pp. JETP, vol 1113-1120.

Rotation of the Spin of a Relativistic Particle with a Magnetic Moment Moving in an External Field, by V. S. Popov, Soviet Physics: JETP, vol. 11, no. 5, Nov. 1960, pp. 1141-1143.

On the Amount of Accelerated Particles in an Ionized Gas Under Various Accelerating Mechanisms, by A. V. Gurevich, Soviet Physics: JETP, vol. 11, no. 5, Nov. 1960, pp. 1150-1157.

On the Amount of Accelerated Particles in an Ionized Gas Under Various Accelerating Mechanisms, by A. V. Gurevich, Soviet Physics: JETP, vol. 11, no. 5, Nov. 1960, pp. 1150–1157.

Investigation of Transient Flow of a Conducting Fluid in a Plane Channel with Moving Walls, by Ya. S. Uflyand and I. B. Chekmarev, Soviet Physics: Tech. Physics, vol. 5, no. 5, Nov. 1960, pp. 437–449

Frontiers of Numerical Mathematics (A Symposium Conducted by the Mathematics Research Center, United States Army and the National Bureau of Standards at the University of Wisconsin, Oct. 30-31, 1959) Rudolph E. Langer, ed., Madison, University of Wisconsin Press, 1960, 132 pp.

Magnetohydrodynamics, by S. Chandrasekhar, paper 7, pp. 99–106.

Influence of Pressure History on Momentum Transfer in Rarefied Gas Flows, by F. C. Hurlbut, *Phys. Fluids*, vol. 3, July-Aug. 1960, pp. 541-544.

Blunt Body Viscous Layer with and Without a Magnetic Field, by Hakuro Oguchi, *Phys. Fluids*, vol. 3, July-Aug. 1960, pp. 567-580.

Flat Plate Drag in Magnetohydrodynamic Flow, by H. P. Greenspan, *Phys. Fluids*, vol. 3, July-Aug. 1960, pp. 581-

Plasma Viscosity in a Magnetic Field, y Allan N. Kaufman, Phys. Fluids, vol. 3, July-Aug. 1960, p. 610.

Experiments on Plasmoid Motion Along Magnetic Fields, by David M. Wetstone, Melvin P. Ehrlich and David Finkelstein, Phys. Fluids, vol. 3, July-Aug. 1960, pp. 617-630.

On Certain Properties of Hydromagnetic Shocks, by W. B. Erickson and J. Bazer, *Phys. Fluids*, vol. 3, July-Aug. 1960, pp. 631-640.

Conference on Applied Gas Dynamics Proceedings, Alma-Ata, Akad. Nauk Kazakhskoi, SSR, 1959, 235 pp. (In

Turbulent Jets in Flowing Liquids, by G. N. Abramovich, pp. 1-16, 22 refs. On the Discharge of Gases from Vessels Through Pipe with Friction and Local Resistance, by I. N. Ginzburg, pp.

Initial Results and Further Problems in the Investigation of Liquid and Gas Jet, by L. A. Vulis, pp. 29–38, 30 refs.

On Mixing and Counter Motion in Double Homogeneous Streams of a Compressible Gas, by V. P. Kashkarov, pp. 55-62, 10 refs.

Diffusion in Axisymmetrical Jets with Mixing and Counter Flow, by T. P. Leont'eva, pp. 62-68

Critical Flow of a Viscous Gas in a Channel Between Parallel Planes, by

M. M. Nazarchuk and N. I. Plo'skii, pp. 69-75.

Diffusion of an Axisymmetrical Gas Jet in a Medium of Different Density, by N. N. Terkhina, pp. 77-85.

Aerodynamics of Twisted Flows and Vortex Chambers, by B. P. Ustimenko, pp. 134-141, 7 refs.

Aerodynamics of Turbulent Gaseous Jets, by Sh. A. Ershin, pp. 168-178, 13 refa

Fundamental Problems of Thermodynamic Flow in the Presence of Real Boundary Conditions, by S. V. Romanenko, pp. 197-208, 6 refs.

On the Rotating Motion of Viscous Gases, by L. A. Vulis, pp. 208-214, 15 refs.

Decennial Symposium, Proceedings, Toronto University, Institute of Aerophysics, Oct. 14-16, 1959, 3 parts, 512 pp.

Spherical Flow and Shock Waves, by I. I. Glass, pp. 233-287.

Summary of Aerodynamic Studies in the Carde Aeroballistic Range, by G. V. Bull and H. F. Waldron, pp. 288-319.

Hypersonic Research at the Naval Ordnance Laboratory, by R. K. Lobb, pp. 320-344.

The Blast Wave from an Impulsively Generated and Driven Plasma, by P. Savic, pp. 345-364.

Flight Mechanics

Drag and Stability Derivatives of Missile Components According to the Modified Newtonian Theory, by J. Don Gray, Arnold Engng. Dev. Center, TN 60-191, Nov. 1960, 36 pp.

Analysis of Trajectory Parameters for Probe and Round-Trip Missions to Venus, by James F. Dugan Jr., NASA TN D-470, Nov. 1960, 44 pp.

A Realistic Approach to Problems of Optimum Rocket Trajectories, by Samuel E. Moskowitz and Lu Ting, Brooklyn Polytechnic Inst., Dept. of Aerospace Engng. and Appl. Mech., PIBAL Rep. No. 625, (AFOSR TN 60-1342), Oct. 1960, 11

Design of Lunar and Interplanetary Ascent Trajectoris, by Victor C. Clarke Jr., Calif. Inst. of Tech., Jet Prop. Lab., Tech. Rep. no. 32-30, July 1960, 16 pp.

Experimental Investigation of a Hypersonic Glider Configuration at a Mach Number of 6 and at Full-Scale Reynolds Numbers, by Alvin Seiff and Max E. Wilkins, NASA TN D-341, Jan. 1961,

Gyroscopic Motion of an Unsymmetrical Satellite Under no External Forces, by Manfred E. Kuebler, NASA TN D-596, Dec. 1960 iv, 30 pp.

The Effect of Lift on Entry Corridor Depth and Guidance Requirements for the Return Lunar Flight, by Thomas J. Wong and Robert E. Slye, NASA Tech. Rep. R-80, 1960, 38 pp.

A Method of Estimating Residuals in Orbital Theory, by Myron Lecar, NASA TN D-493, Jan. 1961, 10 pp.

Perturbations of Orbits of Artificial Satellites Due to Air Resistance, by Yu. V. Batrakov and V. F. Proskurin, NASA Tech. Transl. F-46, Nov. 1960, 13 pp.

Characteristic Orbital Variables and Their Time Rates in Unperturbed Elliptic Orbits, by Helmut G. L. Krause, *NASA TN* D-558, Dec. 1960, 11 pp.

Osculating Elements Derived from the Modified Hansen's Theory for the Motion of an Artificial Satellite, by A. Bailie and

R. Bryant, NASA TN D-568, Jan. 1961, 8 pp.

A Study of the Positions and Velocities of a Space Station and a Ferry Vehicle during Rendezvous and Return, by John M. Eggleston and Harold D. Beck, NASA Tech. Rep. R-87, 1961, 82 pp., 20 figs.

Manned Space Stations Symposium, Los Angeles, April 20–22, 1960, N. Y. Inst. Aeron. Sciences, 1960, 322 pp. Atmospheric Entry of Manned Vehicles, by C. Gazley Jr., pp. 14–23. Effect of Earth's Oblateness on the Calculation of the Impact Point of Ballistic

culation of the Impact Point of Ballistic Missiles, by Ching-Sheng Wu, ARS JOUR-NAL, vol. 30, no. 12, Dec. 1960, pp. 1172-1173

Influence of Gravity on Satellite Spin Axis Attitude, by L. H. Grasshoff, ARS JOURNAL, vol. 30, no. 12, Dec. 1960, p.

Motion of Thin Bodies in a Highly Rarefied Plasma, by Hideo Yoshihara, Phys. Fluids, vol. 4, no. 1, Jan. 1961, pp. 100-103.

The Difference Function Approach to the Overall Aerodynamics of Guided Missiles, by D. A. Forster and A. C. Southgate, Royal Aeron. Soc. J., vol. 64, no. 600, Dec. 1960, pp. 753–763.

A Note on Relay Satellites, by S. W. Greenwood, Brit. Interplan. Soc. J., vol 17, no. 10, Jul.-Aug. 1960, pp. 360-361.

On the Motion of a Satellite in an Asymmetrical Gravitational Field, by P. Musen, J. Geophys. Res., vol. 65, no. 9, Sept. 1960, pp. 2783-2792.

Note on Establishment of a Circular Satellite Orbit by Double Impulse, by G. Leitmann, Brit. Interplan. Soc. J., vol. 17, no. 10, Jul.-Aug. 1960, pp. 358-359.

The Sudden Discontinuity in the Orbital Period of Sputnik 4 Satellite, Nature, vol. 187, no. 4740, Sept. 3, 1960, p. 866.

Angular Motion of the Spin Axis of the Tiros I Meteorological Satellite Due to Magnetic and Gravitational Torques, by W. R. Bandeen and W. P. Manger, J. Geophys. Res., vol. 65, no. 9, Sept. 1960, pp. 2992–2995.

Graphical Plotting of Interplanetary Orbits, by M. Vertregt, Brit. Interplan. Soc. J., vol. 17, no. 10, Jul.-Aug. 1960, pp. 351-358.

Vehicle Design, **Testing and Performance**

A New Type of Thermal Radiator for Space Vehicles, by Roger C. Weatherston and William E. Smith, Aeron. Qtly., vol. 9, part 4, Nov. 1960, pp. 16-17.

Injection Schemes for Obtaining a Twenty-Four Hour Orbit, by Rudolf F. Hoelker and Robert Silber, Aeron. Qtly., vol. 9, part 4, Nov. 1960, pp. 28–29.

Some Requirements for the Efficient Attainment of Range by Airborne Vehicles, by M. Arens, Israel, Inst. of Tech., Dept. of Aeron. Engag., Tech. Rep. 3,

Dept. of Aeron. Enging., Tech. Rep. o, Sept. 1959, 26 pp.
Special Data Reduction Equipment Spectrum Analyzer, by F. J. Honey, Calif. Inst. of Tech., Jet Prop. Lab. Tech. Rep. 32-35, Aug. 1960, 10 pp.

Analytical Study of Soft Landings on Gas-Filled Bags, by Jack B. Esgar and William C. Morgan, NASA Tech. Rep. R-75, 1960, 58 pp.

Long Range Planning for Space Transportation Systems, by H. H. Koelle, NASA TN D-597, Jan. 1961, 36 pp.

Hydrodynamics and Propulsion of Submerged Bodies, by George F. Wislicenus, ARS JOURNAL, vol. 30, no. 12, Dec. 1960, pp. 1140-1147.

Factors Influencing the Size and Weight of Underwater Vehicles, by R. C. Brumfield, ARS JOURNAL, vol. 30, no. 12, Dec. 1960, pp. 1152–1160.

S

Launch Parameters for Interplanetary Flights, by W. C. Riddel, ARS JOURNAL, vol. 30, no. 12, Dec. 1960, pp. 1170-1171.

Some Possible Operations on the Moon, by F. Zwicky, ARS JOURNAL, vol. 30, no. 12, Dec. 1960, pp. 1177-1179.

Designing a Self-Erecting Manned Space Lab, by Emanuel Schnitzer, Astronautics, vol. 6, no. 1, Jan. 1961, p. 22.

New Standards for the Space Age, by A. T. McPherson, Astronautics, vol. 6, no. 1, Jan. 1961, p. 24.

Design Factors for a Missile Range, by B. F. Rose, Jr., ASTRONAUTICS, vol. 6, no. 1, Jan. 1961, p. 26.

Simulated-Altitude Rocket Testing, by B. H. Goethert, Astronautics, vol. 6, no. 1, Jan. 1961, p. 30.

Inert-Gas Spot Welding in the Aircraft and Missile Industry, by R. L. Hackman, Welding J., vol. 40, no. 1, Jan. 1961, pp. 25-33.

Simulated Altitude Testing of Rockets and Missile Components, by B. H. Goethert, Zeitschrift für Flugwissenschaften, vol. 8, no. 10/11, Oct.-Nov. 1960, pp. 317-321.

An Environmental Conditioning System for a Manned Satellite, by N. J. Bowman and F. H. Dingham, Brit. Interplan. Soc. J., vol. 17, no. 10, Jul.-Aug. 1960, pp. 372-380.

Manned Space Stations Symposium, Los Angeles, April 20–22, 1960, N. Y. Inst. Aeron. Sciences, 1960, 322 pp.

Design Criteria and Their Application to Economical Manned Satellites, by H. H. Koelle, E. E. Engler and J. W. Massey, pp. 24–35.

A Modular Concept for a Multi-Manned Space Station, by S. B. Kramer and R. A. Byers, pp. 36-72.

Manned Scientific Orbital Laboratory, by M. Stoiko, G. G. Kayten and J. W. Dorsey, pp. 73–90.

Some Factors Influencing the Selection of a Manned Space Station Concept, by J. H. Doss and L. J. Montaque, pp. 91-95.

Program Costs for a Manned Space Station, by R. H. Lundberg and T. E. Dolan, pp. 120-124.

Satellite Astronomical Observatories, by Nancy G. Roman, pp. 125-127.

Inflatable Manned Orbital Vehicles, by J. W. Carter and B. L. Bogema, pp. 188-196.

Guidance and Control

A Three-Axis Fixed-Simulator Investigation of the Effects on Control Precision of Various Ways of Utilizing Rate Signals, by John W. McKee, NASA TN D-525, Jan. 1961, 54 pp.

A Self-Adaptive Missile Guidance System for Statistical Inputs, by H. Rodney Peery, NASA TN D-343, Nov. 1960, 30 pp.

Determination of Azimuth Angle at Burn-Out for Placing a Satellite over a Selected Earth Position, by T. H. Skopinski and Katherine G. Johnson, NASA TN D-233, Sept. 1960, 33 pp.

Simulator Investigation of Controls and Display Required for Terminal Phase of Coplanar Orbital Rendezvous, by Chester H. Wolowicz, Hubert M. Drake and Edward N. Videan, NASA TN D-511,



The Jet Propulsion Laboratory in Pasadena, California, has been given the responsibility by the National Aeronautics and Space Administration of managing and executing a number of highly significant explorations in space. They include lunar and planetary missions such as fly-bys, orbiters, and unmanned roving vehicles for the observation of the surface of the moon and the planets. Other missions planned for the future involve trips outside of the ecliptic and beyond the confines of the solar system.

The successful execution of these programs requires extensive research efforts of a basic nature in the areas of celestial navigation and the guidance and control of vehicles operating far out in space. The problem areas being investigated include novel concepts in navigation based on astrophysical phenomena as well as research on inertial, optical, and electro-optical sensors of various types.

Other examples of present research activities in this area are cryogenic studies related to gyro and computer techniques, gas lubrication and flotation of sensing masses, research in solid-state physics, and many others.

The Laboratory has a number of positions open for scientists who are facilities for interested in working on challenging cal studies.

problems in these areas and who have the ability to investigate novel concepts and try unconventional methods.

Applicants must have an outstanding academic background with a Ph.D. degree, or equivalent experience and a Masters degree, in physics, astronomy, or electrical engineering. A minimum of five years of industrial or academic experience in the following fields will normally be required: optical physics, astrophysics, cryogenics, inertial guidance, celestial navigation, and computer and logic devices.

Qualified scientists will be offered the opportunity to work in an unusually stimulating atmosphere and will have available excellent supporting facilities for experimental and analytical studies.

Send professional resume to
CALIFORNIA INSTITUTE OF TECHNOLOGY

JET PROPULSION LABORATORY

4800 Oak Grove Drive, Pasadena, California

Oct. 1960, 30 pp.

Self-Adaptive Systems for Automatic Control of Dynamic Performance by Controlling Gain, Phase Shift, Gain Margin, Phase Margin, or Slope, by George Vasu, Amer. Inst. Elec. Engrs., Paper no. CP 60-1381, Oct. 1960, 34 pp., 34 figs.

A Longitudinal Control Feel System for In-Flight Research on Response Feel, by Stanley Faber and Harold L. Crane, NASA TN D-632, Jan. 1961, 31 pp.

Manned Space Stations Symposium, Los Angeles, April 20–22, 1960, N. Y. Inst. Aeron. Sciences, 1960, 322 pp.

Orbital Rendezvous and Guidance, by Ernst A. Steinhoff, pp. 151-164.

Rendezvous in Space-Effects of Launch Conditions, by N. V. Petersen and R. S. Swanson, pp. 165-170.

Ascent Guidance for a Satellite Rendezvous, by T. B. Garber, pp. 171-178.

A Guidance Technique for Achieving Rendezvous, by P. G. Felleman and N. E. Sears Jr., pp. 179-183.

Manned Control of Orbital Rendezvous, by E. Levin and J. Ward, pp. 184-187. Methods of Attitude Sensing, by Robert E. Roberson, pp. 259-266.

Comparison of Some Actuation Methods for Attitude Control of Space Vehicles, by W. Haeussermann, pp. 267-274. Attitude Control of a Space Vehicle by a Gyroscopic Reference Unit, by M. L. Chatkoff and L. G. Lynch, pp. 275-

280.
Attitude and Flight Path Control System for a Space Station Supply Vehicle, by J. Stalony-Dobrzandki, pp. 281-315.

Stabilizing a Spherical Satellite, by Radiation Pressure, by Robert R. Newton, ARS JOURNAL, vol. 30, no. 12, Dec. 1960, pp. 1175–1176.

Extensions in the Synthesis of Time Optimal or "Bang-Bang" Nonlinear Control Systems, Part I. The Synthesis of Quasi-Stationary Optimum Nonlinear Control Systems, Part II. Synthesis and Analytic Studies of Optimum Type II Nonlinear Control Systems, Part III. Synthesis and Analytic Studies of Optimum Type II Nonlinear Control Systems with Complex Roots, by P. Chandaket and C. T. Leondes, Univ. Calif. (Los Angeles) Dept. of Engnga, Rep. no. 60-45, 60-46 and 60-47 (AFOSR TN 60-960) 145 pp.

Flywheel Control of Space Vehicles, by J. E. Vaeth, *IRE Trans. on Automatic Control*, vol. AC-5, no. 3, Aug. 1960, pp. 247-259.

Instrumentation and Communications

Tracking Programs and Orbit Determination, Seminar Proceedings, Calif. Inst. Tech., Jet Prop. Lab., Feb. 23-26, 1960, 208 pp.

Methods for Nonlinear Least Squares Problems and Conversion Proofs, by D. D. Morrison, pp. 1-19.

Tracking and Orbit Determination Program of the Jet Propulsion Laboratory, by R. E. Carr and R. H. Hudson, pp. 10-35.

Evaluation of Pioneer IV Orbit Determination Program, by M. Eimer and Y. Hiroshige, pp. 36-52.

Satellite Orbit Determination and Prediction Utilizing JPL Goldstone 85-ft Antenna and the JPL Tracking Program, by D. Muhleman, pp. 53-61.

Early Orbit Determination Scheme for the Juno Space Vehicle, F. Kurtz and F. Speer, pp. 62-95. Orbital and Rotational Motion of a Rigid Satellite, by C. A. Lundquist, R. J. Naumann, pp. 96–103.

Survey of Space Flight Decks Used at ABMA, by H. J. Sperling, pp. 104-107.

Interim Definitive Orbits Determined at the NASA Computing Center, by R. W. Bryant, pp. 108-113.

NASA Computing Center Predictions, by R. W. Bryant, pp. 114-118.

The Programming System for Orbit Determination at the IBM Space Computing Center, by A. R. Mowlem, pp. 119-127.

Western Satellite Research Network, by G. A. McCue and D. A. Pierce, pp. 128-138.

Differential Orbit Correct Experimentation with Satellites 1958 Alpha One and 1958 Epsilon, by L. G. Walters, G. B. Westrom, C. T. Van Sant, R. H. Gersten and G. L. Matlin, pp. 139-146. Lunar Vehicle Orbit Determination, by C. Tross, pp. 147-160.

Remarks on the Programming System of Project Space Track, by E. W. Wahl, pp. 161-164.

Smithsonian Astrophysical Observatory Differential Orbit Improvement Program, by G. Veis and C. H. Moore, pp. 165-184.

Technical Aspects of Satellite Tracking on IBM Computers at Smithsonian Astrophysical Observatory in Cambridge, Massachusetts, by J. P. Possoni, pp. 185–191.

Tracking a Passive Satellite by the Doppler Method, by P. B. Richards, pp. 192-195.

Lunar and Interplanetary Trajectory Determination Activities at General Electric, by V. G. Szebehely, pp. 196-198,

A Computer Program for First Order Error Propagation in Satellite Orbit Prediction, by P. Swerling, pp. 199–204.

Decennial Symposium, Proceedings, Toronto University, Institute of Aerophysics, Oct. 14-16, 1959, 3 parts, 512 pp.

Radio Tracking and Communication Methods for Space Vehicles, by W. J. Heikkila, pp. 491-500.

Advances in Spectroscopy, vol. 1, 1959, H. W. Thompson, ed., Interscience Publishers, N. Y., 1959, 363 pp.

Spectroscopy in the Vacuum Ultraviolet, by W. C. Price, pp. 56-75, 72 refs.

The Index of Refraction of Air, by D. H. Rank, pp. 76-78, 13 refs.

Determination of the Velocity of Light, by D. H. Rank, pp. 79–90, 101 refs.

High Resolution Raman Spectroscopy, by R. P. Stoicheff, pp. 91-174, 135 refs. Modern Infra-red Detectors, by T. S. Moss, pp. 175-213, 87 refs.

Electronics for Spectroscopists, by Members of the Photoelectric Spectrometry Group and of the Electronics Department of Southampton University, C. G. Cannon, ed., Interscience Publishers, N. Y., 1960, 33 pp.

The Application of Semiconductors to the Detection of Radiation, by E. Schwarz, pp. 201-230.

Detector and Amplifier Systems in Infra-red Spectrometry, by J. C. O. Rochester, pp. 231-244.

Photoelectric Devices and Their Application in the Invisible and Ultraviolet Regions, by P. Popper, pp. 245–267

The Presentation of Infra-red Spectra on

the Cathode-ray Tube, by E. F. Daly, pp. 268-286.

Some Optical Problems, by A. M. Taylor, pp. 287–306.

Polarized-beam Techniques in Infra-red Spectrometry, by A. Elliott, pp. 307-327

International Astronautical Congress, 10th, London, 1959, Proceedings, F. Hecht, ed., Springer-Verlag, Vienna, 1959, 2 vols., 946 pp.

Space Telecommunications and the Characteristics of Its Channels, by A. Boal, vol. 2, pp. 871–910. (In Italian.) Methods of Analyzing Observations on Satellites, by G. V. Groves and M. J. Davies, vol. 2, pp. 933–946.

Magnetic Flow Meters, by J. J. P. Rolff, Archiv fur Technisches Messen, no. 297, Oct. 1960, pp. 197-200. (In German.)

Spectral Report on Microminiaturization, by M. M. Perugini and N. Lindgren, Electronics, vol. 33, Nov. 25, 1960, pp. 77-114.

Tunnel Diode Generates Rectangular Pulses, by G. B. Smith, *Electronics*, vol. 33, Nov. 25, 1960, pp. 124–125.

Regulated Power Supply for Instruments, Simple Circuit Provides 0.1-percent Current Regulation, by W. V. Locenstein, Electronics, vol. 33, Nov. 25, 1960, pp. 132-134.

The Doppler Effect and the Foundations of Physics (II), by H. Dingle, The British Journal for the Philosophy of Science, vol. 11, no. 42, Aug. 1960, pp. 113-129.

Electromagnetic Signals from Nuclear Explosions in Outer Space, by M. H. Johnson and B. A. Tippmann, Phys. Rev., vol. 119, no. 3, Aug. 1, 1960, pp. 827–828.

Space Scintillator-Detector Distinguishing Between Protons and Electrons, by S. D. Bloom, R. C. Kaifer and C. D. Schrader, IRE Trans. on Nuclear Science, vol. NS-7, no. 2-3, June-Sept. 1960, pp. 170-174.

Geomagnetic Noise at 230 kc/s, by R. L. Dowden, *Nature*, vol. 187, no. 4738, Aug. 20, 1960, pp. 677–678.

Elementary Considerations of the Effect of Multipath Propagation in Meteor-Burst Communication, by G. R. Sugar, R. J. Carpenter and G. R. Ochs, National Bureau of Standards, J. Research, Section D-Radio Propagation, vol. 64D, no. 5, Sept.—Oct. 1960, pp. 495—500.

Radio Echoes from the Moon in the X and S Band, by M. M. Kobrin, Radio Engg. and Electronics, vol. 4, no. 5, 1959,

Computation and Measurement of the Fading Rate of Moon-Reflected UHF Signals, by S. J. Fricker, R. P. Ingalls, W. C. Mason, M. L. Stone and D. W. Swift, National Bureau of Standards, J. Research, Section D—Radio Propagation, vol. 64D, no. 5, Sept.-Oct. 1960, pp. 455-465.

Star Tracker Uses Electronic Scanning, by W. D. Atwill, *Electronics*, vol. 33, no. 40, Sept. 30, 1960, pp. 88–91.

Extra-terrestrial Radio Noise as a Source of Interference in the Frequency Range 30-1000 Mc/s, by F. Horner, Inst. Electrical Engrs.; Proceedings, Part B, Radio and Electronic Engng., vol. 107, no. 34, July 1960, pp. 373-376.

Commercial Use of Space Bringing New Problems, by R. Haavind, *Electronic Design*, vol. 8, no. 19, Sept. 14, 1960, pp. 26, 29–35.

Multiphase Radio Interferometers for

Locating the Sources of the Solar Radio Emisssion, by S. Suzuki, Astronomical Society of Japan, Publications vol. 11, no. 4, 1959, pp. 195-215.

A Receiver for Observation of VLF Noise from the Outer Atmosphere, by G. R. A. Ellis, *Proc. IRE*, vol. 48, no. 9, Sept. 1960, pp. 1650–1651.

ly,

M.

ed

9,

he

on

1-

Methods of Predicting the Atmospheric Bending of Radio Rays, by B. R. Bean, G. D. Thayer and B. A. Cahoon, National Bureau of Standards, J. Research, Section D—Radio Propagation, vol. 64D, no. 5, Sept.—Oct. 1960, pp. 487—492.

Design of a Two-Mirror Radiotelescope, by A. E. Salomonovich and N. S. Soboleva, Radio Engineering and Electronics, vol. 4, no. 5, 1959, pp. 92–100.

Some Magnetoionic Phenomena of the Arctic E-Region, by J. W. Wright, J. Atmospheric and Terrestrial Physics, vol. 18, no. 4, Aug. 1960, pp. 276-289.

Changes in the Fading of Low-Frequency Radio Waves, by W. A. Cilliers, J. Atmospheric and Terrestrial Physics, vol. 18, no. 4, Aug. 1960, pp. 339-341.

Fading of Satellite Transmissions and Ionospheric Irregularities, by J. Mawd-sley, J. Atmospheric and Terrestrial Physics, vol. 18, no. 4, Aug. 1960, p. 344.

Radio Communication Using Earth-Satellite Repeaters, by L. Pollack, Electrical Communications, vol. 36, no. 3, 1960, pp. 180-188.

Scintillation Counters in Rockets and Satellites, by C. E. McIlwain, IRE Trans. on Nuclear Science, vol. NS-7, no. 2-3, June-Sept. 1960, pp. 159-164.

On the Behavior According to Newtonian Theory, of a Plumb Line or Pendulum Attached to an Artificial Satellite, by J. I. Synge, Royal Irish Academy, Proceedings, Section A, vol. 60, no. 1, June 1959, pp. 1-6.

Instruments for Space Research, by R. L. F. Boyd, Research Applied in Industry, vol. 13, no. 8, Aug. 1960, pp. 290– 294.

An Analysis of Slug-Type Calorimeters for Measuring Heat Transfer from Exhaust Gases, by J. C. Westkaemper, Arnold Engag. Dev. Center, TN 60-202, Nov. 1960, 44 pp.

Thermoelectricity, Including the Proceedings of the Conferences on Thermoelectricity Sponsored by the Naval Research Laboratory, Sept. 1958, Paul H. Egli, Ed., John Wiley & Sons, N. Y., 1960, 407 pp.

Measurement of Thermoelectric Properties by Using Peltier Heat, by R. C. Harman, J. H. Cahn and M. J. Logan, pp. 235–255.

The S-p Meter, A Device for Rapid Measurement of Seeback Coefficients and Electrical Resistivities at Tempera tures up to 1000°C, by Philipp K. Klein, pp. 256–269.

Thermal Diffusivity Measurements at High Temperatures, by P. H. Sidles and G. C. Danielson, pp. 270–287.

Atmospheric and Space Physics

Observation of the Total Solar Eclipse of February 15, 1960, by A. Koechkelenbergh, J. Meeus and H. Michel, Ciel et Terre, France, vol. 76, no. 7–8, July-Aug. 1960, pp. 209–215. (In French.)

Longitude Effect in Temperature Zone Sporadic E and the Earth's Magnetic Field, by L. H. Heisler and J. D. White-

head, *Nature*, vol. 187, no. 4738, Aug. 20, 1960, pp. 676–677.

Mercury, Venus, and Mars, by P. Moore, Discovery, vol. 21, no. 1, Jan. 1960, pp. 18-23.

Light Curves of Meteors, by R. Ananthakrishman, *Nature*, vol. 187, no. 4738, Aug. 20, 1960, pp. 675–676.

Amplitude Distribution Signals Reflected by Meteor Trials I, by A. D. Wheelon, National Bureau of Standards, J. Research, Section D— Radio Propagation, vol. 64D, no. 5, Sept.-Oct. 1960, pp. 449-454.

Meteorites, by F. Timpone, Rivista Aeronautica, Italy, vol. 36, no. 9, Sept. 1960, pp. 1423–1431. (In Italian.)

Calculations of Atmospheric Infrared Radiation as Seen from a Meteorological Satellite, by S. M. Greenfield and W. W. Kellogg, J. Meteorology, vol. 17, no. 3, June 1960, pp. 283-290.

Variations of the Balance and Abundance Within the Solar and Stellar Photospheres—IV. The Case of Ionized Titanium, by J. C. Rountree, Annales d'Astrophysique, France, vol. 23, no. 4, 1960, pp. 633–654. (In French.)

Variations of the Balance and Abundance Within the Solar and Stellar Photo-spheres—III. Variations of the ETL in the CH 4,300 Band, Solar Case, by F. Eugene-Praderie and J. C. Pecker, Annales d'Astrophysique, France, vol. 23, no. 4, 1960, pp. 622–632. (In French.)

A Synoptic Study of the F2-Region of the Ionosphere in the Asian Zone, by R. G. Rastogi, J. Atmospheric and Terres-trial Physics, vol. 18, no. 4, Aug. 1960, pp. 315-231 pp. 315-331.

Verification of Earth's Pear Shape Gravitational Harmonic, by C. J. Cohen and R. J. Anderle, *Science*, vol. 131, no. 3430, Sept. 23, 1960, pp. 807–808.

On the Possibility of Measuring in the Laboratory the Speed of Propagation of Gravitational Waves, by V. B. Graginskii, D. D. Ivanenko and G. I. Rukman, Soviet Physics—JETP, vol. 11, no. 3, Sept. 1960, pp. 723-724.

Short-Term Differences in the Behaviour of Two Daily Indices of Solar Activity During the I.G.Y., by G. H. Bazzard, J. Atmospheric and Terrestrial Physics, vol. 18, no. 4, Aug. 1960, pp. 290-296.

A Monthly Ionospheric Index of Solar Activity Based on F2-Layer Ionization at Eleven Stations, by C. M. Minnis, G. H. Bazzard, J. Atmospheric and Terrestrial Physics, vol. 18, no. 4, Aug. 1000 pp. 207 207 1960, pp. 297-305.

A World-Wide Semi-Annual Cycle in the E-Layer of the Ionosphere, by C. M. Minnis and G. H. Bazzard, J. Atmospheric and Terrestrial Physics, vol. 18, no. 4, Aug. 1960, pp. 306–308.

The Outer Planets, by G. E. Satter-thwaite, *Discovery*, vol. 21, no. 1, Jan. 1960, pp. 24-30.

Geophysics and Space Research, by A. Croome, *Discovery*, vol. 21, no. 8, Aug. 1960, pp. 362-364.

The Earth-Moon System, by G. Fielder, Discovery, vol. 21, no. 1, Jan. 1960, pp.

Geophysics and Space Research, by A. Croome, Discovery, vol. 21, no. 5, May 1960, pp. 221–223.

Geophysics and Space Research, by A. Croome, *Discovery*, vol. 21, no. 3, Mar. 1960, pp. 123-126.

Possibility of Detecting Ionospheric Drifts from the Occurrence of Spread F Echoes at Low Latitudes, by R. W.

BOOKS

ADAPTIVE CONTROL **PROCESSES**

A Guided Tour

by Richard Bellman. A panoramic view of what an ingenious mathematician does when faced with the myriad problems of automatic control. The author has minimized detailed rigor in the interest of making clear the basic ideas in a broad spectrum of applications. He shows how to get solutions to engineering problems which cannot be solved by conventional methods and provides ways to reformulate problems so they are amenable to machine computation. A RAND Corporation Research Study.

DYNAMIC PROGRAMMING by Richard Bellman. 1957. \$6.75

STABILITY IN **NONLINEAR** CONTROL **SYSTEMS**

by A. M. Letov. Translated by J. George Adashko. An outstanding Russian contribution to an increasingly important field. The author, a Nobel prizewinner, is held in highest esteem by U.S. control experts. He has added to the American translation of this work several additional chapters not included in the original.

"A plain, unsophisticated, painstakingly thorough treatise on application of Lyapunov's direct method."-DR. J. P. LASALLE, Mathematical Reviews \$8.50



Knecht, Nature, vol. 187, no. 4741, Sept. 10, 1960, p. 927.

Determination of the Profiles of Electron Density in the Ionosphere, by K. Rawer and C. Laieb, Comptes Rendus Hebdomadaires des Seances de L'academie des Sciences, France, vol. 251, no. 4, July 25, 1960, pp. 576–578. (In French.)

A Statistical Theory of Ionospheric Drifts, by J. P. Dougherty, *Phil. Mag.*, vol. 5, no. 54, June, 1960, pp. 553–570.

The Effect of Turbulence and Magnetic Field on Electron Density Fluctuations in the Ionosphere, by I. D. Howells, J. Fluid Mech., vol. 8, part 4, Aug. 1960, pp. 545-

Scientific Results of Experiments in Space, by B. Rossi, Amer. Geophys. Union, Trans., vol. 41, no. 3, Sept. 1960, pp. 410-

Statistical Analysis of Fading of a Single Down-Coming Wave, by P. Dasgupta and K. K. Vij, J. Atmospheric and Terrestrial Physics, vol. 18, no. 4, Aug. 1960,

Rapid Reduction of Cosmic-Radiation Intensity Measured in Interplanetary Space, by C. Y. Fan, P. Meyer and J. A. Simpson, *Phys. Rev. Letters*, vol. 5, no. 6, Sept. 15, 1960, pp. 269–271.

Cosmic-Ray Intensity Variation and the Interplanetary Magnetic Field, by H. Elliot, Phil. Mag., vol. 5, no. 54, June 1960, pp. 601–620.

Experiments on the Changes of Cosmic-Ray Intensity Using a Space Probe, by C. Y. Fan, P. Meyer and J. A. Simpson, *Phys. Rev. Letters*, vol. 5, no. 6, Sept. 15, 1960, pp. 272–274.

Atmospheric Temperature Effects on the Solar Daily Variation of Cosmic Ray Intensity, by J. J. Quenby and T. Thambyahpillai, Phil. Mag., vol. 5, no. 4, June 1000 are 1555 600. 1960, pp. 585-600.

Hydrodynamic Origin of Cosmic Rays, by S. A. Colgate and M. H. Johnson, Phys. Rev. Letters, vol. 5, no. 6, Sept. 15, 1060 pp. 325-328 1960, pp. 235-238.

What the Artificial Satellites Have what the Artificial Satellites Have Already Learned About Cosmic Rays and Auroral Particles, by J. Lequeux, La Nature, France, no. 3300, April 1960, pp. 146–154. (In French.)

On the Acceleration of the Earth's Rotation Caused by the Atmospheric Oscillation, by N. Sekiguchi, Astronomical Society of Japan, Publications, vol. 11, no. 1, 1959, pp. 1–8.

Effect of the Solar Activity on the Earth's Rotation, by H. Uyeda, Y. Saburi and H. Iwasaki, Radio Research Laboratories of Japan, vol. 7, no. 31, May 1960, pp. 131–136.

On the Emission Curves of Growth of Fe I and Ti II in the Lower Chromosphere, by I. Kawaguchi, Astronomical Society Japan, Publications, vol. 11, no. 3, 1959, pp. 138-150.

Note on the Excitation of the Ionized Helium in the Solar Chromosphere, by O. Namba, Astronomical Society of Japan, Publications, vol. 11, no. 1, 1959, pp. 50–53. Comets, Meteors, and Minor Planets, by M. P. Candy, Discovery, vol. 21, no. 1 Jan. 1960, pp. 31–35.

Excitation Mechanism of the Swan-Bands of Comets, by A. Stawikouski and P. Swings, Annales d'Astrophysique, P. Swings, Annales d'Astrophysique, France, vol. 23, no. 4, 1960, pp. 585-593. (In French.)

Satellite Measurements of Cosmic Dust, National Academy of Sciences, IGY Bulletin, no. 38, Aug. 1960, pp. 12-15.

Experimental Investigations of the Energy Spectrum of the Penetrating Component of Extensive Air Showers, by E. L. Andronikashvili and R. E. Kazarov, Soviet Physics-JETP, vol. 11, no. 3, Sept. 1960, pp. 507–510.

Arrival Directions of Cosmic-Ray Air Showers From the Equatorial Sky, by E. V. Chitnis, V. A. Sarabhai, G. Clark, Phys. Rev., vol. 119, no. 3, Aug. 1, 1960, pp. 1085-1091.

On the Anisotropy of the Cosmic Radiation, by E. W. Kellermann, and M. S. Islam, Nuovo Cimento, vol. 17, no. 3, Aug. 1, 1960, pp. 334-342.

Increase in the Intensity of Cosmic Radiation on May 4, 1960, by P. L. Marsden, J. B. Crowden and C. J. Hatton, Nuovo Cimento, vol. 17, no. 6, Sept. 1960,

Investigations of Cosmic Radiation and of the Terrestrial Corpuscular Radiation by Means of Rockets and Satellites, by S. N. Vernov and A. E. Chudakov, Sovie Physics: Uspekhi, (transl. of Uspekhi Fizicheskikk Nauk), vol. 3, no. 2, Sept.— Oct. 1960, pp. 230-250.

A Photoelectric Study of Colors of Asteroids and Meteorites, by M. Kita-mura. Astronomical Society of Japan, mura, Astronomical Society of Japan, Publications, vol. 11, no. 2, 1959, pp. 79-

Two Atmospheres, by G. Gardner, Solar Energy, vol. 4, no. 1, Jan. 1960, pp. 28-31.

An Auroral Emission in the 2.0-2.2 μ Region, by J. F. Noxon and A. V. Jones, J. Atmospheric and Terrestrial Physics, vol. 18, no. 4, Aug. 1960, pp. 341-343.

Observations of Non-field-Aligned Auroral Rays, by M. Gadsden and C. J. Loughnan, J. Atmospheric and Terrestrial Physics, vol. 18, no. 4, Aug. 1960, pp.

Atmospheric Temperatures and Solar Activity—I. 100 MB in the Northern Hemisphere Auroral Zone, by F. W. Ward Jr., J. Meteorology, vol. 17, no. 2, Apr. 1960, pp. 130-134.

The Origin of Tektites, by J. A. O'Keefe, NASA TN D-490 (originally presented at the first International Space Symposium sponsored by the Committee on Space Research, Nice, France, Jan. 1960), Nov. 1960, 26 pp.

NASA-Industry Program Plans Conferences, 1st Proceedings, July 28-29, 1960, 23 pp.

Exploration of the Moon, Planets and Interplanetary Space, by Edgar M. Cortright, pp. 65-73.
Frontiers of Numerical Mathematics, a

Symposium Conducted by the Mathematics Center, U. S. Army and the National Bureau of Standards at the University of Wisconsin, Oct. 30–31, 1959, Rudolph E. Langer, ed., University of Wisconsin Press, Madison, 1960, 132

> **Numerical Problems of Contemporary** Celestial Mechanics, by Zdenek Kopal, pp. 45-58.

Physics of the Atmosphere and Space, y Herbert Friedman, Astronautics, vol. 5, Nov. 1960, p. 42.

Certain Thermodynamic and Transport Properties of the Atmospheres of Venus, Mars, and Jupiter, by W. E. Ibele and T. F. Irvine Jr., J. Heat Transfer (ASME Trans.), vol. 82c, no. 4, Nov. 1960, pp. 381–386.

A Method for Detecting the Possible Existence of High Energy Deuterons in the Primary Cosmic Radiation, by R. R. Daniel, P. J. Lavakare and P. K. Aditya, Nuovo Cimento, vol. 17, no. 6, Sept. 1960, pp. 837-844.

Examples of Project Tiros Data and Their Practical Meteorological Use, by William K. Widger Jr., Air Force Res. Div., Geophysics Research Directorate, Res. Notes, no. 38, July 1960, 96 pp.

Reports on Progress in Physics, Vol. XII, A. C. Strickland, Ed., The Physical Society, London, 1959, 634 pp.

Experimental Investigations of the Ionospheric E-Layer, by B. J. Robinson, pp. 241-279.

International Astronautical Congress, 10th London, 1959, Proceedings, F. Hecht, Ed., Vienna, Springer-Verlag, 2 Hecht, Ed., Vient vols., 1959, 946 pp.

> Some Results of the Measurement of the Mass Spectrum of Positive Ions by the 3rd Artificial Earth Satellite, by V. G. Istomin, vol. 2, pp. 756-767

The Meteoritic Environment from Direct Measurements, by M. Dubin, vol. 2, pp. 768-771.

The Abundances of the Elements in the Solar Atmosphere, by Leo Goldberg, Edith A. Muller, and Lawrence H. Aller, Astrophysical J., Supplement Series, vol. Astrophysical J., Supplement S 5, no. 45, Nov. 1960, pp. 1-138.

Internal Atmospheric Gravity Waves at Ionospheric Heights, by C. O. Hines, Canadian J. Physics, vol. 38, Nov. 1960, рр. 1441-1481.

Energy Spectra of the Electron-Proton Component in Extensive Atmospheric Showers Near the Shower Axis, by O. I. Dovzhenko, S. I. Nikol'skii and I. V. Rakobol'skaya, Soviet Physics-JETP, vol. 11, no. 5, Nov. 1960, pp. 981–986.

Human Factors and Bio-Astronautics

Bioengineering Problems in Early Manned Space Flight, by R. W. Lawton, B. J. Smith and D. R. Ekberg, N. Y. Acad. Sciences, Annals, vo 2, Feb. 26, 1960, pp. 29-74. vol. 84, article

New Evidence of Martian Life, by M. H. Briggs, Spaceflight, vol. 2, no. 8, Oct. 1960, pp. 237–238, 259.

Studies on Algal Gas Exchangers with Reference to Space Flight, by A. R. Kroll, and B. Kok, RIAS, Inc. Monograph and B. Kok, RI 60-16, 1960, 12 pp.

Proceedings of Conference on Radiation Problems in Manned Space Flight, Appendix A: Primary Cosmic Rays, by George J. Jacobs and J. R. Winckler, NASA TN D-588, Dec. 1960, 99 pp.

Proceedings of Meeting on Problems and Techniques Associated with the De-contamination and Sterilization of Spacecraft, Appendix: Sterilization of Interplanetary Vehicles, by Jack Posner, Charles R. Phillips and Robert K. Hoff-man, NASA TN D-771, Jan. 1961, 57 pp.

Manned Space Stations Symposium, Los Angeles, April 20-22, 1960, N. Y. Inst. Aeron. Sciences, 1960, 322 pp. Crew Requirements for an Orbiting Space Station, by R. H. Lowry, pp. 96-99.

Work and Living Space Requirements for Manned Space Stations, by Fred

Work and Living Space Requirements for Manned Space Stations, by Fred A. Payne, pp. 100-103.
Gravity Problems in Manned Space Stations, by C. C. Clark and J. D. Hardy, pp. 104-113, 71 refs.
Man's Contribution to an Operations Space Station Concent by M. A.

Man's Contribution to an Operational Space Station Concept, by M. A. Grodsky and R. D. Sorkin, pp. 114-119. Design of an Operational Ecological System, by E. B. Konecci and N. E. Wood, pp. 137-150.

Wood, pp. 137-150.

A Philosophy of Extremes for the Gaseous Environment of Manned, Closed Ecological Systems, by C. J. Lambertin, pp. 316-322.

Lambertin, pp. 316-322.

Atla

Right Now...

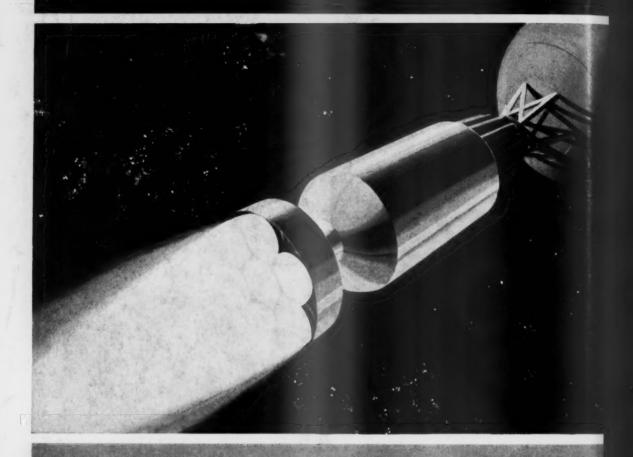
The Air Force's Atlas ICBM is standing ready at Vandenberg and Warren Air Force Bases.

Let everyone remember that!

CONVAIR
DIVISION OF GENERAL DYNAMICS

Alias is built by Convair (Astronautics) Division of General Dynamics and over 3000 associate contractors, subcontractors and suppliers in forty-two states. Additional Atlas bases will become operational with the U.S.A.F. Strategic Air Command in the months immediately ahead.

NUCLEAR ROCKET PROPULSION AT AEROJET-GENERAL



Nuclear rockets, with a performance capability nearly twice that of the highest-specific-impulse chemical rockets, have been of major interest to Aerojef-General for several years.

Exploratory studies were initiated by Aerojet in 1955 to ascertain the feasibility of nuclear rockets, and the technical advances required to develop a successful nuclear propulsion system were determined. This work at Aerojet has undergone continuous expansion under government and company sponsored programs. Included are: preliminary design of engines and vehicles, simulated nuclear engine tests, radiation hazards research, analog computer system design (to simulate nuclear rocket operation), nuclear test facility construction, and the design, development, testing, and manufacture of reactors.

These programs have resulted in aignificant progress toward the development of a practical and reliable nuclear propulsion system. They are based on Aerojet's combined experience in liquid and solid propellant rocketry, nuclear technology, and cryogenics—experience which ensures that the challenge of a new era in propulsion can, and will, be met.



